

# Transient Mathematical Modelling of Loop Heat Pipes and Experimental Validation

by

Hooman Jazebizadeh

A thesis submitted to the Faculty of Graduate and Postdoctoral Affairs in  
partial fulfillment of the requirements for the degree of

Doctor of Philosophy

in

Mechanical Engineering

Carleton University  
Ottawa, Ontario

© 2020, Hooman Jazebizadeh

## **Abstract**

Development of state of the art electronics forces thermal engineers to develop more efficient and innovative heat transfer devices. Modern electronics do not only dissipate more heat per area but also their operation is subject to temperature stability. Loop Heat Pipes offer an important advantage over other heat transfer devices with their unique characteristics. These self-regulated devices utilize the latent heat of the working fluid circulating between a hot source and cold sink by using thermodynamic principles and capillary forces. Experimental work is performed, on two different LHPs under ambient conditions, to investigate the operational characteristics of LHPs and to collect data under different operating conditions for the validation of the numerical model developed in this research. The main investigated characteristics comprise of the operating temperature and its oscillations at given operating conditions, the LHP response to a change in the operating conditions, and the location of the two-phase/liquid interface inside the LHP condenser. Furthermore, the empirical correlations, required to calculate the LHP heat transfer coefficients and pressure drops, are chosen and verified for the numerical model. Following the correlation verification, a modular numerical model is developed and validated to predict the steady-state and transient operation of an LHP with minimum accommodation parameters. The sensitivity studies of the modelling parameters are conducted to investigate their effects on LHP operation. The model can be easily modified or improved because of its modularity feature. Additionally, the minimum number of the accommodation parameters allows the model to predict LHP behavior by relying on only one set of power cycling test results. The mathematical model can be used not only as a design tool in the research and development of new LHPs but also to examine and troubleshoot the operation of an existing LHP in remote locations such as onboard a satellite orbiting Earth.

## Acknowledgements

It was quite a journey. I am now at the end of it.

Thank you, Tarik. Without your guidance and support, I would be lost so many times during this journey.

Thank you, Tarik, John and Bruce. Your approach to research has forever changed mine.

Thank you, Shawn, Juan and Alex. Time spent with you in our laboratory kept me sane.

Thank you, Steve, my Trekkie friend. You are a constant inspiration for me to be a hands-on engineer.

Thank you, Chunyun. Being your partner is the best gift I could imagine during the most challenging times of my journey.

Thank you, mom, dad and my siblings. No amount of words can express my gratitude to you.

So,

Let a new journey begin.

# Table of Contents

<b>Abstract</b> .....	<b>i</b>
<b>Acknowledgements</b> .....	<b>ii</b>
<b>Table of Contents</b> .....	<b>iii</b>
<b>List of Figures</b> .....	<b>vi</b>
<b>List of Tables</b> .....	<b>xi</b>
<b>Nomenclature</b> .....	<b>xii</b>
<b>Chapter 1: Introduction</b> .....	<b>1</b>
1.1 LHP architecture .....	2
1.2 LHP applications .....	5
1.3 LHP operational characteristics .....	6
1.4 LHP control methods .....	10
1.5 Research motivation and objectives .....	12
1.6 Thesis organization .....	13
<b>Chapter 2: Experimental work</b> .....	<b>15</b>
2.1 LHP1 setup.....	15
2.2 LHP2 setup.....	16
2.3 Sink temperature regulation .....	20
2.4 Ambient temperature regulation.....	21
2.5 Applied power regulation.....	21
2.6 Data acquisition and post-analysis .....	23
2.7 Test plans.....	24
2.7.1 Maximum power.....	24
2.7.2 Power cycling.....	25
2.7.3 Sink cycling .....	33
2.8 Uncertainty analysis .....	34
2.9 Summary .....	39
<b>Chapter 3: Working fluid correlations</b> .....	<b>40</b>
3.1 Pressure drop correlations .....	40

3.1.1	Single-phase correlation.....	40
3.1.2	Two-phase flow correlations.....	41
3.1.3	Verification and selection .....	44
3.1.4	Bend correlations .....	48
3.2	Internal flow heat transfer coefficient .....	50
3.2.1	Single-phase flow.....	50
3.2.2	Internal flow convective condensation correlations .....	51
3.2.3	Verification and selection .....	57
3.3	Natural heat transfer coefficient.....	65
3.4	Conductive heat transfer coefficient .....	65
3.5	Summary .....	65
<b>Chapter 4:</b>	<b>Steady-state model.....</b>	<b>67</b>
4.1	Mathematical model.....	69
4.1.1	Evaporator.....	69
4.1.2	Transportation lines .....	71
4.1.3	Condenser .....	73
4.1.4	Reservoir .....	73
4.2	Solution procedure .....	74
4.3	Model validation .....	77
4.3.1	Model validation for LHP1 .....	78
4.3.2	Model validation for LHP2.....	82
4.4	Sensitivity analysis.....	86
4.4.1	Evaporator saddle-to-wick contact conductance .....	86
4.4.2	Condenser contact conductance.....	87
4.4.3	Natural convection heat transfer correlation.....	88
4.4.4	Fluid velocity inside the vapor grooves .....	89
4.4.5	Heat transfer coefficient transition from two-phase to single-phase .....	91
4.4.6	Heat transfer coefficient in the two-phase region .....	93
4.4.7	Viscosity in the two-phase region.....	94
4.4.8	Wick effective thermal conductivity.....	94
4.4.9	Cell length in the transportation lines and condenser .....	94

4.5	Summary .....	97
<b>Chapter 5:</b>	<b>Transient model.....</b>	<b>98</b>
5.1	Mathematical model.....	102
5.1.1	Evaporator.....	102
5.1.2	Transportation lines .....	105
5.1.3	Condenser .....	106
5.1.4	Reservoir.....	106
5.2	Solution procedure .....	107
5.2.1	Algorithm for $T_{int}$ iteration.....	109
5.2.2	Algorithm for cell iteration.....	112
5.2.3	Phase change identification and transition.....	115
5.3	Model validation .....	118
5.3.1	Modelling options.....	118
5.3.2	Model parameters.....	118
5.3.3	Numerical convergence criteria .....	119
5.3.4	Model validation for LHP1 .....	121
5.3.5	Model validation for LHP2.....	130
5.4	Sensitivity analysis.....	138
5.4.1	Thermal inertia of heater block.....	138
5.4.2	Thermal inertia of condenser saddle.....	142
5.4.3	Contact conductance between the heater block and evaporator saddle .....	144
5.4.4	Cell length sensitivity .....	146
5.5	Summary .....	159
<b>Chapter 6:</b>	<b>Concluding remarks.....</b>	<b>161</b>
6.1	Recommendations for future work.....	164
<b>Appendixes.....</b>		<b>166</b>
Appendix A.	LHP1 physical properties .....	166
Appendix B.	LHP2 physical properties .....	168
<b>References .....</b>		<b>171</b>

## List of Figures

Fig. 1 Conventional architecture of an LHP. ....	2
Fig. 2 Complex and advance architecture of LHP. [3] .....	5
Fig. 3 The performance curve of an LHP. ....	7
Fig. 4 Thermodynamic representation of LHP steady-state operation. ....	8
Fig. 5 Schematic of PRVs used in an LHP: (a) three-way and (b) two-way. [23] .....	11
Fig. 6 Effect of two-way PRV on the LHP thermodynamic cycle. ....	12
Fig. 7 Photo of LHP1. ....	15
Fig. 8 Thermocouple locations on LHP1. ....	16
Fig. 9 Photo of LHP2. ....	17
Fig. 10 Sink plate model. ....	18
Fig. 11 Thermocouple locations on LHP2. ....	19
Fig. 12 The fluid line inside the condenser panel (a) three-dimensional model (b) thermal image. .....	20
Fig. 13 RC011 chiller with support plumbing. ....	21
Fig. 14 Equipment used to apply power with wiring. ....	22
Fig. 15 Voltage stability of the AC and DC power supplies at 200 W for LHP1. ....	23
Fig. 16 Results of the maximum applied power tests for LHP2. ....	25
Fig. 17 The overall results of the LHP2-PC5-UP scenario. ....	27
Fig. 18 The performance curve of LHP2 obtained from the LHP2-PC5-UP scenario. ....	29
Fig. 19 The LHP2 condenser temperatures obtained from the LHP2-PC5-UP test. ....	30
Fig. 20 The temperature oscillations in the LHP2-PC5-UP test. ....	32
Fig. 21 The overall results of the LHP1-SC125-UD scenario. ....	34
Fig. 22 Distribution of LHP2 operating temperature at the minimum power. ....	38
Fig. 23 Distribution of LHP2 operating temperature at the maximum power. ....	38
Fig. 24 Continuity of the correlations for the two-phase viscous pressure drop. ....	44
Fig. 25 The measured and predicted results for the 2.58 mm-diameter stainless-steel pipe: (a) the pressure drop gradient and (b) the experimental mass flux. ....	46
Fig. 26 Prediction versus measurement of the viscous pressure gradient for the 2.58 mm-diameter stainless-steel pipe. ....	47
Fig. 27 The geometrical properties of a bend contributing to a pressure drop of fluid flow. (modified) [45]. ....	49
Fig. 28 A simplified model of flow structure and condensation pattern. [58]. ....	52
Fig. 29 Geometrical parameters for the condensation of the stratified flow pattern at the pipe cross- section. (modified) [58] and [60]. ....	53
Fig. 30 Flow pattern diagram for ammonia. (modified) [58] .....	55
Fig. 31 Assessment of the continuity of the correlations for the two-phase heat transfer coefficient. .....	58

Fig. 32 Underprediction of the two-phase heat transfer coefficient in the vicinity of the saturated liquid. ....	59
Fig. 33 Continuous heat transfer coefficient from saturated liquid to saturated vapor.....	60
Fig. 34 The measured and predicted results for the 2.16mm-diameter stainless-steel pipe: (a) the heat transfer coefficient and (b) the mass flux.....	62
Fig. 35 Prediction versus measurement of the heat transfer coefficient for the 2.16 mm-diameter stainless-steel pipe. ....	63
Fig. 36 Flow pattern diagram for the 2.16mm-diameter stainless-steel pipe.....	64
Fig. 37 The evaporator schematic (a) cross-section and (b) cell network. ....	70
Fig. 38 Schematic of the staggered grid in the axial direction for fluid flow. ....	72
Fig. 39 The condenser schematic (a) cross-section and (b) cell network. ....	73
Fig. 40 Top-level algorithm of the steady-state model. ....	75
Fig. 41 Comparison of the experimental and calculated reservoir temperatures for LHP1. ....	79
Fig. 42 Comparison of the experimental and calculated evaporator saddle temperatures for LHP1. ....	80
Fig. 43 Comparison of the experimental and calculated temperatures of the vapor line inlet for LHP1. ....	80
Fig. 44 Comparison of the experimental and calculated evaporator saddle temperatures for LHP1. ....	81
Fig. 45 Comparison of the experimental and calculated reservoir temperatures for LHP2. ....	82
Fig. 46 Comparison of the experimental and calculated evaporator saddle temperatures for LHP2. ....	84
Fig. 47 Comparison of the experimental and calculated temperatures of the vapor line inlet for LHP2. ....	84
Fig. 48 Comparison of the experimental and calculated evaporator saddle temperatures for LHP2. ....	85
Fig. 49 Effect of the evaporator saddle-to-wick contact conductance [ $\text{W}/\text{m}^2 \text{ K}$ ] on the operating temperature of (a) LHP1 and (b) LHP2. ....	86
Fig. 50 Effect of the evaporator saddle-to-wick contact conductance [ $\text{W}/\text{m}^2 \text{ K}$ ] on the saddle temperature of (a) LHP1 and (b) LHP2. ....	87
Fig. 51 Effect of the condenser contact conductance [ $\text{W}/\text{m}^2 \text{ K}$ ] on the operating temperature of (a) LHP1 and (b) LHP2. ....	88
Fig. 52 Effect of multiplier for the natural convection heat transfer correlation on the operating temperature of (a) LHP1 and (b) LHP2. ....	88
Fig. 53 Effect of the fluid velocity correction factor on the operating temperature of (a) LHP1 and (b) LHP2. ....	90
Fig. 54 Effect of the fluid velocity correction factor on the superheat temperature of (a) LHP1 and (b) LHP2. ....	91
Fig. 55 Effect of the transition quality for the vapor/two-phase transition on the operating temperature of (a) LHP1 and (b) LHP2. ....	92

Fig. 56 Effect of the two-phase heat transfer correlations on the operation of (a) LHP1 and (b) LHP2.....	93
Fig. 57 Mass flux inside the condenser and stratified flow limit for (a) LHP1 and (b) LHP2. ....	94
Fig. 58 Effect of the length of the vapor-line cell on the simulation time of (a) LHP1 and (b) LHP2. ....	95
Fig. 59 Effect of the length [cm] of the liquid-line cell on the model results of (a) LHP1 and (b) LHP2.....	96
Fig. 60 Effect of the length [cm] of the condenser cell on the operating temperature of (a) LHP1 and (b) LHP2.....	96
Fig. 61 Comparison of the results of different wick-modelling approaches as the applied power changes.....	104
Fig. 62 Effect of different reservoir solution methods as the applied power changes.....	107
Fig. 63 Top-level algorithm of the transient model.....	108
Fig. 64 $T_{int}$ iterative algorithm of the transient model.....	110
Fig. 65 Cell iterative algorithm of the single-phase fluid.....	113
Fig. 66 Cell iterative algorithm of the two-phase fluid.....	114
Fig. 67 Saturated fluid approach to a phase change.....	115
Fig. 68 Time-division approach to a phase change.....	115
Fig. 69 Sink/source approach to a phase change.....	116
Fig. 70 Comparison of the experimental and calculated temperatures for LHP1 at 5°C sink temperature.....	121
Fig. 71 Temperature difference between the experimental and calculated results for LHP1: (a) absolute and (b) relative.....	123
Fig. 72 Steady-state temperatures from the experimental and calculated results for LHP1: (a) value (b) absolute difference and (c) relative difference.....	124
Fig. 73 Time lag from the experimental and calculated results for LHP1: (a) value (b) absolute difference and (c) relative difference.....	125
Fig. 74 Comparison of the experimental and calculated temperatures for LHP1 at 10°C sink temperature.....	128
Fig. 75 Comparison of the experimental and calculated temperatures for LHP1 during the sink cycling.....	129
Fig. 76 Comparison of the experimental and calculated temperatures for LHP2 at 5°C sink temperature.....	131
Fig. 77 Temperature difference between the experimental and calculated results for LHP2: (a) absolute and (b) relative.....	132
Fig. 78 Steady-state temperatures from the experimental and calculated results for LHP2: (a) value (b) absolute difference and (c) relative difference.....	133
Fig. 79 Time lag from the experimental and calculated results for LHP2: (a) power-up value (b) power-down value (c) absolute difference and (d) relative difference.....	134

Fig. 80 Comparison of the experimental and calculated temperatures for LHP2 at 10°C sink temperature. ....	136
Fig. 81 Comparison of the experimental and calculated temperatures for LHP2 during the sink cycling.....	137
Fig. 82 Effect of the heater-block thermal inertia on the operating temperature of LHP2.....	139
Fig. 83 Effect of the heater-block thermal inertia on the $T_{int}$ iteration of LHP2 after the power change. ....	140
Fig. 84 Effect of the heater-block thermal inertia on the mass flow rate of LHP2.....	140
Fig. 85 Effect of the heater-block thermal inertia on the operating temperature of LHP1 with a zoomed-in transient section. ....	141
Fig. 86 Effect of the heater-block thermal inertia on the two-phase/liquid interface of LHP1..	142
Fig. 87 Effect of the thermal inertia of the condenser saddle on the operating temperature of LHP2. ....	143
Fig. 88 The operating temperature difference as the condenser saddle thermal inertia changes for LHP2. ....	143
Fig. 89 Effect of the thermal inertia of the condenser saddle on the inlet velocity of the vapor line of LHP2.....	144
Fig. 90 Effect of the contact conductance of the heater block on the operating temperature of LHP1 with a zoomed-in transient section. ....	145
Fig. 91 Effect of the heater-block contact conductance on the two-phase/liquid interface of LHP1. ....	146
Fig. 92 Effect of the cell length of the liquid line on the time steps for LHP2.....	147
Fig. 93 Effect of the cell length of the liquid line on the operating temperature in LHP2. ....	147
Fig. 94 Effect of the cell length of the liquid line on the two-phase/liquid interface location in LHP2 after the power change. ....	148
Fig. 95 Effect of the cell length of the liquid line on the operating temperature of LHP1 towards to the end of the VCM.....	149
Fig. 96 Effect of the cell length of the liquid line on the operating temperature of LHP1 in the FCM. ....	150
Fig. 97 Effect of the cell length of the condenser on the time steps of LHP2. ....	151
Fig. 98 Effect of the cell length of the condenser on the operating temperature of LHP2. ....	151
Fig. 99 Effect of the cell length of the condenser on the two-phase/liquid interface location in LHP2 after the power change. ....	152
Fig. 100 Effect of the cell length of the condenser on the operating temperature of LHP1 towards to the end of the VCM. ....	153
Fig. 101 Effect of the cell length of the condenser on the operating temperature of LHP1 in the FCM. ....	154
Fig. 102 Effect of the cell length of the vapor line on the operating temperature of LHP2. ....	155
Fig. 103 Effect of the cell length of the vapor line on the vapor/two-phase interface in LHP2 after the power change. ....	156

Fig. 104 Effect of the cell length of the vapor line on the operating temperature of LHP1 in the VCM with a zoomed-in transient section. ....	157
Fig. 105 Effect of the cell length of the vapor line on the time steps for LHP1 in the VCM.....	158
Fig. 106 Effect of the cell length of the liquid line on the operating temperature of LHP1 in the FCM. ....	159

## List of Tables

Table 1 Test scenarios of power cycling.....	25
Table 2 Test scenarios of sink cycling.....	33
Table 3 Measurement accuracy of primary variables.....	35
Table 4 The systematic uncertainty in measuring the applied power.....	35
Table 5 The total systematic uncertainty of the experiments.....	36
Table 6 The random and total uncertainty of the experiments.....	37
Table 7 Correlations for the homogeneous viscosity of a two-phase flow. [47].....	41
Table 8 Correlations of $XLM$ and $c$ in the LM correlation. [48], [49] and [50].....	43
Table 9 The average relative errors of the predicted pressure drops for the two-phase flow.....	45
Table 10 Comparison of the computational time of the different two-phase correlations.....	48
Table 11 The flow-pattern-dependent parameters required for the P&H correlation.....	56
Table 12 The average relative errors of the predicted heat transfer coefficient for the two-phase flow.....	61
Table 13. Phase-change detection.....	76
Table 14 Matched parameters for the LHP1 model.....	78
Table 15 The average and maximum errors of the predicted values for LHP1.....	81
Table 16 Matched parameters of the model for LHP2.....	83
Table 17 The average and maximum errors of the predicted values for LHP2.....	85
Table 18 Summary of the different solution methods to model the evaporator wick.....	103
Table 19 Summary of approaches to phase transition.....	117
Table 20 Summary of the selected approaches in transient model validation.....	118
Table 21 Model parameters for LHP1 and LHP2.....	119
Table 22 Summary of the parameters for the convergence and stability of the model.....	120
Table 23 The simulation-dependent parameters for the LHP1 validation.....	122
Table 24 Comparison of the experimental and numerical results for the performance variables for LHP1.....	128
Table 25 Comparison of the experimental and numerical results for the performance variables for LHP1 sink cycling.....	130
Table 26 The simulation parameters for the LHP2 validation.....	131
Table 27 The model deviation of the performance variables from the experiment data for LHP2.....	136
Table 28 Comparison of the experimental and numerical results for the performance variables for the LHP2 sink cycling.....	138

## Nomenclature

$A$	Area [m <sup>2</sup> ]
$B$	Bias or systematic uncertainty
$C$	Conductance [W/K], heat capacity [J/K]
$c_p$	Specific heat at constant pressure [J/kg K]
$D$	Diameter [m]
$e$	Error
$f$	Friction (Fanning) factor
$f_i$	Interfacial roughness correction factor
$F$	Darcy friction factor
$Fr$	Froude number
$g$	Gravitational acceleration [m/s <sup>2</sup> ]
$G$	Mass flux [Kg/m <sup>2</sup> s]
$h$	Heat transfer coefficient [W/m <sup>2</sup> K]
$h_c$	Thermal contact conductance [W/m <sup>2</sup> K]
$h$	Specific enthalpy [J/kg]
$I$	Current [A]
$k$	Thermal conductivity [W/mK]
$L$	Length [m]
$\dot{m}$	Mass flow rate [kg/s]
$n$	Number of data points or cells
$Nu$	Nusselt number
$P$	Pressure [Pa], applied power [W], perimeter [m]
$Pr$	Prandtl number
$\dot{Q}$	Rate of heat transfer [W]
$R$	Pore radius [m], electrical resistance [ $\Omega$ ], bend radius [m]
$Re$	Reynolds number
$S$	Random uncertainty
$T$	Temperature [ $^{\circ}$ C]
$t$	Thickness [m], time [s]
$u$	Velocity [m/s]
$u$	Internal energy [J]
$V$	Volume [m <sup>3</sup> ], voltage [V]
$We$	Weber number
$X$	Vapor quality
$X_{LM}$	Lockhart-Martinelli parameter
$X_{tt}$	Martinelli parameter for the turbulent-turbulent flow
$Z$	Height [m]
<b>Greek symbols</b>	
$\alpha$	Bend angle [ $^{\circ}$ ], void fraction, multiplier for ambient heat transfer coefficient
$\beta$	Velocity correction factor inside vapor grooves

$\varepsilon$	Surface roughness [ $m$ ], convergence criteria
$\delta$	Liquid film thickness [ $m$ ], flow direction indication
$\mu$	Dynamic viscosity [ $Pa\ s$ ]
$\kappa$	Permeability [ $m^2$ ]
$\Phi$	Two-phase multiplier
$\rho$	Density [ $kg/m^3$ ]
$\varphi$	A generic fluid property
$\sigma$	Surface tension [ $N/m$ ]
$\theta$	Contact angle between the saturated liquid and wick [ $^\circ$ ], pipe angle for the free convective surface at a stratified flow [ $^\circ$ ]
$\xi$	Pressure drop coefficient
$\omega$	Multiplier
<b>Subscripts</b>	
<i>2ph</i>	Two phase
<i>95</i>	95% confidence
<i>amb</i>	Ambient
<i>app</i>	Applied heat
<i>c</i>	Characteristic
<i>cap</i>	Capillary
<i>cond</i>	Conduction
<i>CS</i>	Condenser saddle
<i>CR</i>	Condenser riser
<i>d</i>	Dimensionless
<i>DAQ</i>	Data Acquisition System
<i>eff</i>	Effective
<i>eva</i>	Evaporator
<i>ES</i>	Evaporator saddle
<i>fld</i>	Fluid
<i>Gr</i>	Grooves
<i>HB</i>	Heater block
<i>homo</i>	Homogeneous
<i>I</i>	Current
<i>IA</i>	Intermittent/Annular
<i>in</i>	Inner
<i>int</i>	Interface
<i>j</i>	Junction number
<i>lam</i>	Laminar
<i>liq</i>	Liquid
<i>ll</i>	Laminar-laminar flow
<i>LL</i>	Liquid line
<i>lt</i>	Laminar-turbulent flow
<i>m</i>	Cell number
<i>P</i>	Power
<i>Par</i>	Parallel

<i>P&amp;H</i>	Park and Hrnjak
<i>res</i>	Reservoir
<i>sat</i>	Saturation
<i>Ser</i>	Series
<i>sld</i>	Solid
<i>strat</i>	Stratified flow
<i>TC</i>	Thermocouple
<i>tl</i>	Turbulent-laminar flow
<i>Tra</i>	Traviss
<i>tt</i>	Turbulent-turbulent flow
<i>tur</i>	Turbulent
<i>V</i>	Voltage
<i>vap</i>	Vapor
<i>VL</i>	Vapor line
<b><i>Superscripts</i></b>	
<i>i</i>	Time step

# Chapter 1: Introduction

Development of state of the art electronic components forces thermal engineers to employ novel heat transfer techniques because the components not only dissipate more heat per area but also their operation is subject to temperature stability. Among the most efficient heat transfer techniques are two-phase capillary devices including Heat Pipes (HPs), Loop Heat Pipes (LHPs) and Capillary Pumped Loops (CPLs) [1]. These self-regulated devices utilize the latent heat of the working fluid circulating between a hot source and cold sink by using thermodynamic principles and capillary forces.

HPs are passive two-phase heat transfer devices comprised of a working fluid contained inside a sealed pipe with a porous inner surface. An HP transfers heat applied to its evaporator section (hot end) to its condenser (cold end) using the latent heat of the working fluid flowing between the two ends. Although the conceptual idea of HP proposed in 1942, the first operational HP was designed and tested by Grover in 1963. In the beginning, HPs were mainly used in the thermal control system of spacecraft. GOES-B launched in 1968 was the first satellite using an HP to reduce temperature gradients of the onboard electronics. [2]

LHP concept was devised in the former Soviet Union in the 1970s to address a higher heat dissipation, robustness and reliability required to cool the electronics used in aerospace systems. Like HPs, an LHP works passively. Hence, it is a suitable solution in the thermal system design of a spacecraft, and several spacecraft have already flown in orbit with LHPs [3] and [4].

LHP mainly consists of an evaporator, a condenser and a reservoir or a compensation chamber. The evaporator connects to the condenser via a vapor line, and the loop closes with a liquid line that connects the condenser to the reservoir. The capillary force is created in the primary wick located in the evaporator.

Despite the design complexity and related drawbacks, LHP provides more gains when compared to the other capillary two-phase devices particularly conventional heat pipes in terms of start-up, maximum heat transfer ability, working in microgravity or adverse gravity, and flexible transport lines with smooth walls.

LHPs and CPLs are similar in architecture and operation. However, their main difference lays on how their reservoirs are linked to the evaporator thermally and hydrodynamically. The LHP reservoir is directly attached to the evaporator, and a secondary wick ensures that the fluid flows from the reservoir to the evaporator primary wick. The CPL reservoir is not in the vicinity of the evaporator, and a fluid line brings the fluid from the reservoir to the evaporator. The direct link between the evaporator and reservoir in an LHP contributes to robust start-ups and operation even though it adds more complexity in design and operation. [5]

## 1.1 LHP architecture

The main components of an LHP were introduced in the previous section. This section addresses the LHP architecture in more depth. Figure 1 illustrates the architecture of a conventional LHP. The wick is a fine porous structure tightly fitted inside the evaporator. The other LHP components are built from smooth pipes.

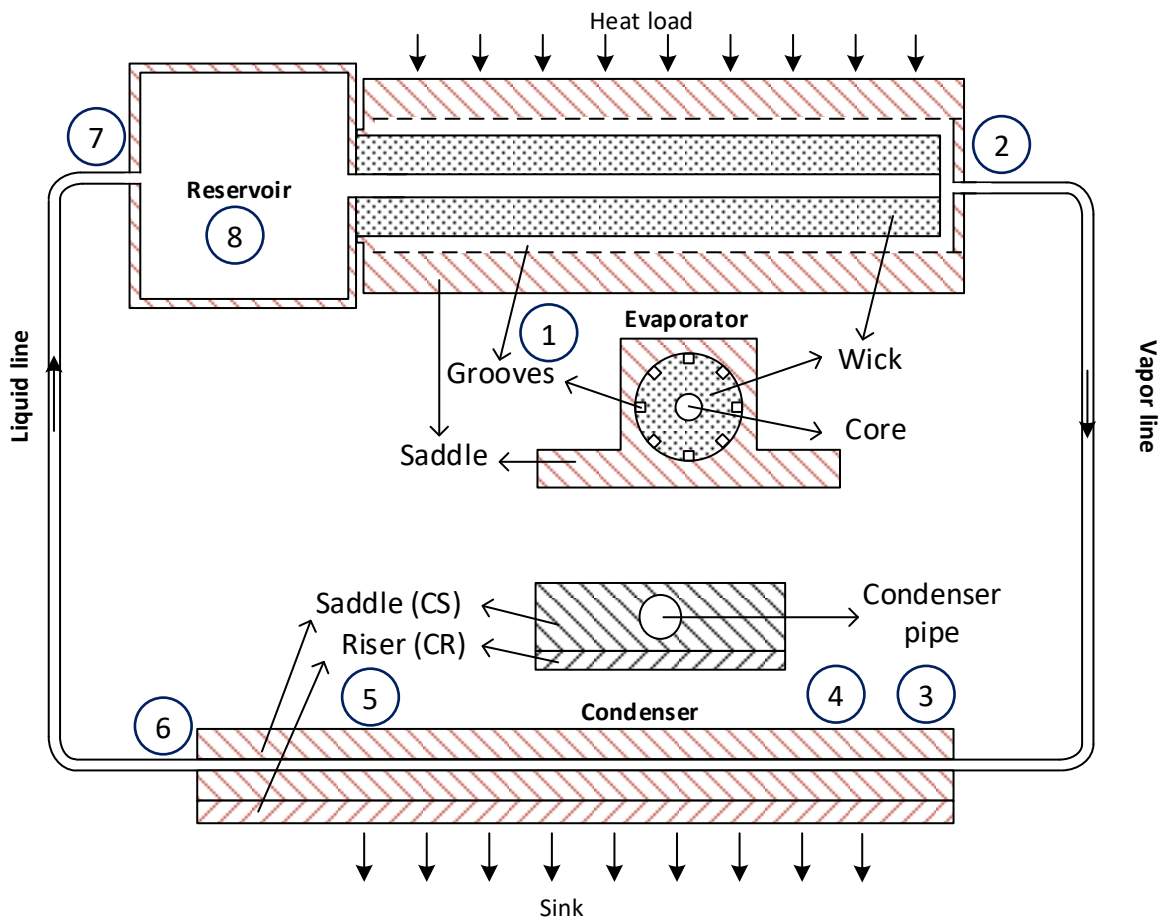


Fig. 1 Conventional architecture of an LHP.

The reservoir section comprises of the evaporator core and fluid inventory where holding the excess working fluid. Therefore, the reservoir volume should be sized to accommodate the excess fluid and density changes in all operating conditions. A secondary wick may be used to connect the reservoir with the primary wick. The evaporator core can be considered as part of the reservoir where the secondary wick is in contact with the primary wick.

The evaporator consists of a saddle, casing, primary wick and vapor grooves. The saddle and casing are used to attach a heat source, such as a power amplifier, thermally and physically to the

LHP. The vapor grooves collect the working fluid evaporated from the primary wick external surface in order to facilitate its movement to the vapor line. The primary wick has fine pores to develop the highest capillary force as possible. Compared to the primary wick, the secondary one is made of large pores since the surface tension is just utilized to supply the liquid to the primary wick in case of adverse gravity when the evaporator is located above the reservoir or in orbit microgravity.

The evaporator-reservoir link closely couples the two components hydraulically and thermally which makes LHPs resistant to dry out; however, it may also result in LHP performance degradation and fluctuation of the operating temperature. Several modifications are proposed and implemented to decouple the thermal link to improve the LHP performance. For instance, a bayonet tube is introduced to directly supply the subcooled liquid from the liquid line to the evaporator core. The LHP design with bayonet influences both the steady-state and transient operation of the LHP [6].

The vapor and liquid transportation lines are made from smooth walled pipes with a small diameter. They can be shaped and bent to fit in tight places. They can also be made from flexible tubing enabling the use of deployable radiators. Moreover, the condenser can be made from the same pipe as the transportation line with the same or bigger diameter, and it is usually connected to a sink environment via a saddle. The saddle can use any heat transfer method to dissipate heat to the sink.

LHPs are usually constructed from stainless steel. Despite of its low thermal conductivity, stainless steel retains high material strength and welding capability. Materials with a higher thermal conductivity, such as aluminum and copper, have been employed less in LHP manufacturing. The wick structure is widely manufactured from sintered nickel or titanium powders. A suitable LHP wick material possesses a small pore size, a wide range of operating temperatures and required strength.

The most common working fluid of LHPs is ammonia particularly in aerospace applications. For terrestrial applications, other working fluids such as water, methanol and ethanol are commonly used. The major criteria in selecting a working fluid are the latent heat of evaporation, surface tension, compatibility with the LHP materials and other thermophysical properties in the LHP operating range. For instance, carbon dioxide has not been used as the working fluid since it has low critical temperature (26 °C), low latent heat and high saturated pressure. The working fluid should exhibit the following characteristics: [1], [2] and [3]

- The fluid should be stable thermally and chemically over its lifetime. For instance, the LHP installed onboard the geostationary communication satellite should flawlessly operate for more than 15 years.
- The high latent heat is required to maximize the ratio of the heat transfer capability to the mass flow rate. This maximization reduces the size and mass of the LHP unit.

- The slope of the pressure-temperature curve  $\left(\frac{dP}{dT}\right)_{sat}$  should be high enough to facilitate the fluid flow from the evaporator to the reservoir. The pressure gradient between the evaporator and reservoir is the driving force to circulate the working fluid in the presence of a low temperature difference between the evaporator and reservoir.
- The fluid should have low viscosity in both liquid and vapor phases to reduce the pressure drop across the LHP. The lower pressure drop relaxes the requirement on  $\left(\frac{dP}{dT}\right)_{sat}$ .
- The fluid also should maintain high surface tension across the range of the operating temperature. The surface tension is a critical factor in producing the capillary forces on the wick outer surface.

The advantages of LHPs can be summarized as follows:

- LHP can be implemented in complex geometries because of flexibility in its transport lines.
- The overall thermal conductance of LHP is much higher than its predecessor HP. Hence, LHP is able to transfer higher heat fluxes between the same heat source and sink.
- Gravity has a minimum influence on an LHP operation compared to other type of two-phase heat transfer systems. Hence, LHPs provide more design flexibility for terrestrial applications. For space applications, the thermal system using an LHP design can be tested on ground making it possible to analyze the LHP operation in microgravity.
- LHP behaves like a diode in an electrical circuit as it transfers heat in one specific direction from the evaporator to the condenser.

The LHP architecture can be expanded by introducing different numbers of evaporators and condensers integrated in various ways, as shown in Fig. 2. These advanced architectures, particularly the multiple evaporator one, provide promising solutions in thermal control of spacecraft where there are multiple heat sources and sinks with varying conditions and when the designer tries to reduce the size and mass of the spacecraft components.

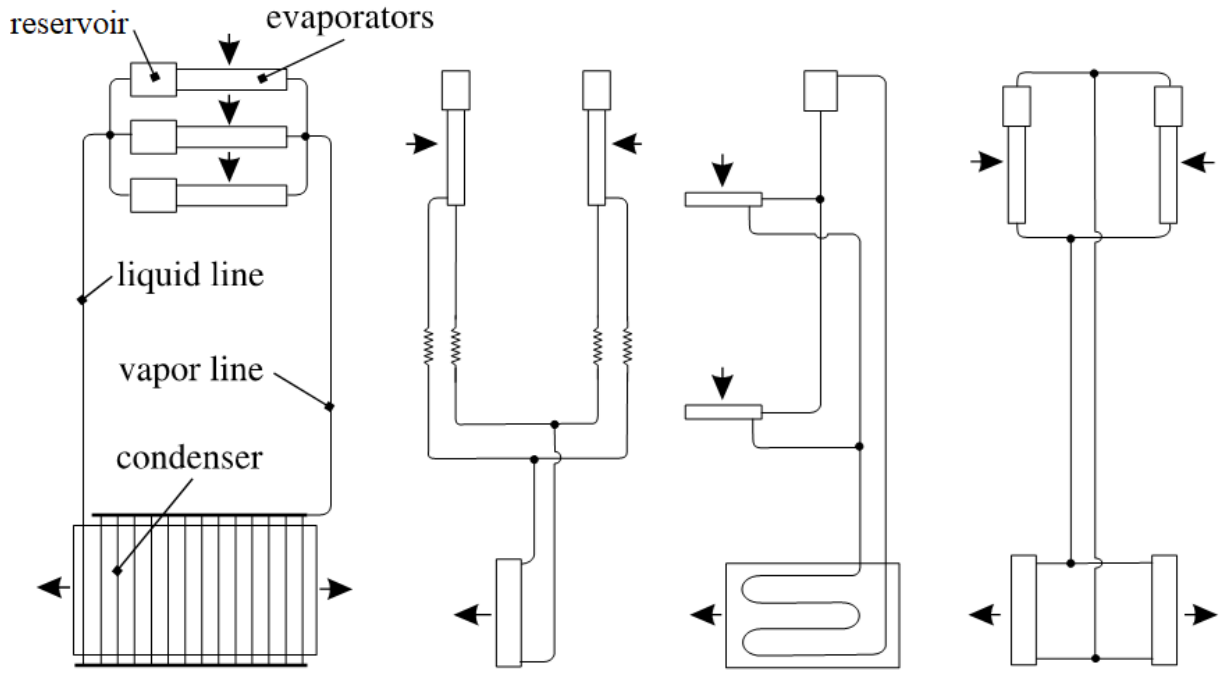


Fig. 2 Complex and advance architecture of LHP. [3]

## 1.2 LHP applications

Currently, LHP has been primarily utilized in space applications. Similar to many engineering systems, the application of LHP started with a technology demonstration. The Russian Gorizont spacecraft was the first technology demonstration satellite with an LHP launched in 1989 [7]. Gorizont's LHP consisted of three evaporators in parallel and a condenser attached to a radiative heat exchanger. The working fluid was Freon-11 which caused problems in the LHP start-up at cold temperatures [3]. The successive in-orbit experiment onboard of Granat spacecraft employed propylene as the working fluid from 1989 to 1996, and the collected telemetry during this period validated the operation of LHP in the space environment [8] and [9]. In the USA, LHP experiments were carried out in two space shuttle demonstration missions in STS-83 and STS-94 in 1997. These LHPs were equipped with titanium wicks and used ammonia as a working fluid. The successful operation of the LHPs was demonstrated during the flight [10].

The Russian Obzor was the first satellite with a thermal control system using LHPs, one unit with propylene and two others with ammonia, to cool optical payloads [11]. A few of the recent space missions with an LHP-based thermal control system have been summarized here:

- ICESat spacecraft employed two propylene LHPs with an active temperature control unit to cool the laser payload called GLAS. The flight data showed only one anomaly in the operation period of six years from 2003 to 2009. [3] and [12]

- Inmarsat-4, with 6 LHPs onboard, was launched in 2005 to geostationary orbit. [13]
- JAXA ETS-VIII (KIKU-8) has equipped with an LHP that has a deployable condenser-radiator. The satellite was launched in 2006, and the flight data over five years showed successful implementation of flexible transportation lines. [14]
- In the Japanese Experiment Module on the International Space Station, an LHP-based system has been used since 2009 to dissipate the heat generated by the CCD sensors. The LHP consists of two condenser-radiator units and several heaters to facilitate startup and shutdown purposes. [4] and [15]
- The TacSat-4, launched in 2011, had an ammonia LHP to thermally connect the COMMX payload to two heat pipes, and flight data showed an overheat problem of its payload. [16]
- The X-ray astronomy satellite (Hitomi) ASTRO-H launched in 2016 carried four LHPs to transfer heat from the payload cryocoolers to two radiators mounted on different sides of the satellite. The LHPs had worked nominally during the launch and in-orbit until the satellite was lost due to attitude control problems. [17] and [18]
- Goes-17 launched in 2018 uses two LHPS in the cooling systems of the ABI payload. However, the LHPs could not effectively transfer the heat load to the radiators. This LHP issue increased the operating temperature by 16°C and degraded the payload performance. [19]

### 1.3 LHP operational characteristics

This section addresses how an LHP works, and some important characteristics of its operation are also discussed. A heat source, e.g. electronics being cooled, provides heat input to the evaporator via its saddle. The main portion of the applied heat evaporates the working fluid on the outer surface of the primary wick. This evaporation surface accommodates the liquid/vapor interface and resulting capillary force. The vapor collected by the vapor grooves, as shown in Fig. 1, becomes superheated by absorbing more heat from the evaporator saddle. The superheated vapor leaving the evaporator has temperature and pressure higher than those of the fluid in the reservoir. The primary wick acts as a thermal lock because of its thermal resistance. The wick resistance is not infinite, and a portion of the applied heat called “heat leak” reaches the reservoir through the wick and casing to increase the fluid temperature in the reservoir. The amount of heat leak is directly proportional to the temperature difference between the evaporator and reservoir. This temperature difference is essential for the LHP startup since it creates pressure difference across the primary wick. This phenomenon can be used for start-up and shut down via implementing heaters on the reservoir and evaporator to control the temperature difference.

In addition to the thermal lock, the wick functions as a hydraulic lock because the capillary forces on the evaporation surface prevent the high-pressure vapor from penetrating inside the wick and subsequently reach the reservoir. So, the pressure difference between the evaporator grooves and reservoir results in the circulation of the working fluid through the transportation lines. The

superheated vapor travels to the condenser via the vapor line and exchanges heat with the surrounding.

The working fluid at the condenser first changes thermodynamic state from superheated vapor to two-phase. The fluid remains in a two-phase state until the whole latent heat dissipates to the sink. The fluid pressure continues to drop because of viscous forces acting on the flow. After the full condensation inside the condenser, the saturated liquid is subcooled before leaving the condenser. The location of the two-phase/liquid interface is an important factor in LHP performance analysis. If the interface is inside the condenser (condenser opening), the LHP is in a Variable Conductance Mode (VCM). As the interface moves to the end of the condenser, the LHP works in a Fixed Conductance Mode (FCM). Figure 3 shows the conductance regions on a typical LHP performance curve. The LHP conductance is defined as the ratio of the applied power (heat load applied to the LHP evaporator) to the temperature difference between the reservoir and open condenser, Eq. (1).

$$C_{LHP} = \frac{\dot{Q}_{applied}}{(T_{res} - T_{cond})} \quad (1)$$

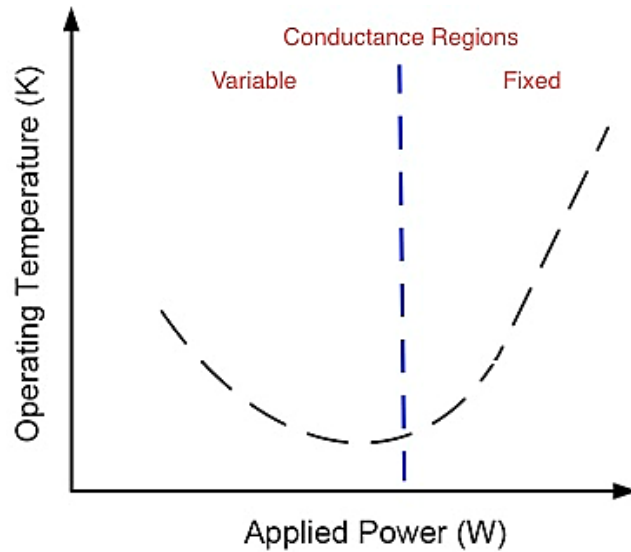


Fig. 3 The performance curve of an LHP.

Then, the subcooled liquid is transported through the liquid line to the reservoir. The heat exchange of the fluid with the surroundings in the liquid line determines the thermodynamic state of the liquid entering the reservoir and consequently influences the LHP performance. The LHP operation reaches a steady state if the heat exchange in the reservoir satisfies the energy balance presented in Eq. (2).

$$\dot{Q}_{heat\ leak} + \dot{Q}_{res-amb} + \dot{Q}_{subcooling} = 0 \quad (2)$$

where  $\dot{Q}_{res-amb}$  is the heat exchange between the reservoir and ambient.  $\dot{Q}_{subcooling}$  is defined as the enthalpy difference between the flows entering and leaving the reservoir. The reservoir saturation temperature is usually defined as the operating temperature of the LHP since measuring the evaporator temperature is more difficult, and the difference between these two is very small.

One of the LHP important characteristics is auto-regulation, which means that the LHP can adjust its operation temperature when any of the boundary conditions, including the heat load, sink or surrounding temperature, changes. For instance, reducing the sink temperature causes a shorter length of the two-phase flow in the condenser and more subcooling. Then, the liquid entering the reservoir has a lower temperature. This results in an increase of the heat leak to compensate for the additional subcooling. Hence, less amount of applied heat is available to superheat the vapor decreasing the operation temperature of the LHP. Thus, the LHP reaches a new equilibrium state.

The LHP operation explained above can also be presented thermodynamically on a P-T diagram as shown in Fig. 4. The temperature axis is exaggerated for greater visibility, and the location of each fluid state in LHP is indicated in Fig. 1. The pressure difference between points 1 and 9 represents the total pressure drop in the LHP. The capillary force on the meniscus compensates for this drop to prevent vapor penetration through the wick. Point 9 in Fig. 4 corresponds to a metastable state of the fluid just under the meniscus.

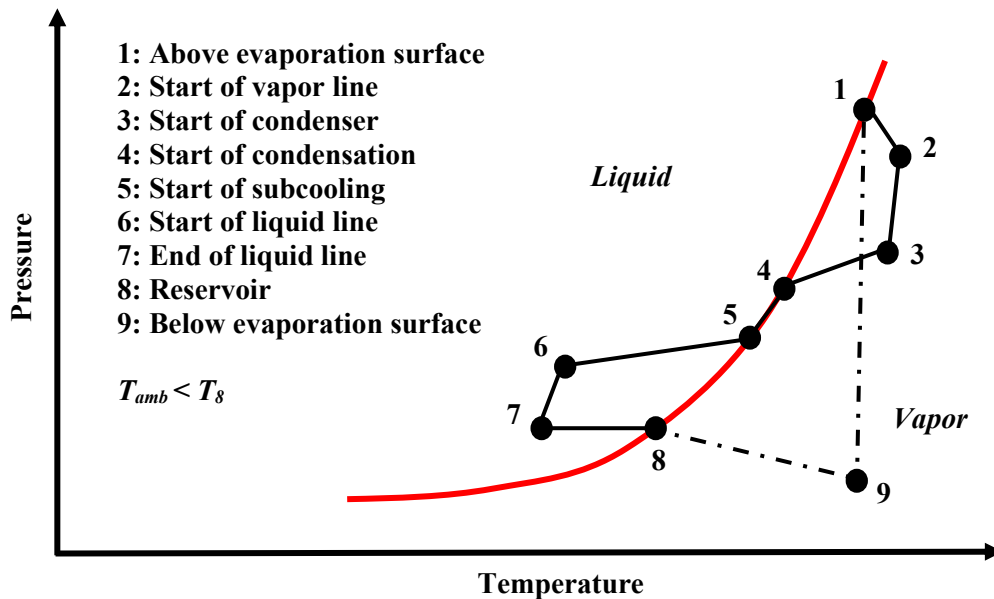


Fig. 4 Thermodynamic representation of LHP steady-state operation.

The LHP operation is subject to several limitations of heat and mass transfer. The major limitations include the temperature gradient of the evaporator and reservoir, capillary pressure, and boiling [1]

and [3]. A sufficient pressure difference between the evaporator and reservoir is required to start the LHP and maintain the circulation of the working fluid, as expressed in Eq. (3).

$$\Delta P_{1-8} = \left( \frac{dP}{dT} \right)_{sat} \Delta T_{1-8} \quad (3)$$

where  $\left( \frac{dP}{dT} \right)_{sat}$  is obtained from the working fluid properties as explained earlier. Therefore, a specific temperature difference between the evaporator and reservoir is required to start-up the fluid circulation. The LHP may reach its maximum operating temperature without a start-up if the required temperature difference is not attained.

The capillary pressure created across the meniscus should be higher than the LHP total pressure drop to maintain the hydraulic lock between the evaporator and reservoir. Otherwise, the high-pressure vapor penetrates the wick causing the LHP operation to cease. This limit can be formulated by Eq. (4).

$$\Delta P_{cap} \geq \Delta P_{VL} + \Delta P_{con} + \Delta P_{LL} + \Delta P_{wick} \quad (4)$$

where the terms on the right side present the fluid pressure drop across each LHP. The capillary pressure can be obtained from Eq. (5).

$$\Delta P_{cap} = \frac{2\sigma}{R} \cos \theta \quad (5)$$

where  $\sigma$  is the surface tension.  $R$  is the effective pore radius of the wick, and  $\theta$  is the meniscus contact angle.

The viscous or vapor-pressure limit is also imposed on LHP operation particularly in a low applied power and cryogenic operating temperature. The viscous limit should be monitored to ensure that the achievable absolute pressure required to establish the pressure difference in the. A low absolute pressure results in a low or no mass flow rate in the loop which degrades the heat transfer capability. This limit is formulated and analyzed in depth in [20].

Although LHPs have a better tolerance of the boiling limit than HPs, the boiling may interrupt the LHP operation if it occurs below the evaporation surface or inside the liquid line. The boiling inside the wick, although very unlikely, may generate vapor bubbles that may disturb the formed meniscus during the venting out. This limit is formulated using the cluster nucleation theory by calculating the superheat limit. Then for each applied power, the maximum temperature under the evaporation surface is obtained by solving the wick governing equations. The boiling is expected in the wick if the maximum wick temperature exceeds the superheat limit. This case can be prevented by maintaining a high contact conductance between the wick and evaporator saddle and minimizing the amount of non-condensable gases in the LHP [21]. The convective boiling in the liquid line may occur when the operating temperature is below the ambient one, and the condenser subcooling is insufficient. In this situation, the liquid line absorbs heat from ambient, which

substantially decreases the amount of subcooling reaching the reservoir. This condition may lead to undesirable temperature oscillations and eventually dry out.

#### **1.4 LHP control methods**

Many electronic devices for a nominal operation require a narrow and precise operating temperature range despite the variation in the heat load, the sink or ambient temperature. Hence, several temperature control methods have been introduced particularly for space applications to achieve the temperature requirement of the spacecraft payloads. The principles, advantages and disadvantages of different control methods are extensively studied in [22] and [23]. The trade-off criteria consist of power of the control heater, passive vs. active operation, mass, reliability, complexity, accuracy and stability. The major controlling methods are reviewed here.

The first method uses a control heater on the reservoir or liquid line near to the reservoir. This method controls the LHP operating temperature by adjusting the reservoir temperature by heating the working fluid. This approach can sustain a set-point temperature if the operating temperature of the LHP without control remains below the set point for operating boundary conditions [24]. Otherwise, a cooler is necessary.

The ICESat was utilized this type of heater on the reservoir and achieved a temperature stability better than  $\pm 0.3$  K. However, the heater power is reported to be as high as 20% of the applied heat to the LHP [12]. The other drawback is the complicated control algorithm which depends on the location and sensitivity of the feedback sensors. Although the reservoir heater method is reliable, easy-to-integrate and light weight, it has a high response time because the reservoir thermal inertia is high. Additionally, the applied power to the heater cannot be very high because of the high probability of the LHP shut down in these situations.

To minimize the mentioned drawbacks, a new location for heater installation has been proposed and tested in [24]. The heater was installed on the liquid line of a miniature LHP to control the reservoir temperature via controlling the subcooling of liquid entering the CC. The major drawback of this method was the undesirable temperature oscillations.

Utilizing the subcooling control concept without consuming additional power has been implemented by thermally coupling the vapor and liquid lines. Different means proposed for coupling include solid blocks in [12], heat pipes in [25] and combination of a heat exchanger and cooler in [26]. However, these couplings add more mass and complexity to the system, and much experimental work is required to find the correct value for design parameters. Another thermal coupling control method is the use of Thermal Electric Cooler (TEC) to control the evaporator-reservoir thermal coupling. TEC devices using the Peltier effect can reduce the heat leak by bringing some of the heat back to the evaporator [27].

Another passive control method utilizes a Pressure Regulated Valve (PRV) [28] and [22]. The two PRV types, three-way and two-way as shown in Fig. 5, are installed on the vapor line and degrade the LHP conductance to keep the evaporator temperature above a certain point. The main drawback of using a PRV is the presence of moving parts.

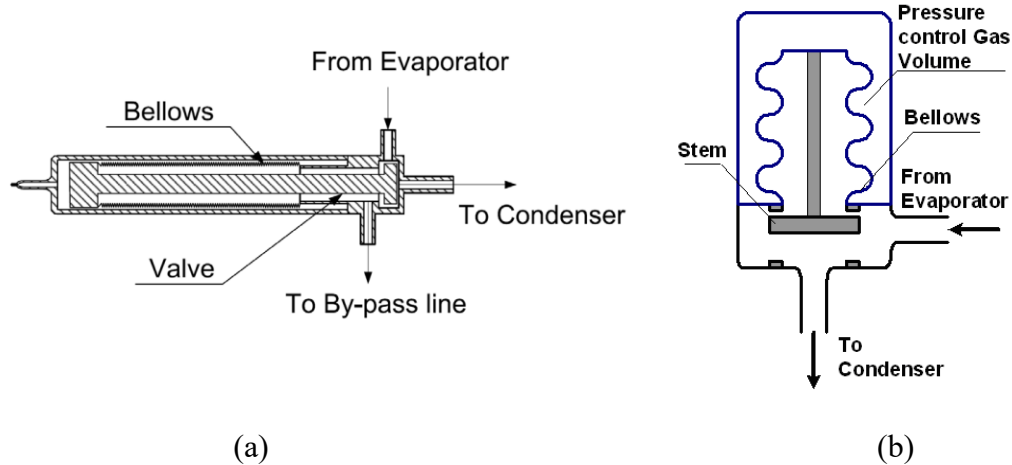


Fig. 5 Schematic of PRVs used in an LHP: (a) three-way and (b) two-way. [23]

A three-way PRV connects the evaporator to the condenser and reservoir. This PRV type has a set point pressure and a regulation point pressure representing respective LHP operating temperature points [23]. If the vapor pressure is below the set point, all the vapor goes to the reservoir via a bypass line. This bypass causes an increase in the vapor quality and temperature of the reservoir fluid. Above the set point, the additional vapor pressure allows some of the vapor to move toward the condenser. When the vapor pressure reaches the regulation point, the PRV completely opens and all the vapor is directed toward condenser. Thus, the three-way valve controls the LHP operating temperature around the regulation point; and beyond that point, LHP works as a normal one without any temperature control. The three-way PRV installed on Yamal 2000 spacecraft showed the possible temperature controllability of  $\pm 2$  K [29].

The set point and regulation point of PRVs are fixed and cannot be modified during the LHP operation unless the pressure of the control gas behind the bellows is controlled. Different techniques are proposed to control the gas pressure using a phase change material (PCM) in [30] and heater in [29] and [31].

A two-way PRV is proposed to replace the three-way one to eliminate the by-pass leakage which significantly impacts the LHP conductance above the regulation point. The LHP temperature is controlled by adjusting the pressure drop. The two-way PRV has a set point and a regulation point as well. When the vapor pressure in the vapor line is below the set point, the valve is closed and there would be no circulation in the loop. A vapor pressure between the set and regulation points opens the stem to a certain degree which causes the loop to start and imposes a pressure drop to change the thermodynamic cycle of the LHP. Figure 6 illustrates the pressure drop effect on the thermodynamic cycle. The pressure drop alters the fluid state in the reservoir from point 8 to 8'

which has a lower temperature that causes an increase in the heat leak compared to the LHP without a valve. After exceeding the pressure of the regulation point, the PRV stem is entirely retracted, and the LHP works as a conventional one without any additionally imposed pressure drop.

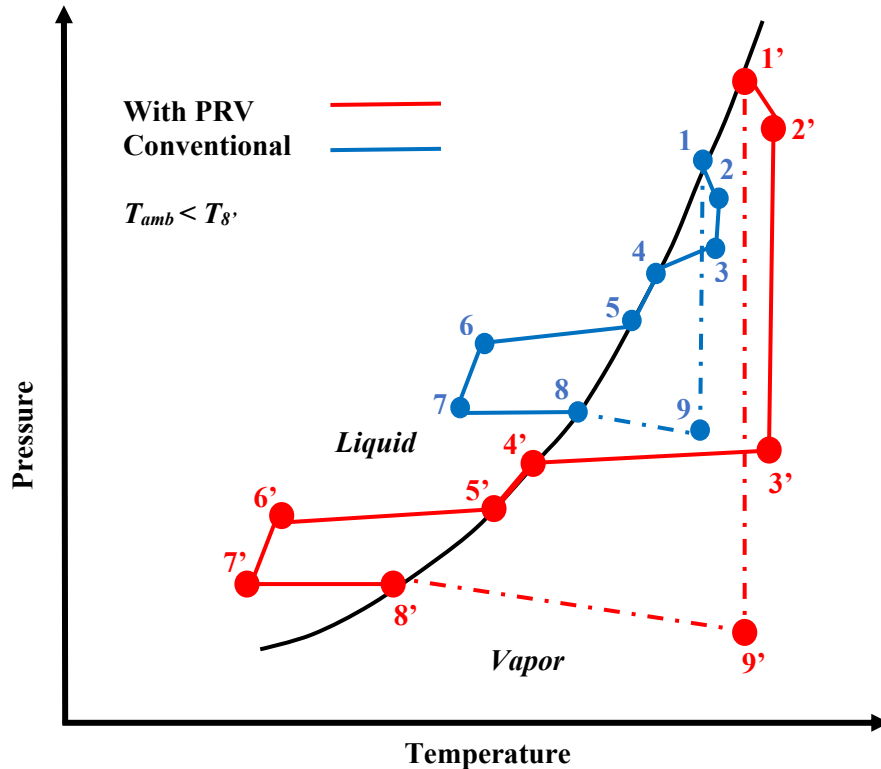


Fig. 6 Effect of two-way PRV on the LHP thermodynamic cycle.

Two-way PRVs were implemented on the LHPs launched onboard of Hispasat-1E. The verification and acceptance tests showed start-up difficulty at the low-power and cold-sink conditions. Therefore, a calibrated orifice added near the steam seat for the flight model [13]. The orifice ensures that the LHP starts up in the worse-case conditions mentioned above.

### 1.5 Research motivation and objectives

The primary objective of this research project is to develop a mathematical model to simulate the transient operation of an LHP. The main emphasis is to reduce the required accommodation parameters such that the model has predictive capabilities. Currently, in many LHP applications, one of the significant difficulties is the lack of accurate and predictive mathematical models. Therefore, the research topic is timely and important.

The model is developed with a modular approach and as a stand-alone simulation. These characteristics provide uniqueness and flexibility to the current and future research work in LHP through understanding the decision-making process and trade-offs in the development of the model. Additionally, the modularity feature allows further improvements or modifications to be easily implemented with minor changes to the model configuration. For example, different correlations and mathematical integration methods can be selected depending on the LHP operation range.

Another objective of the mathematical model is to provide a design tool for the new LHP-based thermal control systems. Such a model reduces the time and cost of research and development by minimizing the number of validation and qualification tests for a new LHP. For instance, a new device for controlling the LHP operating temperature can be assessed using the model before implementation by adding a new module that contains the thermo-fluid working principle of the control device. A customized version of the model validated particularly for an LHP can be utilized to investigate and troubleshoot the LHP anomalous behavior. This utilization is essential for remote applications such as spacecraft thermal control where LHPs are not easily accessible for inspection and maintenance.

A final objective is to develop a model that can be integrated into higher-level thermal modelling software to predict the LHP operation at a spacecraft system level. These objectives are realized by conducting the following tasks:

- Performing a literature review;
- Preparing the experimental setup for two LHP units of different design;
- Establishing the plans and procedures for testing the LHP units;
- Analyzing the test results and performing uncertainty analysis;
- Comparing and verifying the correlations for the fluid pressure drop and the heat transfer coefficients required for the mathematical model;
- Modelling the physical properties and dimensions of the LHPs;
- Formulating the governing equations and corresponding boundary conditions for each element of LHPs;
- Developing the model algorithms to solve the governing equations for both steady-state and transient scenarios;
- Validating the models against the experimental results;
- Evaluating the prediction capability of the models;
- Performing the sensitivity analysis on the modelling parameters in order to provide the user with the model response characteristics.

## **1.6 Thesis organization**

The chapters of this thesis are organized as following:

- Chapter 1 introduces the historical background, conventional architecture, applications and operational principles of LHPs.
- Chapter 2 presents the experimental set-up, procedures and analyzes the experimental results. Uncertainty analysis of the experimental setup is also provided.
- Chapter 3 reviews the selected empirical correlations used to calculate the heat transfer coefficients and pressure drops required in the LHP numerical model and discusses the rationale behind the selection process.
- Chapters 4 and 5 present the mathematical model developed to simulate the steady state and transient LHP operation, respectively. These chapters follow the same format consisting of the literature review, mathematical formulation, implemented algorithm, validation/prediction, and sensitivity analysis.
- Finally, Chapter 6 summarizes the completed tasks, presents the research outcomes and proposes recommendations for future work.

## Chapter 2: Experimental work

Experimental work is performed to investigate the operational characteristics of LHPs and to collect data under different operating conditions for the validation of the mathematical model developed in this research. The experiments are conducted on two different LHPs under ambient conditions. Each test scenario performed three times to ensure the repeatability of the experimental results. Both LHPs are mainly made up of stainless steel with a sintered nickel wick. They use ammonia as the working fluid. One of the LHPs is of a conventional design (LHP1), and the other one, a novel design, contains a two-way PRV to control the operating temperature (LHP2). Heat is applied to the LHPs using film or cartridge heaters and removed by a recirculating chiller. The temperatures at different LHP locations are recorded as a function of the operating conditions and time. A review of the recent LHP experimental investigation can be found in [32] and [33].

### 2.1 LHP1 setup

Figure 7 shows the overall layout of LHP1 attached to a level brass plate. This LHP is a space-qualified unit and manufactured by Lavochkin Association in Russia. The casing and transportation lines are made from stainless steel 304. The saddle material for the evaporator and condenser is aluminum 6082. The evaporator wick is made of a sintered nickel alloy. The physical characteristics of LHP1 are provided in Appendix A.

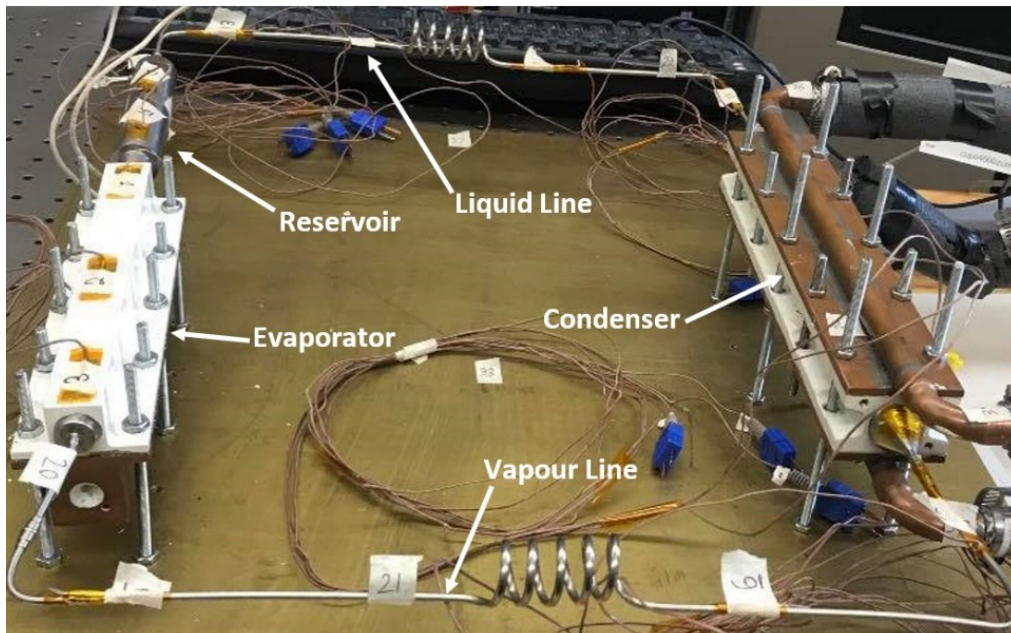


Fig. 7 Photo of LHP1.

A heater block consisting of a cartridge heater embedded in a copper saddle is attached to the bottom of the evaporator saddle as shown in Fig. 7. The power is applied to LHP1 by providing a voltage across the cartridge heater using a DC power supply or an AC variac. The cartridge heater has a resistance of  $110.5 \Omega$  at a room temperature of  $22^\circ\text{C}$ . In addition, two parallel copper pipes carrying fluid cooled by a chiller unit serve as the sink. The condenser saddle is attached to the copper pipes by copper risers. The evaporator and condenser are connected to a common brass baseplate by low conductivity posts. All the tests are conducted in a horizontal position within  $\pm 0.2^\circ$  to minimize the effect of gravity.

LHP1 is instrumented with 31 copper/constantan (type T) thermocouples including two on the heater block, five on the evaporator saddle, five on the vapor line, nine on the condenser saddle, seven on the liquid line and three on the reservoir. The positions of thermocouples are provided in Fig. 8. The condenser thermocouples are mounted such that they can measure the fluid flow temperature as it is forced to gyrate by a spiral wire inside the condenser. Several additional thermocouples are used to obtain the temperature of the sink and ambient. Three thermocouples are attached to the brass plate to measure the ambient temperature. Four other thermocouples are attached to the inlet and exit of the copper pipes to obtain the sink temperature.

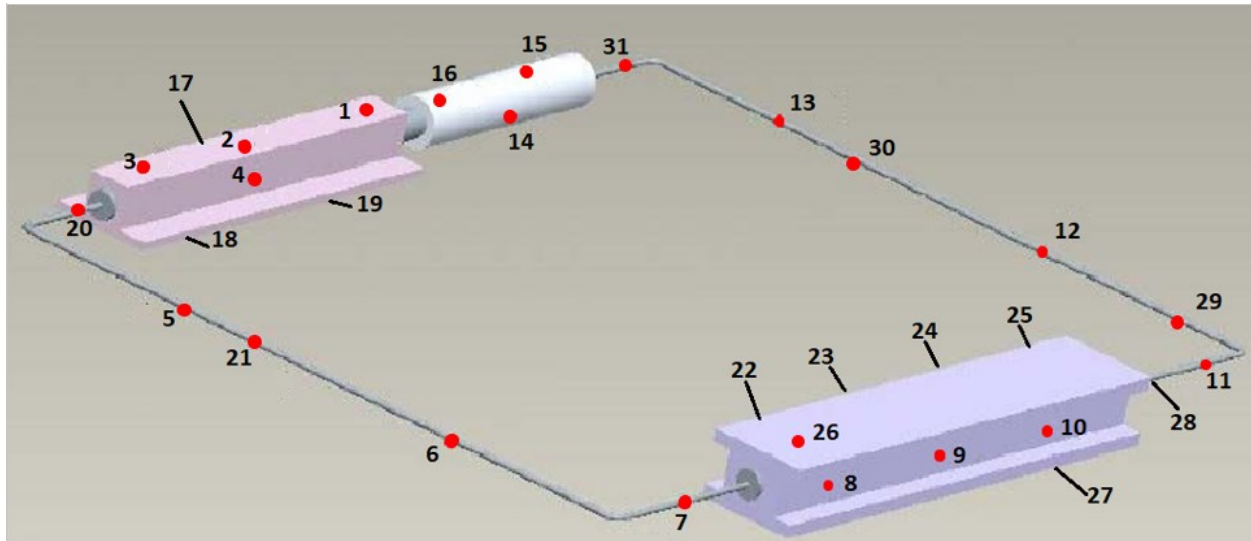


Fig. 8 Thermocouple locations on LHP1.

## 2.2 LHP2 setup

LHP2 is also a spaceflight-qualified unit manufactured by IberEspacio in Spain. It is filled with ammonia and equipped with a two-way PRV. Figure 9 shows LHP2 without insulation. The casing and transportation lines are made of AISI 316L. The heater block of LHP2 is similar to the one installed on LHP1; however, its saddle is made of aluminum, and its cartridge heater has an electrical resistance of  $44.7 \Omega$  at room temperature. The condenser, mated inside an extruded

flange, is embedded inside a honeycomb sandwich panel. All components of the condenser are made of aluminum. The condenser plate is mounted vertically. However, the evaporator and reservoir are maintained in a horizontal position within  $\pm 0.1^\circ$ . The evaporator saddle and wick are made of aluminum 6082 and a sintered nickel alloy, respectively. The detailed physical characteristics of LHP2 is provided in Appendix B.

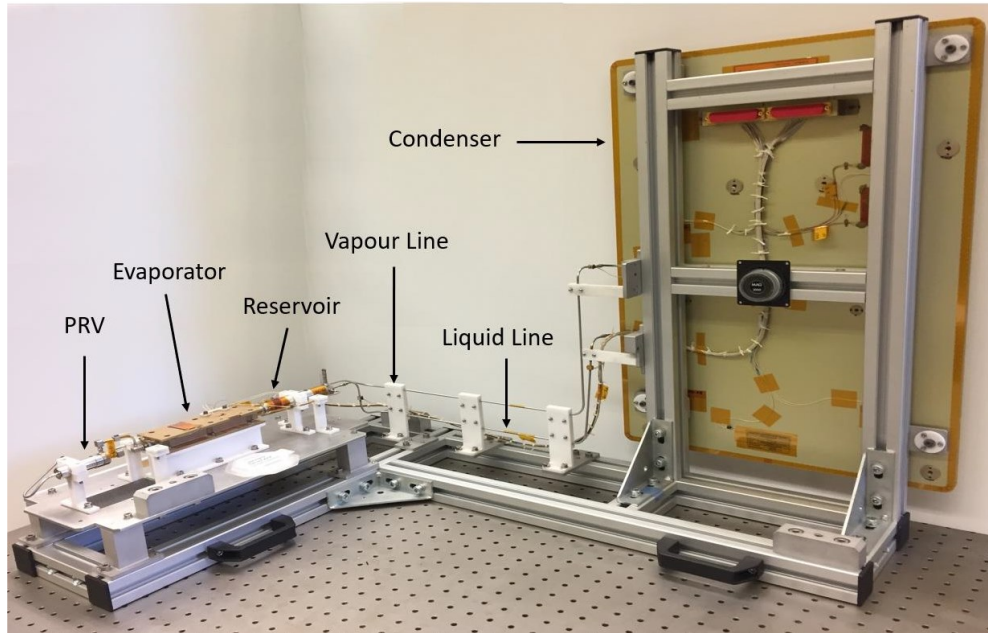


Fig. 9 Photo of LHP2.

LHP2 was previously instrumented to be tested in a vacuum chamber. Therefore, modifications have been performed to prepare LHP2 for ambient testing. The condenser panel was equipped with a radiator and optical solar reflectors (OSR) to dissipate the heat through radiation. For ambient testing, this configuration is altered by manufacturing a sink plate, which is attached to the existing condenser. The sink plate is made of copper and cooled by the chiller through a serpentine copper piping. Several c-clamps and Tpli™ 200 thermal gap filler (with thermal conductivity of  $6 \frac{W}{mK}$ ) are used to improve the thermal conductivity between the condenser and sink plates. Figure 10 presents the model of the sink plate as well as the copper piping and connection ports to the chiller. The piping is attached to the sink plate by using a Boron Nitride epoxy (with thermal conductivity of  $3.6 \frac{W}{mK}$ ).

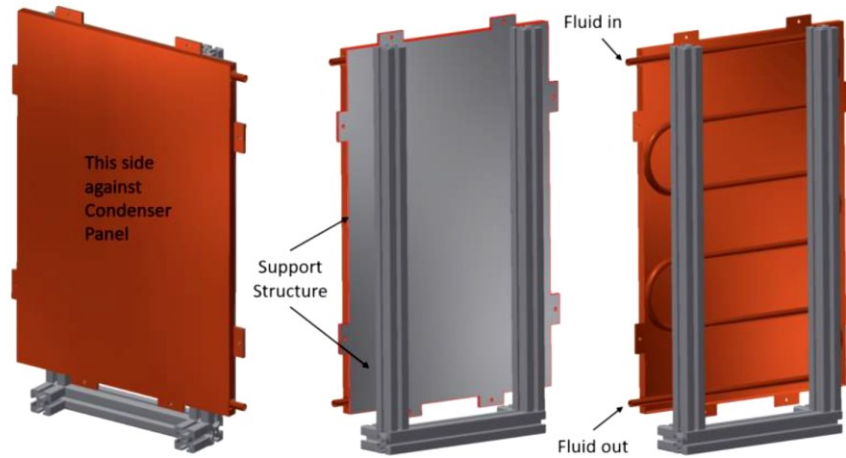


Fig. 10 Sink plate model.

Thirty-three type-T thermocouples are attached to LHP2 including one on the heater block, two on the evaporator saddle, nine on the vapor line, twelve on the condenser saddle, seven on the liquid line and two on the reservoir. The location of the thermocouples is provided in Fig. 11. Three thermocouples to measure the ambient temperature are attached to the table where LHP is placed on. Two more thermocouples are attached to the inlet and exit of the copper pipes of the sink plate.

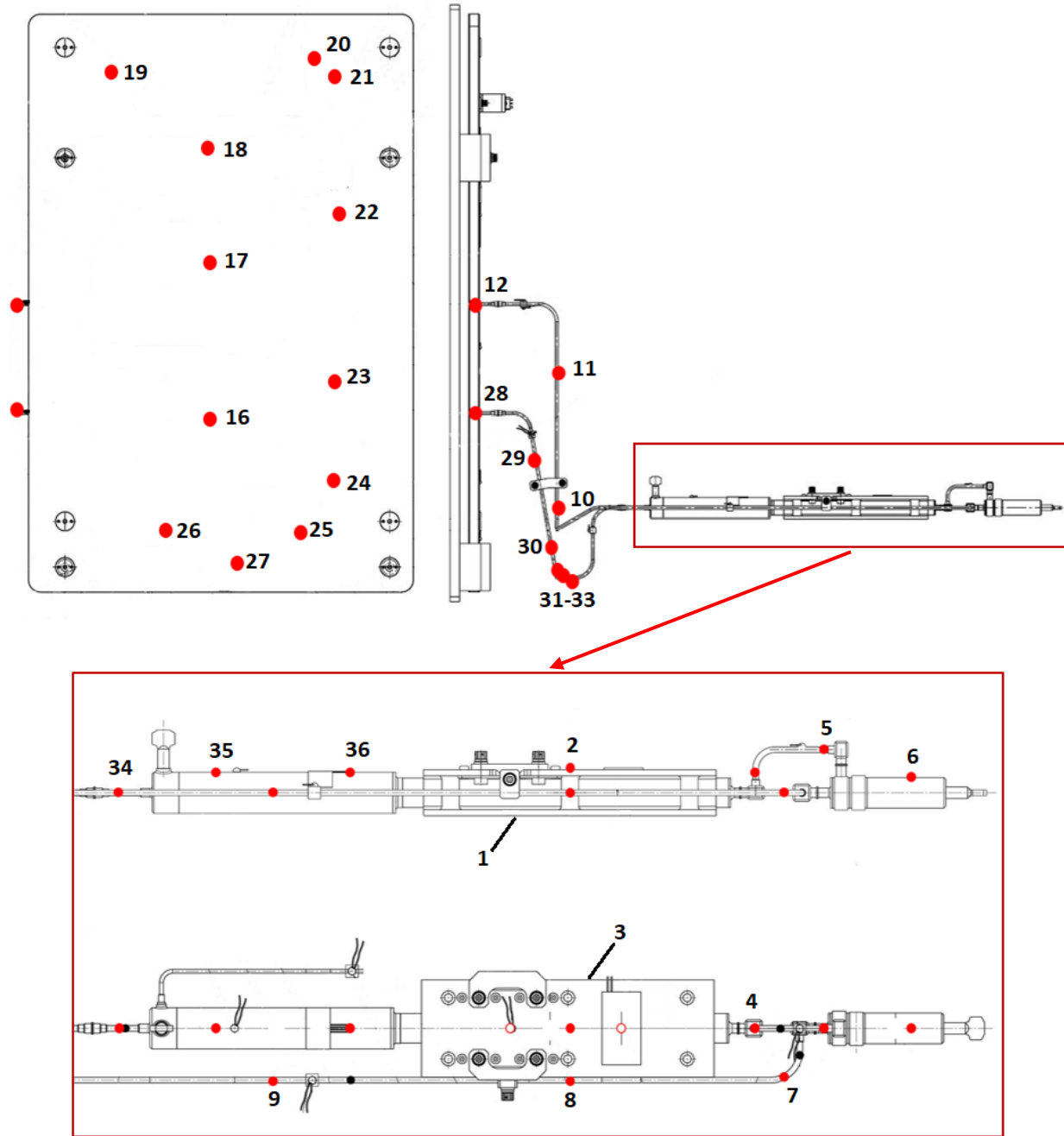


Fig. 11 Thermocouple locations on LHP2.

The three-dimensional CAD images of the condenser together with the thermal images are used to locate the transportation line location such that the thermocouples can be appropriately placed. The sample images are provided in Fig. 12.

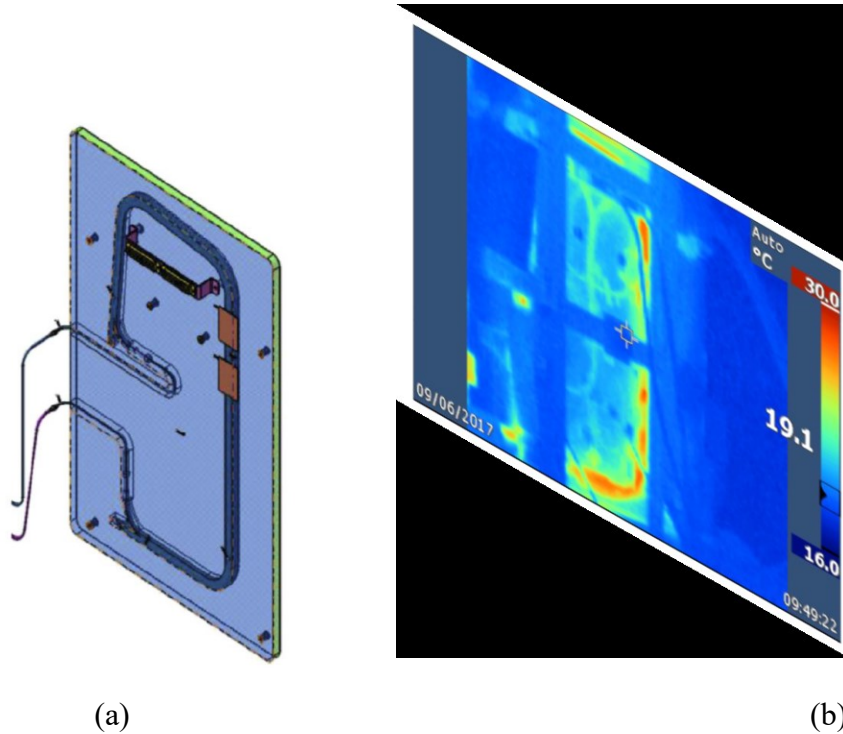


Fig. 12 The fluid line inside the condenser panel (a) three-dimensional model (b) thermal image.

### 2.3 Sink temperature regulation

As mentioned earlier, the temperature of the LHP sink plate is maintained through circulating a coolant by a chiller. The chiller used for the LHP tests is an RC011 KODIAK recirculating chiller from Lytron. This chiller uses a mixture of 70% water and 30% ethylene glycol as the coolant. The chiller is able to maintain the coolant temperature between 5 to 30°C with temperature stability of  $\pm 0.1^\circ\text{C}$  [34]. The cooling capacity of the chiller varies upon the set temperature with a minimum value of 600 W at the 5°C set point. Figure 13 shows the chiller setup including the plumbing that transfers the coolant between the chiller and the sink plate. The plumbing is insulated to minimize the heat transfer with ambient and the condensation on the pipes.



Fig. 13 RC011 chiller with support plumbing.

## 2.4 Ambient temperature regulation

The ambient conditions, including the temperature and humidity, are not fully regulated when performing the experiments. The entire LHP including the heater block and heat exchanger is insulated via 20 mm thick insulation foam made of polyethylene rubber with thermal conductivity of  $0.25 \frac{W}{m^2K}$ . The insulation reduces parasitic heat exchange with the ambient, reduces the effect of ambient temperature variations and eliminates condensation.

## 2.5 Applied power regulation

The required power is applied to the LHP evaporators using cartridge heaters embedded in the heater blocks. The voltage is provided by a DC power supply (BK precision 9206), and its value is obtained from Eq. (6) by knowing the applied power and the electrical resistance of the cartridge.

$$V = \sqrt{PR} \quad (6)$$

where  $P$  is the required applied power and  $R$  is the electrical resistance of the cartridge heater. This resistance changes with temperature. The voltage and current entering the cartridge heater are monitored via integrated digital meters in the power supply. Additionally, two external multimeters (Omega HHM32 and HHM33) are installed in the electric route to provide secondary measurement values. Then, the applied power is calculated from Eq.(7). The operator can compensate for any change in the applied power (caused by the resistance variation) through

adjusting the voltage. Figure 14 shows the equipment used to apply power consisting of the DC power supply, the digital multimeters and wirings to the heater blocks.

$$P = IV \quad (7)$$

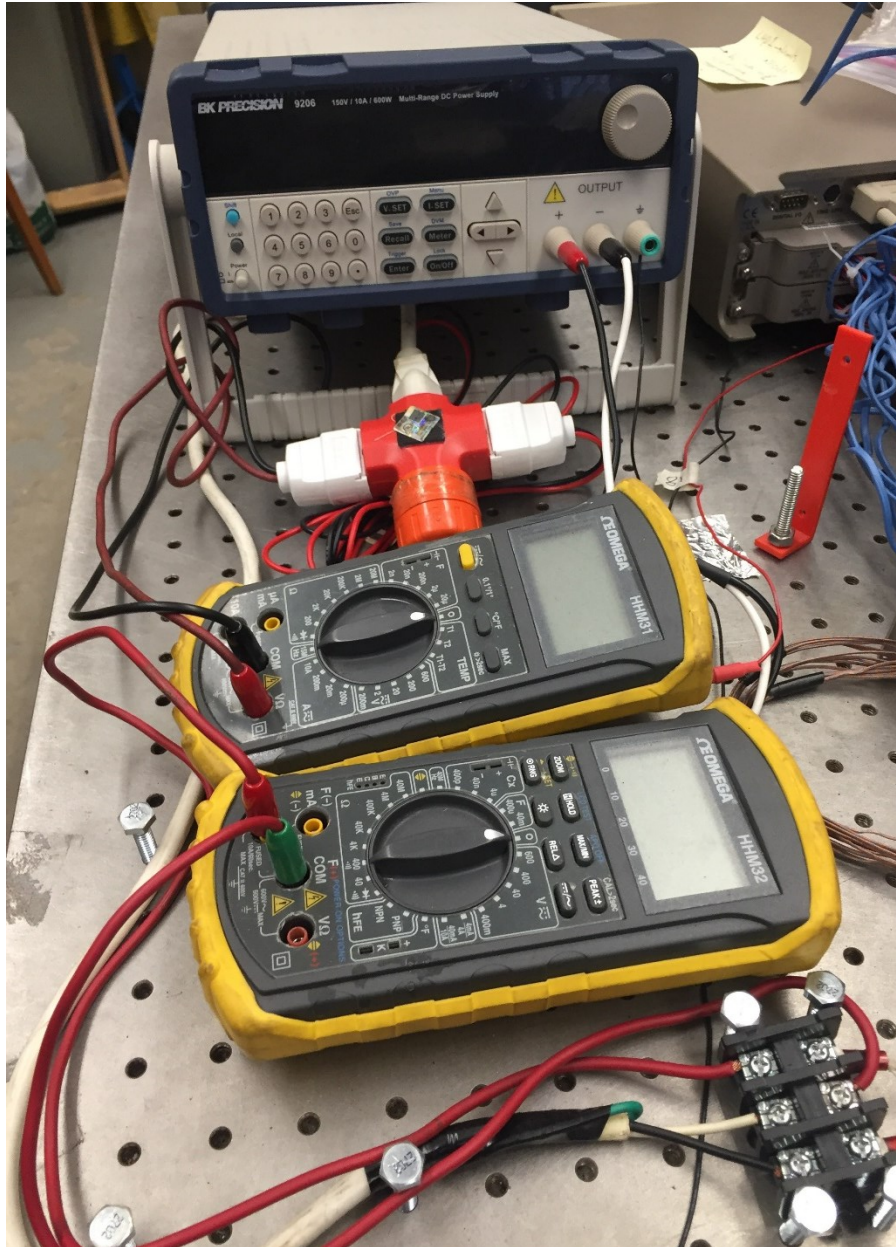


Fig. 14 Equipment used to apply power with wiring.

An AC variable autotransformer (Powerstat 3PN116B Variac with a voltage output within [0 – 140] V) was previously used as the power supply. The measurement showed that the supplied current and voltage have a high-level of uncertainty (around 5%). Particularly at high powers, the voltage is close to the power grid voltage. In those situations, the AC power supply can not regulate the output, and any fluctuation in the power grid appears in the power supply output. Therefore, a BK Precision 9206 DC power supply was purchased to reduce the fluctuations in the applied power and consequently in the temperature measurements. The DC power supply has a measurement accuracy better than  $\pm(0.03\%$  of reading + 20 mV) and  $\pm(0.1\%$  of reading + 25 mA) for the voltage and current, respectively [35]. The supplied voltage to the heater block is recorded to monitor the effect of the power uncertainty on the test results. Figure 15 shows an example of the voltage stability issue of the AC power supply in comparison to the DC one.

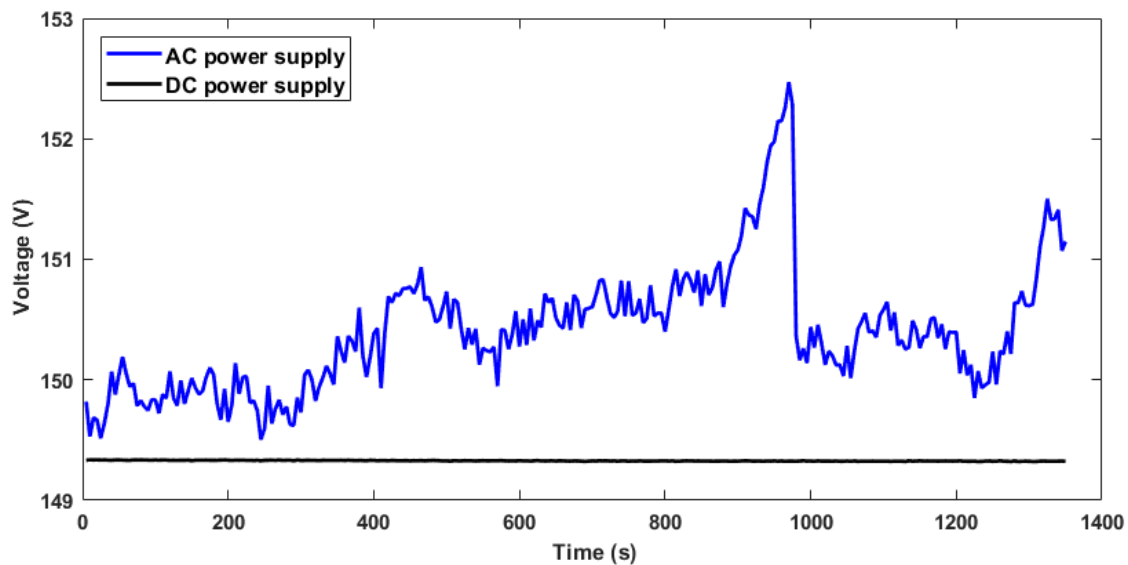


Fig. 15 Voltage stability of the AC and DC power supplies at 200 W for LHP1.

## 2.6 Data acquisition and post-analysis

The thermocouple temperatures and power supply voltage are collected through Keithley 2700 data acquisition system (DAQ). An internally regulated CJC measuring (Cold Junction Compensation) is used in the temperature acquisition. CJC compensates for the variation in the reference point temperature. DAQ converts analog measurements to digital ones and passes them to a personal computer to be recorded and visualized. DAQ has an accuracy of  $\pm 0.2^{\circ}\text{C}$  for the temperature measurements. [36]

“Integra Up And Running TestPoint Runtime” software is used to control the DAQ. The software also allows recording of the gathered data and visualizing any chosen 8 data channels in real-time. DAQ is set to scan all the sensors every 5 seconds to capture the temperature fluctuations. The

operator can use the visualized data to make sure that the LHP is working in the operating range, and the critical data are adequately recorded.

The post analysis is performed on the recorded data using a script written in MATLAB. Each LHP has its script since the thermocouple locations are different. The temperature of each LHP component is obtained and plotted against the time or applied power. The approximate location of the two-phase/liquid interface could also be obtained inside the condenser or liquid line by comparing the values of the temperature sensors installed on different locations.

## **2.7 Test plans**

Several test plans are devised to investigate the performance characteristics of the LHPs in the steady-state and transient modes. These procedures are divided into the following categories:

- Maximum power
- Power cycling
- Sink cycling

### **2.7.1 Maximum power**

The purpose of these tests is to find the maximum power that can be applied without exceeding the maximum LHP operating temperature. This last constraint is to avoid the bursting of the pipes due to the increased internal pressure. LHPs are normally designed to withstand an internal burst pressure of 120 bars.

For LHP1, the maximum applied power is constrained by the 150 V maximum output voltage of the power supply. The maximum applied power is 200 W which results in an operating temperature of 48°C at 200 W and 20°C sink temperature, and it is lower than the operating limit of 56°C.

The maximum applied power for LHP2 is limited by the maximum operating temperature of 65°C. In this case, the temperatures at the reservoir and evaporator should remain below the maximum operating temperature of 72°C with a 10% margin. Figure 16 shows the LHP2 maximum power for each sink condition. The maximum power is decreased as the sink temperature is increased as expected.

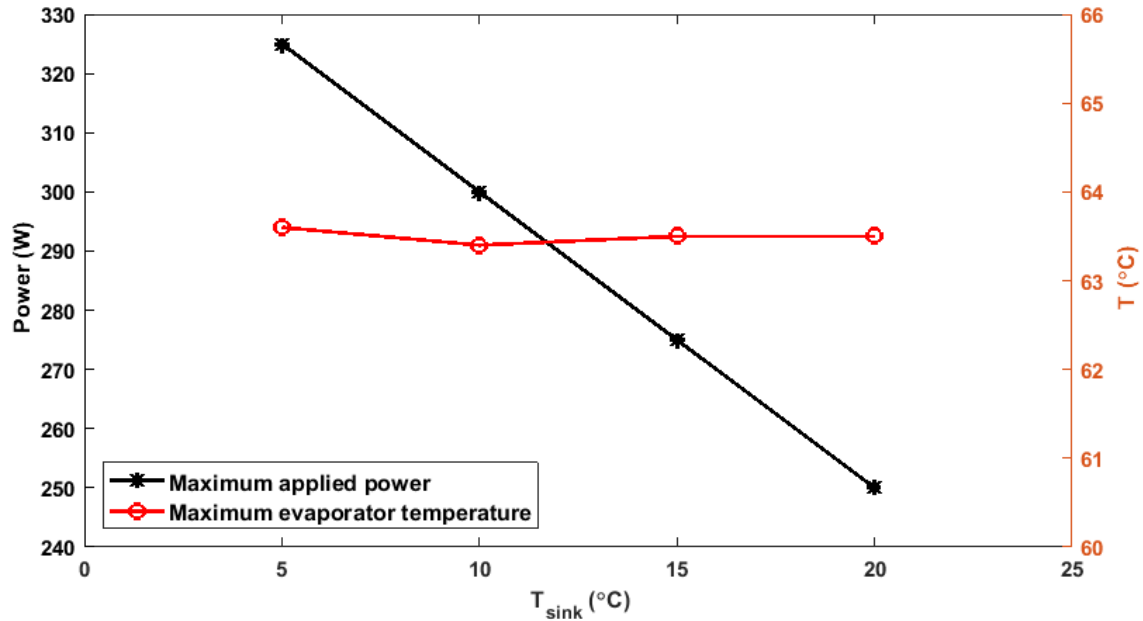


Fig. 16 Results of the maximum applied power tests for LHP2.

### 2.7.2 Power cycling

The power cycling tests are performed at different constant chiller temperatures to investigate the LHP performance over a range of applied power. At each chiller temperature, the applied power is incrementally varied between a chosen minimum power and the maximum power obtained from the previous tests. Table 1 outlines the test scenarios performed in the power cycling category.

Table 1 Test scenarios of power cycling.

Test ID	$T_{chiller}$ (°C)	Power profile (W)
LHP1-PC5-UP	5	20, 30, 40, 50, 60, 70, 80, 100, 125, 150, 200
LHP1-PC10-UP	10	20, 30, 40, 50, 60, 70, 80, 100, 125, 150, 200
LHP1-PC15-UP	15	20, 30, 40, 50, 60, 70, 80, 100, 125, 150, 200
LHP1-PC20-UP	20	20, 30, 40, 50, 60, 70, 80, 100, 125, 150, 200
LHP1-PC5-DN	5	200, 150, 125, 100, 80, 70, 60, 50, 40, 30, 20, 10
LHP1-PC10-DN	10	200, 150, 125, 100, 80, 70, 60, 50, 40, 30, 20, 10
LHP1-PC15-DN	15	200, 150, 125, 100, 80, 70, 60, 50, 40, 30, 20, 10
LHP1-PC20-DN	20	200, 150, 100, 75, 60, 50, 40, 30, 20, 10
LHP1-PC10-UD	10	20, 30, 40, 50, 60, 70, 80, 100, 125, 150, 200, 175
LHP2-PC5-UD	5	<u>125</u> , 150, 200, 250, 300, 325, 300, 275, 250, 225, 200, 175, 150
LHP2-PC10-UD	10	<u>100</u> ,125,150,175,225,275,300,275,225,175,150,125
LHP2-PC15-UD	15	100, 150, 200, 225, 250, 275, 250, 225, 200, 150, 125, 100, <u>75, 80, 90</u>
LHP2-PC20-UD	20	<u>5</u> ,50,75,100,125,175,225,250,225,175,125,100,75
LHP2-PC5-UP	5	<u>10</u> ,25,50,75,100,125,135,145,150,160,175,200,225,250,175

Each test scenario in Table 1 is performed three times to ensure the repeatability of the experimental results. The results of the repeated experiments are within  $\pm 0.2^\circ\text{C}$  of their average. The temperature differences are mainly caused by the variation of the ambient temperature. The power-cycling tests of LHP1 are broken down into power-up (UP) and power-down (DN) divisions because of the time limitation in conducting the full cycle test. Each LHP1 full power-cycling test can take up to 20 hours. For LHP2, each test covers both power-up and power-down (UD) in the average test duration of 12 hours (UD). The powers underlined in the LHP2 test scenarios of Table 1 are in the LHP2 operation region controlled by PRV. For each test scenario, the following procedure is used:

- **Setup initiation:** This step includes turning on the power supply and multimeters, the DAQ system and its computer.
- **Chiller start-up:** The chiller is turned on and set to the selected temperature. It takes up to 30 minutes until the temperature becomes stable in the condenser.
- **LHP start-up:** The first value in the power profile is applied by adjusting the voltage on the power supply. The voltage and current of the power supply are measured to calculate the applied power to ensure the right power is sent to the LHP heater block. Every five minutes, the applied power value is checked. It is adjusted by changing the input voltage if the power reading is drifted more than 0.05 W from the assigned value. This drift may occur because of the change in the temperature of the heater block. During the LHP start-up, the evaporator saddle temperature is monitored to ensure that its value does not exceed the operating limits. If the temperature exceeds a  $5^\circ\text{C}$  margin band from the operation limit, the power needs to be immediately turned off. It means that the LHP could not start, and the operator should wait until the evaporator temperature reaches the ambient.
- **Power change:** The applied power is changed according to the power profile when the temperature of the reservoir reaches a steady state within  $\pm 0.1^\circ\text{C}$ . It generally takes 30 minutes to reach a steady point except for the low applied powers in the variable conductance mode. In that case, it may take up to 60 minutes. Similar to the LHP start-up step, the applied power is monitored every 5 minutes for adjustment if it is necessary.
- **LHP shut down:** After a steady state is reached for the last value in the power profile, the power is turned off. Then, the chiller is turned off after the reservoir temperature drops below 30 degrees.
- **Setup shut down:** All the test instruments are turned off.
- **Post-analysis:** The raw data collected from the experiment are processed with a MATLAB script to obtain the LHP operational characteristic including the operating temperature and the location of the two-phase/liquid interface.

A typical test result is provided in Fig. 17 for the LHP2-PC5-UP scenario. The LHP2 starts at 10 W, and PRV regulates the operating temperature up to 145 W, and LHP2 behaves as a conventional one from 150 to 250 W. The sink temperature remains nearly constant during the whole test. The ambient temperature increases by  $3^\circ\text{C}$  in this period.

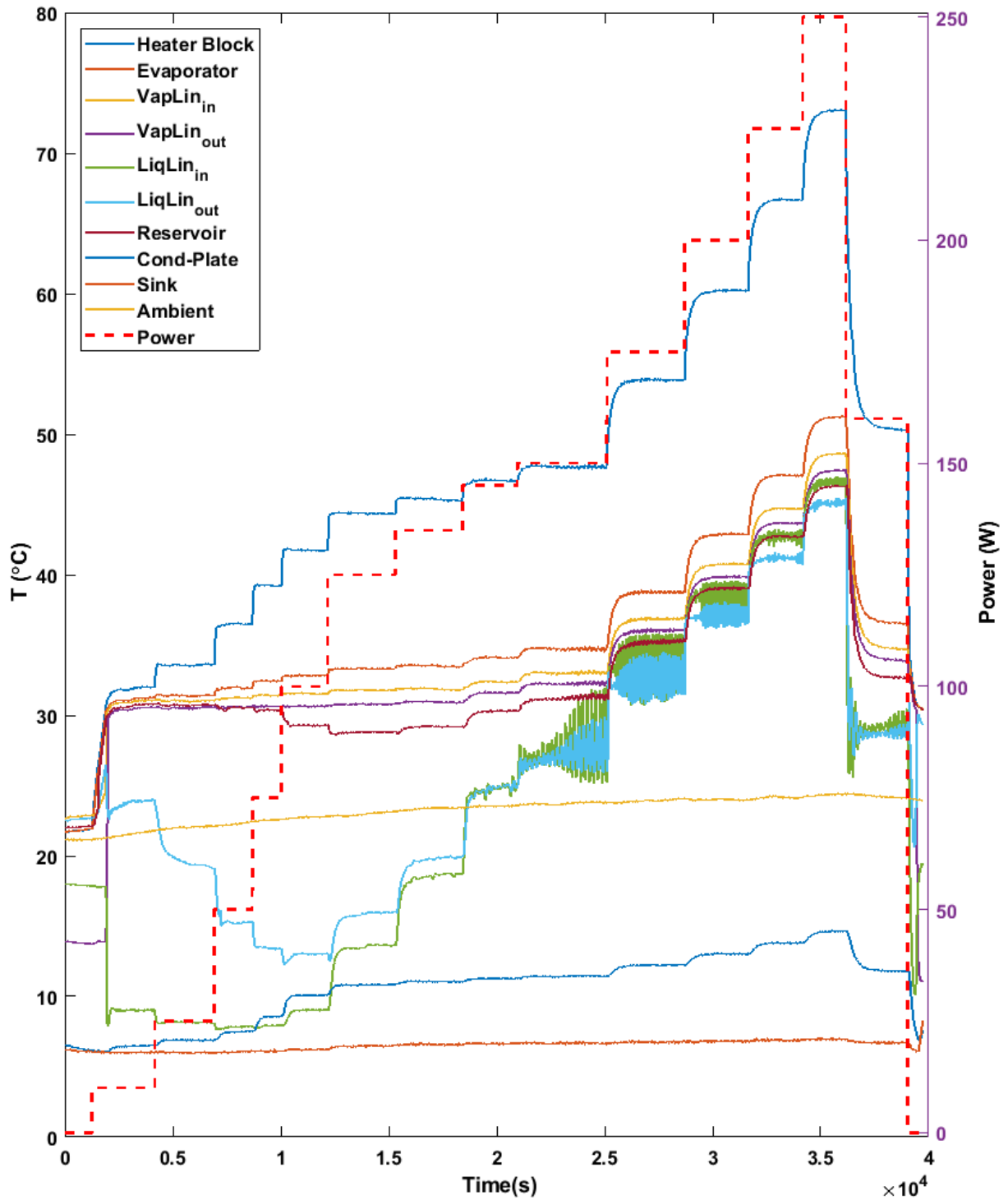


Fig. 17 The overall results of the LHP2-PC5-UP scenario.

The start-up is analyzed through the minimum required start-up power, the time interval between applying the power and initiation of the fluid flow in the loop, and the temperature response of the

reservoir and evaporator saddle to the applied power. The flow initiation is observed via a sudden increase in the temperature of thermocouples on the vapor line. The minimum start-up powers are 20 and 5 W at the 5°C sink temperature for LHP1 and LHP2, respectively. The start-up time is decreased by increasing the applied power for both the LHPs. The LHP1 start-up time is reduced from 180 to 40 s by increasing the applied power from 20 W to 200 W at the 5°C sink temperature. The power increase has a more significant effect on the LHP2 start-up time because of the PRV regulation. For instance, the LHP start-up time is dropped from 1615 to 40 s as the applied power is increased from 5 to 200 W at the 5°C sink temperature. The PRV prevents the LHP start-up until the reservoir temperature exceeds 29°C, which results in a higher start-up time in the PRV regulation mode. As mentioned in Section 1.3, a minimum temperature difference between the evaporator and reservoir is required to initiate the fluid flow in an LHP. When the power is applied to the heater block, both of the evaporator and reservoir temperatures increase, but the evaporator temperature has a steeper slope as it receives the heat directly from the heater block. It is observed that the required temperature difference to start LHP1 is about 1.6°C for the applied power range of [20 200] W. In contrast, the required temperature difference of LHP2 start-up changes from 0.4 to 3.2°C as the power is increased from 5 to 200 W. For LHP1, the evaporator and reservoir temperatures are experienced overshoots. This overshoot is decreased from 2.4 to 0.4°C as the applied power is increased from 20 to 200 W. No temperature overshoot is observed for LHP2. These different temperature responses between the two LHPs are mostly attributed to the presence of the two-way PRV installed on LHP2.

The main effect of the PRV regulation is observed on the temperatures of the vapor line as shown in Fig. 17. When the PRV is regulating, the operating temperature remains between the set point and regulation point of 29 and 31°C, respectively. Between these temperatures, the PRV is activated until the operating temperature exceeds the regulation point. The applied power of the regulation point is decreased by increasing the sink temperature. The regulation point power of LHP2 is 145 W at the 5°C sink temperature, and it is decreased in 25 W increments for every 5°C increase in the sink temperature until it reaches 20°C.

The steady-state information can easily be extracted from the above data. The LHP2 performance curve plotted in Fig. 18 from the LHP2-PC5-UP scenario results clearly shows that the LHP operates in an FCM as soon as the PRV loses its regulation capability at 145 W.

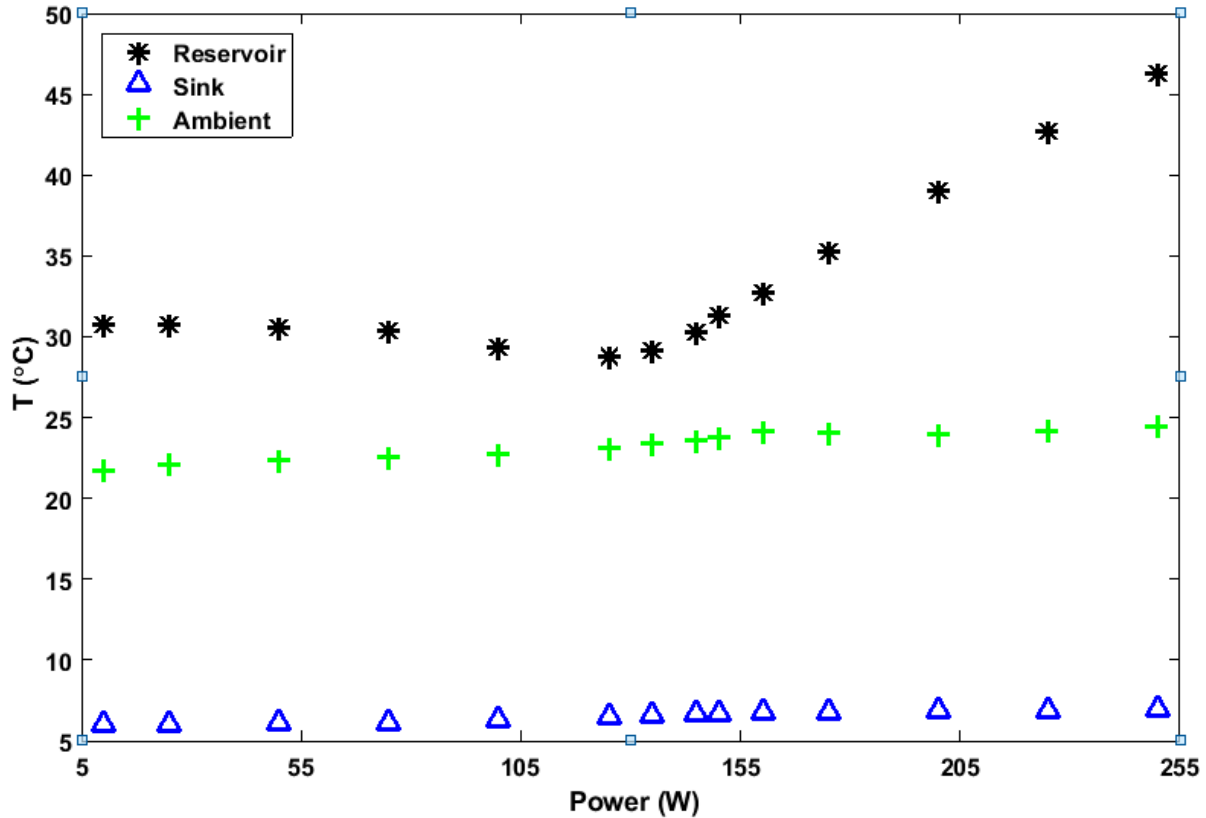


Fig. 18 The performance curve of LHP2 obtained from the LHP2-PC5-UP scenario.

For the LHP2 operating temperature difference between the power-up and power-down is less than 0.2°C under the same operating conditions. The LHP1 operating temperature experiences a more significant temperature difference even though the temperature difference remains below 0.2°C in the FCM. The different operating temperatures between a power-up and power-down test are known as the hysteresis effect, which only occurs in the VCM. The temperature difference in the LHP1 VCM has an average of 2.5°C in the power range of [20 70] W at the 5°C sink temperature. The maximum difference is observed at the lowest applied power.

The temperatures from the thermocouples attached to the condenser are presented in Fig. 19 for the applied power of [50 145] W. The location of the two-phase/liquid interface can be found from this figure. For the applied power of 50 W, the interface location lies between the vapor line exit and thermocouple T-121. There is a temperature difference of 17.5°C between the temperature of the vapor line and T-121. For the applied power 75 W, the interface moves to a location between thermocouples T-121 and T-122 since a temperature difference of 10°C is observed between these two thermocouples. For 100 W, the interface is moved further to a location between T-123 and T-124, which have nearly an 11°C temperature difference. The interface is located between T-124 and T-125 at 125 W as the thermocouples have a temperature difference of 5.6°C. The subcooling capability of the condenser is significantly reduced as all thermocouple temperatures are 7°C above the sink temperature. For 135 W, the interface is before T-126 as its temperature is 5.6°C lower

than T-125 one. For the applied power of 145 W, the interface moves beyond T-126 as all the condenser thermocouples read the temperature above 26.3°C. The comparison between the liquid-line inlet and reservoir temperatures in Fig. 17 shows that the two-phase/liquid interface stays inside the condenser until 150 W. Above this power, the interface resides enters the liquid line.

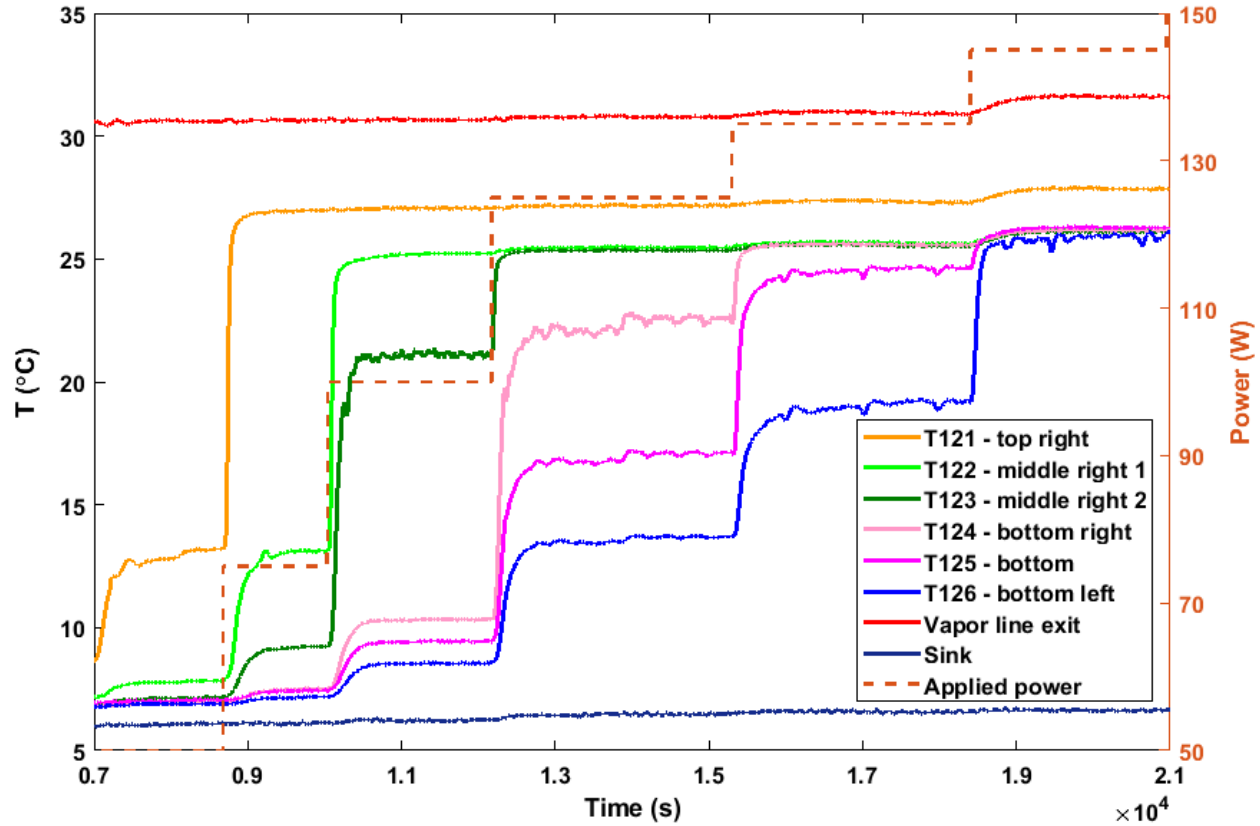


Fig. 19 The LHP2 condenser temperatures obtained from the LHP2-PC5-UP test.

The interface location is essential in investigating the LHP transient characteristics, particularly the temperature oscillations with a high frequency and low amplitude. This kind of oscillations can be explained based on the location of the two-phase/liquid interface and the amount of subcooling provided to the reservoir. If the interface is not close to the condenser exit, the condenser can have enough subcooling-length to bring the temperature of the fluid exiting the condenser to a constant value, close to the sink temperature. Hence, any potential interface oscillation inside the condenser does not have any effect on the liquid line temperature. Consequently, the operating temperature does not change since the subcooling provided to the reservoir remains nearly constant and no oscillation would be observed.

When the interface moves toward the end of the condenser, the oscillations may be triggered. In this case, the condenser exit temperature and subsequently the amount of subcooling reaching reservoir is a function of the subcooling length or in other words interface location. The oscillation could begin as a result of a change in the applied power or sink temperature from an equilibrium condition. For instance, an increase in the applied power results in an instantaneous surge of mass

flow rate. So, this sudden increase moves the interface toward the exit of the condenser and into the liquid line and rushes the subcooled liquid to the reservoir. The additional subcooling and increase in the flow rate would bring down the temperature of the reservoir (operating temperature). This lower operating temperature means that the temperature difference between the sink and fluid inside the condenser is decreased, which in turn degrades the condenser efficiency to dissipate heat to the sink. Therefore, the interface moves further toward the reservoir to dissipate the applied power. This further movement of the interface reduces the subcooling as the fluid entering the reservoir reaches a temperature closer to the two-phase values. This decrease is specifically noticeable when the interface moves inside the liquid line as the liquid line has much lower heat rejection capacity (the ambient has a higher temperature than the sink, and the thermal conductance of the liquid line is lower than the condenser). Hence, there is a discontinuity (a sudden drop) in subcooling when the interface moves from the end of the condenser to the beginning of the liquid line. The operating temperature rises as subcooling is decreased. The condenser can now dissipate the heat more efficiently because of a higher temperature difference between the sink and two-phase flow inside it. As a result, the interface recedes toward the inlet of the condenser. However, this contributes to a higher subcooling and decrease in the operating temperature again which sustains the oscillation. A specific applied power, at a set of sink and ambient, results in oscillation with maximum amplitude. It means that the interface fluctuation provides the maximum change in subcooling. It is worth to mention that the gravity may affect the oscillation but it is not the major playing factor since the oscillation also observed in the test results of LHP1 with horizontal condenser in addition to the operational results of LHPs working in microgravity [37].

Figure 20 provides a detailed view of the oscillations observed in the LHP2-PC5-UP test. The highest amplitude of the oscillation occurs at the applied power of 150 W as the two-phase/liquid interface is moving in and out of the condenser. No oscillation is observed before this power since the interface lays inside the condenser. The oscillation amplitude is decreased by increasing the power after 150 W. At 225 W, the oscillations are mainly observed in the liquid line as the interface is located there. For comparison, the amplitude of the temperature oscillations at the inlet of the liquid line is decreased from 3.4 to 1.1°C by increasing the applied power from 150 to 200 W.

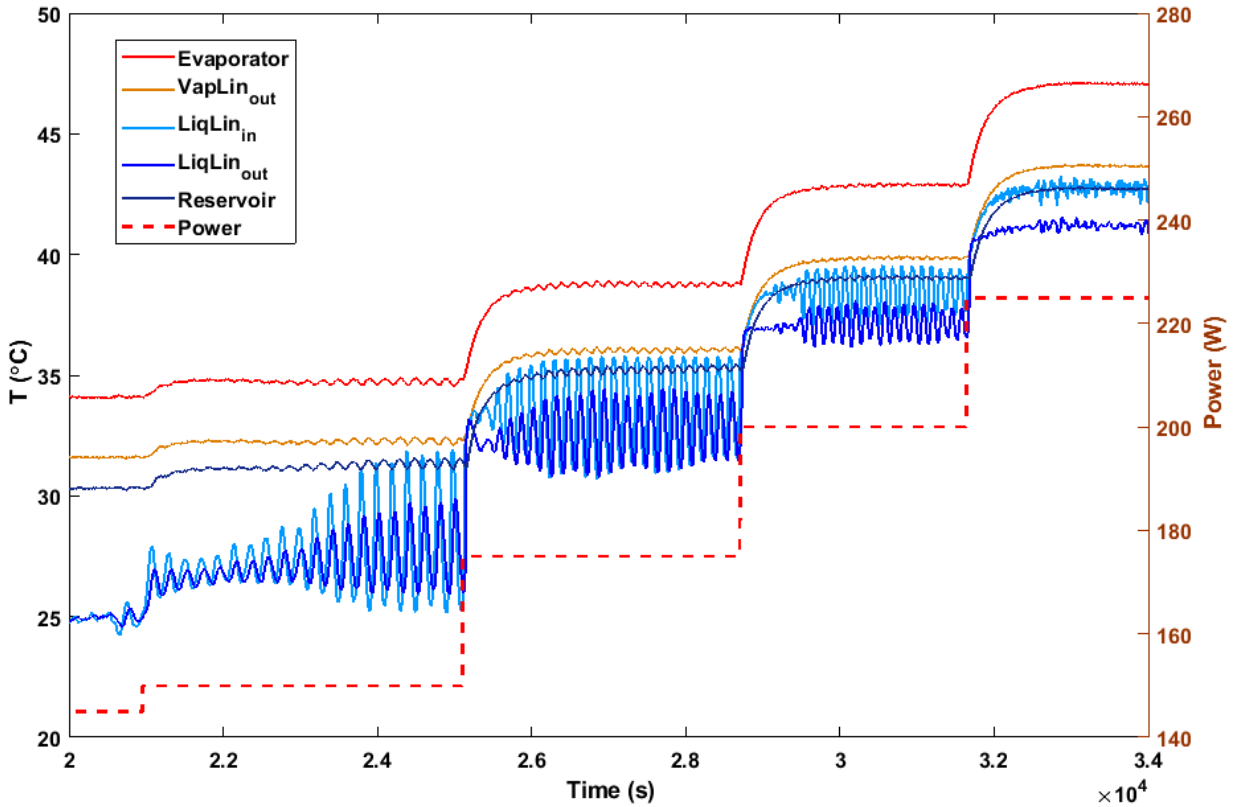


Fig. 20 The temperature oscillations in the LHP2-PC5-UP test.

At each applied power experiencing oscillations in Fig. 20, the liquid line inlet experiences the highest amplitude of oscillations since its temperature is directly proportional to the location of the interface from the condenser's exit (the subcooling length). The amplitude is decreased along the liquid line as the heat transfer with ambient provides additional subcooling. The reservoir, evaporator saddle and vapor line experience a significantly lower amplitude of oscillations as the reservoir inertia acts as a damping mechanism. The temperature oscillations in the liquid-line inlet at 200 W have a maximum amplitude of 2.3°C, which is 0.7°C higher than the oscillation amplitude at the exit of the liquid line. The other components only experience an oscillation amplitude of 0.1°C. The period of oscillations, approximately 130 s, remains the same for all of the LHP2 components at each applied power. However, a phase shift is observed between the inlet of the liquid line and the other LHP components. The most notable phase shift is observed between the liquid line and reservoir temperatures because of the fluid travel time in the liquid line and the damping effect in the reservoir. The observed amplitude of fluctuations at the condenser is smaller than that of the liquid line as the condenser's thermocouples are attached to its saddle wall. In addition to the saddle thermal inertia, the condenser wall temperatures are coupled to both of the sink and working fluid temperatures, and the sink temperature is kept constant.

### 2.7.3 Sink cycling

The sink cycling tests are conducted at fixed applied powers to investigate the LHP characteristics over a range of sink temperatures. While the applied power is kept constant, the chiller temperature is cycled in a 5°C increment between the minimum and maximum values. The chiller limitation imposes a minimum value of 5°C and a maximum value of 20°C. Table 2 presents the test scenarios performed in the sink cycling category.

Table 2 Test scenarios of sink cycling.

Test ID	Power (W)	Chiller profile (°C)
LHP1-SC030 -UD	30	5,10,15,20,15,10,5
LHP1-SC070 -UD	70	
LHP1-SC125 -UD	125	
LHP1-SC150 -UD	150	
LHP1-SC200 -UD	200	
LHP1-SC150 -DU	150	20,15,10,5,10,15,20
LHP1-SC200 -DU	200	
LHP2-SC200 -UD	200	5,10,15,20,15,10,5
LHP2-SC250 -UD	250	

Similar to the power cycling tests, each test scenario in Table 2 is conducted three times to verify the repeatability of the experimental results. The temperature variations among the repeated tests are less than 0.3°C, which is mainly caused by the change in the ambient temperature during the tests. The sink-cycling tests of LHP1 comprise of going up and down (UD) and going down and up (DU) depending on the chiller profile. LHP2 has fewer test scenarios in comparison to LHP1 because of the limitations imposed on the applied power by the PRV regulation and maximum operating temperature. The test procedure is similar to that described previously for the power cycling tests.

As an example, the LHP1-SC125-UD scenario results are presented in Fig. 21. The LHP1 starts 100 s after applying the power at 410 s. The sink temperature remains nearly constant after each change in the chiller temperature. The ambient temperature varies within 2°C in the test interval. The effect of the sink temperature change is observed first on the thermocouples of the liquid line in the form of temperature overshoots for going up and down. These thermocouples are located between the condenser and reservoir. Therefore, the liquid line experiences the temperature change before the reservoir. The low thermal inertia of the liquid line results in these temperature overshoots. The overshoots are disappeared when the chiller reaches its new equilibrium state. The other thermocouples sense the change in the sink temperature through the alternation of the operating temperature. Thus, they mainly follow the same pattern as the reservoir temperature without any overshoot because of the reservoir thermal inertia.

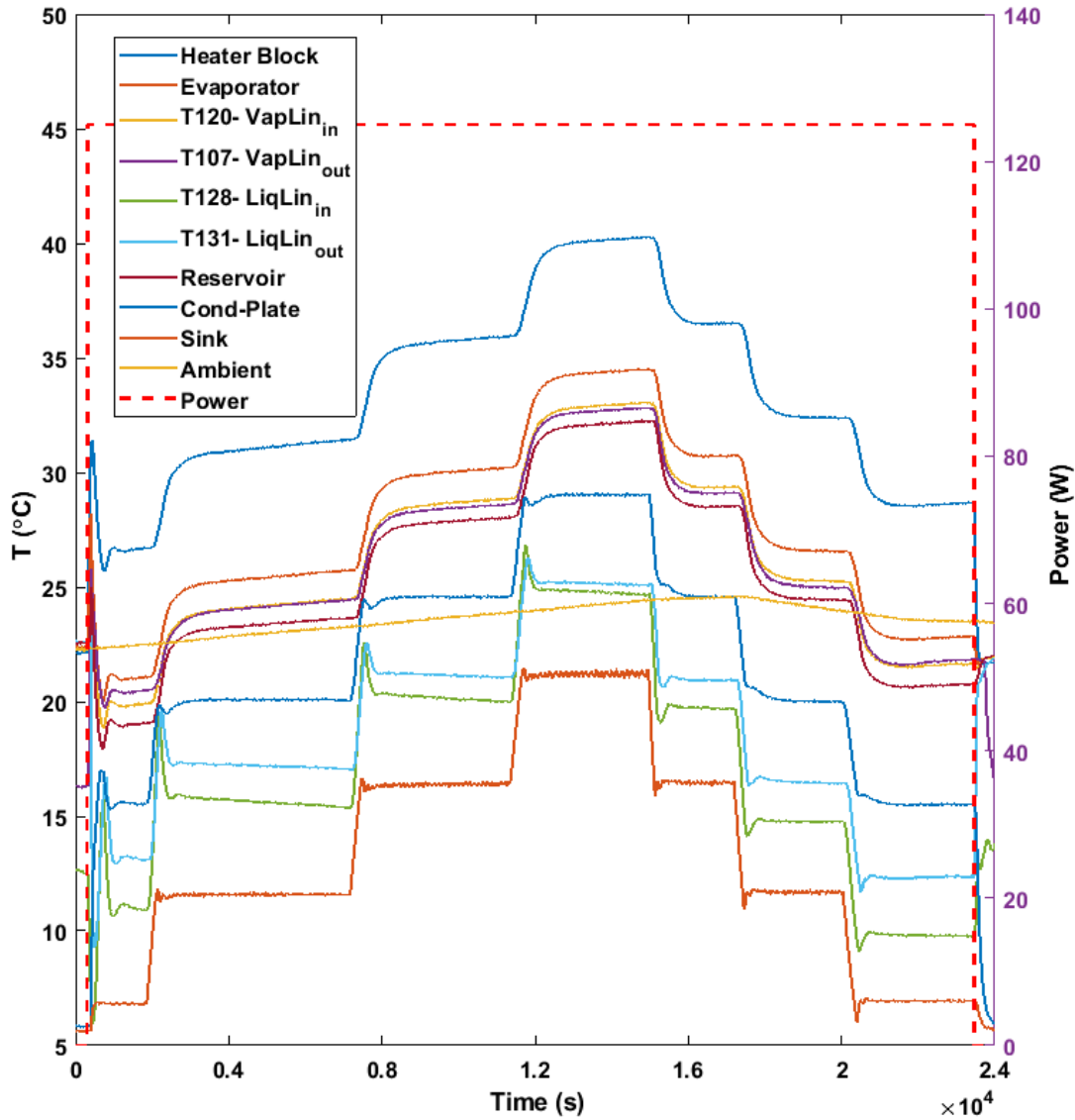


Fig. 21 The overall results of the LHP1-SC125-UD scenario.

## 2.8 Uncertainty analysis

An uncertainty analysis is performed to obtain the total uncertainty of the measurement chain. The total uncertainty is a function of the accuracy in measuring the primary variables in the experiments. Table 3 provides the accuracy of the primary variables which have a normal distribution with a 95% confidence level. These accuracy values are used to calculate the total uncertainty for the power cycling scenarios used to validate the numerical model. The chiller temperature is set to 5°C for the validation scenarios. Both the minimum and maximum applied power used for the validation are considered in each scenario to obtain the total uncertainty.

Table 3 Measurement accuracy of primary variables.

Parameter	Accuracy
Chiller temperature control	$\pm 0.1^\circ\text{C}$
Power supply current	$\pm(0.1\% \text{ of reading} + 25\text{mA})$
Power supply voltage	$\pm(0.03\% \text{ of reading} + 20\text{mV})$
T-type thermocouple	$\pm 0.5^\circ\text{C}$
DAQ temperature measurement	$\pm 0.2^\circ\text{C}$

The thermocouples have a manufacturer (OMEGA Engineering) provided accuracy better than  $\pm 0.5^\circ\text{C}$  [38]. Thermocouples are verified against the calibrated thermistors. The difference in measured temperatures is less than  $\pm 0.3^\circ\text{C}$  which is within the accuracy range that the thermocouple manufacturer is provided. The first step is to obtain the systematic or bias uncertainties ( $B$ ) from the accuracy values introduced in Table 3. The bias uncertainty is the difference between the mean value of the measurements and their actual value. The bias error remains constant for a given test scenario. [39]

The systematic uncertainty (one standard deviation) of the chiller is  $0.05^\circ\text{C}$  as its accuracy with 95% confidence is equal to two times the standard deviation. For the applied power, the errors in measuring the current and voltage are propagated into the power value using Eq.(6). The systematic uncertainty can then be obtained from the Taylor series method shown in Eq.(8).

$$B_P = \pm \left[ \left( \frac{\partial P}{\partial I} B_I \right)^2 + \left( \frac{\partial P}{\partial V} B_V \right)^2 \right]^{0.5} \quad (8)$$

where the first-order derivatives in Eq.(8) called sensitivity terms can be obtained analytically from Eq. (6). The final formula of the power uncertainty is presented in Eq. (9) where the bar sign on top represents the average value for each parameter. Table 4 provides the average applied power and its bias uncertainty calculated for each uncertainty case. The bias uncertainty is below 3% in all cases with a maximum percentage at 20 W and a minimum percentage at 325 W.

$$B_P = \pm [(\bar{V}B_I)^2 + (\bar{I}B_V)^2]^{0.5} \quad (9)$$

Table 4 The systematic uncertainty in measuring the applied power.

Scenario	$\bar{I}$ (A)	$B_I$ (A)	$\bar{V}$ (V)	$B_V$ (V)	$\bar{P}$ (W)	$B_P$ (W)	$B_P$ (%)
LHP1, $T_{\text{sink}5}, P_{\text{min}}$	0.426	0.013	46.984	0.017	<b>20.01</b>	<b><math>\pm 0.59</math></b>	<b><math>\pm 2.95</math></b>
LHP1, $T_{\text{sink}5}, P_{\text{max}}$	1.343	0.013	148.919	0.032	<b>200.00</b>	<b><math>\pm 1.96</math></b>	<b><math>\pm 0.98</math></b>
LHP2, $T_{\text{sink}5}, P_{\text{min}}$	1.830	0.013	81.967	0.022	<b>149.99</b>	<b><math>\pm 1.10</math></b>	<b><math>\pm 0.73</math></b>
LHP2, $T_{\text{sink}5}, P_{\text{max}}$	2.687	0.014	120.958	0.028	<b>325.03</b>	<b><math>\pm 1.67</math></b>	<b><math>\pm 0.51</math></b>

The systematic uncertainty of measuring the temperature is obtained by propagating the uncertainty from the DAQ and temperature sensor based on root-sum-square (RSS) as explained in Eq. (10) [39]. The DAQ and temperature sensor have the uncertainty (one standard deviation) of  $\pm 0.10^\circ\text{C}$  and  $\pm 0.25^\circ\text{C}$ , respectively. These values result in a systematic error of  $\pm 0.27^\circ\text{C}$  for the temperature measurements.

$$B_T = \pm \left[ (B_{DAQ})^2 + (B_{TC})^2 \right]^{0.5} \quad (10)$$

The total systematic uncertainty in the measurements is found using the relative form of RSS as described in Eq. (11). The denominator variables are used to make the RSS dimensionless. [40] and [41]

$$\frac{B_{test}}{\bar{T}_{LHP}} = \left[ \left( \frac{B_P}{\bar{P}} \right)^2 + \left( \frac{B_{chiller}}{\bar{T}_{chiller}} \right)^2 + \left( \frac{B_T}{\bar{T}_{amb}} \right)^2 \right]^{0.5} \quad (11)$$

where  $B_{test}$  is the combined systematic uncertainty (one standard deviation). The average values are assigned to the denominator variables in Eq. (11). Table 5 shows the input values and results of calculating the bias uncertainty in the overall experiments in  $^\circ\text{C}$ . The total systematic uncertainty is mainly affected by the operating temperature and the relative uncertainty of the applied power. For LHP1, the minimum power has a slightly higher total uncertainty than the maximum power. This higher uncertainty is contributed by the higher relative power uncertainty at the minimum power and the small operating-temperature difference between the two powers. LHP2 has the opposite trend because of the larger difference in the operating temperatures.

Table 5 The total systematic uncertainty of the experiments.

Scenario	$\bar{P}$ (W)	$B_P$ (W)	$\bar{T}_{chiller}$ ( $^\circ\text{C}$ )	$B_{chiller}$ ( $^\circ\text{C}$ )	$\bar{T}_{amb}$ ( $^\circ\text{C}$ )	$B_T$ ( $^\circ\text{C}$ )	$\bar{T}_{LHP}$ ( $^\circ\text{C}$ )	$B_{test}$ ( $^\circ\text{C}$ )
LHP1, $T_{sink5}, P_{min}$	20.0	$\pm 0.6$	5.0	$\pm 0.05$	20.3	$\pm 0.27$	16.6	$\pm 0.57$
LHP1, $T_{sink5}, P_{max}$	200.0	$\pm 2.0$			21.8		23.4	$\pm 0.44$
LHP2, $T_{sink5}, P_{min}$	150.0	$\pm 1.1$			23.0		31.1	$\pm 0.53$
LHP2, $T_{sink5}, P_{max}$	325.0	$\pm 1.7$			24.0		55.4	$\pm 0.88$

The total uncertainty of the test is a combination of systematic and random uncertainties ( $S$ ). The random or precision uncertainty does not remain constant during the test, and its value is obtained via the standard deviation of their random distribution. The RSS method in the form of Eq. (12) is utilized from the ASME standards to calculate the total uncertainty in the test. [40] and [42]

$$U_{test} = \pm t_{95} \left[ \left( \frac{B_{test}}{2} \right)^2 + (S_{T-LHP})^2 \right]^{0.5} \quad (12)$$

where  $U$  is the total uncertainty in a test and  $t_{95}$  is “Student’s t” at 95% confidence for the available degrees of freedom (DOF).  $t_{95}$  can be obtained from t-tables by knowing DOF which is the number of data points gathered in each experiment.  $S_{T-LHP}$  is the random uncertainty in the test which is obtained for the operating temperature because it is the most significant measured parameter in the experiments. In each uncertainty scenario, this random uncertainty is obtained by calculating the standard error of the operating temperature variation at the steady state. Table 6 presents the input values and the total uncertainty for each scenario using Eq. (12). In all the cases, the total uncertainty is primarily influenced by the systematic uncertainty as it is one order of magnitude more significant than the random uncertainty. The maximum total uncertainty of  $\pm 0.87^\circ\text{C}$  is obtained at the LHP2 maximum power. The LHP1 minimum power case holds the highest relative total uncertainty of  $\pm 3.38\%$ . Overall, the total uncertainty remains in an acceptable range for the experiments [43].

Table 6 The random and total uncertainty of the experiments.

<b>Scenario</b>	$\bar{T}_{LHP}(\text{°C})$	$B_{test}(\text{°C})$	$S_{T-LHP}(\text{°C})$	<b>DOF</b>	$t_{95}$	$U_{test}(\text{°C})$	$U_{test}(\%)$
LHP1, $T_{\text{sink}5}, P_{\text{min}}$	16.6	0.6	0.024	221	1.971	$\pm 0.56$	$\pm 3.38$
LHP1, $T_{\text{sink}5}, P_{\text{max}}$	23.4	0.4	0.016	350	1.967	$\pm 0.43$	$\pm 1.84$
LHP2, $T_{\text{sink}5}, P_{\text{min}}$	31.1	0.5	0.044	209	1.971	$\pm 0.53$	$\pm 1.70$
LHP2, $T_{\text{sink}5}, P_{\text{max}}$	55.4	0.8	0.014	205	1.972	$\pm 0.87$	$\pm 1.57$

Among the scenarios, the LHP2 minimum power has the highest random uncertainty since the steady-state temperature oscillates in this operating condition. The oscillation effect on the temperature distribution can be illustrated through a histogram graph shown in Fig. 22. The temperature in the figure has a bimodal distribution compared to the temperature distribution with a normal distribution in Fig. 23 for the LHP2 maximum power.

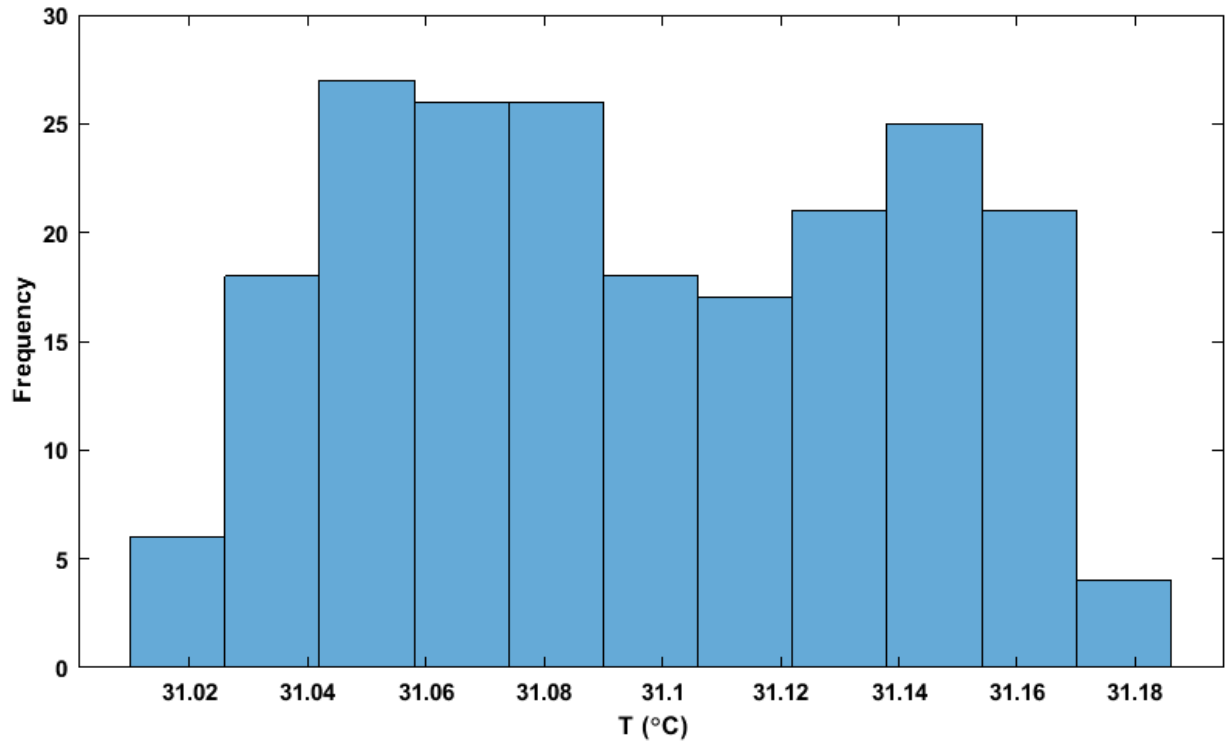


Fig. 22 Distribution of LHP2 operating temperature at the minimum power.

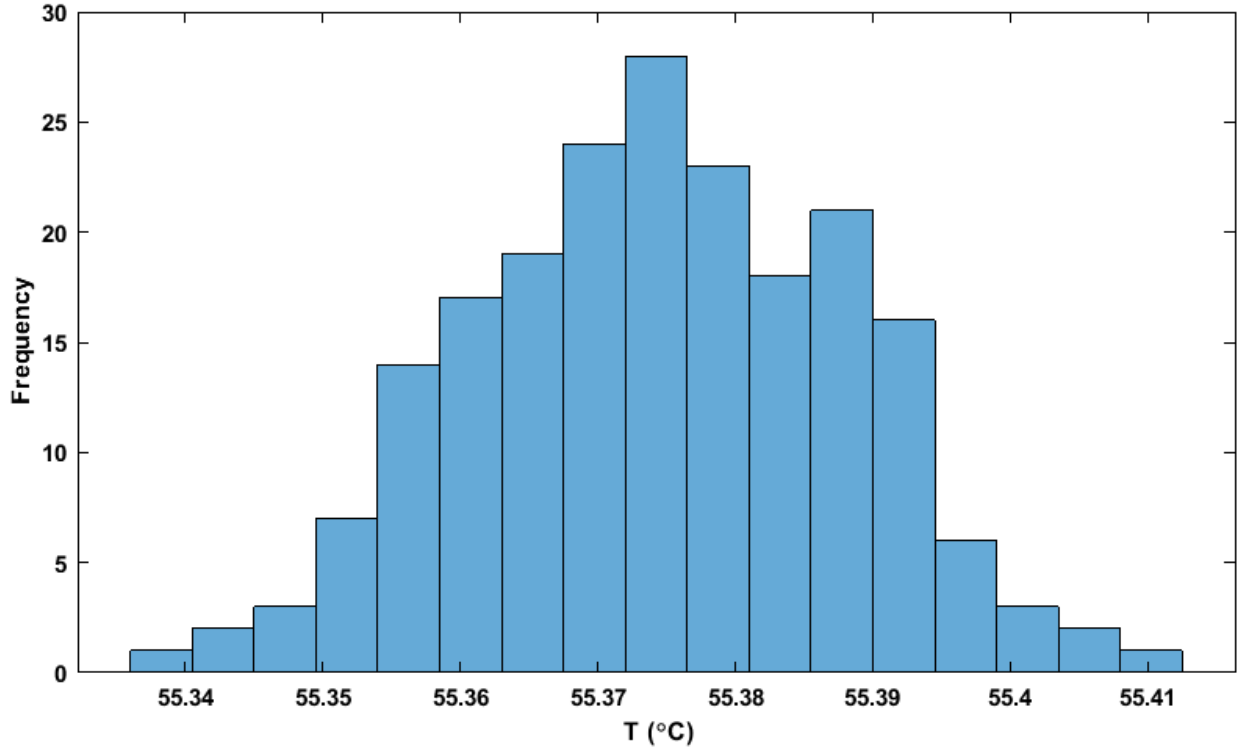


Fig. 23 Distribution of LHP2 operating temperature at the maximum power.

## 2.9 Summary

In this chapter, the experimental setup is presented in detail. The setup consists of two LHPs of different designs: a conventional one and another one with a two-way PRV. The LHPs are instrumented with three voltmeters, two ammeters and more than thirty thermocouples each to measure and record the voltage and current applied to the heater in addition to the temperatures at critical locations.

Different test scenarios are devised to determine the applied-power limits and collect data to investigate the steady-state and transient characteristics of each LHP. These characteristics include the operating temperature, the temperature response to the change in the applied power or sink temperature, the location of two-phase/liquid interface, and the oscillations in both the steady-state and transient regimes.

For LHP1, the maximum power that can be applied is 200 W due to the DC power supply limitation rather than the LHP limits. For LHP2, the maximum power is dictated by the maximum safe operating temperature and it is 325 W at the 5°C sink temperature.

The typical LHP responses to the power changes are observed during the tests. For the LHP2, during the PRV regulating mode, the operating temperature remains nearly constant as the applied power increases. The PRV regulates the operating temperature from the start-up until the temperature exceeds the 31°C set point. The applied power associated with the set point is decreased from 145 to 70 W as the sink temperature is increased from 5 to 20°C. The temperature hysteresis is only observed in the performance curve of the LHP1 VCM, and its effect is reduced as the applied power increases.

The sink cycling results show that the change in the chiller temperature propagates from the condenser plate through the liquid line to the reservoir and other LHP elements. The thermocouples on the liquid line follow the same trend (including overshoots) as the ones installed on the sink plate. The remaining thermocouples follow the reservoir temperature as its thermal inertia smoothens the effect of the change in the sink temperature.

The oscillations observed in the power and sink cycling tests have a high frequency and low amplitude. This type of oscillation occurs as the two-phase/liquid interface moves to the condenser exit and enters the liquid line. This movement causes fluctuation of subcooling in the reservoir, which initiates and sustains the oscillation of the operating temperature. The highest oscillation amplitude is observed in the liquid line inlet, and the other sections experience a lower amplitude because of the heat transfer with ambient and the thermal inertia of the reservoir.

The total uncertainty is calculated for different test scenarios. The measured operating temperatures have an uncertainty of less than  $\pm 1.0^\circ\text{C}$  with a confidence level of 95%.

## Chapter 3: Working fluid correlations

Several empirical or analytical formulas are required to obtain the fluid pressure drop and heat transfer rate in the LHP mathematical model. The heat transfer occurs via conduction between solid elements and via convection between a solid element and fluid. The flow can be either external, the ambient air surrounding an LHP, or internal. It can also be laminar or turbulent. It is essential to select suitable correlations that provide sufficiently accurate answers for the range of operating conditions of the LHP. Also, the numerical implementation of the correlations and formulas should not require high computational time or CPU utilization. The fluid properties need to be calculated considering the state of the fluid. In this work, thermodynamic properties of the working fluid, such as density and viscosity, are obtained using NIST REFPROP 10.0 from the two independent fluid properties [44].

### 3.1 Pressure drop correlations

The pressure drop terms in the momentum equation of a horizontal pipe can be calculated from Eq. (13) where the first term ( $\xi$ ) is the pressure drop coefficient. The second term is known as dynamic pressure.

$$\Delta P = \xi \left( \frac{\rho u^2}{2} \right) \quad (13)$$

$\xi$  is obtained from Eq. (1) including the viscous friction and bend terms.

$$\xi = f \frac{A_{friction}}{A_{cross}} + \xi_{bends} \quad (14)$$

The viscous friction term is a combination of the Fanning factor and the ratio of friction area to the cross-section area in the pipe. The former parameter is a function of the Reynolds number and the pipe roughness. The latter parameter is calculated from the geometry of the control volume. The total bend pressure drop ( $\xi_{bends}$ ) represents the effect of all the bends on the pressure drop coefficient and is obtained from the correlations provided in Idelchik [45]. These terms are explained thoroughly in the following subsections.

#### 3.1.1 Single-phase correlation

The Fanning factor can be calculated from the Churchill correlation presented in Eq. (15), and it is valid for laminar, transient and turbulent flows [46].

$$f = 2 \left[ \left( \frac{8}{Re} \right)^{12} + \left( \frac{1}{(A+B)^{\frac{3}{2}}} \right) \right]^{\frac{1}{12}} \quad (15)$$

$$\text{where: } A = \left\{ 2.457 \ln \left[ \frac{1}{\left( \frac{7}{Re} \right)^{0.9} + 0.27 \frac{\varepsilon}{D_{in}}} \right] \right\}^{16}, \quad B = \left( \frac{37530}{Re} \right)^{16}$$

where  $\varepsilon$  represents the surface roughness of the pipe and  $Re$  is the Reynolds number defined by the Eq. (16) for a fluid flow inside a pipe.

$$Re = \frac{\rho u D_{in}}{\mu} \quad (16)$$

The inner diameter ( $D_{in}$ ) of the pipe is used as the characteristic length for circular transportation lines in an LHP. The fluid properties and flow velocity ( $u$ ) should be known to calculate the Fanning factor. The density and viscosity of the fluid can be obtained depending on the fluid states. For the single-phase flow, these properties are directly obtained from the temperature and pressure of the fluid.

### 3.1.2 Two-phase flow correlations

The recent work by Awad and Muzychka [47] proposes the use of the Churchill correlation for the two-phase flow. They assume a homogenous flow where both the liquid and vapor flows have the same velocity. Thus, the two-phase flow is treated as a combination of single-phase liquid and vapor flows. The viscosity is obtained from the saturated liquid and vapor values as a function of the vapor quality ( $X$ ) using one of the correlations provided in Table 7. These correlations are developed for minichannels, inner-diameter of [1 10] mm, using an analogy between viscosity in two-phase flow and effective thermal conductivity in porous media. The two-phase fluid density is directly obtained from the saturated temperature and vapor quality.

Table 7 Correlations for the homogeneous viscosity of a two-phase flow. [47]

Name	Formula
Parallel (Par)	$\mu_{2ph,Par} = \left( \frac{1-X}{\mu_{liq}} + \frac{X}{\mu_{vap}} \right)^{-1}$
Series (Ser)	$\mu_{2ph,Ser} = (1-X)\mu_{Liq} + X\mu_{vap}$
Maxwell-Eucken 1 (ME1)	$\mu_{2ph,ME1} = \mu_{Liq} \frac{2 + \frac{\mu_{vap}}{\mu_{liq}} - 2 * X * \left( 1 - \frac{\mu_{vap}}{\mu_{liq}} \right)}{2 + \frac{\mu_{vap}}{\mu_{liq}} + X * \left( 1 - \frac{\mu_{vap}}{\mu_{liq}} \right)}$

Name	Formula
Maxwell-Eucken 2 (ME2)	$\mu_{2ph,ME2} = \mu_{vap} \frac{2 + \frac{\mu_{liq}}{\mu_{vap}} - 2 * (1 - X) * \left(1 - \frac{\mu_{liq}}{\mu_{vap}}\right)}{2 + \frac{\mu_{liq}}{\mu_{vap}} + (1 - X) * \left(1 - \frac{\mu_{liq}}{\mu_{vap}}\right)}$
Maxwell-Eucken Average (MEA)	$\mu_{2ph,MEA} = \frac{\mu_{2ph,ME1} + \mu_{2ph,ME2}}{2}$
Effective Medium Theory (EMT)	$\mu_{2ph,EMT} = 0.25 \left[ A + \sqrt{A^2 + 8\mu_{liq}\mu_{vap}} \right]$ $A = (3X - 1)\mu_{vap} + (3\{1 - X\} - 1)\mu_{liq}$ <p>Obtained by solving:</p> $(1 - X) \frac{\mu_{liq} - \mu_{2ph,EMT}}{\mu_{liq} + 2\mu_{2ph,EMT}} + X \frac{\mu_{vap} - \mu_{2ph,EMT}}{\mu_{vap} + 2\mu_{2ph,EMT}} = 0$

Nishikawara et al. [4] employed the Lockhart-Martinelli (LM) method in their LHP numerical model to directly obtain the viscous friction term in the pressure drop equation of the two-phase flow. In the LM method, the two-phase viscous pressure drop is calculated from the pressure drop obtained for saturated vapor or liquid using the two-phase multipliers of  $\Phi_{vap}$  and  $\Phi_{liq}$  as shown in Eqs. (17) and (18) [48]. The pressure drop ratio of the saturated states are also proportional as a function of the Lockhart-Martinelli parameter ( $X_{LM}$ ) as described in Eq. (19). Chisholm [49] introduced correlations to obtain the two-phase multipliers from the Lockhart-Martinelli parameter as described in Eqs. (20) and (21).

$$\Delta P_{2ph,v} = \Phi_{vap}^2 \Delta P_{vap} \quad (17)$$

$$\Delta P_{2ph,l} = \Phi_{liq}^2 \Delta P_{liq} \quad (18)$$

$$X_{LM}^2 = \frac{\Delta P_{liq}}{\Delta P_{vap}} = \frac{\Phi_{vap}^2}{\Phi_{liq}^2} \quad (19)$$

$$\Phi_{vap}^2 = 1 + cX_{LM} + X_{LM}^2 \quad (20)$$

$$\Phi_{liq}^2 = 1 + \frac{c}{X_{LM}} + \frac{1}{X_{LM}^2} \quad (21)$$

$X_{LM}$  and  $c$  are functions of the flow regime (laminar and turbulent) and vapor portions of the two-phase flow. Table 8 provides the values of these parameters in each combination of the flow

regimes. Subscripts used to identify the flow regimes as “l” and “t” stand for laminar and turbulent. The first letter of the subscript is for the liquid portion and the second one for the vapor portion.

Table 8 Correlations of  $X_{LM}$  and  $c$  in the LM correlation. [48], [49] and [50]

Liquid regime	Vapor regime	$X_{LM}$	$c$
$Re_{liq} < 2000$	$Re_{vap} < 2000$	$X_{ll} = \left(\frac{1-X}{X}\right)^{0.5} \left(\frac{\rho_{vap}}{\rho_{liq}}\right)^{0.5} \left(\frac{\mu_{liq}}{\mu_{vap}}\right)^{0.5}$	$c_{ll} = 5$
$Re_{liq} < 2000$	$Re_{vap} \geq 2000$	$X_{lt} = 18.65 \left(\frac{1-X}{X}\right) \left(\frac{\rho_{vap}}{\rho_{liq}}\right)^{0.5} \frac{Re_{vap}^{0.1}}{Re_{liq}^{0.5}}$	$c_{lt} = 12$
$Re_{liq} \geq 2000$	$Re_{vap} < 2000$	$X_{tl} = \frac{1}{18.65} \left(\frac{1-X}{X}\right) \left(\frac{\rho_{vap}}{\rho_{liq}}\right)^{0.5} \frac{Re_{vap}^{0.5}}{Re_{liq}^{0.1}}$	$c_{tl} = 10$
$Re_{liq} \geq 2000$	$Re_{vap} \geq 2000$	$X_{tt} = \left(\frac{1-X}{X}\right)^{0.9} \left(\frac{\rho_{vap}}{\rho_{liq}}\right)^{0.5} \left(\frac{\mu_{liq}}{\mu_{vap}}\right)^{0.1}$	$c_{tt} = 20$

The Reynolds numbers in Table 8 are used to obtain the fluid regimes and can be calculated from Eqs. (22) and (23). [50]

$$Re_{liq} = \frac{(1-X)GD_{in}}{\mu_{liq}} \quad (22)$$

$$Re_{vap} = \frac{XGD_{in}}{\mu_{vap}} \quad (23)$$

where the mass flux ( $G$ ) can be obtained by multiplying the density and velocity of the two-phase flow. Finally, the viscous pressure drops for the single phase ( $\Delta P_{vap}$  and  $\Delta P_{liq}$ ) are obtained from Eqs. (24) and (25) to be used in the LM correlation for the two-phase flow.

$$\Delta P_{vap} = f_{vap} \left(\frac{A_{friction}}{A_{cross}}\right) \left(\frac{\rho_{vap}u^2}{2}\right) \quad (24)$$

$$\Delta P_{liq} = f_{liq} \left(\frac{A_{friction}}{A_{cross}}\right) \left(\frac{\rho_{liq}u^2}{2}\right) \quad (25)$$

The Fanning factor can be obtained from the Churchill correlation introduced in Eq. (15). For the circular pipes without area change, these equations can be presented in the simplified forms introduced in Eqs. (26) and (27).

$$\Delta P_{vap} = f_{vap} \left(\frac{2L}{D}\right) \left(\frac{(XG)^2}{\rho_{vap}}\right) \quad (26)$$

$$\Delta P_{liq} = f_{liq} \left( \frac{2L}{D} \right) \left( \frac{((1-X)G)^2}{\rho_{liq}} \right) \quad (27)$$

### 3.1.3 Verification and selection

The eight correlations of the viscous pressure drop introduced above for the two-phase flow should be analyzed to choose an optimum correlation to be implemented in the LHP numerical model. The main criteria considered in the selection process include the pressure-drop continuity over the vapor quality range, the prediction capability with the smallest error and the shortest computational time. All of the correlations are coded in MATLAB to investigate the selection criteria.

First, a scenario is simulated to investigate the continuity criterion of the correlations. In this continuity scenario, ammonia flow in a straight, horizontal, stainless-steel pipe with a diameter of 2 mm is considered. The temperature and mass flux of the flow are 15.8°C and  $26.4 \frac{kg}{sm^2}$ , respectively. The surface roughness of the pipe is assumed as 15  $\mu m$  [51]. Figure 24 provides the gradient of the pressure drop for 1000 data points equally distributed over the vapor quality domain.

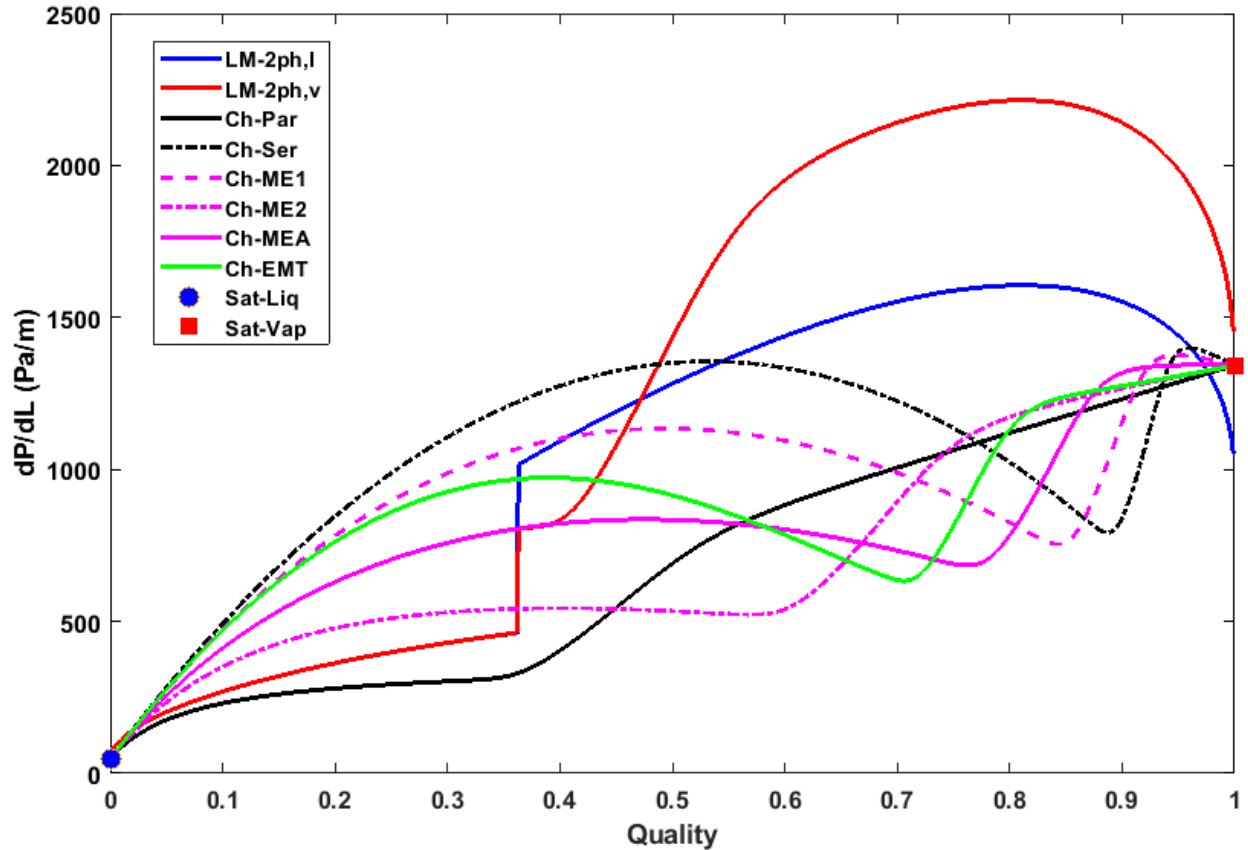


Fig. 24 Continuity of the correlations for the two-phase viscous pressure drop.

In Fig. 24, Both of the LM correlations experience a discontinuity at 36.2% vapor quality where there is a sudden jump in the gradient. The discontinuity location is a function of  $Re_{liq}$  and  $Re_{vap}$  as they change the regime of  $X_{LM}$  in Table 8. Before the sudden jump, the two correlations followed the same line. The LM-2ph,l line has a higher gradient at the point of discontinuity. However, the LM-2ph,l line falls behind the LM-2ph,v at the higher vapor quality. Moreover, the LM result does not approach the gradient of the saturated vapor at vapor quality of one.

In contrast, all six Churchill methods in Fig. 24 not only are continuous functions across the vapor quality but also match the gradient value of the saturated liquid and saturated vapor at the transition points. The Ch-Pra line has the smoothest transition over the vapor quality range with no peak or drop. The Ch-Ser line has higher gradients in the low qualities and experiences a sharp transition at the vapor quality close to one. The other Churchill lines lay between the Ch-Pra and Ch-Ser ones.

Second, the prediction capability of the correlations is assessed by comparing the calculated results to the data published by Ungar and Cornwell [52] for ammonia flow inside a straight horizontal pipe. The data for the pipe inner diameters of 1.78 and 2.58 mm are selected since they are the closest values to the inner diameters of the condenser and transportation lines in LHP1 and LHP2. The fluid has an approximate temperature of 24.5°C, and its mass flux varies from 10 to 63  $\frac{kg}{s\ m^2}$ . The surface roughness and material of the pipes are not mentioned in the publication. Thus, two selected scenarios are a smooth pipe and a stainless-steel pipe with a surface roughness of 15  $\mu m$ . Table 9 presents the average errors of the correlation predictions in the relative format, as defined in Eq. (28) where  $n$  is the number of data points.

$$e_{relative} = \frac{\sum_{i=1}^n \frac{|dP_{Correlation,i} - dP_{experiment,i}|}{dP_{experiment,i}}}{n} * 100 \quad (28)$$

Table 9 The average relative errors of the predicted pressure drops for the two-phase flow.

Pipe	Smooth ( $\epsilon = 0$ )		Stainless steel ( $\epsilon = 15\ \mu m$ )	
	2.58	1.78	2.58	1.78
<b><math>D_{in}</math> (mm)</b>	<b>2.58</b>	<b>1.78</b>	<b>2.58</b>	<b>1.78</b>
<b>LM-2ph,v</b>	75.1	31.3	94.8	52.5
<b>LM-2ph,l</b>	68.1	23.6	68.1	23.6
<b>Ch-Pra</b>	15.7	29.4	15.2	18.9
<b>Ch-Ser</b>	56.5	37.0	58.6	38.2
<b>Ch-ME1</b>	42.3	35.2	44.9	35.3
<b>Ch-ME2</b>	17.8	27.3	19.9	20.9
<b>Ch-MEA</b>	26.3	30.8	29.0	28.5
<b>Ch-EMT</b>	32.4	36.3	34.4	32.1

In Table 9, the minimum average relative error belongs to the Ch-Pra correlation with the values of less than 20% for all columns except for the smooth pipe with the inner diameter of 1.78 mm. In that case, the average relative error for the Cha-Pra method is 29.4%. Considering that many correlations are accurate within 30%, this is high but still an acceptable value. The LM-2ph,l has a minimum average of 23.6% for the 1.78 mm smooth pipe. It is worth to mention that the surface roughness does not affect the LM-2ph,l value. This independence implies that the LM-2ph,l may not be a suitable correlation. The results of other correlations change by the surface roughness. Increasing the roughness improves the predictions of the Churchill methods but worsens the LM-2ph,v prediction.

The scenario of the 2.58 mm-diameter stainless-steel pipe is selected to conduct a more thorough analysis of the prediction capability of the correlations, particularly for the LM and Chu-Pra. Among all the Churchill correlations, the parallel method is selected because of its minimum average relative errors. Figure 25 presents both the gradients of the viscous pressure drop and their associated mass flux. In a given mass flux, increasing the vapor quality increases the pressure drop through an increase in the fluid velocity resulting in higher dynamic pressure and friction factor. The results of the correlations, particularly LM ones, deviate more from the measurements as the mass flux increases.

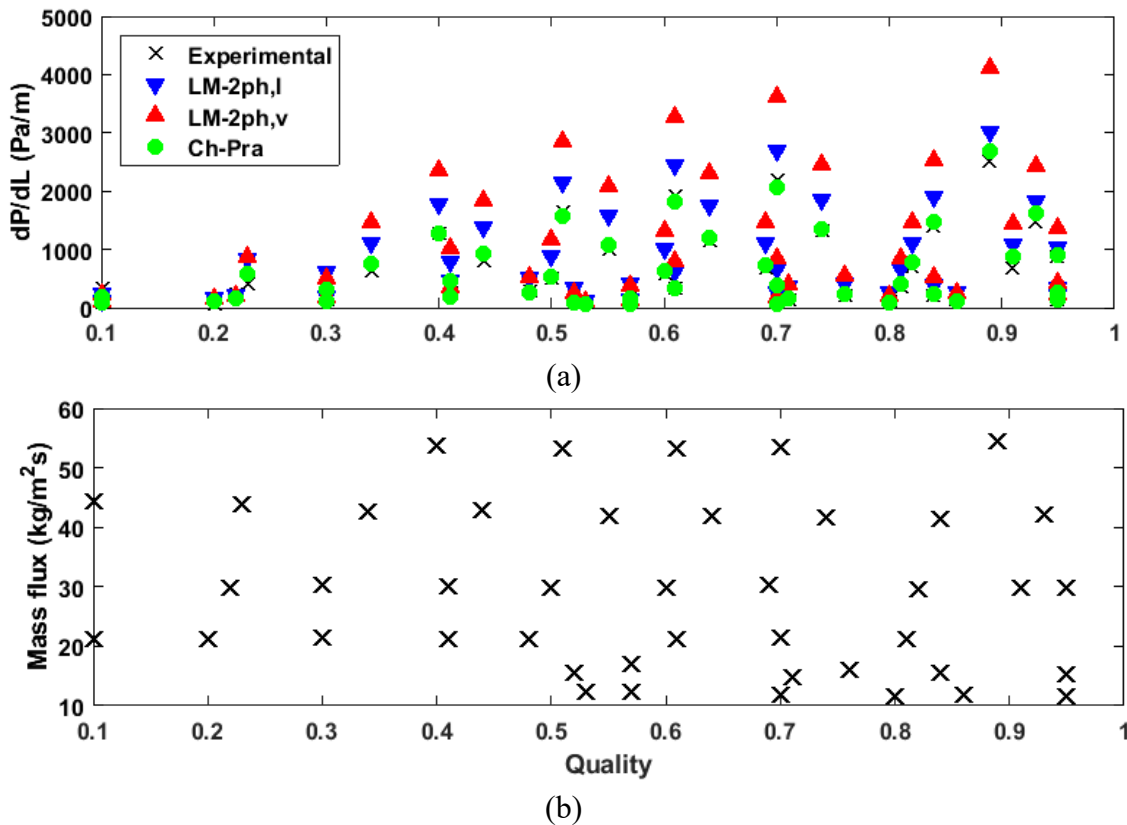


Fig. 25 The measured and predicted results for the 2.58 mm-diameter stainless-steel pipe: (a) the pressure drop gradient and (b) the experimental mass flux.

In Fig. 26, for better clarity, the viscous pressure drops for the 2.58 mm-diameter stainless-steel pipe are shown together with the relative error lines of -30%, 0% and +30%. The LM-2ph,v correlation overpredicts the pressure gradients above +30% margin. The predictions of the LM-2ph,l correlation also exceed the measurement, but they are around the +30% margin. The relative error is decreased as the pressure gradient increases. The results of the Ch-Pra correlation are mostly located between  $\pm 30\%$  margin lines. For the measured gradients below 350 Pa/m, the Ch-Pra correlation underpredicts the gradients. Then, it overpredicts the gradient in the measured range of [350 – 500] Pa/m. Above this range, the calculated data is smaller than the measured one except for the last data point. The pressure drop values analyzed in Fig. 26 is the approximate range expected in the LHP operation.

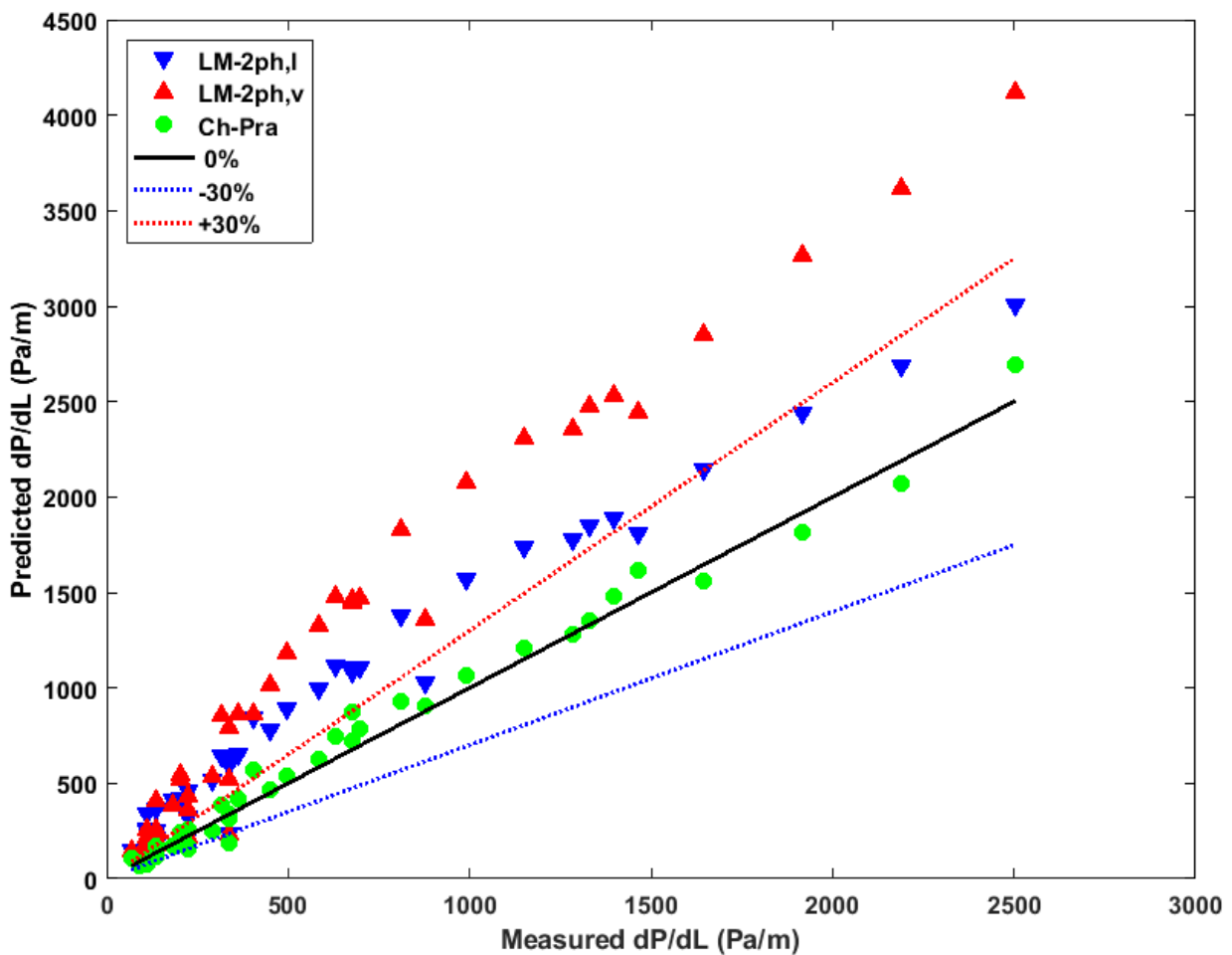


Fig. 26 Prediction versus measurement of the viscous pressure gradient for the 2.58 mm-diameter stainless-steel pipe.

Finally, the computational time to run each correlation is evaluated to find the minimum computational requirement. The minimum computational time is an essential criterion as the correlation script or function is called for each LHP fluid control volume at each time step during the simulation. Therefore, running the correlation script can take up a significant portion of the processing time. For instance, the correlation script should be run roughly  $9 \times 10^6$  times to simulate the transient behavior of an LHP with 30 control volumes for 30,000 seconds. The evaluation of the computational time is conducted by running the MATLAB scripts of the correlations for the continuity scenario with 1000 data points as shown in Table 10, using a computer with Intel Core i7-3770 CPU and 16 GB of RAM. The LM correlations take the longest time of 0.58 s, and the Churchill correlations require around 0.12 s less time. Among the Churchill correlations, the Ch-Pra and Ch-Ser have the lowest computational time of 0.44 s. Therefore, choosing the Ch-Pra method instead of LM-2ph,l reduces the required computational time by 24.1%. This reduction totals to a savings of 21 minutes when running the correlation script for  $9 \times 10^6$  times.

Table 10 Comparison of the computational time of the different two-phase correlations.

Correlations	LM-2ph,v	LM-2ph,l	Ch-Pra	Ch-Ser	Ch-ME1	Ch-ME2	Ch-MEA	Ch-EMT
Computational time (s)	0.58	0.58	0.44	0.44	0.46	0.46	0.47	0.47

In conclusion, the Ch-Pra correlation is selected to obtain the viscous pressure gradient for two-phase flow. This correlation is continuous over the vapor quality domain as shown in Fig. 24. Moreover, the correlation has the minimum average relative error when predicting the pressure gradients for three out of the four scenarios, as shown in Table 9. For the fourth scenario, the average is within the acceptable range of  $[-30 +30]\%$ . The Ch-Pra correlation also requires the minimum computational time among the correlations introduced above. It should be noted that the correlations introduced in this section are normally valid for the steady-state case, but it is assumed that it is also valid for the transient case. This is a common assumption and the errors introduced by this assumption should be acceptable, especially considering the large uncertainties associated with the correlations.

### 3.1.4 Bend correlations

Idelchik [45] introduced a set of correlations to obtain the total bend pressure drop coefficient ( $\xi_{\text{bends}}$ ) which is the sum of all individual ones as shown in Eq. (29).

$$\xi_{\text{bends}} = \sum_{i=1}^n \xi_i \quad (29)$$

where  $i$  and  $n$  are the bend number and the total number of the bends in the pipe, respectively.  $\xi_i$  is the pressure drop coefficient of each bend and it can be obtained by multiplying the contribution of each bend property as described in Eq. (30). These properties consist of the bend angle ( $\alpha$ ), the

relative bend radius ( $\frac{R}{D_{in}}$ ) and the relative bend roughness ( $\frac{\varepsilon}{D_{in}}$ ). The relative values are obtained by dividing the parameters by the pipe inner diameter. The bend angle and radius are illustrated in Fig. 27.

$$\xi_i = \xi_\alpha \xi_{\frac{R}{D_{in}}} \xi_{\frac{\varepsilon}{D_{in}}} \quad (30)$$

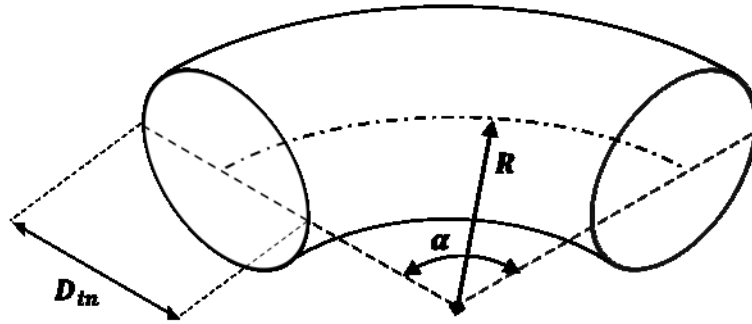


Fig. 27 The geometrical properties of a bend contributing to a pressure drop of fluid flow.  
(modified) [45]

The angle contribution ( $\xi_\alpha$ ) is calculated from the correlation represented in Eq. (31) where the angle values should be inserted in degrees.

$$\xi_\alpha = 0.957 \frac{\alpha}{90} + 0.226 \sqrt{\frac{\alpha}{90}} + 0.407 \sin(\alpha) - 0.833 \sin\left(\frac{\alpha}{2}\right) \quad (31)$$

The radius contribution ( $\xi_{\frac{R}{D_{in}}}$ ) is obtained from Eq. (32) by assuming that the bend radius should be more than half of the inner diameter. This assumption is always valid for the LHP transportation lines as their inner diameter is in the order of millimeters.

$$\xi_{\frac{R}{D_{in}}} = \begin{cases} \frac{0.21}{\left(\frac{R}{D_{in}}\right)^{2.5}} & 0.5 < \frac{R}{D_{in}} < 1 \\ \frac{0.21}{\left(\frac{R}{D_{in}}\right)^{0.5}} & 1 < \frac{R}{D_{in}} \end{cases} \quad (32)$$

Finally, the roughness contribution ( $\xi_{\frac{\varepsilon}{D_{in}}}$ ) is calculated based on the relative radius of the bend.

$$\xi_{\frac{\varepsilon}{D_{in}}} = \begin{cases} \min\left(1.5, 1 + 0.5 * 10^3 \frac{\varepsilon}{D_{in}}\right) & \frac{R}{D_{in}} < 0.55 \\ \min\left(2, 1 + 10^3 \frac{\varepsilon}{D_{in}}\right) & 0.55 < \frac{R}{D_{in}} \end{cases} \quad (33)$$

### 3.2 Internal flow heat transfer coefficient

The heat transfer coefficient of the fluid flow inside the transportation lines is required to calculate the amount of heat exchange between the fluid and pipe wall. The coefficients for the single-phase and two-phase flow are obtained from separated correlations as explained below. The coefficients should be a continuous function over the range of the temperature and vapor quality. Additionally, there should be no discontinuity in the transition between single-phase and two-phase at the saturated points.

#### 3.2.1 Single-phase flow

The heat transfer coefficient of the single-phase fluid flow inside a circular pipe is calculated from Eq. (34).

$$h = Nu \frac{k}{D_{in}} \quad (34)$$

where the Nusselt number is obtained using Eq. (35) based on the laminar and turbulent flow regimes. This power law is used to avoid discontinuities transitioning from the laminar to turbulent flow.

$$Nu = (Nu_{lam}^{16} + Nu_{tur}^{16})^{\frac{1}{16}} \quad (35)$$

Nusselt number of the laminar flow is calculated from correlations introduced by Edwards et al. [53], and it is equal to 3.66 and 4.36 under the conditions of uniform surface temperature and uniform surface heat flux, respectively. Those laminar values are calculated for fully developed flow inside a circular tube. An arithmetic average of the values, which is equal to four, is used for the laminar Nusselt number, Eq. (36).

$$Nu_{lam} = \frac{3.66 + 4.36}{2} = 4 \quad (36)$$

The Nusselt number of turbulent flow is calculated from the Gnielinski correlation as shown in Eq. (37) [54].

$$Nu_{turb} = \frac{\left(\frac{F}{8}\right) (Re - 1000) Pr}{1 + 12.7 \left(\frac{F}{8}\right)^{\frac{1}{2}} \left(Pr^{\frac{2}{3}} - 1\right)} \quad (37)$$

where the Darcy friction factor ( $F$ ) can be obtained by multiplying the Fanning friction factor by four. The Gnielinski correlation is valid for the Prandtl number range of [0.5 2000] and Reynolds number range of [3000  $5 \times 10^6$ ]. The same correlation is also recommended by [55] for transition flow although it has slightly higher errors. The Prandtl number is given by Eq. (38).

$$Pr = \frac{c_p \mu}{k} \quad (38)$$

### 3.2.2 Internal flow convective condensation correlations

The internal flow convection correlations of two-phase flow can be divided into convective condensation and boiling categories depending on the temperature difference between the fluid and pipe wall. The convective condensation is only considered here since the two-phase fluid in the condenser and liquid lines for the analyzed cases is always warmer than the sink and ambient temperatures. The convective condensation coefficient can be obtained from several correlations including the following ones:

#### 3.2.2.1 Correlation by Traviss

The heat transfer coefficient of the internal convective condensation in two-phase fluid flow can be obtained from a correlation developed by Traviss et al. (Tra) shown in Eq. (39). This correlation works in every flow regime (laminar, transient or turbulent) and annular flow for the entire quality range. [56]

$$h_{Tra} = \frac{k_{liq}}{D} \frac{0.15 Pr_{liq} Re_{liq}^{0.9}}{F_t} \left( \frac{1}{X_{tt}} + \frac{2.85}{X_{tt}^{0.476}} \right) \quad (39)$$

where the Reynolds and Prandtl numbers are calculated for the liquid portion of the two-phase flow.  $X_{tt}$  is the Lockhart-Martinelli parameter for the turbulent-turbulent flow which is defined in Eq. (40) and  $F_t$  is calculated from Eq. (41) for the different ranges of  $Re_{liq}$  [57].

$$X_{tt} = \left(\frac{1-X}{X}\right)^{0.9} \left(\frac{\rho_{vap}}{\rho_{liq}}\right)^{0.5} \left(\frac{\mu_{liq}}{\mu_{vap}}\right)^{0.1} \quad (40)$$

$$F_t = \begin{cases} 5 Pr_{liq} + 5 \ln(1 + 5 Pr_{liq}) + 2.5 \ln(0.0031 Re_{liq}^{0.812}) & Re_{liq} > 1125 \\ 5 Pr_{liq} + 5 \ln(1 + 5 Pr_{liq}) [0.0964 Re_{liq}^{0.585} - 1] & 50 < Re_{liq} < 1125 \\ 0.707 Pr_{liq} Re_{liq}^{0.5} & Re_{liq} < 50 \end{cases} \quad (41)$$

### 3.2.2.2 Correlation by Park and Hrnjak

An alternative and more recent correlation proposed by Park and Hrnjak (P&H) take into account the flow patterns including stratified, stratified-wavy and annular [58]–[60]. This correlation, shown in Eq. (42), is more comprehensive than the earlier ones. The calculation steps required to obtain the RHS parameters in Eq. (42) are summarized here.

$$h_{P\&H} = h_{forced} \left( \frac{2\pi - \theta}{2\pi} \right) + h_{free} \left( \frac{\theta}{2\pi} \right) \quad (42)$$

$\theta$  is the angle for the surface where free convective condensation occurs as shown in Fig. 28.  $h_{forced}$  and  $h_{free}$  are the heat transfer coefficients for the forced and free convection, respectively.

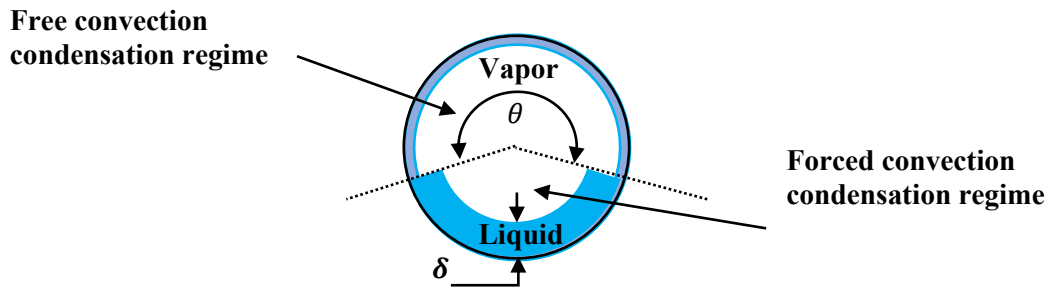


Fig. 28 A simplified model of flow structure and condensation pattern. [58]

$h_{free}$  is only a function of the fluid properties and the temperature difference between the fluid and wall as shown in Eq. (43). However, obtaining  $\theta$  and  $h_{forced}$  in Eq. (42) requires more information about the flow pattern inside the pipe.

$$h_{free} = 0.279 \left[ \frac{\rho_{liq} (\rho_{liq} - \rho_{vap}) g h_{liq,vap} k_{liq}^3}{\mu_{liq} D_{in} (T_{sat} - T_{wall})} \right]^{0.25} \quad (43)$$

First, the void fraction should be obtained to determine the flow pattern. The void fraction as defined in Eqs. (44) to (46) is a function of the vapor quality ( $X$ ), saturated densities ( $\rho$ ), surface tension ( $\sigma$ ) and mass flux ( $G$ ).

$$\alpha = \frac{\alpha_{homo} - \alpha_{drift}}{\ln\left(\frac{\alpha_{homo}}{\alpha_{drift}}\right)} \quad (44)$$

$$\alpha_{homo} = \left[1 + \left(\frac{1-X}{X}\right) \frac{\rho_{vap}}{\rho_{liq}}\right]^{-1} \quad (45)$$

$$\alpha_{drift} = \frac{X}{\rho_{liq}} \left[ \left\{1 + 0.12(1-X)\right\} \left(\frac{X}{\rho_{vap}} + \frac{1-X}{\rho_{liq}}\right) + \frac{1.18(1-X)[g\sigma(\rho_{liq} - \rho_{vap})]^{0.25}}{G\rho_{liq}^{0.5}} \right]^{-1} \quad (46)$$

where  $g$  is the Earth gravitational acceleration at the sea level. Note that the gravity influences the void fraction. For example, it may lead to the stratified flow in a horizontal pipe. This gravity effect is not directly considered in the calculations.

Second, the void fraction is used via Eqs. (47) and (48) respectively to calculate the nondimensionalized areas occupied by the liquid and vapor in the cross section of the pipe as illustrated in Fig. 29.

$$A_{liq,d} = \frac{A(1-\alpha)}{D_{in}^2} \quad (47)$$

$$A_{vap,d} = \frac{A\alpha}{D_{in}^2} \quad (48)$$

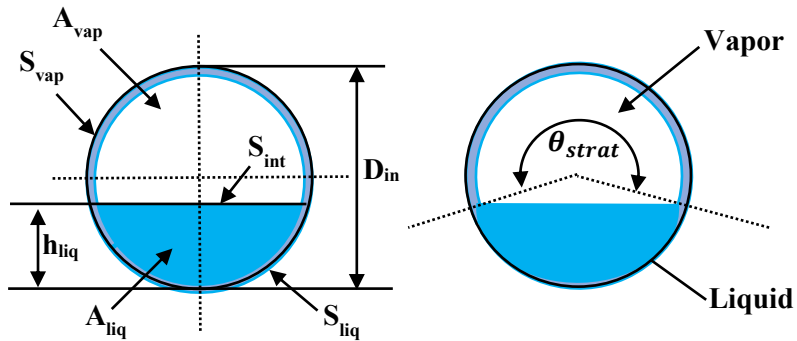


Fig. 29 Geometrical parameters for the condensation of the stratified flow pattern at the pipe cross-section. (modified) [58] and [60]

Then, the nondimensionalized areas are used to calculate the surface angle for the stratified flow ( $\theta_{strat}$ ), the height of the liquid flow ( $h_{liq}$ ) and the perimeter of the vapor/liquid interface ( $s_{int}$ ) through Eqs. (49) to (51), respectively. The two latter parameters are calculated in nondimensional forms.

$$\theta_{strat} = 2\pi - 2\left\{\pi(1 - \alpha) + (3\pi/2)^{1/3}\left[1 - 2(1 - \alpha) + (1 - \alpha)^{1/3} - \alpha^{1/3}\right] - 1/200(1 - \alpha)\alpha[1 - 2(1 - \alpha)][1 + 4(1 - \alpha)^2 + \alpha^2]\right\} \quad (49)$$

$$h_{liq,d} = \frac{1}{2}\left(1 - \cos\left(\frac{2\pi - \theta_{strat}}{2}\right)\right) \quad (50)$$

$$s_{int,d} = \sin\left(\frac{2\pi - \theta_{strat}}{2}\right) \quad (51)$$

Third, the calculated geometrical parameters are used to determine the boundary lines in the flow-pattern diagram, as shown in Fig. 30. The boundary lines consist of  $G_{strat}$ ,  $G_{wavy}$  and  $X_{LA}$ .  $G_{strat}$  is the maximum mass flux where the flow pattern remains stratified.  $G_{wavy}$  is the minimum mass flux where the flow pattern is wavy. Since the condensation is only considered for the two-phase flow inside the LHP transportation lines, the minimum  $G_{wavy}$  is extrapolated for the vapor quality larger than the vapor quality of the minimum  $G_{wavy}$  as illustrated in Fig. 30 [58].  $X_{LA}$  is the vapor quality that divides the wavy pattern into the intermittent and annular regions. However, P&H treats both of the wavy patterns as the same in obtaining the heat transfer coefficient and therefore,  $X_{LA}$  is not required to be calculated. The values of the two former boundaries can be obtained using Eqs. (52) and (53).

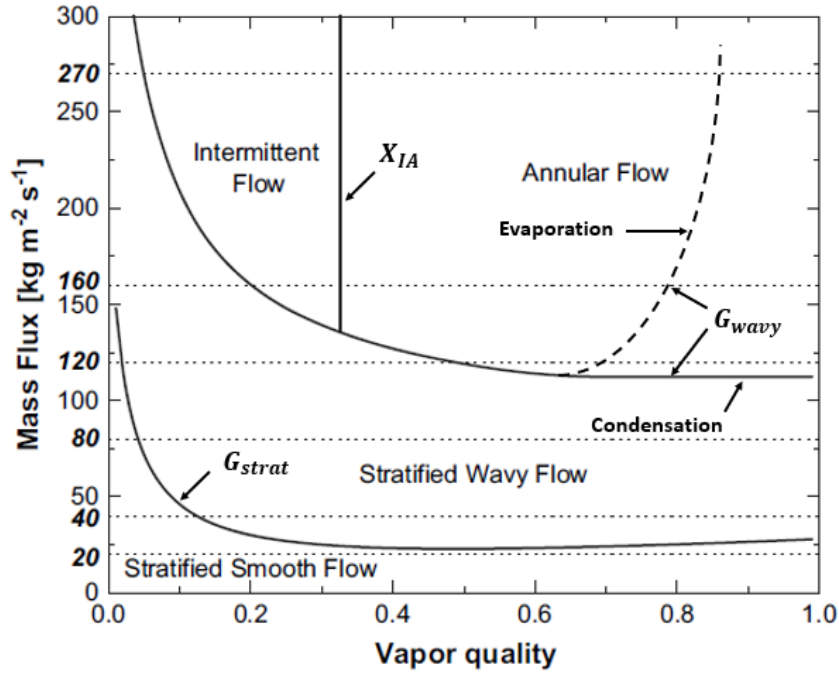


Fig. 30 Flow pattern diagram for ammonia. (modified) [58]

$$G_{strat} = \left\{ \frac{226.3^2 A_{liq,d} A_{vap,d}^2 \rho_{vap} (\rho_{liq} - \rho_{vap}) \mu_{liq} g}{X^2 (1-X) \pi^3} \right\}^{\frac{1}{3}} + 20X \quad (52)$$

$$G_{wavy} = \left\{ \frac{16 A_{vap,d}^3 g d \rho_{liq} \rho_{vap}}{X^2 \pi^2 (1 - (2h_{liq,d} - 1)^2)^{0.5}} \left[ \frac{\pi^2}{25 h_{liq,d}^2} \left( \frac{We}{Fr} \right)_{liq}^{-1.023} + 1 \right] \right\}^{0.5} + 50 - 75e^{-\frac{(X^2 - 0.97)^2}{X(1-X)}} \quad (53)$$

where the Weber to Froude number ratio can be calculated from Eq. (54) for the saturated liquid using its density, the surface tension and the pipe diameter.

$$\left( \frac{We}{Fr} \right)_{liq} = \frac{\rho_{liq} g D_{in}^2}{\sigma} \quad (54)$$

Finally, the two-phase mass flux is compared to the calculated boundaries to determine the flow pattern at the known saturated temperature and vapor quality. The forced convection coefficient ( $h_{forced}$ ) and surface angle ( $\theta$ ) in Eq. (42) can be obtained for each flow pattern. The general equation of  $h_{forced}$  is presented in Eq. (55) where the liquid film thickness ( $\delta$ ) and the interfacial

roughness correction factor ( $f_i$ ) are dependent on the flow pattern. Figure 28 illustrates the liquid film thickness, which is a function of the void fraction and surface angle, as expressed in Eq. (56).

$$h_{forced} = \frac{9.803}{10^4} \left[ \frac{4G(1-X)\delta}{(1-\alpha)\mu_{liq}} \right]^{0.79} \text{Pr}_{liq}^{0.3} \left( \frac{k_{liq}}{\delta} f_i \right) \quad (55)$$

$$\delta = \frac{D}{2} \left\{ 1 - \left[ 1 - 2\pi \left( \frac{1-\alpha}{2\pi-\theta} \right) \right]^{0.5} \right\} \quad (56)$$

As the flow pattern is determined, equations introduced in Table 11 can be used to calculate the remaining of the parameters required to obtain the heat transfer coefficient for two-phase condensation.

Table 11 The flow-pattern-dependent parameters required for the P&H correlation.

Flow pattern	Parameters
Stratified	$\theta = \theta_{strat}$ $f_i = 1 + \left( \frac{u_{vap}}{u_{liq}} \right)^{0.5} \left( \frac{(\rho_{liq} - \rho_{vap})g\delta^2}{\sigma} \right)^{0.25} \left( \frac{G}{G_{strat}} \right)$
Stratified and Wavy	$\theta = \theta_{strat} \left( \frac{G_{wavy} - G}{G_{wavy} - G_{strat}} \right)^{0.5}$ $f_i = 1 + \left( \frac{u_{vap}}{u_{liq}} \right)^{0.5} \left( \frac{(\rho_{liq} - \rho_{vap})g\delta^2}{\sigma} \right)^{0.25}$
Wavy	$\theta = 0$ $f_i = 1 + \left( \frac{u_{vap}}{u_{liq}} \right)^{0.5} \left( \frac{(\rho_{liq} - \rho_{vap})g\delta^2}{\sigma} \right)^{0.25}$

The  $\left(\frac{u_{vap}}{u_{liq}}\right)$  parameter in the  $f_i$  equations is called the slip ratio or phase-velocity ratio, and it is obtained from Eq.(57).

$$\left(\frac{u_{vap}}{u_{liq}}\right) = \frac{X}{1-X} \left(\frac{\rho_{liq}}{\rho_{vap}}\right) \left(\frac{1-\alpha}{\alpha}\right) \quad (57)$$

### 3.2.3 Verification and selection

The two correlations, Traviss (Tra) and Park and Hrnjak (P&H), are assessed to select the most suitable one for the numerical modelling of the two-phase flow inside an LHP. The assessment criteria are identical to the ones used for the selection of the viscous-pressure-drop correlation: the continuity of the results over the input range, the prediction capability and computational time.

First, the continuity criterion is assessed through obtaining the heat transfer coefficient for the continuity scenario introduced in Section 3.1.3 when the temperature of the pipe wall is 1°C colder than the fluid. Figure 31 shows the calculated heat transfer coefficients for 1000 data points equally distributed over the vapor quality range. The heat transfer coefficient line obtained from the P&H correlation is continuous over the plotted range. The Traviss line experiences discontinuity at the vapor quality of 86.7% where the heat transfer coefficient drops by 4.6%. However, this discontinuity is small compared to the trend line of the heat transfer coefficient. Further analysis shows that the location of the drop is a function of  $Re_{liq}$  as it changes the formula used to calculate  $F_t$  in the Traviss correlation. Increasing  $Re_{liq}$ , through higher mass flux, moves the discontinuity point to the higher vapor quality values even though the discontinuity value remains around 4%.

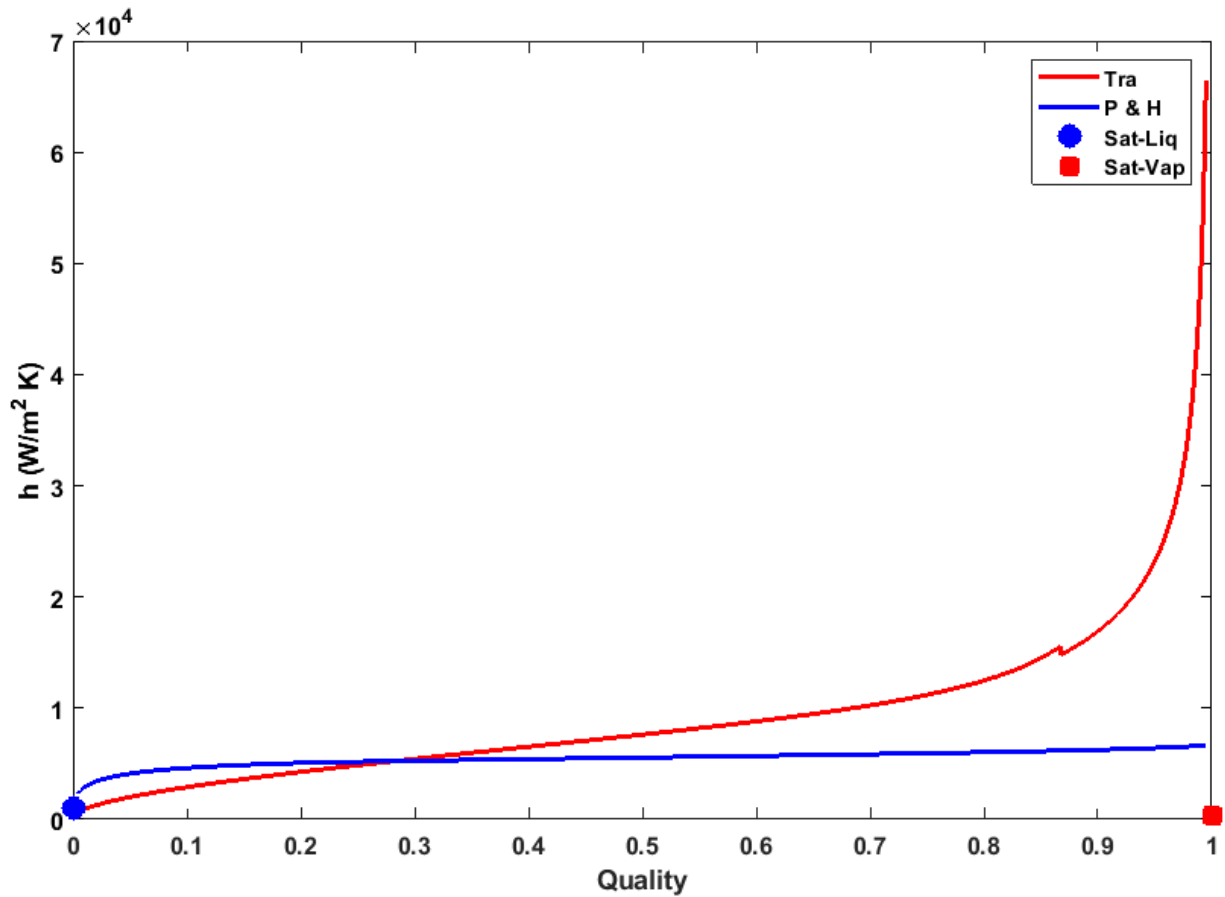


Fig. 31 Assessment of the continuity of the correlations for the two-phase heat transfer coefficient.

Both of the correlation lines are failed to converge to the single-phase values at the saturated-liquid and saturated-vapor points. These discontinuities occur because the two-phase correlations are not valid at very low and high qualities. The correlations overpredict the heat transfer coefficient for the saturated vapor as shown in Fig. 31 and underpredict for the saturated liquid as illustrated in Fig. 32.

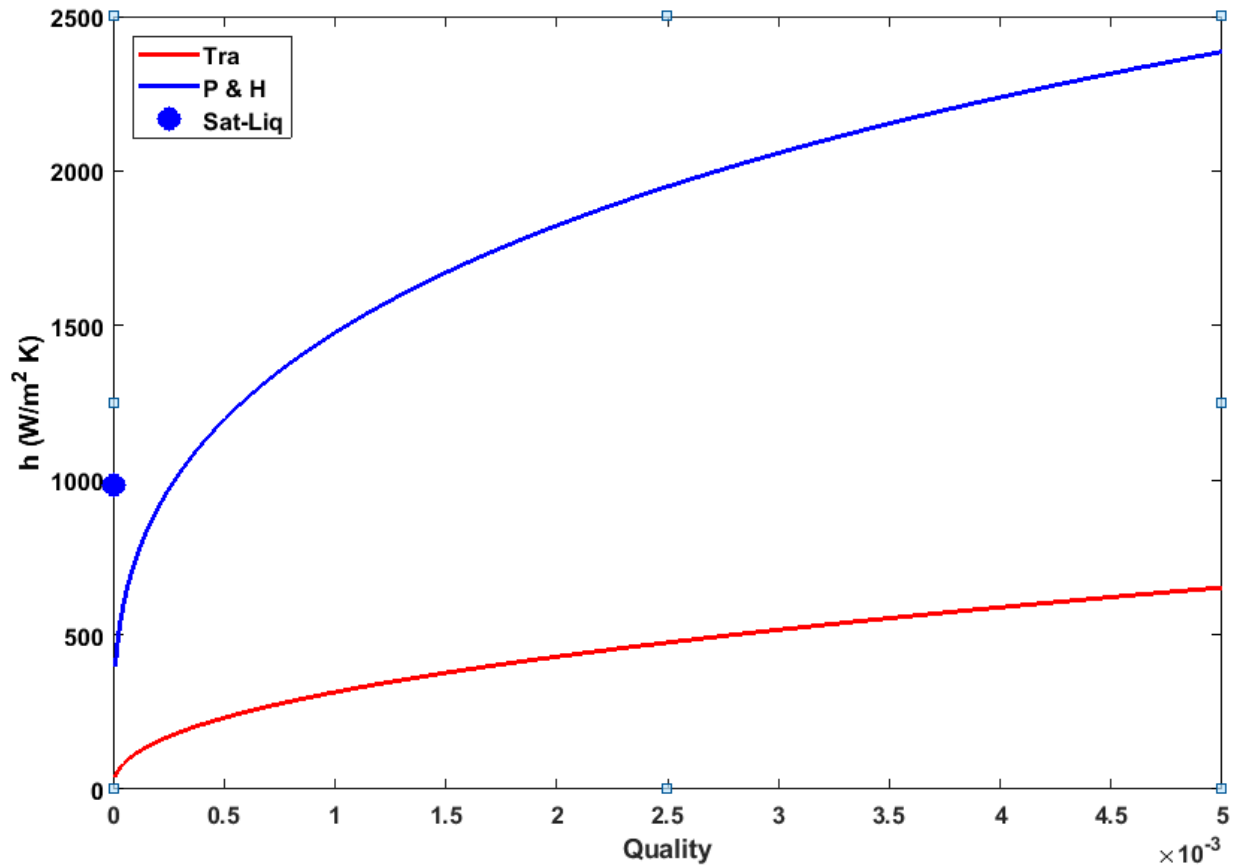


Fig. 32 Underprediction of the two-phase heat transfer coefficient in the vicinity of the saturated liquid.

Therefore, there is a need to obtain a continuous variation for the heat transfer coefficient. The discontinuities are avoided by smoothing functions, as shown in Fig. 33. Two vapor quality values are chosen to obtain a single smooth function across the entire quality range of [0 1]. For instance, in Fig. 33, the qualities of 0.2 and 0.8 are selected as the upper limit of the liquid/two-phase transition and the lower limit of the two-phase/vapor transition, respectively.

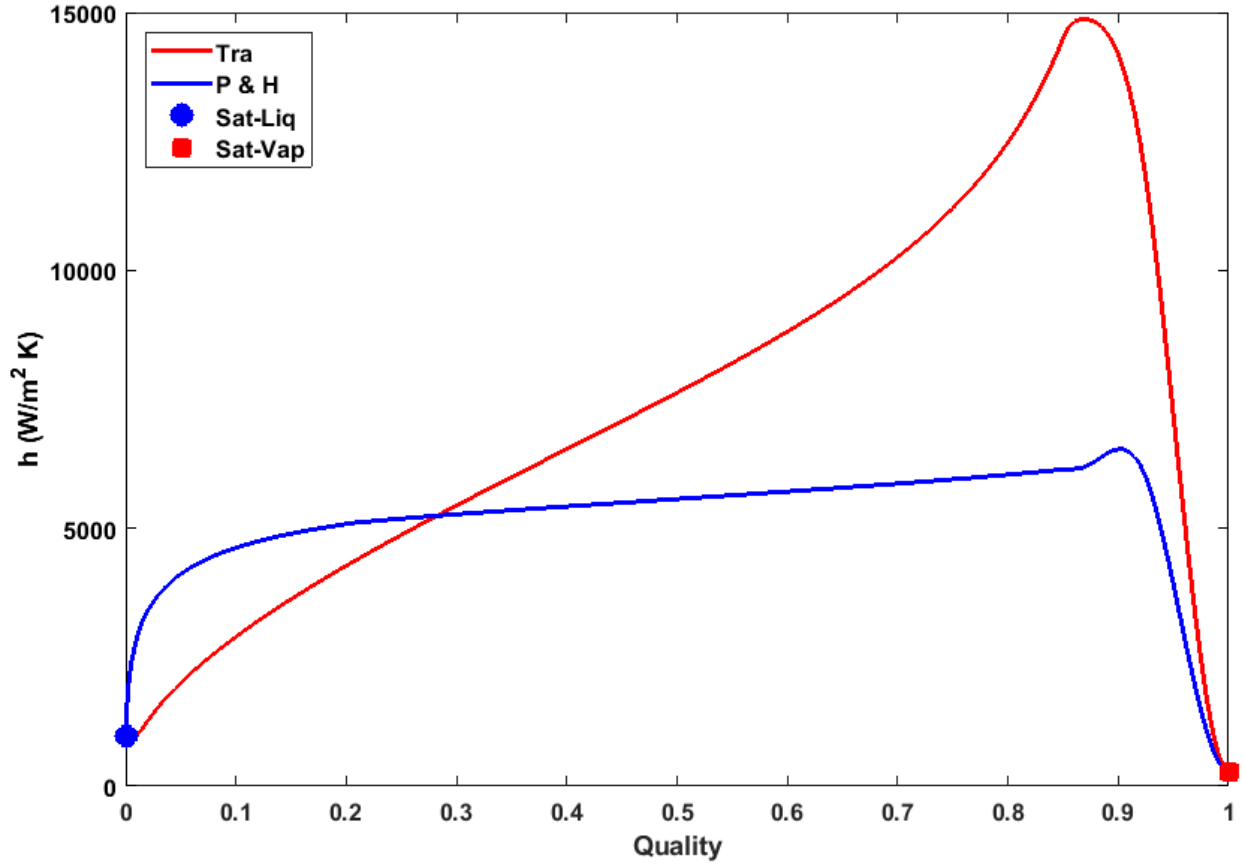


Fig. 33 Continuous heat transfer coefficient from saturated liquid to saturated vapor.

For the liquid/two-phase transition, Eq. (58) is used to obtain a continuous heat transfer coefficient. This function brings the two-phase values above the saturated liquid one by smoothly increasing it. For the two-phase/vapor transition, the continuous heat transfer coefficient variation is obtained by using a spline function. The spline function creates a continuous transition by gradually decreasing the two-phase correlation values as the quality increases. The effects of these choices on the overall results will be discussed in later chapters.

$$h_{smooth} = \sqrt[16]{h_{2ph}^{16} + h_{sat-liq}^{16}} \quad 0 < X < 0.2 \quad (58)$$

Second, the prediction capability of the correlations is analyzed by comparing the calculated results with the measured values published by Fronk and Garimella in [61] and [62] for ammonia flow inside the straight horizontal pipes. The measurements are selected for the inner diameters of 1.44 and 2.16 mm since they are close to the inner diameter of the transportation lines in LHP1 and LHP2. The fluid temperature flowing inside the 1.44-mm pipe is varied from 30 to 60°C with 10°C increments. In contrast, the fluid temperature remains constant at 60°C in the 2.16-mm pipe. Table 12 provides the average relative errors according to Eq. (59) for the predictions of the heat

transfer coefficient for the different mass flux values. In the equation,  $n$  is the number of data points gathered for each mass flux setting.

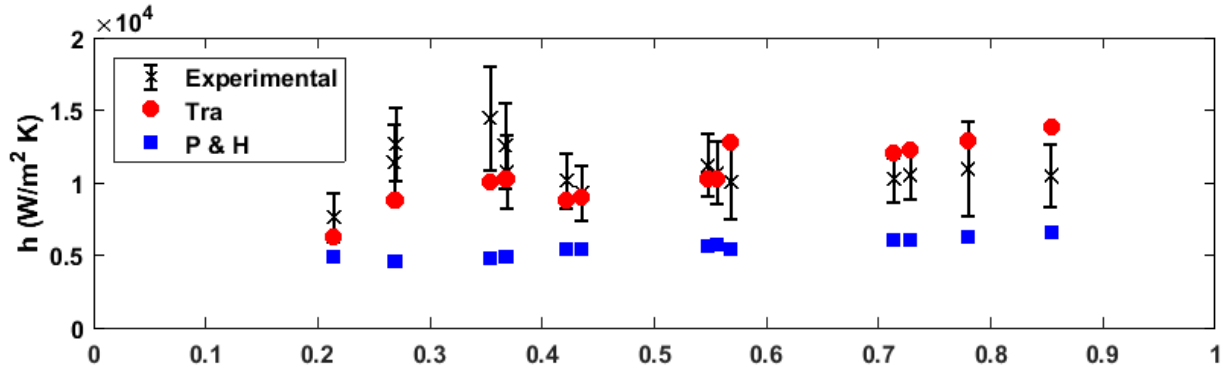
$$e_{relative} = \frac{\sum_{i=1}^n \frac{|h_{Correlation,i} - h_{experiment,i}|}{h_{experiment,i}}}{n} * 100 \quad (59)$$

Table 12 The average relative errors of the predicted heat transfer coefficient for the two-phase flow.

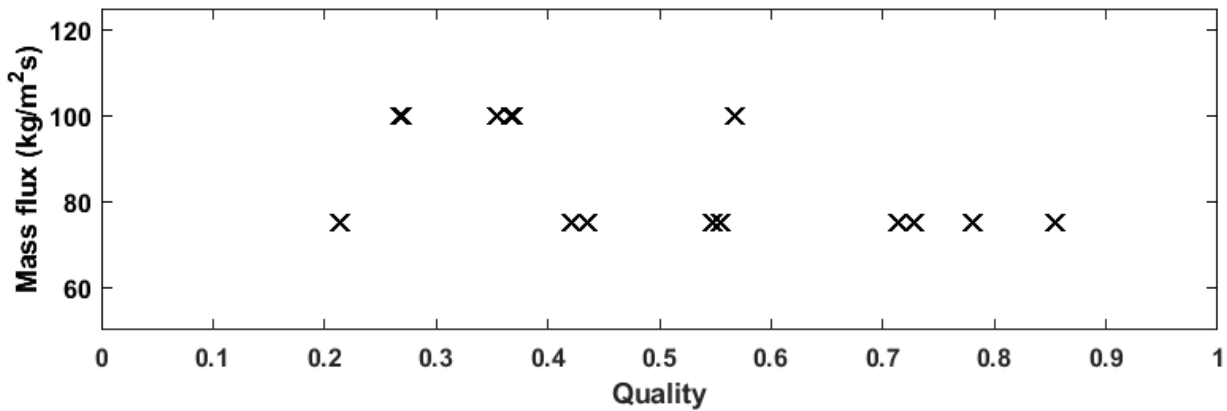
$D_{in}$ (mm)	1.44			2.16	
Mass Flux ( $\frac{kg}{s m^2}$ )	75	100	150	75	100
Tra Corr.	28.5	17.5	21.7	14.3	22.3
P&H Corr.	57.5	61.7	73.8	42.9	58.9

Concluding from Table 12, the Traviss correlation has significantly lower relative errors compared to the P&H one in all the diameter/mass-flux cases. For the Traviss correlation, the average of the relative errors remains below 30% in all of the cases. For the P&H correlation, the average errors are above 30% in all the cases and an increase in the mass flux increases the errors in the prediction of the heat transfer coefficient. The average error is decreased by increasing the inner diameter of the pipe at the constant mass flux of  $75 \frac{kg}{s m^2}$ . In the  $100 \frac{kg}{s m^2}$  mass flux, change of the pipe diameter has a negligible effect on the average error.

A more detailed analysis is also conducted for each pipe diameter. The pipe with the inner diameter of 2.16 mm is selected for further analysis as its diameter is closer to the transportation line diameters of LHP1 and LHP2. Figure 34 provides the heat transfer coefficients obtained from the measurement and calculation and the corresponding mass flux values. The measured values have uncertainty ranges presented as the error bars in Fig. 34 (a). The calculated values from the Traviss correlation lay inside the error bars except for the two data points with the vapor quality of 35.4% and 85.5%. The change of the mass flux does not have any significant effect on the heat transfer coefficient obtained from the P&H correlation.



(a)



(b)

Fig. 34 The measured and predicted results for the 2.16mm-diameter stainless-steel pipe: (a) the heat transfer coefficient and (b) the mass flux.

The prediction capability of the correlations can also be visualized in Fig. 35 by plotting the calculated results versus measured ones. This visualization assists in investigating the relative accuracy of the correlations for each data point. The Traviss results are mostly within  $\pm 30\%$  of the measurements. For the P&H correlation, all the data points are below the  $-30\%$  threshold line.

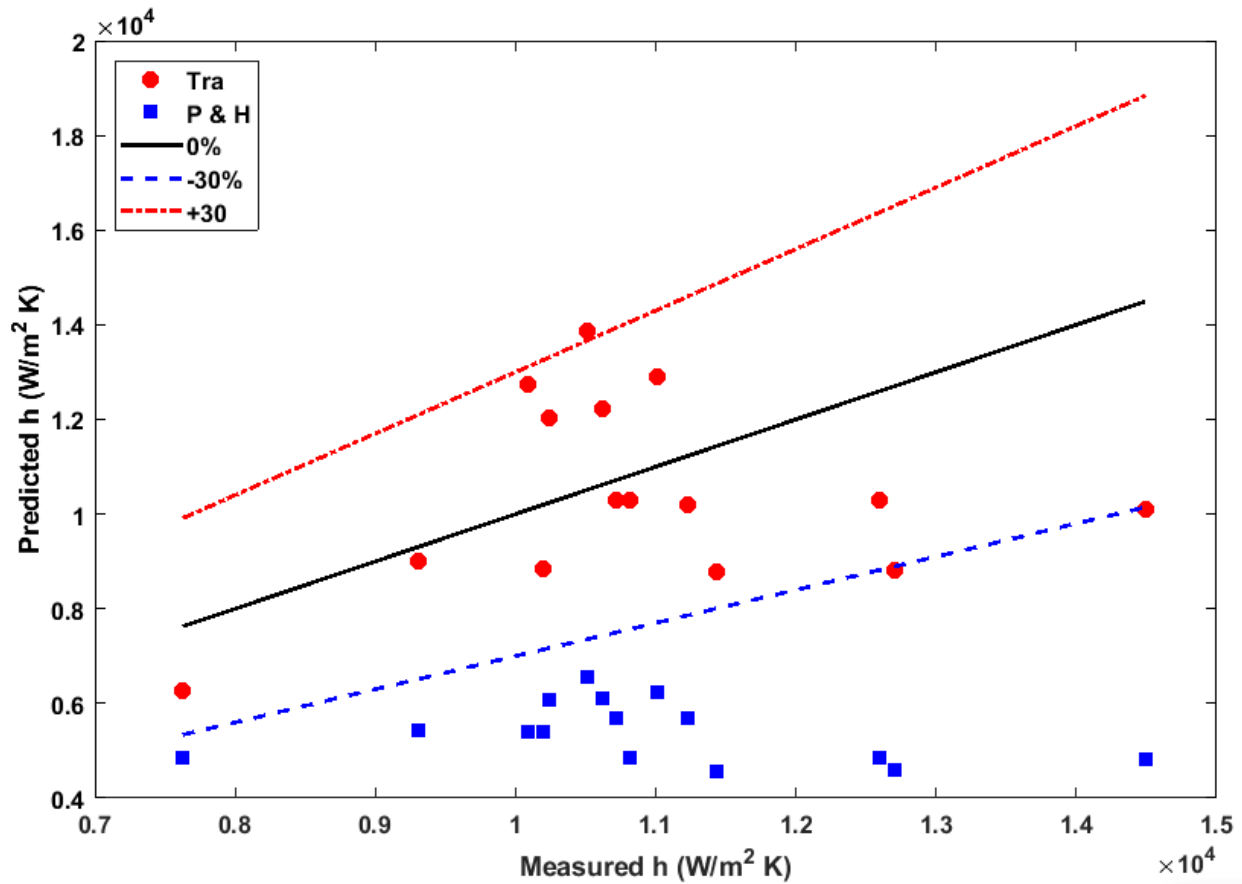


Fig. 35 Prediction versus measurement of the heat transfer coefficient for the 2.16 mm-diameter stainless-steel pipe.

As mentioned earlier, the P&H correlation takes into account the two-phase flow regime as introduced in Fig. 30 to calculate the heat transfer coefficient. Thus, further investigation of the correlation underprediction can be conducted by mapping out the flow regime of the experimental data as shown in Fig. 36. All of the data points are located in the stratified wavy flow region where the correlation underpredicts the heat transfer coefficient. Unfortunately, there are no experimental data available to assess the predictability of the correlations in a stratified smooth flow. The two-phase flow inside the LHP condenser is expected to be in the stratified smooth region at the low applied power.

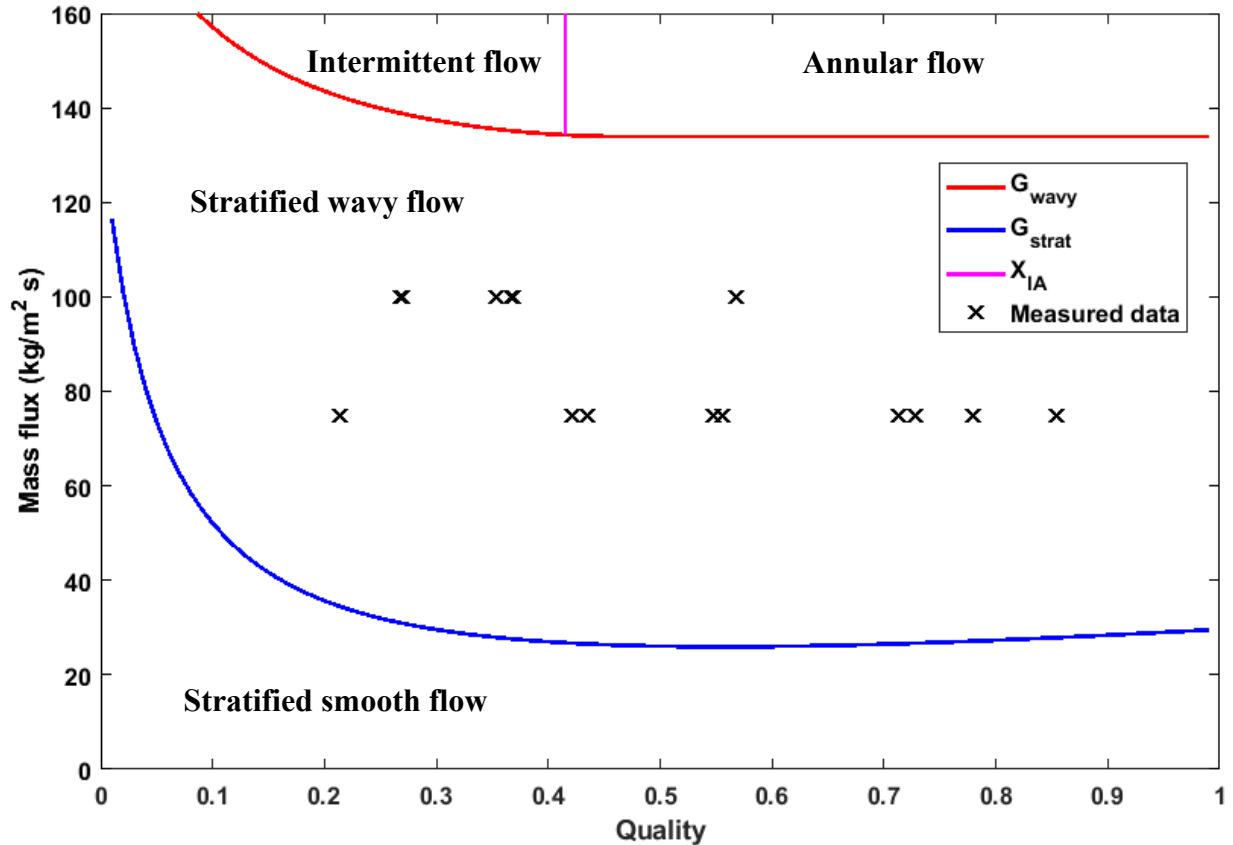


Fig. 36 Flow pattern diagram for the 2.16mm-diameter stainless-steel pipe.

As the last selection criterion, the computational time is evaluated for each correlation by running the continuity scenario on the same computer specifications introduced in Section 3.1.3. As mentioned earlier, the minimum computational time is important as the correlation will run for all the LHP control volumes containing the two-phase fluid flow at each time step. The Traviss correlation requires 2.05 s to calculate all the 1000 data points in the continuity scenario. In contrast, running the P&H correlation takes 150.86 s for the continuity scenario which requires 73.6 times more time.

In conclusion, the Traviss correlation is chosen to calculate the heat transfer coefficient for the two-phase flow. This correlation has one negligible discontinuity across the vapor quality range, and the smoothing functions create seamless transitions of the heat transfer coefficient between the two-phase and saturated flows as presented in Fig. 33. It is shown that the Traviss correlation predicts the experimental results with average relative errors of less than 25% in the minichannels similar to the one used in LHP1 and LHP2. Finally, the selected correlation has one order-of-magnitude lower computational time than the P&H correlation.

### 3.3 Natural heat transfer coefficient

The heat transfer coefficient between an LHP cylindrical solid element, such as the transportation lines, and ambient is calculated from the natural convection correlation provided by Holman [63], as described in Eq. (60). The natural convection is considered the dominant means of heat transfer. The radiation heat transfer is negligible in the ambient testing as the LHP transportation lines have small diameters, low emissivity and small temperature difference with ambient.

$$h_{amb} = 1.32 \left( \frac{|T_{sld} - T_{amb}|}{D_{out}} \right)^{0.25} \quad (60)$$

where  $T_{sld}$  and  $D_{out}$  are the temperature and outer diameter of the solid element, respectively. The accuracy of this correlation is expected to be within 30%. Further discussion on this coefficient will be presented in Section 4.3.

### 3.4 Conductive heat transfer coefficient

The conductive heat transfer coefficient ( $h_{A,B}$ ) between the two solid cells A and B is calculated, as shown in Eq. (61), based on the thermal conductivity, the thickness of the cells and the contact conductance between them. This equation is used to obtain the conductive heat transfer between the heater block and evaporator saddle; the condenser saddle and its riser; and the riser and sink plate.

$$h_{A,B} = \left( \frac{t_A}{k_A} + \frac{1}{h_{contact}} + \frac{t_B}{k_B} \right)^{-1} \quad (61)$$

where the contact conductance ( $h_{contact}$ ) is the only parameter subject to uncertainty, which will be addressed in detail in Section 4.3.

### 3.5 Summary

In this chapter, the correlations are introduced and selected to be used in the numerical modelling of LHP. For the single-phase flow, the Churchill and Gnielinski correlations are introduced to obtain the viscous pressure drop and the heat transfer coefficient, respectively. These correlations are valid for the flow characteristics inside LHPs and are commonly used in the thermo-fluid applications.

However, the two-phase flow is treated differently since the related correlations have a higher level of uncertainty in their predictions. Therefore, two widely used two-phase correlations are assessed to obtain the pressure drop and the heat transfer coefficient, respectively. The assessment criteria consist of the data continuity over the vapor quality range, prediction capability and computational time. The prediction capability is evaluated by verifying the correlation results against the experimental data published for the flow characteristics similar to ones inside LHP1 and LHP 2.

The Churchill parallel correlation is selected to calculate the two-phase pressure drop. The correlation meets all the assessment criteria. For the heat transfer coefficient, the Traviss correlation is chosen as it has the smallest prediction error and computational time. Additionally, the small discontinuity observed in the Traviss results is not significant in the whole vapor quality range.

In addition to the internal flow correlations, formulas are introduced to calculate the heat transfer rate between a solid part and ambient and between two solid parts. The ambient formula is based on a natural convection correlation between pipe outer surface and the surrounding air. The conductive heat transfer formula is using the thermal resistance circuit including the contact conductance between surfaces.

## Chapter 4: Steady-state model

In the past two decades, several steady-state LHP models have been developed. Some models simulated a specific section of an LHP, particularly the evaporator and others considered the complete LHP. The published steady-state models that considered the complete LHP are reviewed in this chapter. Note that Siedel et al. [64] conducted a thorough literature review of the steady-state models introduced before 2015.

A steady-state one-dimensional model using continuity, energy and momentum equations is presented by Kaya and Hoang in [65]. It is assumed that the fluid is always saturated inside the evaporator and reservoir. The heat exchange between the LHP and ambient is taken into account. The model also assumes that the evaporator wick is always filled with saturated liquid, and evaporation occurs only on the wick outer surface. The operating temperature is calculated by an iterative procedure such that the two heat leak values calculated separately from the heat conduction through the wick and reservoir energy equation are equal within a prescribed margin. The fluid properties are calculated as a function of saturated temperature using fifth order polynomials. The single-phase correlations are used for pressure drop and heat transfer coefficients to find the vapor-liquid interface in the condenser. This model is later improved in [66] for small LHPs by introducing a two-phase correlation for the pressure drop and also considering the fluid flow through the wick when calculating the conductive heat leak.

Chuang [67] introduced a global model to investigate the effect of gravity for the low applied power operation of LHPs in terrestrial applications. This model considers the superheat inside the grooves using empirical formulas. Furthermore, the two-phase heat transfer correlations and pressure losses due to bends are implemented. The saturation temperature is considered as constant in the two-phase section of the condenser. Qu et al. [68] and Zhou et al. [69] have later improved Chuang's model by adding a bayonet tube through the reservoir and by considering the existence of bubbles inside the wick, respectively.

Adoni et al. [70]–[72] developed a steady-state model with increasing complexity over several years. The main features of the model lay on the detailed simulation of the reservoir, particularly the evaporator core and bayonet tube. A hard-filled reservoir is also considered. The model utilizes REFPROP software to obtain the working fluid properties and more recent correlations for the two-phase heat transfer coefficient inside the condenser. The fluid state inside the liquid line is assumed as subcooled or saturated liquid and inside the vapor line as saturated vapor.

A steady-state model introduced by Bai et al. [73] is further improved in later publications [74]–[76]. More sophisticated versions of the model include the analysis of the thermal conductivity of compound wicks and the effect of gravity on the evaporator. The model uses a control volume approach for the numerical calculation, but not enough information is provided on the loop discretization. Although the thermal conduction through the solid wall is considered for the heat transfer between the fluid flow and ambient, the wall temperatures are not calculated except for

the reservoir section. Two accommodation parameters are introduced to calculate the amount of heat transferred from the evaporator saddle to the wick and from the saddle to the reservoir casing. Their values are obtained from the experiments.

Hodot et al. [77] developed a global LHP model based on a one-dimensional model introduced by Rivière et al. [78]. They added a three-dimensional model of the evaporator for which the vapor grooves and saddle are modelled in detail. The three-dimensional model is used to optimize the number, size and location of the vapor grooves according to the applied heat conditions. In addition, the longitudinal heat leak is taken into account considering the conduction through the casing of the evaporator and reservoir. However, the model is not validated in the variable conductance region.

Siedel et al. [79] and [80] are developed the numerical and analytical models with a two-dimensional wick for both cylindrical and flat evaporators. A control volume discretization is used for the fluid flow with a nodal point for the adjacent solid cell. The energy and momentum equations are considered for the transportation lines and condenser. The implementation of the equations to the control volumes are not explicitly discussed. The models obtained a good agreement between experimental and calculated results. The experimental results are obtained from other previously published articles.

The steady-state models introduced after Siedel et al. [80] have similar features with some unique additions. The model developed by Esarte et al. [81] used Engineering Equation Solver (EES) to calculate the fluid properties. Weng and Leu [82] focused on the two-phase condensation in 1 to 5 mm diameter pipes taking into account the surface tension. Fukushima and Nagano [83] discretized the LHP into 100 nodes to apply the conservation laws for incompressible and viscous flow. The model is used to predict the operating behavior of a micro LHP equipped with a new evaporator structure. Ramasamy et al. [84] built a model based on the Singh et al. [85] algorithm and added the most recent two-phase correlations for the pressure drop and heat transfer. In this model, the heat transfer coefficient between the fluid inside the condenser and sink is considered as an accommodation factor, which is obtained experimentally.

This chapter introduces a numerical model to predict the global steady-state operation of an LHP. The LHP components are discretized into several control volumes. The model is developed with a modular approach such that it can be applied to a specific LHP geometry without modifying the whole algorithm. Also, the modularity feature makes it possible to study the effects of different correlations and accommodation factors and to refine the model for different operation conditions. The model is developed in a way that it can be easily extended to a transient model, which will be presented in the next chapter. The steady-state model is obviously necessary to determine the initial conditions for the transient simulation. It is also useful in identifying the accommodation parameters which are used in the transient simulation. The sensitivity analysis performed on the steady-state model also provides a better understanding of several parameters for the transient LHP

modelling. Moreover, four main accommodation parameters are considered in the model, and their effects on the results are analyzed.

Additionally, the model considers superheated vapor flow in the evaporator grooves. Four phase-change regions are considered: exterior surface of the wick, reservoir, superheated-vapor/two-phase and two-phase/subcooled-liquid interfaces inside the transportation lines and condenser. The exact locations of the last two phase-change regions in the loop are obtained using a phase-check algorithm. The pressure drop in a control volume is calculated from the viscous friction, gravity effect, existence of bends using a staggered-grid model. The model considers the reservoir in a two-phase state even though the hard-filled condition is monitored. Implementation of these features results in a better prediction capability of the mathematical model compared to previously published works while using a minimum number of accommodation factors. A comprehensive analysis of the modelling parameters presented in this chapter also provides insights for the decision-making process used in the development of the model, which has not been previously reported in similar works.

In the following sections, the governing equations for each segment of a conventional LHP are first discussed and the corresponding assumptions and discretization methods are explained. Secondly, the solution algorithm is described. Then, the model results are validated by comparing them with experimental values obtained from two different LHPs to demonstrate the predictive capability of the model. Finally, a thorough sensitivity analysis is presented to address the effects of various essential parameters on the model results.

## 4.1 Mathematical model

The model employs one-dimensional mass, energy and momentum conservation equations. These equations are written for a control volume as the LHP segments are discretized into several solid and fluid control volumes or cells. The properties of working fluid such as density and enthalpy are obtained using REFPROP from the two independent parameters. The model uses a Eulerian approach. First, the evaporator and the fluid properties are determined at the wick and grooves. Then, the analysis moves toward the condenser and finally reaches the reservoir where the energy and mass equations are used to close the loop.

### 4.1.1 Evaporator

Evaporator section is divided into the heater block, evaporator saddle including the evaporator casing, wick and vapor grooves as shown in Fig. 37 (a). The cell network of the evaporator shown in Fig. 37 (b) is then developed comprising of two solid cells ( $T_{HB}$  and  $T_{ES}$ ), two fluid cells ( $T_{int}$  and  $T_{Gr}$ ) and one combined solid/fluid cell ( $T_{wick}$ ).  $T_{int}$  is the fluid interface temperature at the wick outer surface, and  $T_{Gr}$  is the temperature of superheated vapor in the vapor grooves.

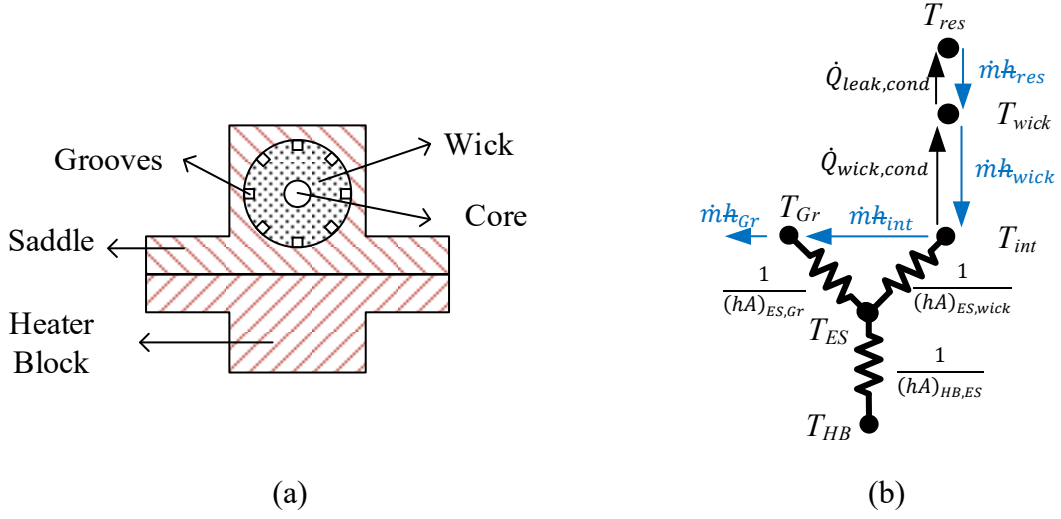


Fig. 37 The evaporator schematic (a) cross-section and (b) cell network.

The energy equations for the solid cells are shown in Eqs. (62) and (63) for the heater block and evaporator saddle, respectively. It is assumed that there is no heat transfer between these cells and ambient since they are well insulated during the experiment. This was done to avoid the uncertainties associated with the calculation of the heat transfer by natural convection. The axial heat conduction from the evaporator to the reservoir is also ignored because the casing is very thin. The calculation shows that the axial heat conduction from the evaporator to the reservoir is approximately 2% of the radial heat conduction through the wick. Therefore, its effect on the overall results is negligible.

$$\dot{Q}_{app} = (hA)_{HB,ES}(T_{HB} - T_{ES}) \quad (62)$$

$$(hA)_{HB,ES}(T_{HB} - T_{ES}) = (hA)_{ES,wick}(T_{ES} - T_{int}) + (hA)_{ES,Gr}(T_{ES} - T_{Gr}) \quad (63)$$

The heater-block/evaporator-saddle total conductance ( $h_{HB,ES}$ ), as explained in Section 3.4, is a function of the contact conductance and thermal conductivities of the two parts, and it is mainly required if the heater block temperature needs to be calculated. The evaporator saddle-to-wick contact conductance ( $h_{ES,wick}$ ) is difficult to calculate since it is a complex function of wick porosity, contact conductance and thermal conductivity. Therefore,  $h_{ES,wick}$  is an accommodation factor in the model. Finally, the heat transfer coefficient between the saddle and the fluid inside the grooves ( $h_{ES,Gr}$ ) will be discussed when the equations for the vapor grooves are introduced.

The wick section is divided into the two cells representing the wick and liquid-vapor interface. The wick cell is a cylinder where the saturated liquid moves radially from the evaporator core to the interface cell, and the heat is conducted in the opposite direction. It is assumed that the fluid inside the evaporator core is in the saturated liquid state at the same temperature as the reservoir.

The interface cell is a thin layer on the exterior surface of the wick where evaporation occurs. The energy equations for the interface and wick are provided in Eqs. (64) and (65), respectively.

$$\dot{Q}_{wick,cond} = (hA)_{ES,wick}(T_{ES} - T_{int}) + \dot{m}(h_{wick,liq} - h_{int,vap}) \quad (64)$$

$$\dot{Q}_{leak,cond} = \dot{Q}_{wick,cond} + \dot{m}(h_{res,liq} - h_{wick,liq}) \quad (65)$$

where  $h$  is the enthalpy of fluid, and it is a function of temperature only since the fluid is in a saturated state. The conductive heat flow through the wick ( $\dot{Q}_{wick,cond}$ ) can also be obtained from Eq. (66).

$$\dot{Q}_{wick,cond} = \frac{2\pi k_{eff} L_{wick} (T_{int} - T_{wick})}{\ln\left(\frac{D_{wick,external}}{D_{wick,internal}}\right)} \quad (66)$$

where the effective thermal conductivity ( $k_{eff}$ ) is calculated from the Maxwell correlation [65]. It is important to note that  $k_{eff}$  is a function of the interface temperature.

In addition, the pressure of fluid below the interface is determined by Eq. (67) derived from Darcy's equation for the radial viscous flow through a porous media. This pressure is used to verify that the LHP is operating below its capillary limit.

$$P_{wick} = P_{res} - \frac{\dot{m}}{2\pi L_{wick} \kappa} \frac{\mu_{int,liq}}{\rho_{int,liq}} \ln\left(\frac{D_{wick,external}}{D_{wick,internal}}\right) \quad (67)$$

In the grooves, the saturated vapor flow changes direction from the radial to axial direction and absorbs heat from the evaporator saddle. The grooves are modelled as a single cell, and the energy conservation equation is given by Eq. (6).

$$(hA)_{ES,Gr}(T_{ES} - T_{Gr}) = \dot{m}(h_{Gr} - h_{int,vap}) \quad (68)$$

$h_{ES,Gr}$  is calculated using the single-phase correlation for the heat transfer coefficient introduced in Section 3.2.1. It is a function of the mass flow rate and interface temperature. As a result of the heat addition, the fluid exits the grooves as superheated vapor.

#### 4.1.2 Transportation lines

The fluid leaving the grooves enters the vapor line and then passes through the condenser to dissipate the latent heat to the sink. Then, the fluid reaches the reservoir through the liquid line. These segments of an LHP are discretized into several parts. Each part contains a fluid cell and an adjacent solid one.

The control volume for the fluid is defined using the staggered grid concept. Figure 38 shows the schematic of the grid. The fluid properties are defined at the center of a control volume, called

“node”, and the flow velocity is defined at the control-volume boundary called “junction”. The velocity at any node, if it is required, is obtained from averaging the velocity values at the two adjacent junctions.

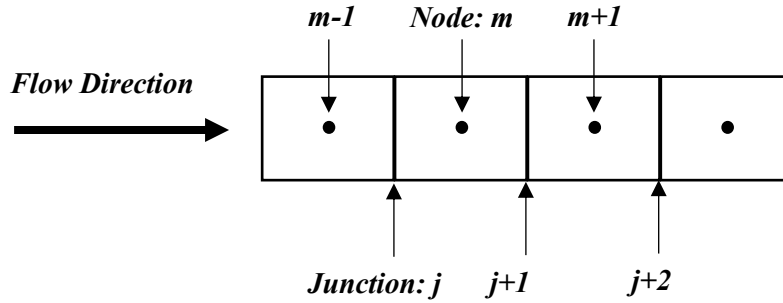


Fig. 38 Schematic of the staggered grid in the axial direction for fluid flow.

The fluid properties at each junction are defined as a function of the adjacent nodes based on the direction of the flow as described in Eq. (69).  $\varphi$  can be any fluid property.

$$\varphi_j = \delta \varphi_{m-1} + (1 - \delta) \varphi_m$$

$$\delta = \begin{cases} 1 & \text{if } u_j \geq 0 \\ 0 & \text{if } u_j < 0 \end{cases} \quad (69)$$

The conservation equations for energy and mass are solved for the nodes, and the momentum equation is solved for the junctions. Equations (70) to (72) present the steady-state momentum, continuity and energy equations for a fluid cell.

$$P_m - P_{m-1} = (\rho g)_j (Z_m - Z_{m-1}) + \xi \frac{\rho u_j^2}{2} \quad (70)$$

$$(A\rho u)_j = (A\rho u)_{j+1} \quad (71)$$

$$(A\rho u k)_j - (A\rho u k)_{j+1} = [(hA)_{inside} (T_{fld} - T_{slid})]_m \quad (72)$$

In the momentum equation, Eq. (70), the pressure drop coefficient ( $\xi$ ) includes the friction factor and effects of bends (See Section 3.1). The heat transfer coefficient between the fluid cell and its adjacent solid cell ( $h_{inside}$ ) in Eq. (72) is calculated from different correlations introduced in Section 3.2 depending on the fluid phase.

The liquid and vapor lines are discretized as the solid cylindrical cells with the same length as the fluid cell contained by the solid cell. The heat flows radially from the fluid node to the ambient node via the solid node or vice versa, as described in Eq. (73). The heat conduction through the solid cell is considered negligible as the pipe walls are generally very thin in the order of 0.5 mm.

$$[(hA)_{inside}(T_{fld} - T_{wall})]_m = [(hA)_{outside}(T_{wall} - T_{amb})]_m \quad (73)$$

where,  $h_{outside}$  is the natural heat transfer coefficient between the solid cell and ambient, and it is calculated from the correlation introduced in Section 3.3.

#### 4.1.3 Condenser

In the condenser, depending on the design, there may be more than one solid cell to connect a fluid node to a sink node. The solid cells could include both a condenser saddle and a riser as shown in Fig. 39 (a).

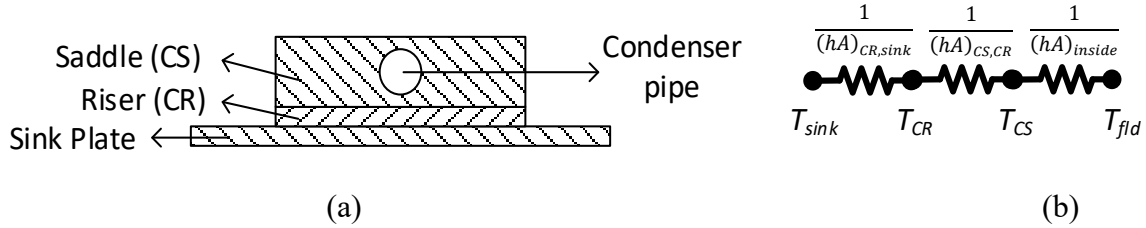


Fig. 39 The condenser schematic (a) cross-section and (b) cell network.

The heat would then flow from the fluid node through the saddle and riser to the sink as presented in Eqs. (74) and (75).

$$[(hA)_{inside}(T_{fld} - T_{CS})]_m = [(hA)_{CS,CR}(T_{CS} - T_{CR})]_m \quad (74)$$

$$[(hA)_{CS,CR}(T_{CS} - T_{CR})]_m = [(hA)_{CR,sink}(T_{CR} - T_{sink})]_m \quad (75)$$

where the areas ( $A$ ) are calculated based on condenser geometry. The heat transfer coefficients except for  $h_{inside}$  are a function of the thermal conductivities of the two adjacent components and the contact conductance between them. For instance,  $h_{CR,sink}$  is a function of the thermal conductivity of both riser block and sink plate in addition to the contact conductance between them. The formulas, to calculate these coefficients, are provided in Section 3.4. Note that the contact conductance in the condenser is difficult to measure. Therefore, the contact conductance is one of the accommodation coefficients in the model as it will be discussed later.

#### 4.1.4 Reservoir

The LHP reservoir modelled by one cell where the conservation of mass, momentum and energy equations are satisfied for the entire loop. The amount of fluid and consequently its density in the reservoir can be obtained from Eq. (76) as the loop fluid charge ( $m_{fld,loop}$ ) and the density of all the other cells are known.

$$\rho_{res} = \frac{m_{fld\ charge} - \sum_{\substack{cells \\ \text{except } res}} \rho V}{V_{res}} \quad (76)$$

where the reservoir volume includes the evaporator core as well. The reservoir pressure can be obtained from the last liquid-line cell using the momentum equation, Eq. (70). By assuming the reservoir fluid is in a two-phase state, the temperature can be calculated from its pressure. Moreover, it is assumed that the fluid velocity is negligible inside the reservoir, and the reservoir solid wall has the same temperature as the fluid inside. With these assumptions, the energy equation of the reservoir is described by Eq. (77).

$$\dot{Q}_{leak,res} = (hA)_{res,out}(T_{res} - T_{amb}) - \dot{m}(\hbar_{LL,out} - \hbar_{res,liq}) \quad (77)$$

where  $\hbar_{LL,out}$  is the enthalpy of the fluid leaving the liquid line to enter the reservoir.  $h_{res,out}$  is the heat transfer coefficient for the natural heat convection between the reservoir wall and ambient.  $\dot{Q}_{leak,res}$  is the heat leak entering the reservoir from the wick, and it is the only unknown parameter in Eq. (77). If the heat leak values obtained from Eqs. (65) and (77) are equal, the loop is closed from the energy point of view. This condition allows for the capability to calculate the operating temperature through an iterative procedure, as explained below.

## 4.2 Solution procedure

Figure 40 illustrates the top-level steps of the solution algorithm to obtain the LHP operating temperature. First, a physical model of the LHP is established to determine all the required dimensions and properties of the LHP sections. For instance, the physical model of the wick includes the length, internal diameter, external diameter, thermal conductivity, density, porosity, permeability and pore radius. Next, a discretized model is developed to create fluid and solid cells. For example, the transportation lines and condenser are discretized into “ $n$ ” parts, and each part contains one fluid cell and one or several solid cell(s) as described in the previous section.

The solution of the governing equations of the discretized model requires an algorithm containing several loops. For any set of the operating conditions, the procedure starts by guessing values for  $\dot{Q}_{wick,cond}$  and  $T_{int}$ . These values will be updated after each iteration using the calculated  $T_{res}$ , and the difference between the two heat leak values calculated from the different equations, as discussed previously. If this difference is less than the convergence criterion ( $\varepsilon$ ), the calculated  $T_{res}$  is the operating temperature of the LHP for the prescribed set of operating conditions.

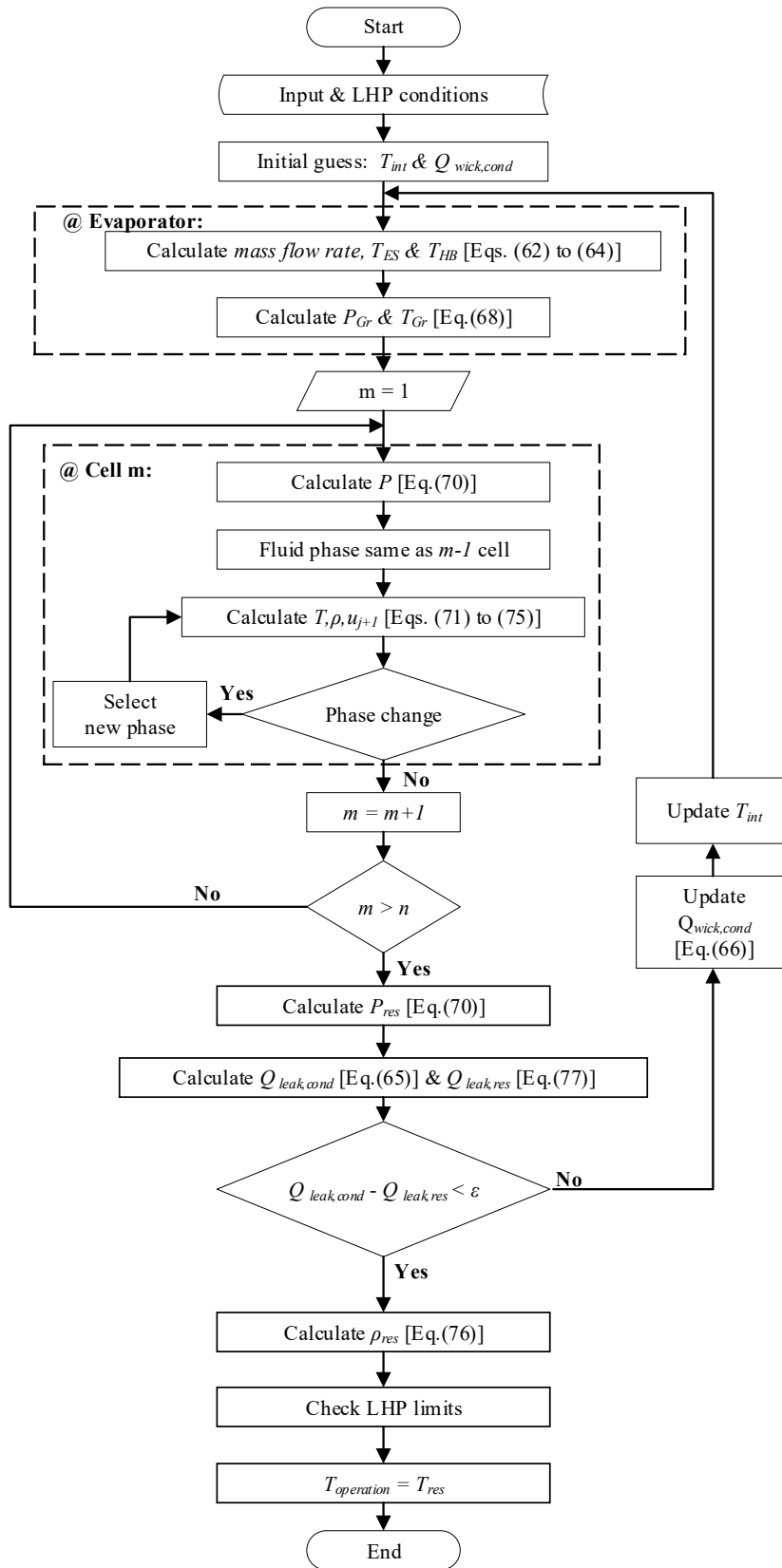


Fig. 40 Top-level algorithm of the steady-state model.

In the evaporator block in Fig. 40, the mass flow rate, saddle and heater temperatures are obtained by simultaneously solving Eqs. (62) to (64). Then, the vapor groove pressure is set to the saturated pressure at the interface temperature.

In the “cell m” block in Fig. 40, the temperatures, fluid density and velocity are determined by concurrently solving a set of equations. The equation set includes Eqs. (9), (10) and (12) for the transportation lines and Eqs. (9), (10), (13) and (14) for the condenser.

These equation sets are solved using three different algorithms depending on the nature of the fluid phase in the cell: two-phase, subcooled liquid and superheated vapor. First, as an initial guess, the fluid phase of the previous cell (m-1) is assigned to the current cell (m). Then, for the two-phase algorithm, the equation sets are solved through an iterative process on the vapor quality. For the other two algorithms, the fluid temperature is used as the iteration parameter to obtain the fluid properties and solid temperature(s). Finally, in the “cell m” block, the fluid phase is checked for any phase change to ensure that the obtained results realistically represent the LHP operation. Table 13 provides the criteria to detect a phase change. If the fluid is two-phase, the vapor quality ( $X$ ) is used as the phase identifier. Otherwise, the temperature of the fluid is compared to its saturated value, calculated from the pressure, to identify a phase change from liquid or vapor to two-phase as described in Table 13.

Table 13. Phase-change detection.

Old phase	Criterion	New phase
Two-phase	$X < 0$	Subcooled liquid
Two-phase	$X > 1$	Superheated vapor
Subcooled liquid	$T - T_{sat} \geq 10^{-10}$	Two-phase
Superheated vapor	$T - T_{sat} \leq 10^{-10}$	Two-phase

In Table 13, the value of  $10^{-10}$  K is selected as the phase change limit considering the REFPROP accuracy in determining the saturated temperature. Therefore, the temperature differences should exceed the limit to identify the phase change.

If a phase change is detected in the cell, the equation set is recalculated through the algorithm of the newly identified phase. For instance, if the cell fluid is assumed subcooled liquid, the fluid temperature obtained from the subcooled liquid algorithm is compared to the saturated fluid temperature. The calculated fluid properties are valid only if the fluid temperature is lower than the saturated one. Otherwise, a fluid temperature higher than the saturated one indicates that the energy in the cell exceeds the saturated liquid enthalpy, and consequently the fluid is two-phase. Therefore, the governing equations for the cell have to be solved again by calling the two-phase algorithm.

It is important to check the LHP operational limits, as shown in Fig. 40. These limits introduced in Section 1.3 include the wick capillary limit and the condition of the reservoir: whether the reservoir is dried out or hard filled. Checking the capillary limit ensures that the pressure across the interface cell (evaporating meniscus) is less than the capillary pressure available. Otherwise, the vapor from the grooves penetrates inside the wick, and the LHP operation stops. The dry-out condition in the reservoir can be checked by selecting a maximum value for the vapor quality of the reservoir to make sure the reservoir contains enough liquid for continuous operation. The maximum vapor quality, currently set to 0.5, is a design choice that can be changed by the user. The hard-filled situation occurs if the vapor quality inside the reservoir is zero or negative. This condition means that the LHP reservoir is working under a condition which is not considered in the present model. Note that this condition is not observed for the experimental operational limits studied in Chapter 2.

### 4.3 Model validation

Data collected from the testing of LHP1 and LHP2 under ambient conditions are used to validate the steady-state model. The LHP test apparatus and test scenarios are described in Chapter 2.

In the model, there are four major unknown or uncertain parameters in obtaining the operating temperature. These parameters are the evaporator saddle-to-wick contact conductance, the contact conductance at the condenser, the convective heat transfer coefficient between the LHP and ambient, and finally the fluid velocity in the grooves. The latter is used to estimate the heat transfer coefficient inside the vapor grooves. Almost all the LHP models are subject to similar unknown parameters, which need to be determined by experimentation. Note that different parameters are used in different mathematical models.

$h_{ES,wick}$  is necessary to simultaneously solve Eqs. (62) to (64). As mentioned previously, it is difficult to obtain an accurate value for  $h_{ES,wick}$ . Similarly, the thermal contact conductance ( $h_c$ ) from the condenser plate to the sink plate via a riser is also difficult to calculate because of its dependency on the contact pressure, surface roughness, and gap filler such as thermal paste. However, using the geometry and published values, it is possible to predict a reasonable range for these parameters.

The correlations for the natural convective heat transfer coefficient are widely available. However, the correlations are known to be within  $\pm 30\%$ . Based on this fact, a multiplier is introduced for the ambient heat transfer coefficient ( $\alpha$ ) to vary the amount of heat exchange obtained from the natural heat convection correlation presented in Section 3.3.

Finally, there is also uncertainty in determining what portion of the applied power goes from the evaporator saddle to the wick and vapor grooves. In most of the previous models, for example [65], [66], [84], this distribution of the applied power is ignored. Chuang [67] used an empirical

correlation to obtain the fraction of the applied power going to the grooves. Bai [74] and Hodot [77] considered the power distribution; however, the implementation steps were not explained in detail. It is not possible to calculate this value in a one-dimensional model. To predict how the applied power is divided between the wick and vapor grooves, the model utilizes a correction multiplier for the fluid velocity inside the grooves ( $\beta$ ). The heat transfer coefficient inside the grooves is a function of the groove fluid velocity through the correlation presented in Section 3.2.1. Consequently, the amount of the applied power transferred from the evaporator saddle to the wick and grooves can be changed by varying the value of  $\beta$ .

#### 4.3.1 Model validation for LHP1

The introduced accommodation parameters are varied to match the model predictions as close as possible to the experimental values at a chiller temperature of 5°C. The final values of the parameters are presented in Table 14.

Table 14 Matched parameters for the LHP1 model.

Parameter	Value
$h_{ES,wick}$	12,000 W/m <sup>2</sup> K
$h_c$	2,950 W/m <sup>2</sup> K
$\alpha$	0.825
$\beta$	0.8

With these values, the experimental and model results are compared in Fig. 41, where the average temperature of the reservoir wall is represented as a function of the applied power. The average sink temperature is 6.4°C and the average ambient temperature is 20.9°C.

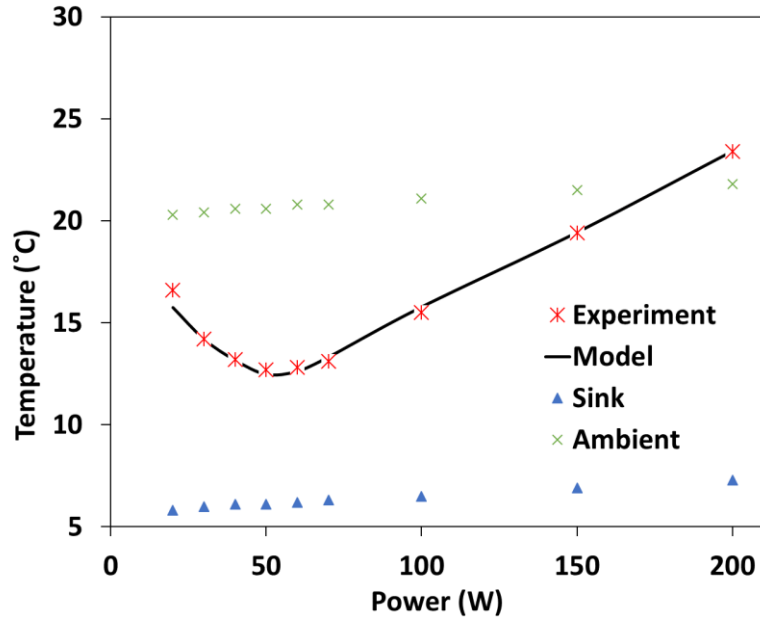


Fig. 41 Comparison of the experimental and calculated reservoir temperatures for LHP1.

The model results are on average within the absolute error of 0.20°C and the relative error of 1.33%, as defined in Eqs. (78) and (79). The maximum absolute and relative errors are 0.85°C and 5.1%, respectively at the applied power of 20 W.

$$e_{absolute} = T_{model} - T_{experiment} \quad (78)$$

$$e_{relative} = \frac{T_{model} - T_{experiment}}{T_{experiment}} * 100 \quad (79)$$

The saddle temperature as a function of applied heat is shown in Fig. 42. The saddle temperature has an average difference of 0.3°C (1.7%) and a maximum difference of 0.9°C (4.9%) at 200 W.

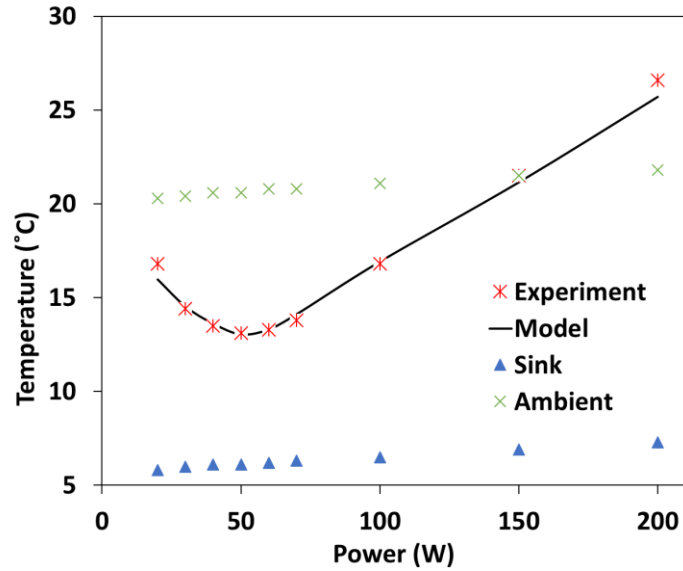


Fig. 42 Comparison of the experimental and calculated evaporator saddle temperatures for LHP1.

Figure 43 shows the measured and calculated temperatures at the inlet of the vapor line. The close agreement of the temperature values, as shown in Fig. 43, confirms the selected  $\beta$  value. It is important to note that the axial heat conduction from the evaporator to the vapor line is negligible because of the thin wall of the vapor line. Additionally, an analysis of experimental results showed that the heat conduction is 100 times smaller than the heat convection. The model values are on average within 0.24°C (1.55%) of the experimental values. The maximum deviation is 0.86°C (5.14%) at 20 W.

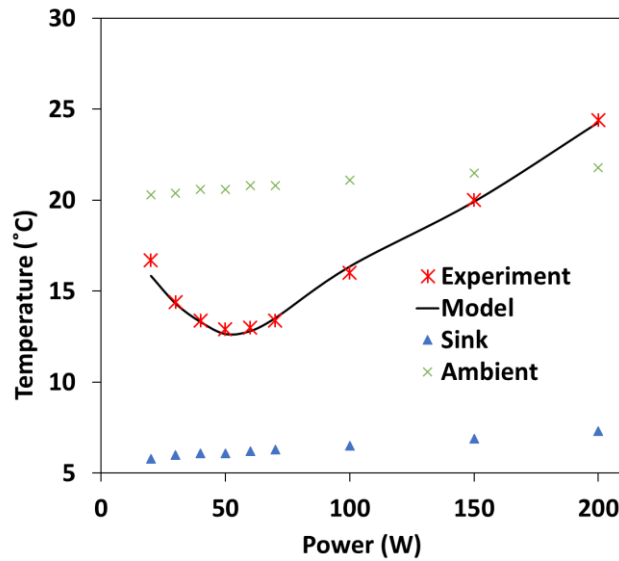


Fig. 43 Comparison of the experimental and calculated temperatures of the vapor line inlet for LHP1.

Once the accommodation coefficients are experimentally determined at a chiller temperature of 5°C, the predictive capability of the mathematical model is examined by comparing the model results to the experimental values obtained at different chiller conditions (10, 15 and 20°C). Figure 44 presents the comparison of the experimental and calculated saddle temperatures of the evaporator for LHP1 at different chiller temperatures. The performance curve is nearly a straight line at a sink temperature of 20°C as this temperature is higher than the ambient temperature.

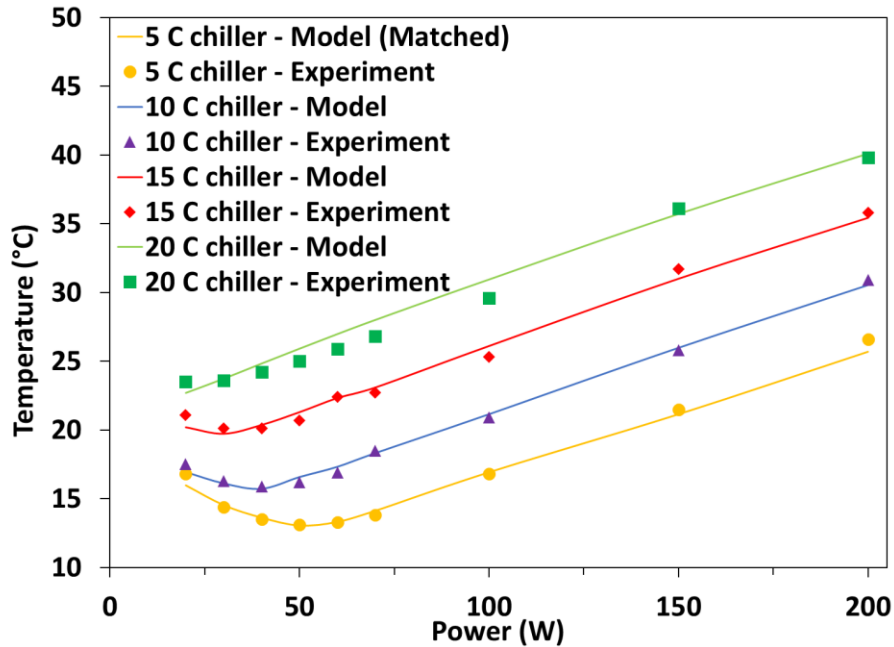


Fig. 44 Comparison of the experimental and calculated evaporator saddle temperatures for LHP1.

The average and maximum errors are shown in Table 15. The errors are generally increased with increasing chiller temperature as the operating condition moves away from the reference case. For all the cases studied, the maximum temperature difference is less than 1.8°C. A broader range of values could not be explored because of chiller limitations. However, the presented results show that once the model parameters are matched for a reference case, it is possible to predict the LHP behavior with an acceptable accuracy at different conditions.

Table 15 The average and maximum errors of the predicted values for LHP1.

Chiller (°C)	Average Ambient (°C)	Reservoir Average Error (°C [%])	Reservoir Maximum Error (°C [%])	Evap. Saddle Average Error (°C [%])	Evap. Saddle Maximum Error (°C [%])
5 (matched)	20.9	0.2 [1.33]	0.8 [5.11]	0.3 [1.71]	0.9 [4.91]
10	20.6	0.4 [2.00]	0.6 [3.32]	0.3 [1.59]	0.5 [3.16]
15	22.3	0.5 [2.28]	1.0 [4.11]	0.5 [2.09]	0.9 [4.26]
20	21.7	1.0 [3.71]	1.8 [5.80]	0.8 [2.83]	1.4 [4.59]

### 4.3.2 Model validation for LHP2

As mentioned in Section 2.2, LHP2 is equipped with a PRV which opens completely when the operating temperature of the loop exceeds 31°C. Thereafter, LHP2 operates as an unregulated and simple LHP. Figure 45 shows the comparison of the results between the experimental and model results for LHP2. As it is shown in Fig. 45, the operating temperature is nearly constant at around 31°C until the applied power reaches 150 W. Then, the PRV can no longer control the LHP operating temperature. The steady-state operating temperature values are calculated after this point when the PRV is fully open. The model values for powers lower than 150 W are not presented in Fig. 45 because the calculated values are not representative of the operating temperature of LHP2 in the presence of a PRV.

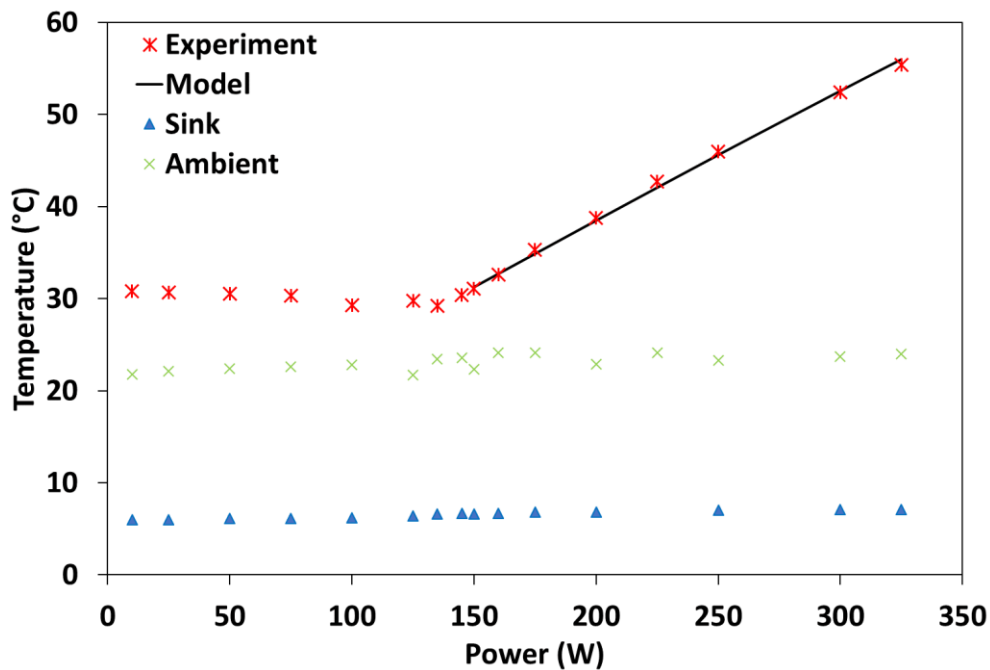


Fig. 45 Comparison of the experimental and calculated reservoir temperatures for LHP2.

Similar to LHP1, the accommodation parameters introduced earlier are obtained for LHP2, shown in Table 16, through matching the model results to the experimental values presented in Fig. 45 at a chiller temperature of 5°C. With these values, the model temperatures are within an average error of 0.3°C (0.71%) with a maximum error of 0.6°C (1.1%) at an applied power of 325 W. During the tests, the ambient temperature is varied from 21.7°C to 24.4°C. Note that the thermal contact conductance of the LHP2 condenser is lower than that of LHP1 condenser because the condenser lines are embedded inside an aluminum honeycomb that does not conduct heat very well from the condenser lines to the sink plate. For the thermal contact conductance in the evaporator section,

the difference values between LHP1 and LHP2 is contributed by different wick manufacturing and integration process used by the LHP manufactures. Additionally, different  $\alpha$  values of the two LHPs can be explained by the lack of full control over the ambient condition in the test rooms. Different air current might exist at different testing conditions. Also, the difference in the shape and orientation of the transportation lines may be a factor in the variation of  $\alpha$ . On one hand, LHP1 has horizontal transportation lines with concentric spiral sections. On the other hand, some sections of LHP2 transportation lines have mounted vertically.

Table 16 Matched parameters of the model for LHP2.

<b>Parameter</b>	<b>Value</b>
$h_{ES,wick}$	7,400 W/m <sup>2</sup> K
$h_c$	610 W/m <sup>2</sup> K
$\alpha$	1.1
$\beta$	1.1

The evaporator saddle temperatures are presented in Fig. 46. The average and maximum difference between experimental and model values are 0.1°C (0.27%) and 0.3°C (0.53%), respectively. It is important to note that the maximum differences in the temperature of both the reservoir and evaporator saddle occur at 325 W, where the temperature is close to the maximum operating temperature. At this power, it is numerically and experimentally observed that the liquid line temperature exceeds the reservoir temperature. The fluid is in a two-phase state in the entire liquid line, and the subcooling is provided through heat transfer from the reservoir to ambient.

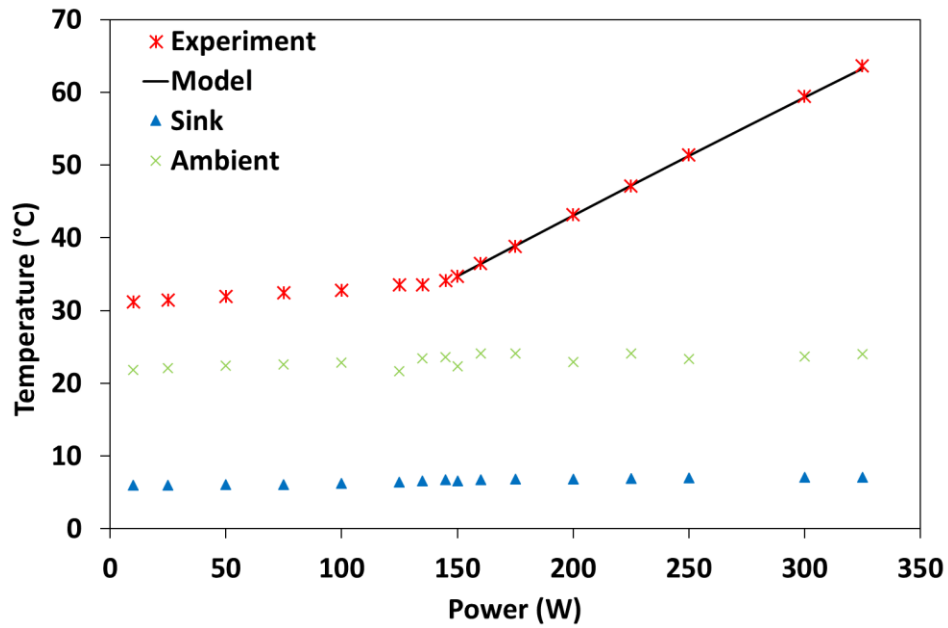


Fig. 46 Comparison of the experimental and calculated evaporator saddle temperatures for LHP2.

Figure 47 shows the measured and calculated temperatures of the vapor line inlet to validate the selected  $\beta$ . The calculated temperatures have an average difference within  $0.4^{\circ}\text{C}$  (1.0%) and a maximum difference of  $-0.6^{\circ}\text{C}$  (1.9%), at 150-W applied power, with respect to the measured values.

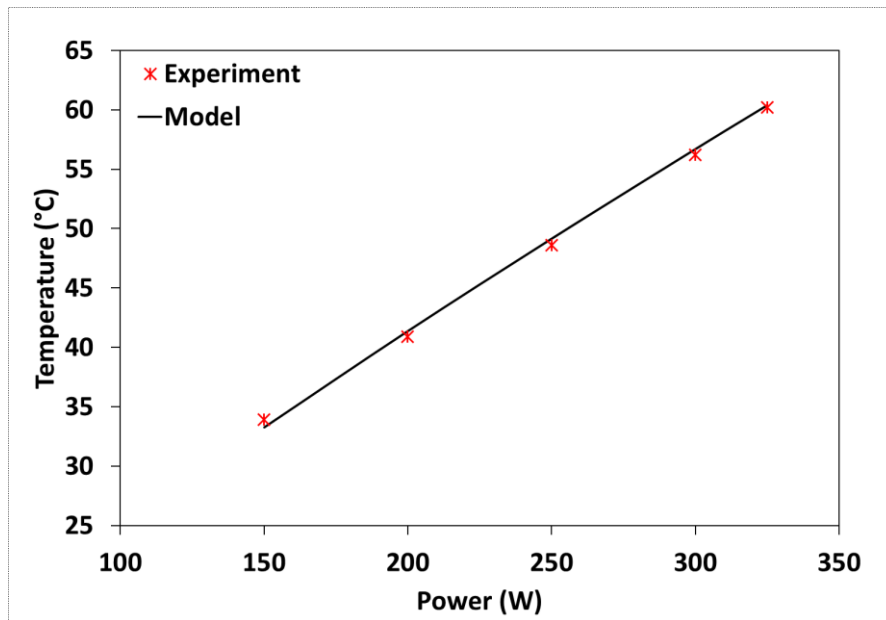


Fig. 47 Comparison of the experimental and calculated temperatures of the vapor line inlet for LHP2.

The predictive capability of the mathematical model is demonstrated by comparing the model results with the experimental results obtained at different chiller conditions (10, 15 and 20°C). The reference values given in Table 16 are used to obtain the results for the new chiller temperatures. The results are presented in Fig. 48.

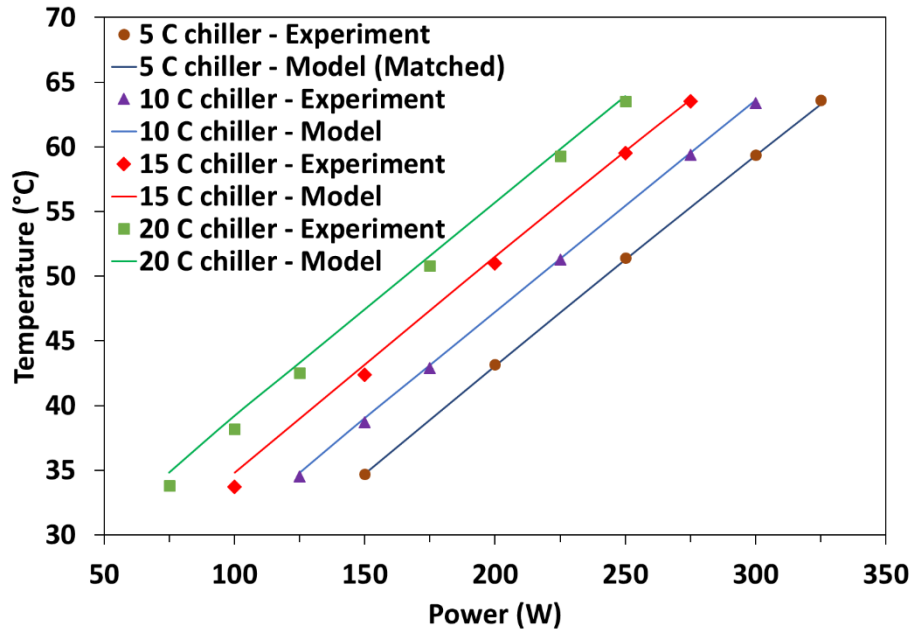


Fig. 48 Comparison of the experimental and calculated evaporator saddle temperatures for LHP2.

Table 17 provides the average and maximum values for the absolute and relative errors, which are calculated using Eqs. (78) and (79). The errors are on average increased with increasing chiller temperature. The maximum temperature difference is less than 2°C. Figure 48 also shows that the PRV opens at a lower power as the chiller temperature is increased.

Table 17 The average and maximum errors of the predicted values for LHP2.

Chiller (°C)	Average Ambient (°C)	Reservoir Average Error (°C [%])	Reservoir Maximum Error (°C [%])	Evap. Saddle Average Error (°C [%])	Evap. Saddle Maximum Error (°C [%])
5 (matched)	23.7	0.3 [0.71]	0.5 [1.06]	0.1 [0.27]	0.3 [0.53]
10	23.4	0.4 [1.02]	0.9 [1.70]	0.2 [0.48]	0.3 [0.90]
15	23.7	0.9 [2.00]	1.3 [3.62]	0.5 [1.32]	1.1 [3.28]
20	23.7	1.3 [2.94]	1.9 [3.64]	0.7 [1.74]	1.0 [2.95]

## 4.4 Sensitivity analysis

This section covers the sensitivity assessment of several model parameters as well as the heat transfer and pressure drop correlations. This analysis can provide the user with detailed information on how the choices of different parameters would affect the LHP performance curve. For each parameter, a reference value is selected through the validation process explained earlier. Then, the reference value is increased and decreased by 10, 20 and 50 % to investigate their effect on the results. As it is reasonable to expect that the actual parameters should reside well within  $\pm 10$  to  $\pm 50\%$  of the reference value, these extremes are considered as the worst-case scenarios.

### 4.4.1 Evaporator saddle-to-wick contact conductance

The contact conductance between evaporator saddle and wick ( $h_{ES,wick}$ ) is varied from the reference value (matched condition) to see its effect on the LHP characteristics. As shown in Fig. 49,  $h_{ES,wick}$  does not have a significant effect on the operating temperature. The maximum absolute and relative variations in the temperatures occurred at the minimum value of  $h_{ES,wick}$ , are  $0.8^\circ\text{C}$  (3.5%) and  $-0.1^\circ\text{C}$  (-0.2%) for LHP1 and LHP2, respectively. The temperature difference of  $0.8^\circ\text{C}$  occurs at 200 W where the operating temperature of LHP1 is close to the ambient temperature. As a result, the additional heat absorbed by the superheated vapor cannot be efficiently dissipated to the ambient in the vapor line.

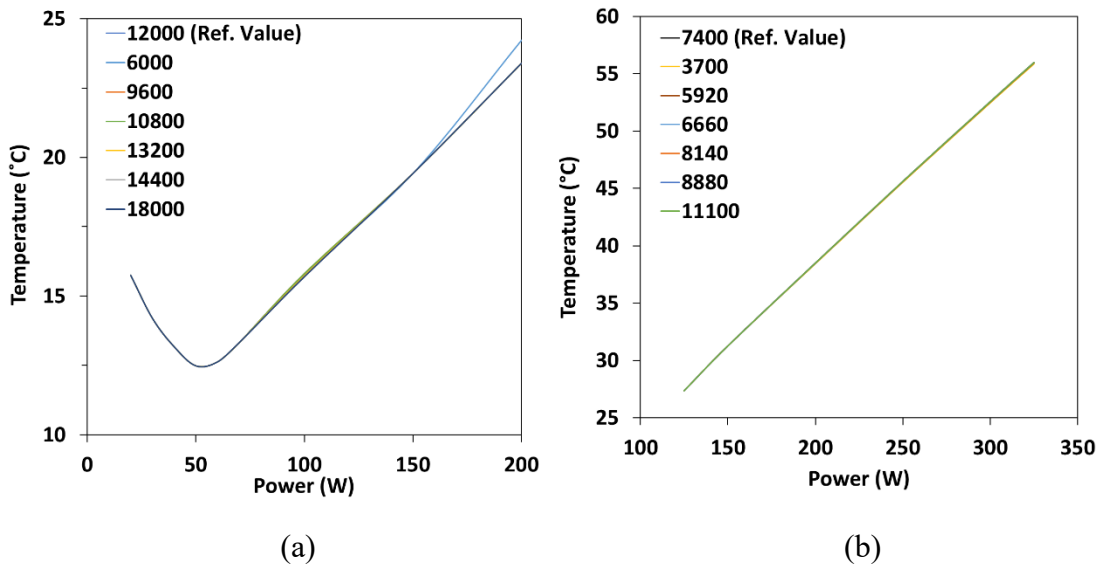


Fig. 49 Effect of the evaporator saddle-to-wick contact conductance [ $\text{W}/\text{m}^2 \text{K}$ ] on the operating temperature of (a) LHP1 and (b) LHP2.

Figure 50 shows the temperature of the evaporator saddle as a function of the applied power. The effect of  $h_{ES,wick}$  on the temperature is evident at higher powers as a higher temperature difference between wick and evaporator saddle is required to transfer the applied power to the LHPs. The

average absolute and relative differences in the temperature have their maximum at -50% with 2.1°C (5.8%) and 9.9°C (10%) for LHP1 and LHP2, respectively.

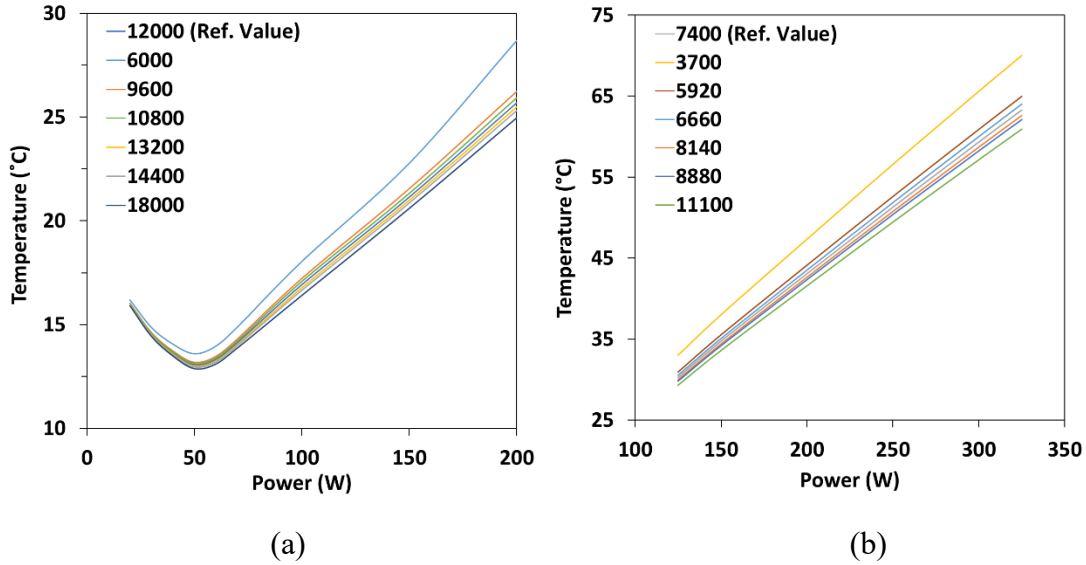


Fig. 50 Effect of the evaporator saddle-to-wick contact conductance [ $\text{W}/\text{m}^2 \text{K}$ ] on the saddle temperature of (a) LHP1 and (b) LHP2.

These results show that although  $h_{ES,wick}$  influences the temperature of the evaporator saddle, the effect on the LHP operating temperature is negligible. Therefore, if only the operating temperature is of interest, there is no need to match this parameter. In that case, a high value, such as 10,000  $\text{W}/\text{m}^2 \text{K}$ , can be assigned to  $h_{ES,wick}$ . Such a choice is well justified since the LHP evaporators are manufactured with a tight fit between the wick and casing.

#### 4.4.2 Condenser contact conductance

Figure 51 presents the sensitivity of the operating temperature to  $h_c$ , when it is varied from the reference value. For LHP1, it can be seen in Fig. 51 (a) that the contact conductance essentially has no significant effect on the Variable Conductance Mode (VCM), but it affects the power at which the LHP switches from a VCM to a Fixed Conductance Mode (FCM). This transition occurs when the two-phase/liquid interface approaches the end of the condenser. Increasing the contact conductance causes this transition to occur at a higher power and results in a lower operating temperature for the same applied power. In the FCM, not surprisingly, the LHP operates at a higher temperature for a given power as  $h_c$  is decreased. The observed change in the slopes in Fig. 51 (a) and (b) means that the condenser conductance affects the operating temperature most at the highest applied power. For instance, as shown in Fig. 51 (b), a 50% decrease in  $h_c$  for LHP2 results in a change of the slope from  $0.15^\circ\text{C}/\text{W}$  to  $0.25^\circ\text{C}/\text{W}$  and an average temperature increase of 59.3% with respect to the reference temperature. The temperature increase at 125 W is  $16.3^\circ\text{C}$  (54.9%) in comparison to  $35.8^\circ\text{C}$  (63.9%) at 325 W.

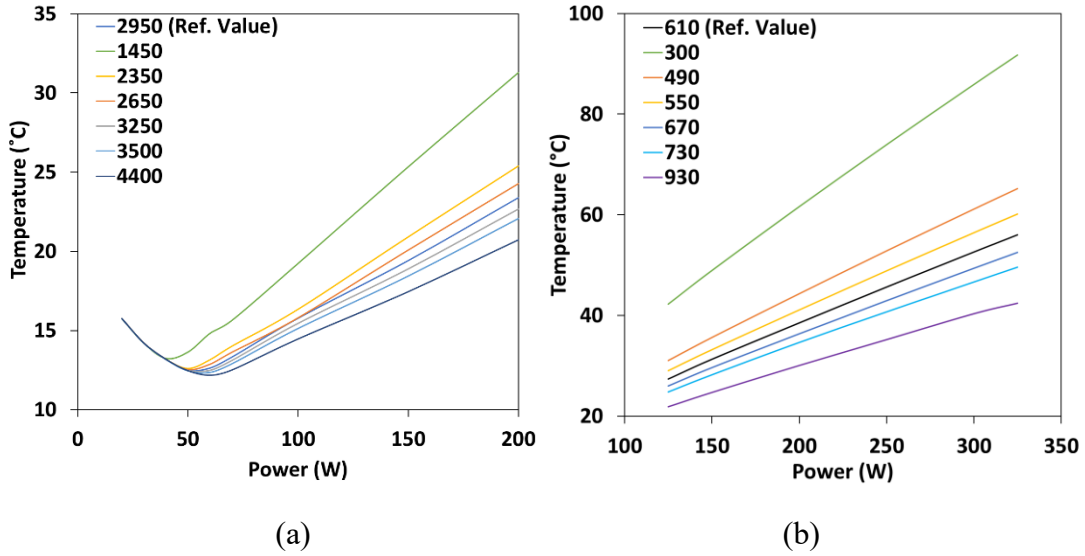


Fig. 51 Effect of the condenser contact conductance [ $\text{W}/\text{m}^2 \text{K}$ ] on the operating temperature of (a) LHP1 and (b) LHP2.

#### 4.4.3 Natural convection heat transfer correlation

Figure 52 illustrates the effect of the multiplier for the natural convection heat transfer correlation ( $\alpha$ ) on the operating temperature when the multiplier is varied from the reference value. The ambient temperature is set to  $22^\circ\text{C}$ .

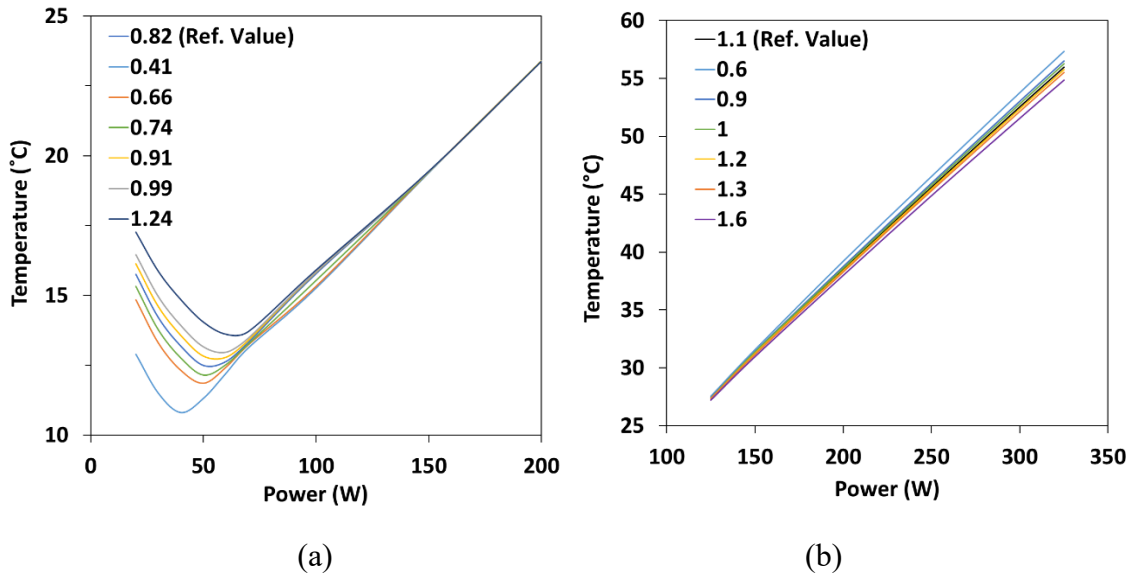


Fig. 52 Effect of multiplier for the natural convection heat transfer correlation on the operating temperature of (a) LHP1 and (b) LHP2.

In the VCM, as shown in Fig. 52 (a), where the condenser is not fully open, the operating temperature increases with increasing  $\alpha$  since the operating temperature is lower than that of the ambient, and there is more heat transferred from ambient to the LHP liquid line and reservoir. Changing  $\alpha$  has more effect on the VCM operating temperature since the lower mass flow rate results in longer dwelling time in the liquid line.

The power corresponding to the minimum operating temperature (the transition point from VCM to FCM) increases with increasing  $\alpha$ . This increase in the transition power is contributed to the higher operating temperature when  $\alpha$  is increased. In this case, the condenser works more efficiently due to the higher temperature difference between the fluid and sink. In other words, the applied power is rejected to the sink within a shorter length of the condenser. Thus, the occurrence of the minimum point is observed at a higher power. For instance, the two-phase/liquid interface at 40 W is receded from junction 29 to junction 21 as  $\alpha$  is changed from 0.41 to 1.24. Note that the condenser is located between junctions 12 and 32. The power corresponding to the minimum point increased from 40 W to 70 W. In the FCM,  $\alpha$  has a minimum effect as the operating temperature is close to the ambient temperature. However, small changes in the operating temperature are observed at the high powers for LHP2 because of the temperature difference between the loop and ambient. In the high powers, the liquid line works as an inefficient extension of the condenser. Therefore,  $\alpha$  influences the slope of the performance curve as well. The slope of the line decreases as  $\alpha$  increases since more heat dissipates to ambient.

#### 4.4.4 Fluid velocity inside the vapor grooves

The fluid velocity inside the vapor grooves is the fundamental variable for using the heat transfer and pressure drop correlations. As a result, a correction parameter for the fluid velocity ( $\beta$ ) is chosen as a matching parameter. As shown in Fig. 53,  $\beta$  variation from the reference value does not have a significant effect on the operating temperature. The maximum absolute and relative differences in the temperatures occur at the maximum values for  $\beta$ , are 0.8°C (3.5%) and 0.1°C (0.1%) for LHP1 and LHP2, respectively. The temperature difference of 0.8°C occurs at 200 W where the operating temperature of LHP1 is close to the ambient temperature. In this case, the additional heat absorbed by the superheated vapor cannot be efficiently dissipated to the ambient in the vapor line. The LHP1 operating temperature obtained for  $\beta$  of 1.2 at 200 W is similar to the value obtained for  $h_{ES,wick}$  of 6000 W/m<sup>2</sup> K scenario at the same power. Both of the scenarios are affected by the close proximity of the operating temperature to the ambient temperature.

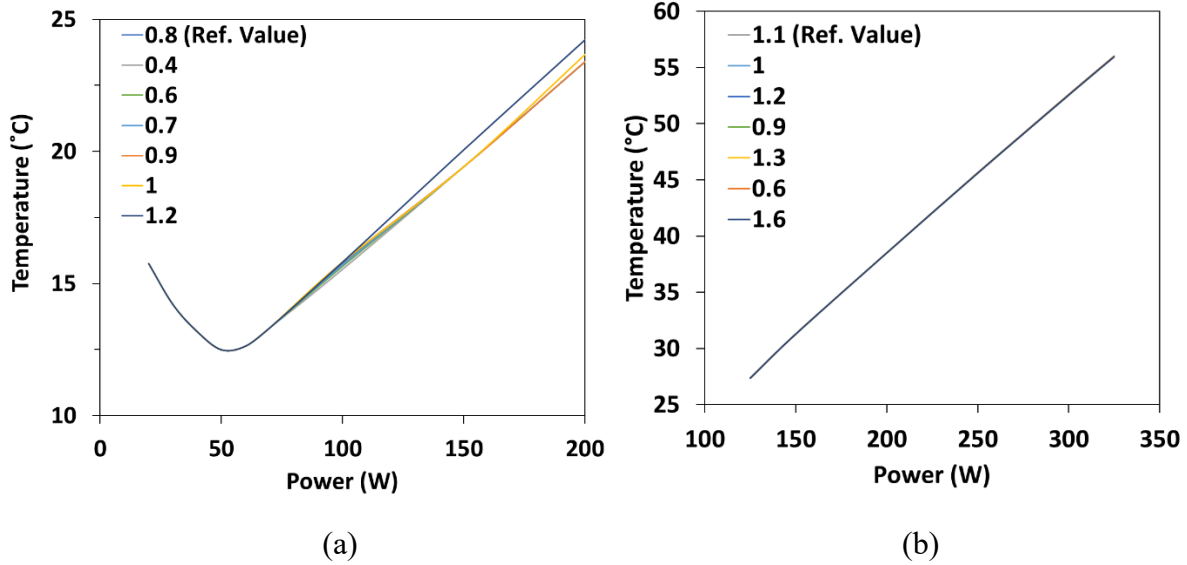


Fig. 53 Effect of the fluid velocity correction factor on the operating temperature of (a) LHP1 and (b) LHP2.

Figure 54 shows the vapor groove superheat temperature as a function of the applied power. The effect on the superheat temperature is evident at higher powers because of the increased flow velocity in the grooves. The velocity increase changes the flow regime from laminar to turbulent flow. At the turbulent regime, the heat transfer correlation is more sensitive to the velocity. This flow-regime change directly affects the slope of the superheat curves in Fig. 54. No change in the slope of the LHP1 superheat temperatures is observed for  $\beta$  of 0.4 as the flow remained laminar across the power range. However, when  $\beta$  is varied from 0.6 to 0.7, the flow switched from laminar to transitional flow at around 100 W. When  $\beta$  is between 0.9 and 1.0, there is a sudden change from laminar to transitional flow at 70 W and another one from transitional to turbulent flow at 150 W, as shown in Fig. 54 (a). For  $\beta$  of 1.2, these changes occur at 60 and 100 W.

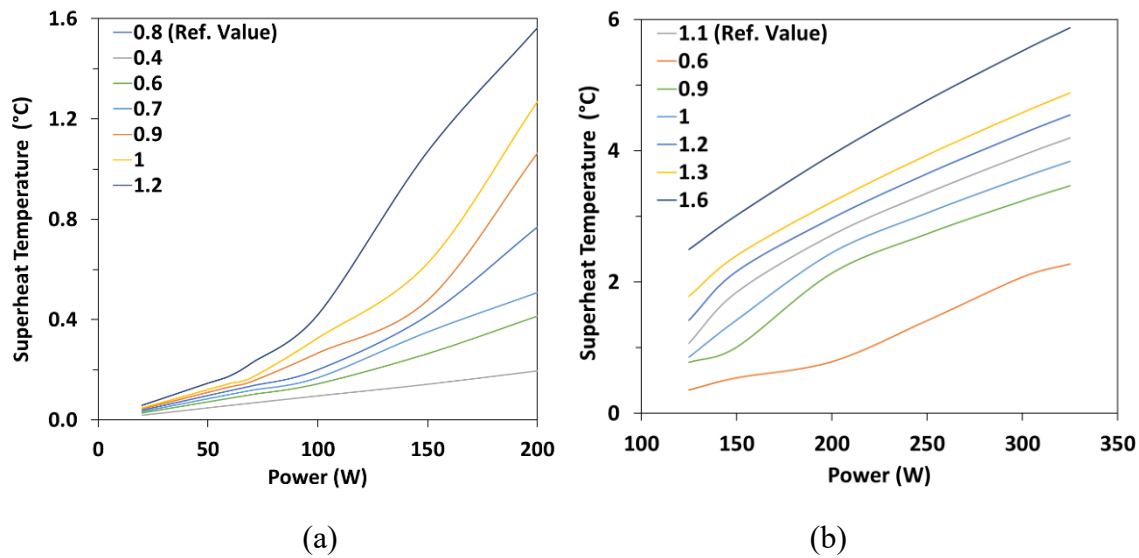


Fig. 54 Effect of the fluid velocity correction factor on the superheat temperature of (a) LHP1 and (b) LHP2.

In the case of LHP2, Fig. 54 (b), the change from laminar to transitional flow can only be seen when  $\beta$  is between 0.6 and 0.9 at 200 W and 150 W, respectively. The other lines in Fig. 54 (b) do not have this transition because of the higher velocity in the applied power range. When  $\beta$  is changed from 0.6 to 1.3, the power at which the flow became turbulent is decreased from 300 W to 150 W with increasing  $\beta$ . For  $\beta$  of 1.6, no change in the slope means that the flow is turbulent for all the applied powers.

These results suggest that although the fluid velocity correction factor has some influence on the vapor superheat, the effect on the LHP operating temperature is negligible. Therefore, if the user does not need high accuracy in predicting the operating temperature, this parameter can easily be removed from the matching parameter list.

#### 4.4.5 Heat transfer coefficient transition from two-phase to single-phase

As explained in Section 3.2.3., the heat transfer coefficients of the single and two-phase flow are given by different correlations and there exist discontinuities between the heat transfer coefficient correlations at the single and two-phase regions. The discontinuities are avoided by using smoothing functions at very low and high vapor qualities. The upper limit quality for the liquid/two-phase transition and the lower limit quality for the vapor/two-phase transition are defined to implement the smoothing functions. The vapor quality value of the upper limit for the liquid/two-phase transition is currently set to 0.2. The sensitivity analysis shows that the upper limit quality value does not have a significant effect on the operating temperature of the LHPs. The temperature varies less than  $0.1^\circ\text{C}$  when the upper limit is changed from 0.05 to 0.5.

For the vapor/two-phase transition, Fig. 55 presents the results of the sensitivity analysis conducted to see the effect of the transition quality. As shown in Fig. 55, the performance curve is not sensitive to the choice of quality values higher than 0.85.

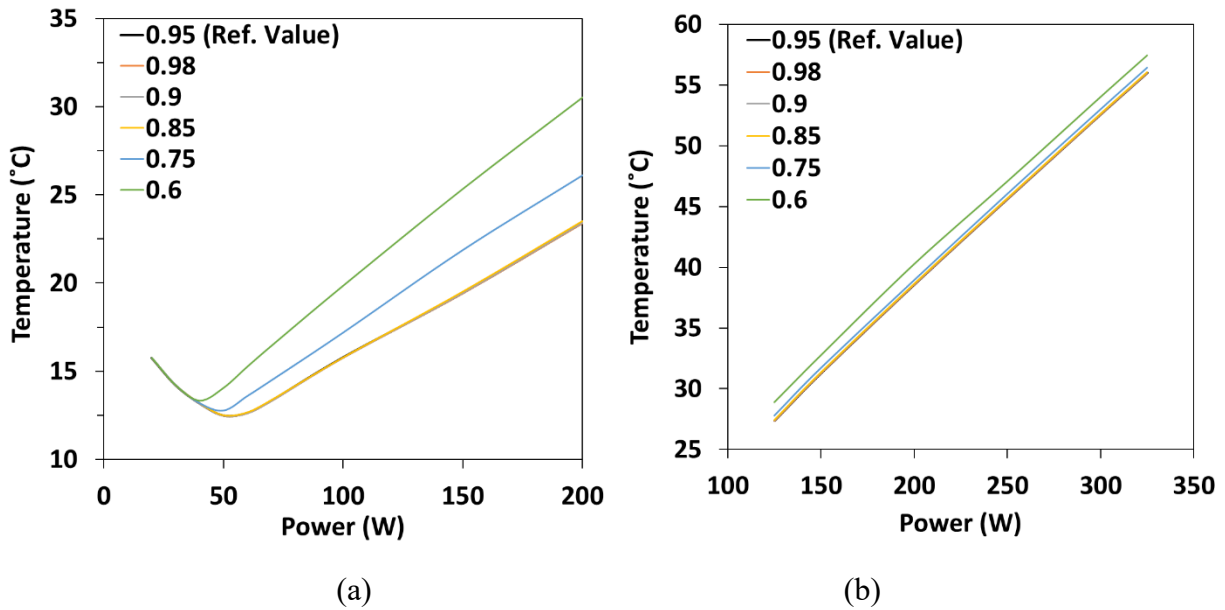


Fig. 55 Effect of the transition quality for the vapor/two-phase transition on the operating temperature of (a) LHP1 and (b) LHP2.

For the quality values less than 0.85, as shown in Fig. 55 (a), the transition quality value does not affect the LHP operating temperatures in the VCM, although it does change the transition point from VCM to FCM. In the VCM, the condenser is not fully open, and the interface lays far away from the end of the condenser. Therefore, the subcooled section is long enough to bring the condenser exit temperature close to the sink temperature when the transition quality changes. In the case of the VCM-to-FCM transition, reducing the transition quality shifts the VCM-to-FCM transition point to a lower applied power and a higher temperature. A decrease in the transition quality translates into a smaller heat transfer coefficient for a broader range of quality. Hence, a longer two-phase length of the condenser is required to dissipate the same amount of heat. As a result, the interface moves toward the end of the condenser at a lower applied power where the transition occurs. The increase in the operating temperature is due to the reduced flow rate as the applied power is reduced. The elevated operating temperature results in a higher heat transfer from ambient to the liquid line and a decrease in the amount of subcooling entering the reservoir. In FCM, the operating temperatures for both LHPs are inversely proportional to the transition quality below 0.85. In that case, a decrease in the transition quality results in a decrease in the heat transfer coefficient value. Therefore, the subcooling provided to the reservoir is decreased and consequently the LHP operating temperature increases. However, the transition is expected to take place at relatively high qualities. Therefore, using a quality value of 0.85 or higher is justified.

#### 4.4.6 Heat transfer coefficient in the two-phase region

The two-phase flow heat transfer correlations directly influence the operating temperature as demonstrated in Section 3.2.3. As concluded in that section, the Traviss' correlation is chosen to obtain the heat transfer coefficient. However, a more recent and comprehensive correlation presented by Park and Hrnjak is also implemented in the steady-state model to examine the sensitivity of the operating temperature to the two-phase correlations. Figure 56 shows the changes in the operating temperature when utilizing these two correlations. As shown in Fig. 56 (a), VCM of LHP1 is not affected by choice of the correlation since the condenser subcooling is not a function of the two-phase heat transfer coefficient.

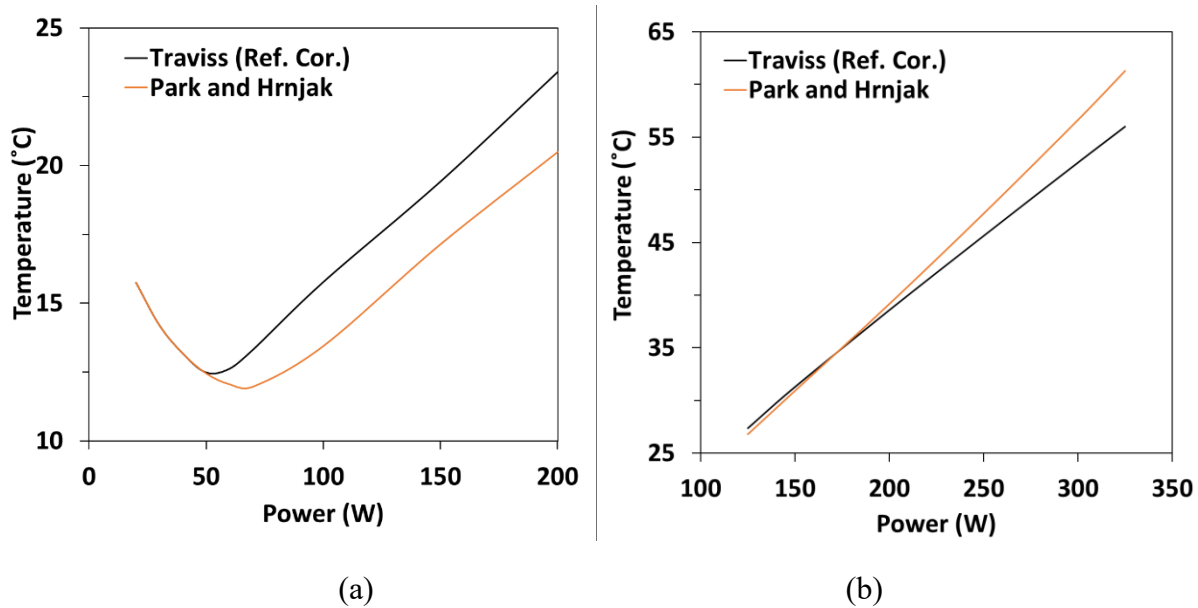


Fig. 56 Effect of the two-phase heat transfer correlations on the operation of (a) LHP1 and (b) LHP2.

Furthermore, Fig. 56 (a) illustrates a lower operating temperature for both the minimum point on the performance curve and the FCM region when the Park and Hrnjak's correlation is used since this correlation provides a higher heat transfer coefficient value than that of Traviss' in the stratified region. As a result, the condenser subcooling increases and the operating temperature decreases.

Figure 57 (a) shows the mass flux of the LHP1 condenser, which has a maximum of  $6.5 \text{ kg/m}^2\text{s}$  at 200 W, and this maximum mass flux is much smaller than its stratified limit of  $29.9 \text{ kg/m}^2\text{s}$ . For the LHP2, as shown in Fig. 56 (b), the Traviss' curve drops below the Park and Hrnjak's one after 175 W since the flow pattern in the LHP2's condenser enters into the stratified-wavy region, as shown in Fig. 57 (b). In this flow region, the Traviss' correlation provides a higher heat transfer coefficient value than that of the Park and Hrnjak, resulting in a higher condenser subcooling and consequently lower operating temperature. For the LHP1, the crossover occurs at an applied power of 500 W, not shown in Fig. 57 (a), resulting in similar observations as that of the LHP2.

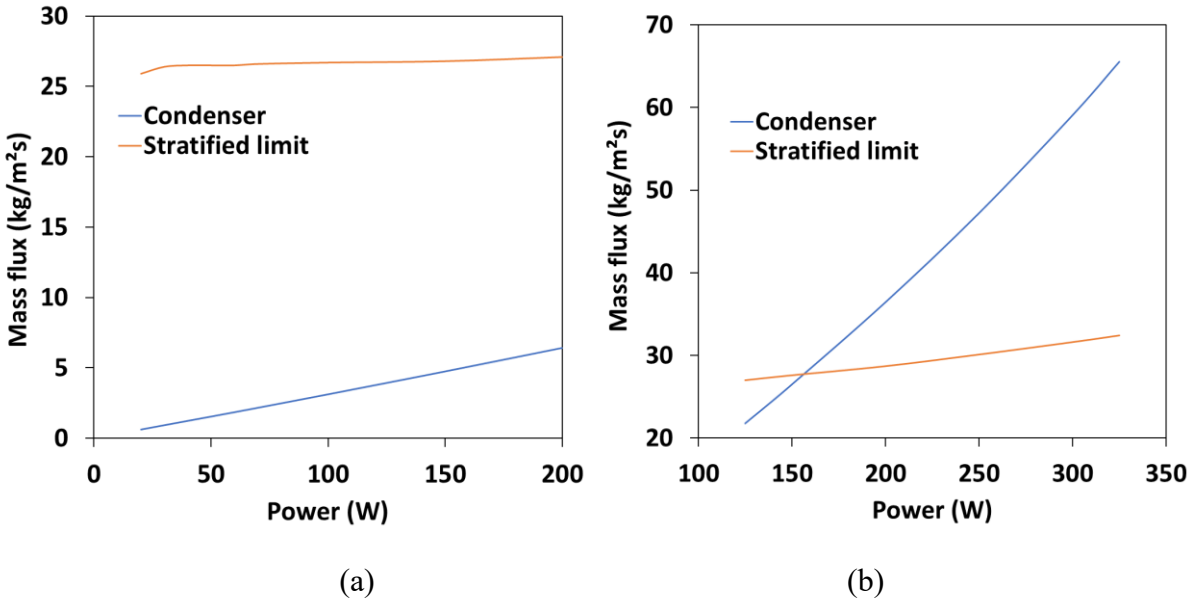


Fig. 57 Mass flux inside the condenser and stratified flow limit for (a) LHP1 and (b) LHP2.

#### 4.4.7 Viscosity in the two-phase region

As mentioned in Section 3.1.3, the two-phase friction factor is calculated from the Churchill correlation by assuming a homogenous flow where both the liquid and vapor flow have the same velocity. The two-phase viscosity is then obtained from the saturated viscosities and the vapor quality using the empirical correlations presented in Table 7. It is found that the results obtained using different viscosity correlations do not have a significant effect on the LHP temperatures.

#### 4.4.8 Wick effective thermal conductivity

The effective thermal conductivity of the wick needs to be known to calculate the heat leak through the wick. The effective thermal conductivity is a function of the wick porosity, the thermal conductivities of the wick material and fluid inside the wick. The available correlations are similar to that of the two-phase viscosity presented earlier in Table 7. To obtain the effective thermal conductivity relations,  $\mu_{2ph}$  in Table 7 should be replaced by  $K_{eff}$ ,  $\mu_{liq}$  by  $K_{wick}$  and  $\mu_{vap}$  by  $K_{liq}$ . The results obtained by using the different correlations do not have an important effect on the LHP operating temperature. For instance, the maximum change in the LHP1 operating temperature is  $0.3^{\circ}\text{C}$  at an applied power of 50 W. In the case of LHP2, the operating temperature varies with a maximum of  $0.2^{\circ}\text{C}$  at applied powers of 150 W and 200 W.

#### 4.4.9 Cell length in the transportation lines and condenser

A sensitivity analysis is performed to see the influence of the cell length on the results and to investigate the effect of the cell length on the numerical convergence.

When the length of the vapor line cells is increased from 2.5 cm to 40 cm for both of the LHPs, the change in the operating temperature is found to be within  $0.1^{\circ}\text{C}$ . Therefore, the minimum

computational time is used as the criterion to find the smallest cell length of the vapor line. As shown in Fig. 58, the minimum computational time can be obtained for a vapor line cell length of 10 cm for the LHP1 and 40 cm for the LHP2.

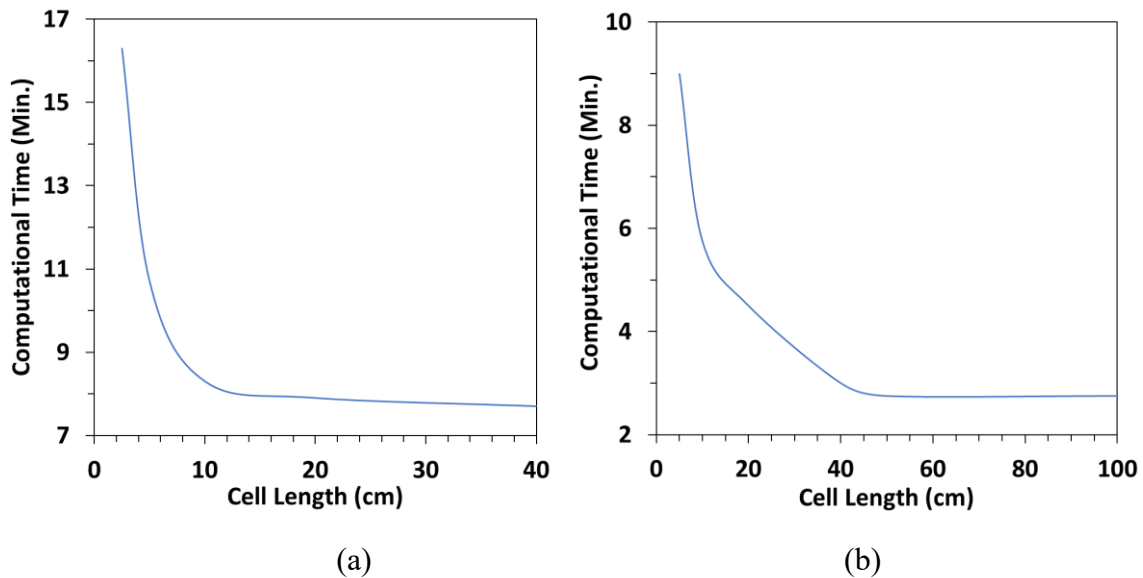


Fig. 58 Effect of the length of the vapor-line cell on the simulation time of (a) LHP1 and (b) LHP2.

Figure 59 shows no change in the operating temperature of LHPs in the FCM as the cell length of the liquid line is increased from 2.5 cm to 40 cm. However, the LHP1 operating temperature in the VCM is increased as the cell length is decreased as shown in Fig. 59 (a). The temperature increase is less than 0.1°C for the cell lengths below 10 cm. Hence, this cell length is selected for the LHP1 liquid line.

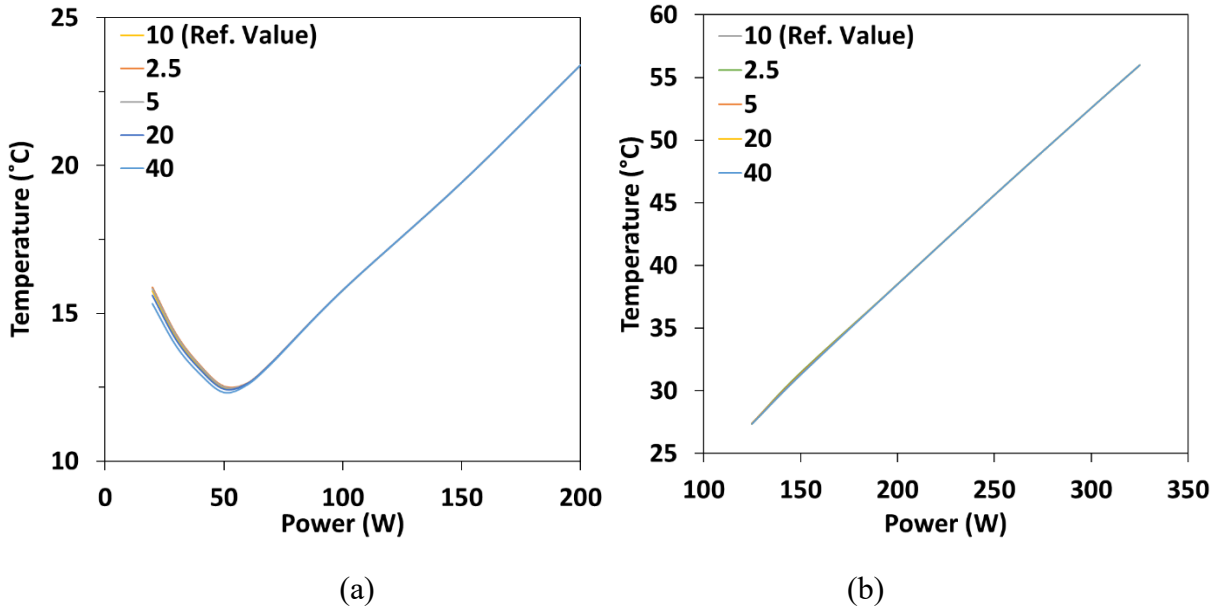


Fig. 59 Effect of the length [cm] of the liquid-line cell on the model results of (a) LHP1 and (b) LHP2.

In the case of the condenser, as it is shown in Fig. 60, the cell length is changed from 1 cm to 20 cm. It is found that a cell length of 5 cm is optimum for both LHPs as the temperature difference is within 0.1°C below this cell length.

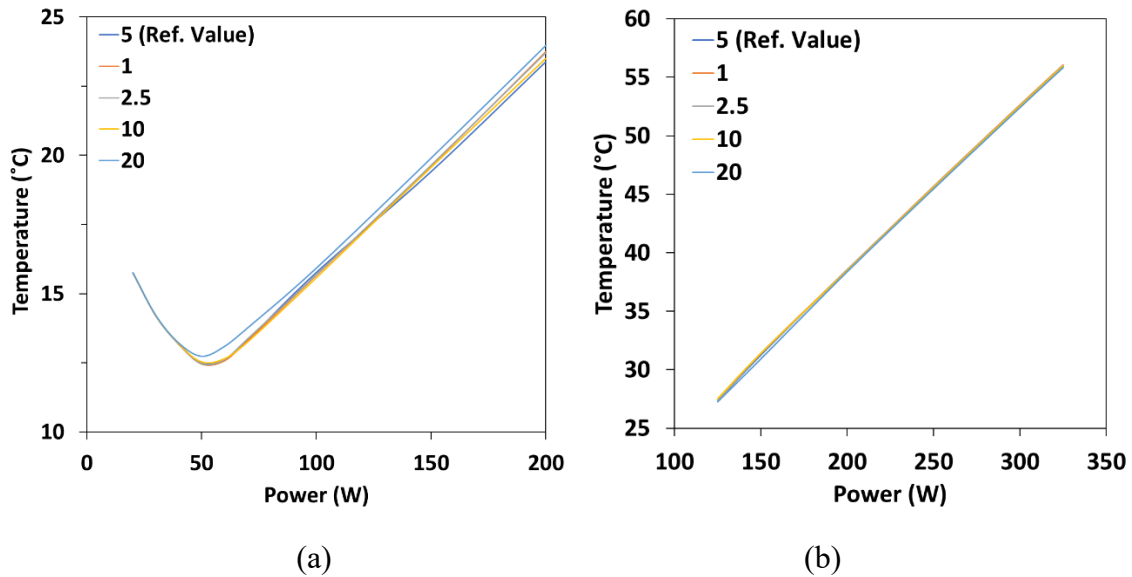


Fig. 60 Effect of the length [cm] of the condenser cell on the operating temperature of (a) LHP1 and (b) LHP2.

## 4.5 Summary

A new mathematical model to simulate the steady-state behavior of LHPs is presented in this chapter. The LHP components are discretized into cells and one-dimensional compressible mass, momentum and energy conservation equations are solved by using a staggered-grid approach. The fluid phase (subcooled liquid, two-phase or superheated vapor) in each cell is determined based on the saturated temperature and vapor quality.

To obtain the LHP operating temperature, a highly iterative scheme is required. After obtaining the operating temperature, the model checks the LHP limits including the capillary pressure limit and whether the reservoir is dried out or hard filled. The model uses four accommodation parameters: evaporator saddle-to-wick contact conductance, condenser-to-sink contact conductance, transportation lines-to-ambient thermal conductance and vapor velocity in the grooves. It is shown that the two parameters (evaporator saddle-to-wick contact conductance and vapor velocity in the grooves) have a negligible effect on the LHP operating temperature; thus, only two accommodation parameters would be sufficient to model the steady-state operating temperature of an LHP.

The presented model is validated against the experimental results obtained from the two different LHPs: one with a conventional design and one containing a PRV on its vapor line. The accommodation parameters are determined at a chiller temperature of 5°C. Then, the model prediction capability is demonstrated by comparing the results at chiller temperatures of 10, 15 and 20°C. The model predicts the operating temperature of both of the LHPs with an average absolute error of less than 1.5°C and an average relative error lower than 4% across the chiller conditions studied.

The sensitivity analysis shows that the LHP operating temperature in the FCM is primarily influenced by the heat transfer parameters of the condenser including the contact conductance, two-phase heat transfer coefficient and its two-phase/vapor transition. The VCM temperatures are mainly influenced by the heat transfer between the liquid line and ambient. The proposed mathematical model proved to be successful in analyzing the steady-state performance characteristics of LHPs, such as overall thermal conductance and operating limits. It can be used to calculate the pressure drops in the specific segments, investigate the influence of wick properties and fluid charge on the overall performance. The model is also useful to obtain the initial conditions for a transient model, which will be presented in a separate paper.

## Chapter 5: Transient model

Although several steady-state LHP models were developed in the past, only a few transient models have been published in the open literature. The transient modelling of the LHP has several challenges: complex heat and mass transfer through a porous wick, moving liquid-vapor front in the condenser and time-varying vapor quality in the reservoir. All of the existing models use correlations and experimentally adjusted parameters to deal with the various challenges. It is obviously very important to minimize the use of the adjusted parameters to improve the model predictivity.

Similar to steady-state models, the published transient models can be divided into two main categories based on their focus: the investigation of the overall transient behavior of the LHP or transient operation of a specific component of the LHP. In the overall category, the transient response of a typical LHP to changes in the operating conditions (e.g. the applied power, sink temperature and ambient temperature) is investigated. The models in the specific category study particular components such as evaporator or condenser and its effect on the LHP operation. One of the advantages of the global LHP models is that they can be integrated into a system-level thermal model to analyze the thermal behavior of complex systems such as a spacecraft [28].

The transient model presented by Wrenn et al. [86] solves the time-dependent, one-dimensional governing equations in conjunction with a nodal thermal analyzer to predict the state of the fluid when the boundary conditions change. The entire LHP is modelled as a dynamic system of a mass-spring-damper. The model runs in SINDA/FLUINT software. The model temperature results are within 5°C of the experimental result. However, the computational and experimental temperatures reach their steady-state values at different times. This type of time lag has been observed in many numerical simulations.

Hoang and Ku [87] developed a model based on similar assumptions in [86]. In other words, they considered the LHP as a mass-spring-damper system with one-dimensional governing equations. The equations are rearranged to create a second-order ordinary differential equation for the vapor flow in the reservoir and condenser. The operating temperature of the LHP is obtained by solving this ordinary differential equation. The model is implemented in FORTRAN, and it can be integrated into the spacecraft thermal analyzers such as SINDA or TMG. The thermal interaction between the LHP and time-varying boundary conditions is provided by introducing thermal nodes for each LHP components. These nodes are coupled with the boundary nodes in their vicinity. The temperature results are within 5°C agreement with the available validation data, although the time lag is observed. The model underestimates the heat leak at low power operations. As a result, the authors recommended employing different models for low- and high-power conditions. Using different models would require a better understanding of mass and heat transfer across the wick. Later, Hoang, Baldauff, and Mahony [88] presented an improved version of this model. The new version has the capability to analyze LHPs filled with 88 possible working fluids for space or

terrestrial applications. In addition, the model can be integrated into a thermal analyzer environment. The model uses a lumped parameter method with meshing capability up to 6032 nodes. In the reservoir section, the fluid and wall are lumped together. The model can demonstrate most of the transient behavior of an LHP except the low-amplitude, high-frequency oscillations in the liquid line. No information is provided regarding the improvement of the time lag.

Launay et al. [89] developed a transient model to study the LHP temperature oscillations. The casing of the evaporator and reservoir are analyzed separately, and working fluid is assumed to be incompressible in the derivation of conservation equations. The condenser model uses the void fraction method developed by Wedekind et al. [90] to deal with two-phase condensation. The heat and mass transfer equations are coupled, and the inertia terms are ignored in the condenser transient model. The momentum equation is used to obtain the evaporator saturation pressure and temperature from the vapor properties at the entrance of the condenser, assuming an isothermal vapor line. A time lag between the simulation and test results is observed like the other models mentioned above. The time lag is attributed to the absence of thermal inertia terms in modelling the evaporator, reservoir and condenser

Vlassov and Riehl [91] published a transient model requiring experimentally adjusted thermal conductance of vapor/liquid interfaces in the primary wick and reservoir. The two-phase condensation and the rate of flooding of the reservoir are numerically simulated. The LHP is divided into small isothermal control volumes. The mass and momentum equations are combined for each control volume. The conservation equations, consisting of algebraic and partial differential equations, are solved implicitly and are integrated by a predictor-corrector algorithm with one intermediate step using a fixed time step. The model shows a good agreement (within  $\pm 3^\circ\text{C}$ ) between the prediction and experimental results in a wide range of boundary conditions. The time lag prediction is improved compared to the previously published models although some discrepancies are observed comparing the results of the simulations and tests.

Kaya et al. [92] presented another transient model, which is based upon the one-dimensional transient conservation equations. The fluid is assumed to be compressible and viscous. The equations are derived as a set of differential-algebraic relations for staggered grid nodes representing the entire LHP. Then, the set of equations is solved by the DASSL method within the EcosimPro software. The software has the capability of integrating the LHP model within more complex thermal architectures [13]. The model capability, to predict the LHP behavior, is validated through several experiments within an accuracy of  $\pm 3^\circ\text{C}$  [92], [28] and [13]. The start-up is also numerically simulated; however, this requires experimental temperature overshoot data and a heat leak adjustment to reproduce a start-up which agrees with the experimental results.

Nishikawara et al. [4] presented a transient model developed upon one-dimensional conservation equations. In these equations, the fluid is assumed to be incompressible and viscous. The inertia term is neglected in the momentum equation. The derived differential equations are solved explicitly using the Euler method and coded in FORTRAN. The heat transfer coefficients for the

evaporator casing-to-wick and groove-to-wick are experimentally fitted for each power setting, somehow limiting the predictive capability of the model. The experimental results show no time lag even though some temperature overshoots observed in the simulations are not observed in the experiments. The numerical results are in good agreement with the experimental. However, some significant differences are also obtained. For instance, the difference in the operating temperature was 8.6°C at 50 W at an operating temperature of 22°C.

Blet et al. [93] developed a systemic transient model for CPLs using staggered grid nodes (similar to an electrical network) that was adopted from Kaya et al. [92]. The governing equations are similar to [92] with several modifications, including new correlations for the convective heat transfer coefficient of the two-phase flow and nondimensionalization of the variables. A simplified model of the wick is used in the evaporator section. The enthalpy and pressure are used to identify other properties of the working fluid. The accommodation factors (e.g. the conductance of the evaporator and reservoir) are obtained by matching a steady-state model to the experimental results. The model is validated by comparing the calculated temperature, pressure and mass flow rate against the experimental results. Also, the applied power change is implemented with different rates (W/s) to investigate the effect of the power rate on transient behavior. Some temperature overshoots are observed, and the calculated time lag is found to be close to the experimental values. The error analysis is not performed to present the quantitative difference between the model and experiment results. It is reported that it takes five minutes of computational time to calculate the LHP response to a single power change.

Bernagozzi et al. [94] introduced a one-dimensional lumped parameter model (LPM) to investigate the transient behavior of the LHPs designed for electric vehicles. The model uses the thermal-electrical and hydraulic-electrical analogies. These analogies help to simplify the governing equations to a system of ordinary differential equations for the discrete nodes representing the LHP components mathematically. The LPM is implemented in Octave (open source) software. The computational time is reported to be close to the experimental simulation time. The saturated properties of three different working fluids are modelled via the temperature-dependent polynomials. Then, the two-phase properties are calculated from the vapor quality. The vapor is treated as an ideal gas. It is also assumed that the vapor flow entering the condenser is saturated although the vapor in the grooves is superheated with no heat transfer between the ambient and vapor line. The authors provide a new condenser model using only the vapor quality to solve the two-phase flow inside the condenser. The number of nodes inside the condenser is a function of the applied power and decreases as the applied power increases. No mass change inside the two-phase node is assumed. The model is validated by comparing the results with previously developed models and experiments. The model results have an average temperature difference of 1°C and 2.5°C from the experimental values for the evaporator saddle and reservoir, respectively.

Meinicke et al. [95] presented a mathematical model that captures the transient behavior of an LHP. It is called a “lean” model as the model only uses mass and energy conservation equations in solving the transportation lines and treats the evaporator as a black box. In other words, the

experimental results, such as heat leak, are used to model the evaporator section in the absence of information about the internal structure of the evaporator. As a result, the model relies on the experimental values and its predictive capability is highly limited. Six accommodation factors are utilized to match the simulation results to the experimental results. They include a heat convection correction factor between the transportation lines and ambient, a conductive conductance parameter between the condenser and sink, the heat leak, the thermal conductivity between the reservoir and evaporator, the thermal capacity of the reservoir, and an exponential time-factor to simulate the applied power. The last two factors directly affect the transient behavior, e.g. the response time. The other factors affect transient simulation indirectly. In the condenser section, the heat exchanger is modelled as well. The simulation time step is fixed to be one second. The condenser is discretized into fine control volumes to make sure that the fluid mass inside each control volume at each time step is equal to the mass flow rate times the time step. The working fluid properties are calculated using the NIST database. The transient model is implemented in MATLAB as an iterative process for each time step with specified criteria for the convergence and numerical stability. The computational time is almost four times the time set to be simulated. The model is validated against two LHPs. The model results are in good agreement in terms of the temperatures and response time with the experimental values in the high-power region. The transient results in the low-power region are not as accurate as those of the high power. For instance, the model underpredicted the evaporator temperature by 2°C at 20 W.

This chapter introduces a new mathematical model to predict the global transient behavior of a conventional LHP. A modular approach is implemented to easily assess the effects of utilizing different accommodation factors and correlations on the transient results. This assessment provides the insight required to modify and use the model for a specific LHP design or working condition in minimum time and effort. Additionally, the transient model is developed on the foundation of the steady-state model. The steady-state model algorithm and prediction capability were validated in the previous chapter. The steady-state model is also utilized to determine the initial condition and LHP specific accommodation factors. The transient governing equations in each LHP section are solved implicitly after discretizing the section into control volumes. For a liquid control volume, the pressure drop and heat transfer coefficient are obtained by two-phase and single phase correlations verified for mini pipes. The wick, reservoir and fluid phase transition are modeled with methods, which were not discussed in the previously published works. The model can handle the phase transition across all the LHP sections particularly inside the condenser and transportation lines. By implementing these features inside several iterative algorithms, the model with a minimum number of accommodation factors can predict the transient behavior particularly time lag more accurately than other previously published methods.

In the next sections, the mathematical model of LHP segments, consisting of the assumptions, discretization methods and governing equations, is first described. Then, the algorithm required to implement the model is discussed followed by the model validation through comparing the model and experimental results for a conventional LHP using three performance parameters.

## 5.1 Mathematical model

Similar to the steady-state model, the transient model employs one-dimensional conservation equations of mass, energy and momentum. The LHP is discretized into several solid and fluid control volumes or cells, and the equations are written for each cell. The model uses an Eulerian approach and REFPROP software. First, the solid and fluid cells of the evaporator are solved, including the wick and grooves. Then, the transportation lines and condenser are analyzed cell by cell from the evaporator exit to the reservoir entrance. Finally, the conservation equations of the reservoir are analyzed to close the loop hydraulically and thermodynamically. Special attention is given to minimize the experimentally determined accommodation parameters.

### 5.1.1 Evaporator

The evaporator segment comprises of the heater block, evaporator saddle, wick and vapor grooves as described earlier in Fig. 37. The transient energy equations for the solid cells are shown in Eqs. (80) and (81) for the heater block and evaporator saddle, respectively. It is assumed that there is negligible transfer between these cells and ambient since they are insulated.

$$C_{HB} \frac{dT}{dt_{HB}} = \dot{Q}_{app} - (hA)_{HB,ES}(T_{HB} - T_{ES}) \quad (80)$$

$$C_{ES} \frac{dT}{dt_{ES}} = (hA)_{HB,ES}(T_{HB} - T_{ES}) - (hA)_{ES,wick}(T_{ES} - T_{int}) - (hA)_{ES,Gr}(T_{ES} - T_{Gr}) \quad (81)$$

The heat transfer coefficients ( $h$ ) in the above equations are obtained as explained in Section 4.1.1 for the steady-state model. The wick is a solid/liquid section that can be discretized and solved in three different ways. The main objectives are to calculate the evaporation rate and heat leak from the inner layer of the wick to the evaporator core.

In the first approach, the wick is modelled with the two liquid/solid cells named as the wick and interface. The wick cell is a cylinder where the saturated liquid from the reservoir moves radially to the interface cell, and the heat is conducted in the opposite direction. The interface cell is a thin layer on the exterior surface of the wick where evaporation occurs. The thermal inertia of the wick and interface is assumed negligible. Therefore, the energy equations for the interface and wick are identical to the steady-state equations provided in Eqs. (64) and (65), respectively. The mass flow rate is calculated from Eq. (64) assuming that the interface cell is very thin, and it does not have thermal or mass inertia. However, strictly speaking this equation is not valid for the transient case. Most of the previously published transient models have used the same equation, for example [92], [4], [93] and [94]. However, they did not justify why this equation can be used for modelling the transient behavior of an LHP. In this work, we compare this approach with other more realistic

formulations. It is important to note that the transient conductive heat flow through the wick ( $\dot{Q}_{wick,cond}$ ) can still be obtained from Eq. (66).

The second approach is similar to the first one except that the thermal inertia is considered for the wick cell. Therefore, its energy equation is provided by Eq. (82).

$$C_{wick} \frac{dT}{dt}_{wick} = \dot{Q}_{wick,cond} + \dot{m}(\dot{h}_{res,liq} - \dot{h}_{int,liq}) - \dot{Q}_{leak,cond} \quad (82)$$

where the heat capacity ( $C_{wick}$ ) is determined according to Eq. (83). In this equation, the solid and liquid heat capacities are combined using the series method.

$$C_{wick} = V_{wick} \left[ (1 - \varepsilon) \rho_{wick} c_{wick} + \varepsilon \rho_{wick,liq} \frac{d\dot{h}}{dT}_{wick,liq} \right] \quad (83)$$

where the wick volume ( $V_{wick}$ ) is calculated from the geometry, and the porosity ( $\varepsilon$ ) is a wick property in addition to the density and specific heat. The temperature derivative of the internal energy ( $\frac{d\dot{h}}{dT}_{wick,liq}$ ) is only used for the fluid portion, which is assumed to be saturated and incompressible. Hence, no density change is considered.

The third and final approach considers the entire wick as one cell with thermal inertia. Its energy equation given by Eq. (84) is used to calculate the mass flow rate. In this approach, the heat leak ( $\dot{Q}_{leak,cond}$ ) is obtained from  $\dot{Q}_{wick,cond}$  equation, Eq.(66), by replacing  $(T_{int} - T_{wick})$  with  $(T_{wick} - T_{res})$ . Table 18 summarizes the mathematical methods developed to solve the evaporator wick.

$$C_{wick} \frac{dT}{dt}_{wick} = (hA)_{ES,wick}(T_{ES} - T_{wick}) + \dot{m}(\dot{h}_{res,liq} - \dot{h}_{wick,vap}) - \dot{Q}_{leak,cond} \quad (84)$$

Table 18 Summary of the different solution methods to model the evaporator wick.

<b>Solution Method</b>	<b># cells</b>	<b>Thermal inertia</b>
WM-1	2: interface and wick	No
WM-2	2: interface and wick	Only wick
WM-3	1: wick	Yes

Figure 61 compares the effect of the three wick methods on the LHP operating temperature under varying applied power. Method 3 is chosen as the primary simulation method as it considers inertia terms in obtaining the mass flow rate; thus, it is more realistic. Method 2 takes an alternative temperature path during the transition time with a maximum difference of 0.3°C at 667s. In contrast, Method 1 closely follows the Method 3 trends in Fig. 61 with the temperature difference

within  $\pm 0.05^\circ\text{C}$ . The main reason behind these differences and similarities lies beneath the effect of the wick thermal inertia on the mass flow rate. Method 1 calculates the mass flow rate without any thermal inertia term. In Method 2, the thermal inertia indirectly affects the mass flow rate through  $\dot{Q}_{wick,cond}$  term. In Method 3, the effect of  $\dot{Q}_{wick,cond}$  term on the mass flow rate is canceled with direct insertion of thermal inertia term ( $C_{wick} \frac{dT}{dt}_{int}$ ) in the mass-flow-rate equation.

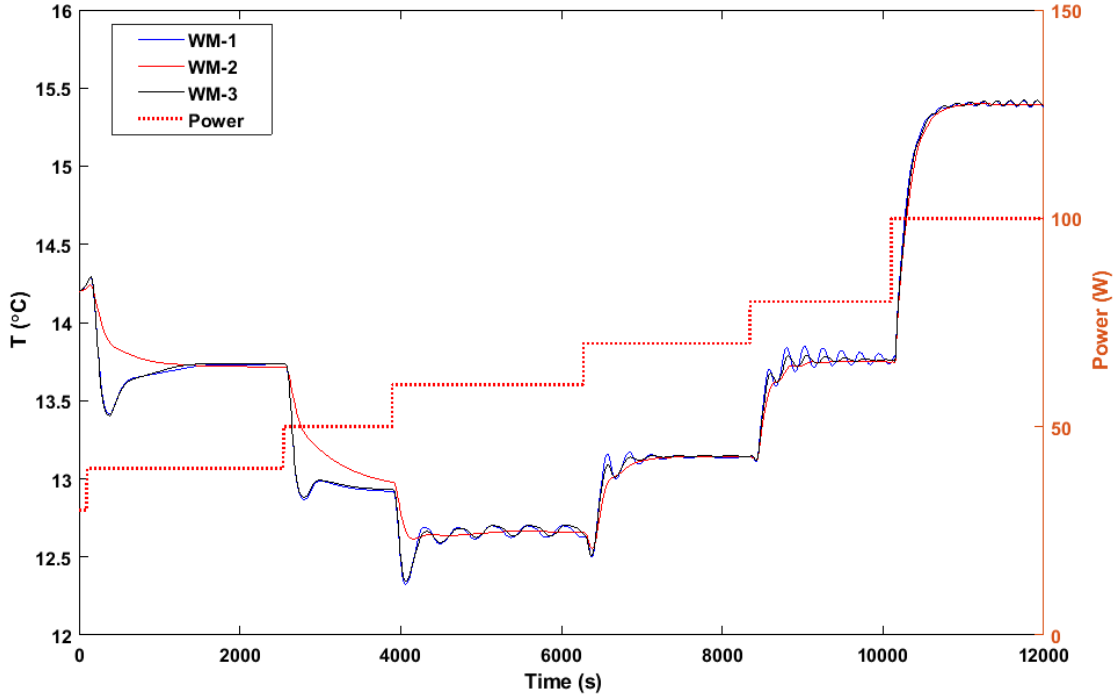


Fig. 61 Comparison of the results of different wick-modelling approaches as the applied power changes.

In all the three approaches, the fluid pressure under the evaporation surface is calculated from the Darcy's equation, Eq. (67), for radial viscous flow through a porous media. Similar to steady-state model, the wick pressure value is later used to verify that the LHP is operating below its capillary limit.

Inside the vapor grooves, the flow changes from the saturated vapor to the superheated one in the axial direction as heat is absorbed from the evaporator saddle. This section is modelled as a single cell with Eqs. (85) and (86).

$$\left( V \frac{d\rho}{dt} \right)_{Gr} = (A\rho u)_{int,vap} - (A\rho u)_{Gr} \quad (85)$$

$$C_{Gr} \frac{dT}{dt}_{Gr} = (hA)_{ES,Gr} (T_{ES} - T_{int}) + (A\rho u \dot{h})_{int,vap} - (A\rho u \dot{h})_{Gr} \quad (86)$$

where  $h_{ES,Gr}$  is defined in the Section 4.1.1 for the steady-state equation of the vapor grooves.

### 5.1.2 Transportation lines

The working fluid in the LHP after being evaporated first enters the vapor line and then goes through condenser. Finally, it reaches the reservoir after passing through the liquid line. It is assumed that the flow exchanges heat with ambient in the vapor and liquid lines and dissipates the latent heat to a sink via the condenser. Depending on the operation conditions, the vapor and liquid lines may also act as a condenser. The transportation lines are modelled by several units, each containing one fluid cell and one solid cell.

Similar to the steady-state model, the staggered grid concept (as introduced in Section 4.1.2 and shown in Fig. 38) outlines the discretization of the fluid cells and the calculation of the fluid properties. The fluid properties at any junction are defined using adjacent nodes and flow direction, as described in Eq. (69).

The transient form of the momentum, continuity and energy equations for a fluid cell are presented from Eq. (87) to (89). The energy and mass equations are solved at the fluid nodes, and the momentum equation is solved at the fluid junctions.

$$P_m - P_{m-1} = (\rho g)_j (Z_m - Z_{m-1}) + \xi \frac{\rho u_j^2}{2} \quad (87)$$

$$\left( V \frac{d\rho}{dt} \right)_m = (A\rho u)_j - (A\rho u)_{j+1} \quad (88)$$

$$\left( V \left( \rho \frac{d\mathfrak{u}}{dt} + \mathfrak{u} \frac{d\rho}{dt} \right) \right)_m = (A\rho u \mathfrak{k})_j - (A\rho u \mathfrak{k})_{j+1} - [(hA)_{inside} (T_{fld} - T_{slid})]_m \quad (89)$$

The momentum equation is identical to its steady-state form by assuming that the inertia term is negligible compared to other terms. The pressure drop coefficient ( $\xi$ ) and the heat transfer coefficient ( $h_{inside}$ ) are introduced in Section 4.1.2.

The transient energy equation for the solid cells of the liquid and vapor line is described in Eq. (90). The assumptions and terms in the right hand side of the equation are explained in Section 4.1.2 of the steady-state chapter.

$$C_{wall} \frac{dT}{dt}_{wall} = (hA)_{inside} (T_{fld} - T_{wall}) - (hA)_{outside} (T_{wall} - T_{amb}) \quad (90)$$

### 5.1.3 Condenser

The solid part of the condenser, depending on the design, can be modelled with more than one solid cell to connect a fluid node to the sink as shown in Fig. 39. The transient heat flow from the fluid node to the sink through the saddle and riser is modelled in Eqs. (91) and (92).

$$C_{CS} \frac{dT}{dt}_{CS} = (hA)_{inside}(T_{fld} - T_{CS}) - (hA)_{CS,CR}(T_{CS} - T_{CR}) \quad (91)$$

$$C_{CR} \frac{dT}{dt}_{CR} = (hA)_{CS,CR}(T_{CS} - T_{CR}) - (hA)_{CR,sink}(T_{CR} - T_{sink}) \quad (92)$$

The parameters in the right hand side of the above equations are explained in Section 4.1.3.

### 5.1.4 Reservoir

The reservoir is modelled by one cell that includes the evaporator. The reservoir pressure can be obtained from the last liquid cell using Eq. (87). By assuming that the reservoir fluid is in a two-phase state, the temperature can then be calculated from the pressure. Moreover, it is assumed that the fluid velocity is negligible inside the reservoir and that the reservoir walls have the same temperature as the fluid inside the reservoir.

The fluid density inside the reservoir can be obtained from the two different approaches: the continuity equation (RM-1) and fluid charge (RM-2). In the continuity approach, the density is calculated from its time-derivative obtained from the continuity equation as described in Eq. (93).

$$\left( V \frac{d\rho}{dt} \right)_{res} = (A\rho u)_{LL,out} - (A\rho u)_{res,liq} \quad (93)$$

where the subscript “*LL,out*” indicates the fluid properties at the exit of the liquid line before entering the reservoir. The subscript “*res,liq*” specifies the properties of the saturated-liquid entering into the wick. In the fluid charge approach, the reservoir density is calculated from Eq. (76) of Section 4.1.4 by taking into account the loop fluid charge and density of all the other fluid cells.

With the assumptions explained above, the energy equation of the reservoir can be given by Eq. (94). The left hand side of the equation represents the thermal inertia for both of the fluid and solid sections of the reservoir.

$$\left( V \left( \rho \frac{d\mathbf{u}}{dt} + u \frac{d\rho}{dt} \right) \right)_{res,flid} + \left( C \frac{dT}{dt} \right)_{res,sld} = \dot{Q}_{leak,res} - (hA)_{res,out}(T_{res} - T_{amb}) + \dot{m}(h_{LL,out} - h_{res,liq}) \quad (94)$$

where the parameters in the right hand side are defined in Section 4.1.4. Similar to the steady-state model, an iterative process is required to solve the equations introduced above for each time step.

Figure 62 illustrates the effect of the two reservoir modelling approaches on the LHP operating temperature when the applied power is varied. Method 2 is chosen as the primary simulation method since it ensures that the fluid charge constraint is met. The two reservoir methods follow the same trends within  $\pm 0.06^\circ\text{C}$ .

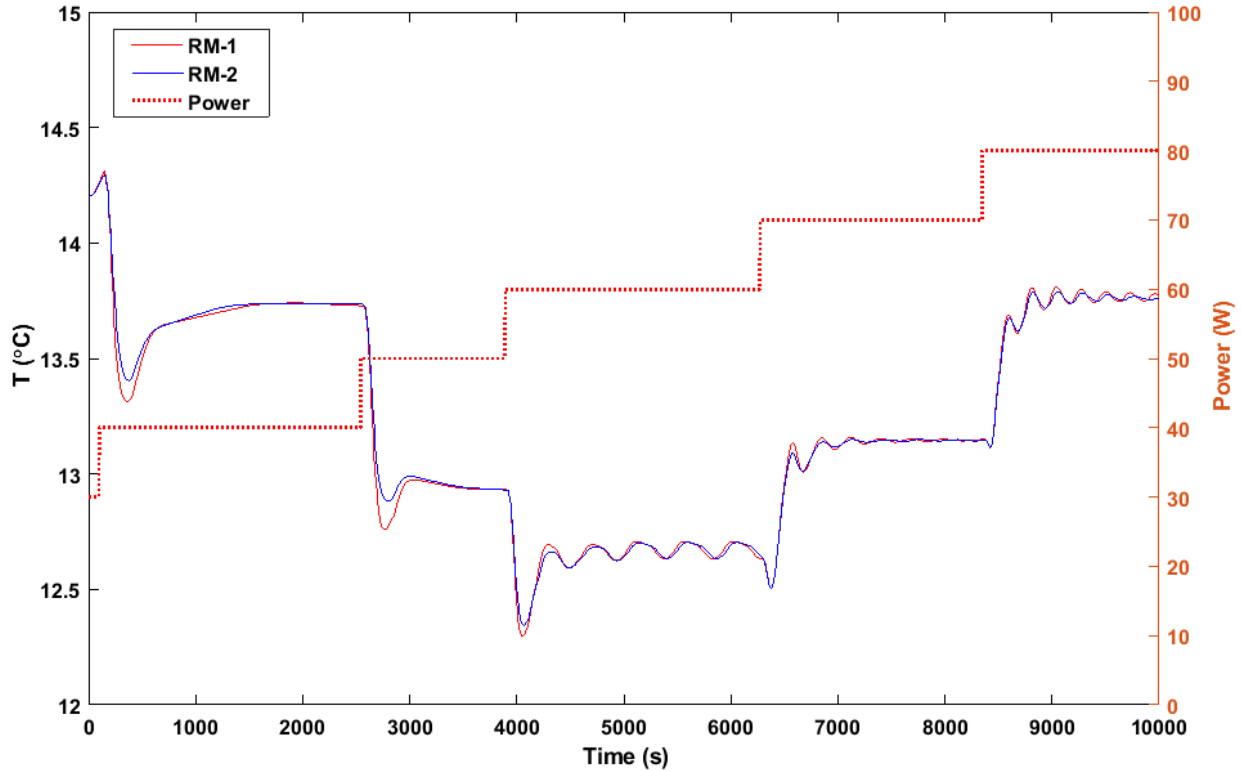


Fig. 62 Effect of different reservoir solution methods as the applied power changes.

## 5.2 Solution procedure

Figure 63 illustrates the top-level algorithm to solve the transient model. First, the physical and discretized model developed in the steady-state model is used to obtain the cell dimensions and material properties of the LHP components.

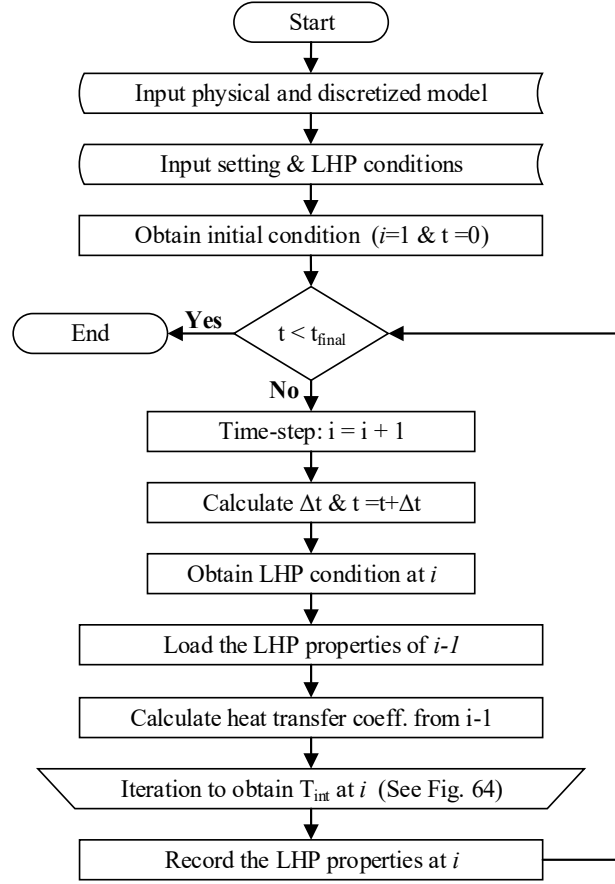


Fig. 63 Top-level algorithm of the transient model.

Second, the modelling parameters, including steady-state and transient ones, are provided to the solver. The steady-state parameters are covered in detail in Section 4.3. The transient parameters will be analyzed in detail in the model validation section of this chapter.

Third, the LHP operating conditions (the applied power, sink temperature and ambient temperature) are prescribed for the whole duration of the simulation. These operating conditions can remain constant or change over time. Finally, an initial condition is calculated for a given set of operating conditions, from the steady-state model, before running the transient algorithm.

An iterative scheme is used to move forward in time and solve the transient equations, as shown in Fig. 63, for a prescribed convergence criterion. At each iteration, the time step ( $\Delta t$ ) is calculated based on the CFL (Courant–Friedrichs–Lewy) stability condition, as given in Eq. (95). This constraint implies that the time step should be smaller than the time required for fluid to go through the smallest fluid cell. This condition is critical for the stability of an explicit solution. The velocity values from the previous time step ( $i-1$ ) are used in this calculation.

$$\Delta t_{explicit} = C \min_{1 < m < n} \left( \frac{L}{u} \right)_m, \quad C \leq 1 \quad (95)$$

where  $C$  is the Courant number and is set to 0.5 in this model. The transient model uses an implicit discretization scheme to solve the differential equations; thus, the time step can be larger than  $\Delta t_{explicit}$ . However, when large time steps were used, the solution becomes unstable specially as the two-phase/liquid interface moves inside the condenser or liquid line. It is well known that an implicit method can face instabilities when solving the nonlinear equations, where the time derivatives are high. In this case, the model uses CFL condition as a reference to set the time step. For smaller time derivatives, a time-step multiplier ( $\omega_{time}$ ) is introduced to increase the time step value and reduce the computational time.  $\omega_{time}$  can be set by the user as an input.

The implicit method uses the Backward (BWD) Euler scheme as shown in Eq. (96). The BWD Euler term replaces the time derivative of the fluid properties in the governing equations. Then, the equation could be solved implicitly since the only unknown parameters are the fluid properties at the current time step ( $i$ ).

$$\frac{d\varphi^i}{dt} = \frac{\varphi^i - \varphi^{i-1}}{\Delta t} \quad (96)$$

In the case of the solid cells, the energy conservation equations are solved using the analytical methods as the temperature of the adjacent fluid cell is known. More explanation will be provided later in the related sub-algorithm sections.

As shown in Fig. 63, the transient code obtains the LHP conditions at the current time step. In the following time step, the code recalls the properties of all the cells at the previous time step ( $i-1$ ) as the initial condition to solve the governing equations at the current time step. In addition, the convective heat transfer coefficients are calculated using the properties at the previous time step ( $i-1$ ) to reduce the computational time in obtaining the interface temperature ( $T_{int}$ ). Finally, to determine  $T_{int}$ , the code solves the governing equations for the entire discretized model using an iterative scheme. Then, all the obtained properties are recorded. The simulations show that obtaining the heat transfer coefficients outside the  $T_{int}$  iteration loop (based on the previous time step) has an effect of less than  $10^{-4}$  °C on calculating  $T_{int}$  in comparison to obtaining the heat transfer coefficients inside  $T_{int}$  iteration loop. Calculating the heat transfer coefficient outside the iteration loop instead of inside the iteration loop reduces the computational time by a factor of two.

### 5.2.1 Algorithm for $T_{int}$ iteration

Figure 64 describes the iterative process of obtaining  $T_{int}$ . In the first step, initial guesses are introduced for the interface and reservoir temperatures in addition to  $\dot{Q}_{wick,cond}$  from Eqs. (97) to (99). The time-derivative multiplier ( $\omega_{int}$ ) of the interface temperature in Eq.(97) is a transient input parameter ranging from zero to one. Selecting a low-value for the time-derivative multiplier results in a more stable liquid/two-phase interface position; however, this requires a longer computational time.

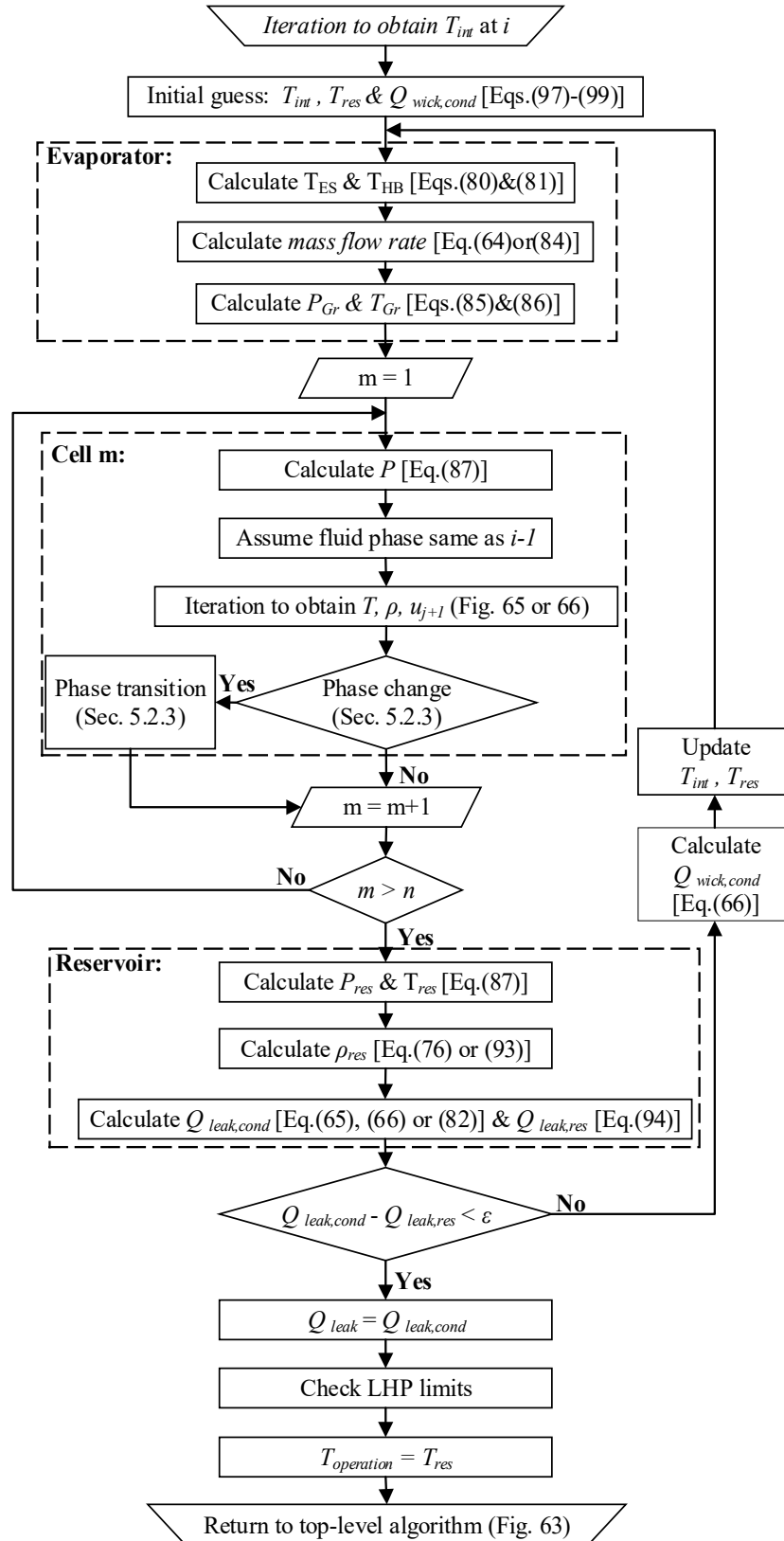


Fig. 64  $T_{int}$  iterative algorithm of the transient model.

$$T_{int,guess} = T_{int}^{i-1} + \omega_{int} \frac{dT_{int}^{i-1}}{dt_{int}} \Delta t \quad (97)$$

$$T_{res,guess} = T_{int}^{i-1} \quad (98)$$

$$\dot{Q}_{wick,cond,guess} = \dot{Q}_{wick,cond}^{i-1} \quad (99)$$

In Fig. 64, the evaporator block contains three steps. First, the temperatures of the heater block and evaporator saddle are calculated using analytical solutions for Eqs. (62) and (63), respectively. Second, the mass flow rate ( $\dot{m}$ ) is obtained using Eq. (64) if WM-1 or WM-2 is selected and Eq. (84) if EM-3 is selected. Lastly, the vapor groove equation is solved in the step three. The groove pressure is assumed to be equal to the saturated pressure at the interface temperature. Then, the groove equations, Eqs. (85) and (86), are solved to obtain the temperature and velocity at the grooves. It should be noted that the fluid in the grooves is allowed to be at the superheated state. The calculated pressure, temperature and velocity of the grooves are set as the upstream condition to obtain the fluid properties in the vapor line.

The “cell m” block of Fig. 64 consists of four steps to solve the cells in the transportation lines and condenser. First, the pressure at the fluid cell “m” is obtained by applying the momentum equation, Eq. (87), at its upstream junction “j”. Second, it is assumed that the fluid cell at the current time step has the same phase as the previous time step. Third, depending on the fluid phase, an iterative algorithm is executed to obtain the fluid properties and the temperature of the adjacent solid cell(s). Fourth, the calculated fluid properties are checked to detect whether a phase change takes place in the cell. If there is a phase change, a separate algorithm is used to deal with the transition from the old phase to the new one. The iterative algorithm for the phase change detection and phase transition process will be explained later in this chapter. These four steps are executed cell-by-cell until the last cell in the liquid line. Then, the conservation equations are solved for the reservoir.

The reservoir block in Fig. 64 contains the required steps to close the whole loop for a given time step. The assumptions for solving the reservoir were previously explained in the mathematical model section. In the first step, the pressure and temperature of the reservoir are obtained. In the second step, if RM-1 is selected, the time derivative of the density is calculated from Eq. (93) and the density is obtained from the BWD Euler formula. In the case of RM-2, the density is calculated from Eq. (76), and its time derivative is again obtained from the BWD Euler method. The last step uses the energy equation of the reservoir to calculate the heat leak ( $\dot{Q}_{leak,res}$ ). As explained previously, the heat leak is also calculated from the wick equations ( $\dot{Q}_{leak,cond}$ ) based on the selected method to solve the wick. WM-1 and WM-2 use Eq.(65) and Eq.(82) to obtain the heat leak value, respectively; whereas, Method 3 uses Eq.(66) by replacing  $(T_{int} - T_{wick})$  with  $(T_{wick} - T_{res})$ .

As shown in Fig. 64, the difference between the calculated heat leaks from the reservoir energy and wick equations is used to check the convergence of the  $T_{int}$  loop. If the heat leak difference is less than a chosen convergence criterion ( $\epsilon_{int}$ ), the resulting  $T_{res}$  represents the operating temperature of the LHP at the current time step. Otherwise, the heat leak difference is used to update  $T_{int}$ . Also, the heat transfer by conduction via wick ( $\dot{Q}_{wick,cond}$ ) and reservoir temperature are updated from the previous iteration. Then, the code uses the updated values to perform another iteration until the convergence criterion is met. The convergence criterion is one of the parameters that the user can change in the model settings. The final step in Fig. 64 is to check the LHP operation limits introduced in Section 4.2 for the steady-state model.

## 5.2.2 Algorithm for cell iteration

The iteration step of the “cell m” introduced in Fig. 64 is required to obtain the fluid properties and solid temperature(s) of any part in the transportation lines and condenser. The algorithm of this iteration step varies based on the assumed phase for the fluid. In other words, the algorithm differs for a single-phase fluid cell in comparison to the algorithm of a two-phase one. The following subsections describe the algorithms for each of the fluid phases.

### 5.2.2.1 Single-phase algorithm

The single-phase algorithm, as shown in Fig. 65, considers a subcooled liquid or superheated vapor. In the first step, the saturated temperature is obtained from the calculated pressure. This value is used to determine if the cell fluid changes from a single-phase state to a two-phase one. Then, the fluid temperature of the previous time step is considered as an initial guess for the temperature of the fluid at the current time step. At this point, an iterative procedure is implemented on the temperature of the fluid cell until its energy equation, Eq. (89), is satisfied.

First, as shown in Fig. 65, the fluid density and internal energy are obtained using REFPROP as the pressure and temperature are known. Second, the time derivative of all the fluid properties (except pressure) is calculated using the BWD Euler formula introduced in Eq. (96). Third, the left-hand side (LHS) of the energy equation is calculated as all the properties are known. In addition, the velocity at the downstream junction ( $j+1$ ) is calculated via the mass conservation, Eq.(88). Forth, the temperature of the solid cell(s) is calculated by analytically solving the energy equation as previously described. For cells in the vapor or liquid line, only the pipe wall temperature is calculated through solving Eq. (90). Otherwise, the temperature of the condenser saddle and riser are obtained from Eqs. (91) and (92), simultaneously. Fifth, the right-hand side (RHS) of the fluid energy equation is calculated as all the variables are obtained.

Finally, as shown in Fig. 65, the iterations are continued until a set convergence criterion ( $\epsilon_{cell}$ ) is satisfied. Then, the calculated values are recorded for the solid and fluid cells at the current time step. Otherwise, a function that uses the calculated difference between the RHS and LHS terms is called to update the fluid temperature. Then, the steps of the iteration are repeated using the new values until the convergence criterion is met.

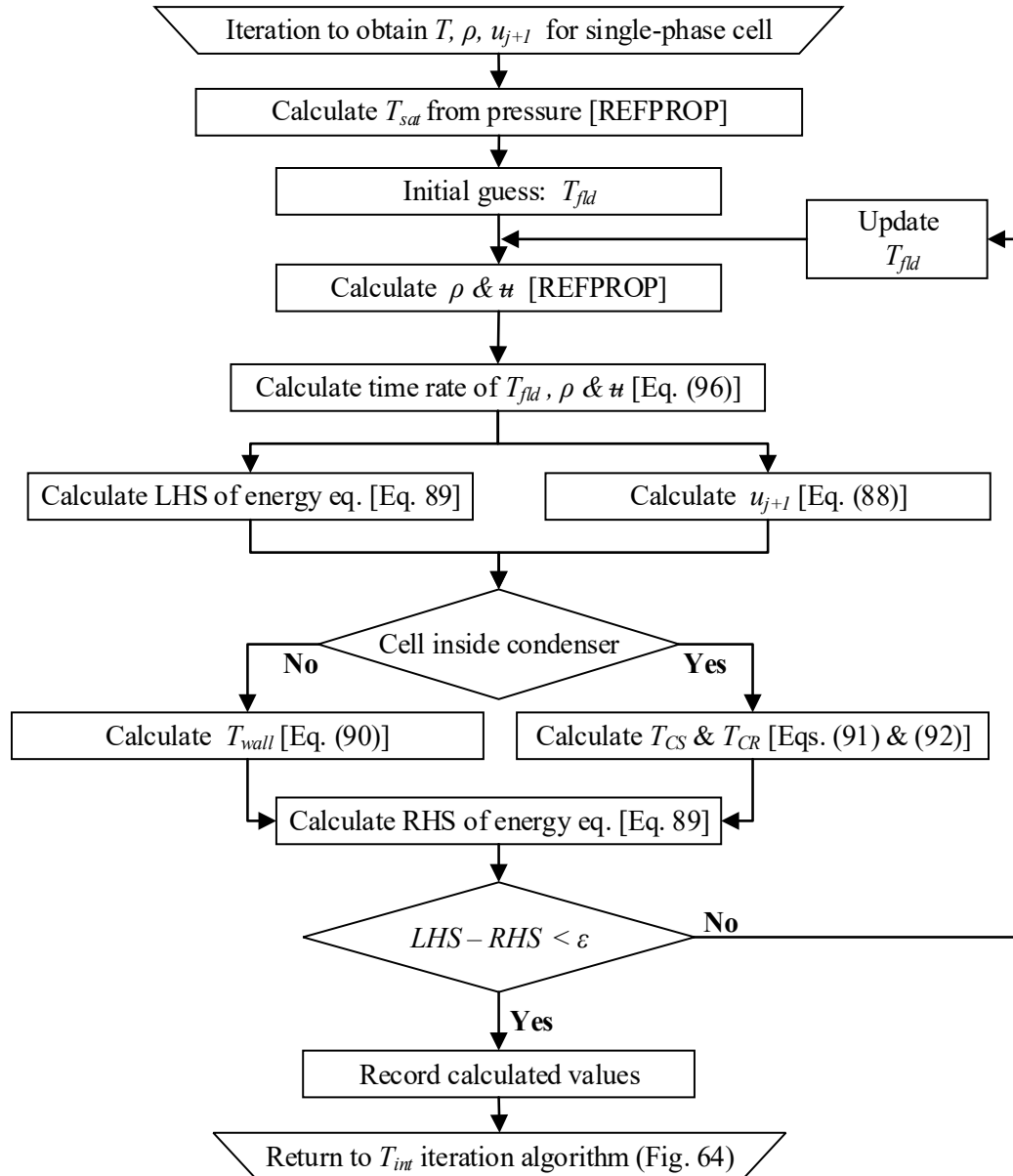


Fig. 65 Cell iterative algorithm of the single-phase fluid.

### 5.2.2.2 Two-phase algorithm

Figure 66 presents the algorithm for solving the two-phase fluid cell. This algorithm is similar to the single-phase one. However, the order of steps is different, and the vapor quality ( $X_{fld}$ ) is used as the iteration parameter instead of the fluid temperature. The algorithm is also valid for the saturated liquid and vapor.

The fluid temperature is calculated from the pressure as the temperature is only a function of the pressure for the two-phase state. Then, the wall temperature(s) are obtained via solving the solid energy equations as the fluid temperature is known and remains constant during the iterative

process while the vapor quality varies. At this point, the two-phase iteration is initiated by choosing the vapor quality of the previous time step as the initial guess.

In the first step of the iteration in Fig. 66, the fluid properties, consisting of density and internal energy, are calculated as the temperature and vapor quality are known. Second, the time derivatives required in the LHS of the energy and continuity equations are determined from the BWD Euler scheme. Third, the LHS of the energy equation is calculated, and the velocity of the downstream junction ( $j+1$ ) is obtained. Forth, the RHS of the energy equation is calculated. The final step of the solution is the same as the single-phase one as explained above.

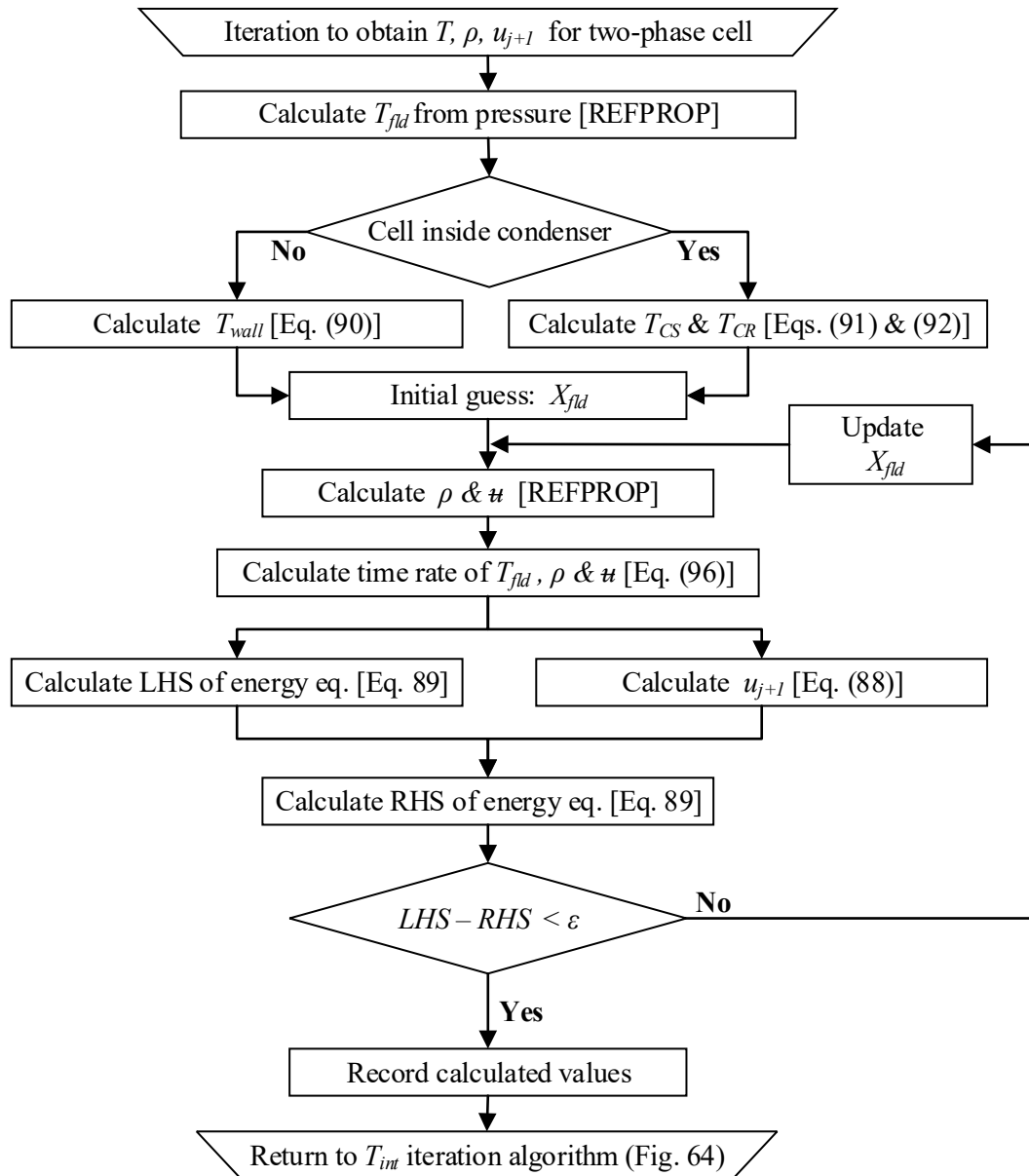


Fig. 66 Cell iterative algorithm of the two-phase fluid.

### 5.2.3 Phase change identification and transition

The phase of the fluid needs to be checked after obtaining its properties through the iterative process. The identification criterion varies depending on the current phase of the fluid, as explained in Table 13 in Section 4.2. In the case of the two-phase cell, the calculated vapor quality out of acceptable range determines the existence of a phase change. For a subcooled liquid or superheated vapor cell, the comparison between the calculated fluid temperature and the corresponding saturated temperature is used to check the phase change.

A procedure is required to deal with a change of fluid phase in a given cell if it takes place. The main challenge in the procedure is the transition from the previous phase to the new phase in a given time step. Three different approaches to this problem are considered: saturated fluid, time division and sink/source. These approaches are then implemented to recalculate the energy and mass conservation equations when the phase change occurs.

The saturated fluid approach considers the cell, where a phase change takes place, as a saturated one in the current time step. This method, as summarized in Fig. 67, provides an estimated state because the energy and mass gained or lost by the cell via condensation or evaporation after reaching saturation are not considered.

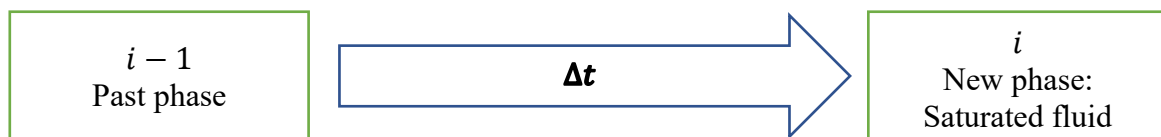


Fig. 67 Saturated fluid approach to a phase change.

The time-division approach splits the time step into a past phase and a new phase. Figure 68 illustrates the central concept behind the time-division technique. The duration of the past phase is determined as the amount of time it takes to go from the past phase to the saturation state. For instance, the duration is equal to the time needed for the vapor quality to decrease from the past value to zero in a two-phase to liquid phase change. Then, the saturation state is marked as an intermediate step to recall the iterative process of the new phase for the remaining time in the time step.

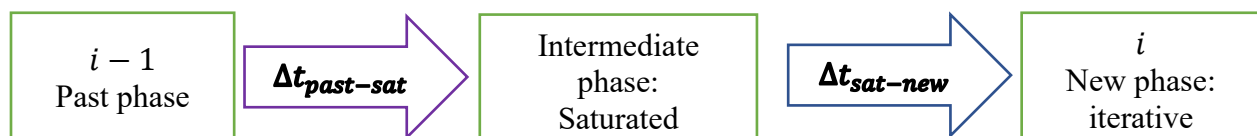


Fig. 68 Time-division approach to a phase change.

Equations (100) and (101) provide the mathematical method to calculate the duration of the past-phase and the new-phase inside the time step, respectively. The  $\varphi$  parameter is replaced by the vapor quality if the fluid changes phase from a two-phase state to a single-phase one. Similarly,

the fluid temperature is used as  $\varphi$  when transitioning from a single-phase state to a two-phase one. The time-derivative of  $\varphi$  in Eq. (100) is obtained from the current time step before a phase change detected through Eq. (96).

$$\Delta t_{past-sat} = \frac{\varphi_{sat} - \varphi^{i-1}}{\frac{d\varphi^i}{dt}} \quad (100)$$

$$\Delta t_{sat-new} = \Delta t - \Delta t_{past-sat} \quad (101)$$

The sink/source approach uses the iterative process of the new phase during the current time step. It introduces sink/source terms at the LHS of the mass and energy equations to compensate for the energy or mass changes from the past fluid state to a saturated state. Figure 69 summarizes how the sink/source technique deals with a phase change.

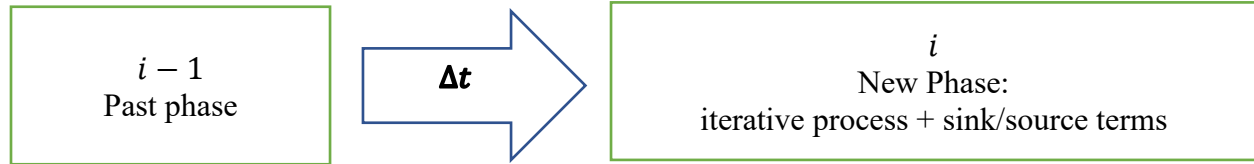


Fig. 69 Sink/source approach to a phase change.

The sink/source terms are derived from expanding the time derivatives in the LHS of the governing equations, as shown in Eq. (102). The obtained mass and energy terms are presented in Eqs. (103) and (104), respectively. These terms are representing the change of energy and mass in a cell from the previous state to a saturated one.

$$\frac{d\varphi}{dt} = \frac{(\varphi_{new} - \varphi_{sat}) + (\varphi_{sat} - \varphi_{past})}{\Delta t} \quad (102)$$

$$mass\ term = V \frac{\rho_{sat} - \rho_{past}}{\Delta t} \quad (103)$$

$$energy\ term = V \frac{(\rho u)_{sat} - (\rho u)_{past}}{\Delta t} \quad (104)$$

The sink/source terms are added to the LHS of the energy and mass equations in the iterative process to solve the new phase. The time derivatives of the properties in the new phase iteration are just calculated from the saturated state to a new state.

Each term can be a source or sink depending on the phase-change. For example, the mass term, Eq. (30), behaves as a sink when the fluid changes from the liquid state to a two-phase state since the mass term, added to the LHS of the continuity equation, has a negative value. From a physical point of view, the fluid cell loses mass for a given cell when going from a subcooled state to a two-

phase state. In contrast, the mass term is a source in case of a phase change from the two-phase to subcooled liquid as the term is added to the LHS of the continuity equation. Table 19 summarizes the actions required for the different approaches in the case of each possible phase change.

Table 19 Summary of approaches to phase transition.

Type	Saturated Approach (PTM-1)	Time-division approach (PTM-2) $\Delta t_{sat-new} = \Delta t - \Delta t_{past-sat}$	Sink/Source approach (PTM-3) [Eqs. (103) and (104) ]
Two-phase ↓ Liquid	$\varphi_{new} = \varphi_{sat,liq}$	$\Delta t_{past-sat} = \frac{0 - X_{past}}{\frac{dX}{dt}}$	Mass: source term  Energy: sink term
Two-phase ↓ Vapor	$\varphi_{new} = \varphi_{sat,vap}$	$\Delta t_{past-sat} = \frac{1 - X_{past}}{\frac{dX}{dt}}$	Mass: sink term  Energy: source term
Liquid ↓ Two-phase	$\varphi_{new} = \varphi_{sat,liq}$	$\Delta t_{past-sat} = \frac{T_{sat} - T_{past}}{\frac{dT}{dt}}$	Mass: sink term  Energy: source term
Vapor ↓ Two-phase	$\varphi_{new} = \varphi_{sat,vap}$	$\Delta t_{past-sat} = \frac{T_{sat} - T_{past}}{\frac{dT}{dt}}$	Mass: source term  Energy: sink term

The phase transition approaches summarized in Table 19 are compared through simulation of a transient scenario where a phase change occurs from a liquid to a two-phase state. Each approach has unique behavior during the transition. However, the results at the end of the simulation are almost identical because of the small time steps used in the calculations. It is also observed that the simulation stability can be affected by choice of the phase change approach. The saturated approach has been the most stable option of the three in addition to requiring less computational time.

The time-division and source/sink methods are more representative of the phase change process; however, they are computationally more demanding than the saturated fluid approach. Although the saturated-fluid method approximates the phase transition, its results are in good agreement with other methods for the small time steps. Thus, the saturated fluid approach is used in the simulations to minimize computational time and instability.

### 5.3 Model validation

Experimental results of LHP1 and LHP2 are utilized under the ambient environment to validate the transient model. The detail information about the test apparatus and plans is provided in Chapter 2. In addition, obtaining the numerical results for the test condition requires specifying the model settings. The model settings comprise of the modelling options and parameters necessary to run the transient simulation. Some of these parameters are introduced to ensure the convergence and stability of the numerical method.

#### 5.3.1 Modelling options

Modelling options are alternative approaches that give the users the capability to simulate the LHP operation (modelling of evaporator wick and reservoir, and phase transition) in different and physically valid approaches. These approaches have already been explained in the solution procedure section above. The chosen methods for the simulations and the rationale are explained here.

The evaporator wick can be modelled in three different ways, as summarized in Table 18. For the model validation, Method 3 is chosen since it represents the wick behavior more realistically by taking into account the transient terms in calculating the mass flow rate. As previously explained, the mass flow rate in the many early works was calculated from the steady-state relation which is not realistic.

The two different approaches of the reservoir modelling stem from the method of calculating the fluid density. The density can be calculated either from the continuity equation or from the fluid charge. For validation purposes, the fluid charge approach is selected as it represents an actual physical constraint, i.e. the fixed amount of fluid mass in the LHP.

The phase transition can be approached from three different ways as mentioned in Table 19. As it was shown earlier, the preliminary simulations show that the choice of the approach only affects the simulation time and stability. Therefore, the saturated approach is utilized in model validation. Table 20 recaps the modelling approaches used in the validation of the transient model.

Table 20 Summary of the selected approaches in transient model validation.

Modelling topic	Chosen approach	Rationale
Evaporator wick	WM-3 (one cell with inertia)	$\dot{m}$ calculated from a transient equation
Reservoir	RM-2 (fluid charge)	Real constraint in the LHP physics
Phase transition	PTM-1 (saturated)	Lower computational time and better stability

#### 5.3.2 Model parameters

As it was demonstrated in the steady-state model, there are three main accommodation parameters: the thermal contact conductance from the condenser plate to the sink plate ( $h_c$ ), the contact conductance between the evaporator saddle and wick ( $h_{ES,wick}$ ), and the multiplier for natural heat transfer coefficient ( $\alpha$ ) from the LHP components to ambient. The effects of these three parameters

on the results were discussed in detail in Section 4.4. These parameters are matched by using the experimental results obtained at a reference setting with a sink temperature of 5°C. Table 14 summarizes the value of these parameters for the transient model.

Table 21 Model parameters for LHP1 and LHP2.

Parameter	LHP1	LHP2
$h_c$	2,950 W/m <sup>2</sup> K	610 W/m <sup>2</sup> K
$h_{ES,wick}$	12,000 W/m <sup>2</sup> K	7,400 W/m <sup>2</sup> K
$\alpha$	0.825	1.1
Cell length in the vapor line	10 cm	40 cm
Cell length in the condenser	5 cm	5 cm
Cell length in the liquid line	10 cm	10 cm

For the presented solutions, the cell length is set to 10 cm for the vapor and liquid lines, and 5 cm in the condenser for LHP1 as shown in Table 14. These lengths result in 8 cells each for the vapor and liquid lines and 20 cells for the condenser. For LHP2, the cell length for the vapor and liquid lines is 40 cm and 10 cm, respectively. The condenser cell length is set to 5 cm. With these lengths, there are 5 cells for the vapor line, 12 cells for the liquid line and 24 cells for the condenser. A grid sensitivity analysis is presented later.

### 5.3.3 Numerical convergence criteria

Some parameters in the model settings deal with the iteration criteria. They are required to implement the iterative algorithms explained in the previous section. First, the cell convergence criterion ( $\varepsilon_{cell}$ ) is defined to obtain the cell properties using the iterative algorithms introduced in Fig. 65 and Fig. 66.

Second, the  $T_{int}$  convergence criterion ( $\varepsilon_{int}$ ) is used to find the operating temperature from the algorithm presented in Fig. 64. Both convergence criteria are set to  $10^{-4}$  W in validating the model. The results show that the absolute accuracy of the target parameters ( $T_{cell}$ ,  $X_{cell}$ , and  $T_{int}$ ) is below  $10^{-4}$  when the iterative algorithms meet the set of convergence criteria.

Third, the time-derivative multiplier ( $\omega_{int}$ ) of the interface temperature, introduced in the  $T_{int}$  algorithm, is used to calculate the initial guess for  $T_{int}$  at each time step from Eq. (97).  $\omega_{int}$  only affects computational time and convergence of the  $T_{int}$  iteration. Different values of  $\omega_{int}$  are chosen for each LHP.

Fourth, the time multiplier ( $\omega_{time}$ ) and explicit time step ( $\Delta t_{explicit}$ ) are introduced in the top-level algorithm. The purpose of the former parameter is to reduce the computational time, and the latter one is used to ensure the stability of the results when the sharp changes occur in a given time step. The optimum value for  $\omega_{time}$  is found to be 30 to minimize the computational time while maintaining the stability and accuracy of the results.  $\Delta t_{explicit}$  is obtained at each time step from

Eq. (95). Implementing these two parameters requires several criteria, as explained below, to identify sharp changes and smoothen them.

- A time-derivative limit ( $\dot{T}_{limit}$ ) is introduced, as given in Eq. (105), to obtain the value of each time step in the top-level algorithm. In other words, the time multiplier is used in calculating the time step if the time derivative of the interface temperature is below the limit. The limit value is determined for the simulations of each LHP by a trial and error process.

$$\Delta t^i = \begin{cases} 0.9 \Delta t_{explicit}^i & \dot{T}_{int}^{i-1} \geq \dot{T}_{limit} \\ \omega_{time} \Delta t_{explicit}^i & \dot{T}_{int}^{i-1} < \dot{T}_{limit} \end{cases} \quad (105)$$

- A maximum iteration number ( $n_{max}$ ) for the  $T_{int}$  algorithm is defined to change the time step as presented in Eq. (106). This criterion controls the time step when the algorithm cannot obtain the operating temperature in  $n_{max}$  iterations. In this case, the simulation moves  $\Delta i_{back,loop}$  steps backward in time and then marches forward with the minimum time-step value for  $\Delta i_{forward,loop}$  steps. The model can resolve occasional divergences, attributed to large time steps, by implementing this criterion.

$$\Delta t^a = \begin{cases} 0.9 \Delta t_{explicit} & n \geq n_{max} & a \in [i - \Delta i_{back,loop}, i + \Delta i_{forward,loop}] \\ \omega_{time} \Delta t_{explicit} & n < n_{max} & a = i \end{cases} \quad (106)$$

Table 22 summarizes the criteria to ensure the convergence and stability of the model with the minimum computational time. The parameters with no exact value in Table 22 are determined in each LHP scenario to optimize the numerical convergence.

Table 22 Summary of the parameters for the convergence and stability of the model.

Symbol	Assigned value
$\epsilon_{cell}$	$10^{-4}$ W
$\epsilon_{int}$	$10^{-4}$ W
$\omega_{int}$	Simulation dependent $\in [0,1]$
$\omega_{time}$	30
$\Delta t_{explicit}$	Eq. (95)
$\dot{T}_{limit}$	Simulation dependent
$n_{max}$	Simulation dependent
$\Delta i_{back,loop}$	Simulation dependent
$\Delta i_{forward,loop}$	Simulation dependent

### 5.3.4 Model validation for LHP1

Figure 70 represents a comparison of the experimental and calculated LHP temperatures as a function of the time. The reservoir, evaporator saddle, sink and ambient temperatures together with the applied power are shown in this figure. Both of the sink and ambient temperatures are varied less than  $1.2^{\circ}\text{C}$  during the test. The sink and ambient temperature profiles from the tests are introduced as an input to the numerical simulations for better accuracy.

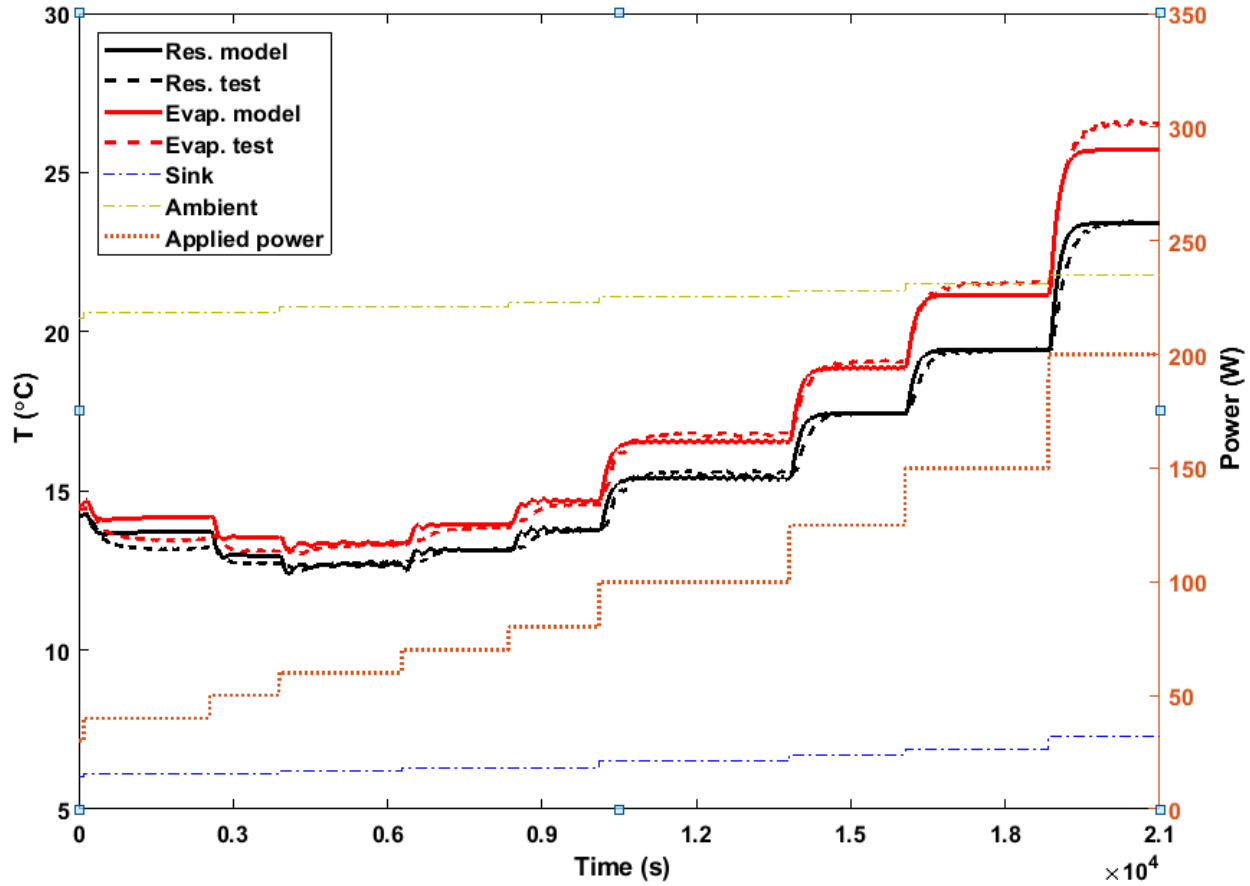


Fig. 70 Comparison of the experimental and calculated temperatures for LHP1 at  $5^{\circ}\text{C}$  sink temperature.

The model results plotted in Fig. 70 are obtained by setting the simulation parameters to the values provided in Table 23. Note that these parameters do not affect the final numerical results. They either optimize the computational time or improve the numerical convergence.

Table 23 The simulation-dependent parameters for the LHP1 validation.

Symbol	Assigned value
$\omega_{int}$	0.5
$\dot{T}_{limit}$	0.005
$n_{max}$	300
$\Delta i_{back,loop}$	2
$\Delta i_{forward,loop}$	35

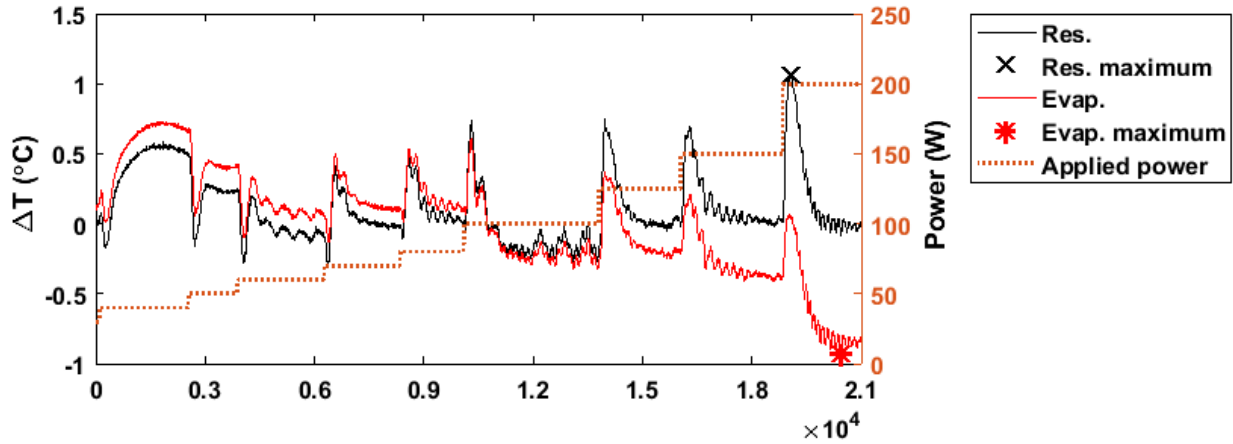
Three performance variables are defined for the model validation: the temperature difference during transients, the difference in steady state temperatures and time lag.

The first variable represents the difference in the temperature between the experimental and model results. Its absolute and relative values are respectively calculated from Eqs. (107) and (108) for the reservoir and evaporator saddle and represented in Fig. 71.

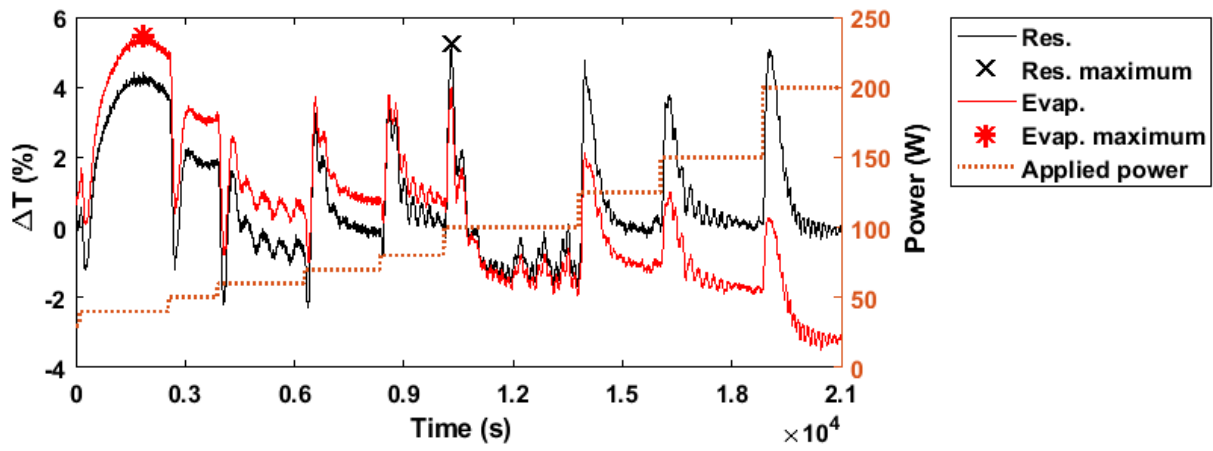
In the case of the reservoir, the absolute temperature difference is in the range of -0.3 to 1.0°C with an average of 0.2°C. The maximum difference of 1.0°C is observed during the transition from 150 to 200 W, where the model responds faster to the power change than the experiment. The relative temperature difference of the reservoir varies from -2.3 to 5.2% during the simulated time interval, with an average of 1.2%. The relative difference reaches its maximum of 5.2% when the applied power changes from 80 to 100 W, and this is different from the location of the maximum absolute difference.

$$\Delta T_{absolute} = T_{model} - T_{experiment} \quad (107)$$

$$\Delta T_{relative} = \frac{\Delta T_{absolute}}{T_{experiment}} * 100 \quad (108)$$



(a)



(b)

Fig. 71 Temperature difference between the experimental and calculated results for LHP1: (a) absolute and (b) relative.

For the evaporator results as shown in Fig. 71, the absolute temperature difference is in the range of  $-0.9$  to  $0.7^{\circ}\text{C}$  with an average of  $0.3^{\circ}\text{C}$ . The absolute difference has a pick value of  $-0.9^{\circ}\text{C}$  when the LHP1 reaches steady state at  $200\text{ W}$ . The absolute difference decreases after the maximum point as the temperature oscillations in the experimental fades. The relative difference of the evaporator temperatures varies from  $-3.5$  to  $5.4\%$  during the simulated time interval with an average of  $1.6\%$ . The maximum relative difference of  $5.4\%$  is observed during the steady-state region of  $40\text{ W}$ . The temperature-difference lines of the reservoir and evaporator follow the same trend in Fig. 71, even though their maximum values occur in different locations.

The second performance variable is the temperature difference at the steady state between the experimental and model results at each applied power. The steady-state temperatures both for the reservoir and evaporator saddle together with the temperature differences, extracted from the transient data, are presented in Fig. 72. For the reservoir, the steady-state temperature obtained

from the model closely follows the experimental trends except for 40 and 50 W. The absolute and relative deviations have an average of  $0.1^{\circ}\text{C}$  and  $0.9\%$ , respectively. The maximum difference is detected at 40 W with an absolute value of  $0.5^{\circ}\text{C}$  and a relative value of  $4\%$ .

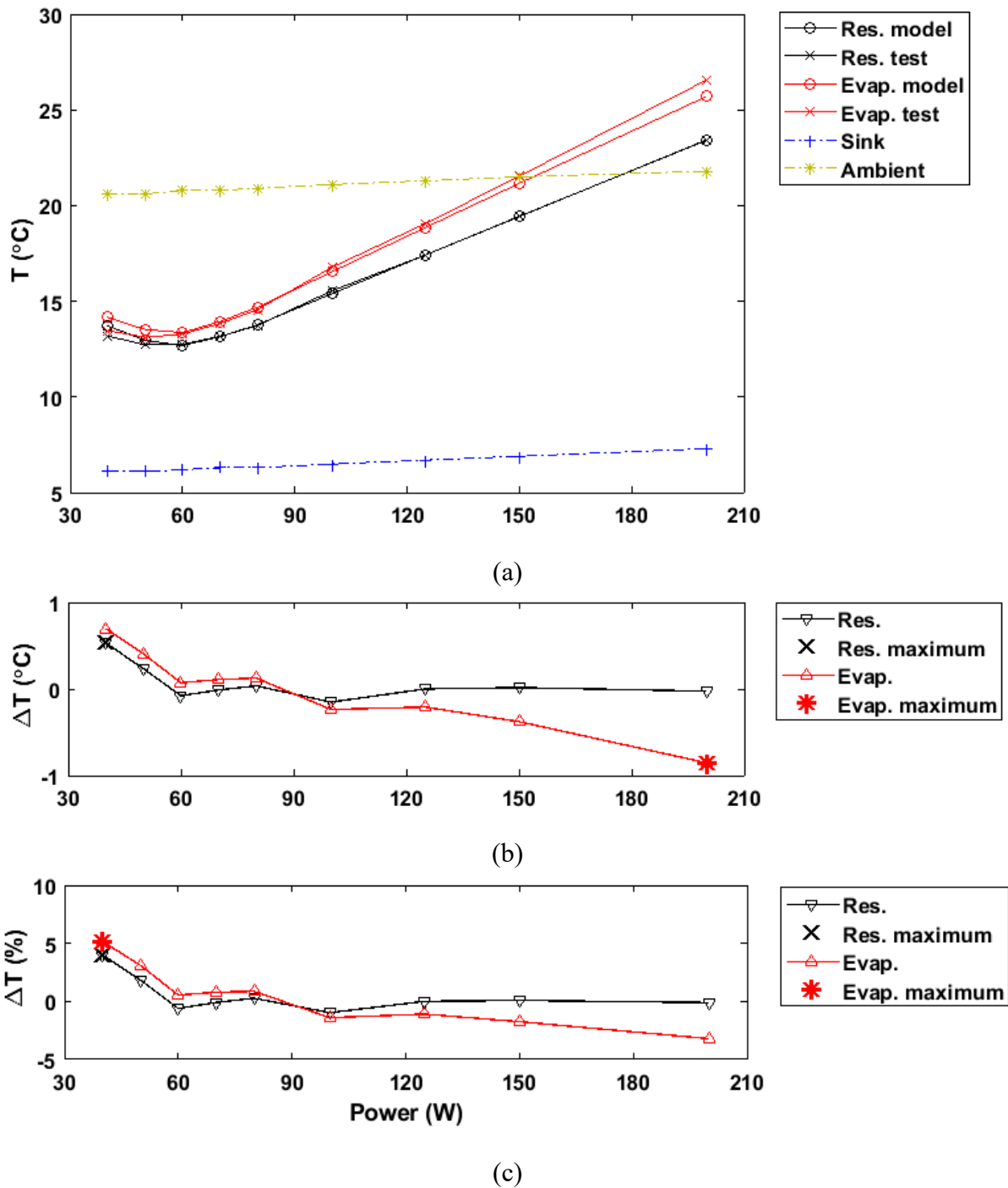


Fig. 72 Steady-state temperatures from the experimental and calculated results for LHP1: (a) value (b) absolute difference and (c) relative difference.

As shown in Fig. 72, the evaporator steady-state temperature obtained from the model follows the experimental trends. The absolute and relative temperature differences have an average of  $0.3^{\circ}\text{C}$  and  $2.0\%$ , respectively. The maximum absolute difference is detected at  $200\text{ W}$  with a value of  $-0.9^{\circ}\text{C}$ , and the relative difference has its maximum of  $5.2\%$  at  $40\text{ W}$  even though its absolute difference is  $0.7^{\circ}\text{C}$ .

The third and final performance variable is the difference in the time lag between the test and model results. The time lag is defined as the time required to go from one steady state to another when the LHP operating condition is changed. Figure 73 provides the time lag values for each power change and its difference between the experimental and numerical results. The time lag at each power level is extracted from the transient data by calculating the time elapsed from the applied-power change to the time when the temperature varies within  $\pm 0.1^{\circ}\text{C}$  of the final steady-state value. The time lag difference is calculated in the forms of absolute and relative values from Eqs. (109) and (110), respectively.

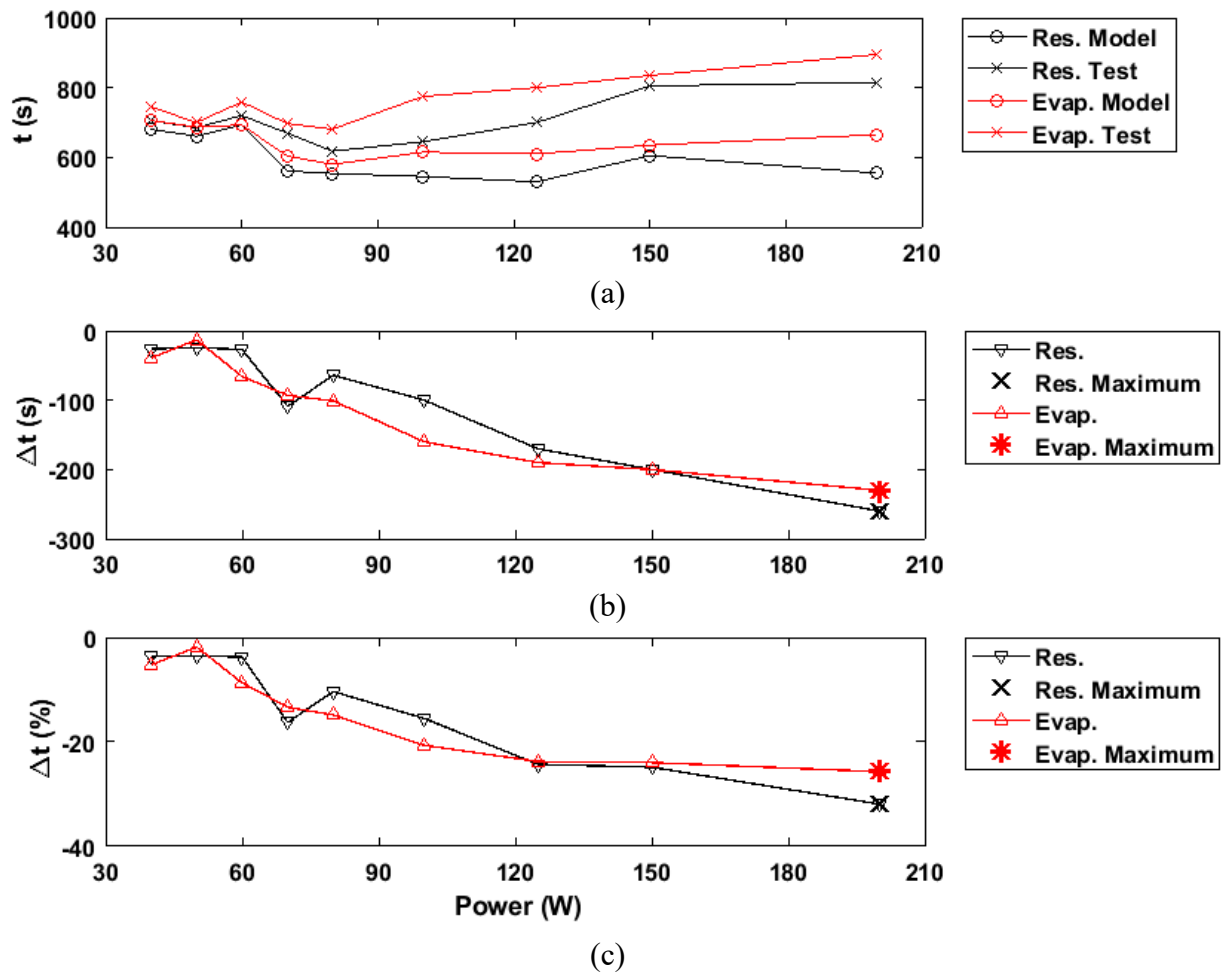


Fig. 73 Time lag from the experimental and calculated results for LHP1: (a) value (b) absolute difference and (c) relative difference.

$$\Delta t_{absolute} = t_{model} - t_{experiment} \quad (109)$$

$$\Delta t_{relative} = \frac{\Delta t_{absolute}}{t_{experiment}} * 100 \quad (110)$$

As shown in Fig. 73, the time lag has a higher value for the evaporator saddle than that for the reservoir because of the additional thermal inertia of the evaporator saddle. In the variable conductance mode (VCM) from 40 to 60 W, the time lag is around 700 s. As the LHP starts operating in the fixed conductance mode (FCM), the time lag first drops and then rises with the applied power.

Figure 73 also shows that the model underestimates the time lag. The calculated time lag is within 10% of the experimental values in the VCM. Then, the time lag difference increases with the applied power. The reservoir time lag difference increases with a steeper slope than the evaporator one, resulting in a higher time lag difference for the reservoir at 200 W. For the reservoir time lag, the absolute and relative differences have an average of -109 s and 14.9%, respectively. The maximum difference is detected at 200 W with an absolute value of 260 s and a relative value of 31.9%. In the case of the evaporator, the time lag difference generally follows the reservoir trend with an average difference of -121 s and 15.3%. The maximum difference, with an absolute value of -230 s and a relative value of -25.7%, is observed at the applied power of 200 W.

Note that in the previously published numerical models, the time lag was discussed only qualitatively (e.g. [4], [87] and [89]). It can easily be observed that the time lag error presented in these works is more significant than the results presented here. However, there was no comparison possibility because of the lack of published quantitative data.

In addition to the performance variables, a qualitative investigation is also performed to discuss the transient temperature response characteristics. As shown in Fig. 70, a small shallow temperature dip is observed at 40 W. This dip is recovered quicker in the model than in the experiment because of a 0.2°C increase in the ambient temperature. The operating temperature is highly dependent on the heat exchange with the ambient in the VCM. In other words, the LHP would reach a lower operating temperature if the ambient increase did not occur.

At 60 W, the temperature lines dip after the power change with higher magnitude in the model than in the experimental results. The dip is most likely due to the sudden rush of the subcooled liquid from the condenser to the reservoir as the mass flow rate increases, and the interface is pushed further into the condenser. The interface movement brings a high-amplitude (0.1°C), low-frequency oscillation in the steady-state region. This oscillation however is not observed in the experimental results.

Figure 70 shows a similar dip in the reservoir lines as the power is changed to 70 W. The temperature increases as soon as the power changes. A step change appears as the reservoir temperature reaches its minimum value resulting in more heat transfer from the evaporator saddle to the wick. The model transient response is in the form of the oscillation, which is completely damped as the steady state is reached. The oscillation is due to the fact that the two-phase/liquid interface is very close to the condenser exit. The 80-W dynamic response is similar to the 70-W one except for no dips in the temperature lines. The temperature oscillations at 80 W in the model results take a longer time to stabilize than that required for 70 W.

The temperature oscillations are observed for the temperature lines at 100 W. The calculated temperatures have a lower amplitude and a higher frequency in comparison to the experimental results. This difference may indicate that the interface movement in the numerical model (approximately 5 cm) has a shorter stroke than that in the experimental results at the condenser exit. Also, no dip is observed at the power change since the interface is close to the condenser exit, and no subcooled liquid is rushed to the reservoir.

Finally, the calculated evaporator saddle temperature at 150 and 200 W, in Fig. 70, closely follows the experimental one, but reaches a different steady-state plateau. In the case of the reservoir, the model responds faster than the experiment, but it reaches the same steady-state temperatures as the experiment.

The experimental results show low amplitude and high frequency oscillations. These oscillations are observed in the model lines as well. These oscillations are related to the location of the two-phase/liquid interface as explained in Section 2.7.2. The model predicts that the interface location approaches the condenser exit at a lower power than that occurred in the experiment. This prediction is most likely a result of the complex geometry of the condenser and underprediction of the friction factor inside the condenser.

The predictive value of the mathematical model is assessed by comparing the model results to the experimental values at a different sink temperature of 10°C from the reference sink temperature of 5°C, for which the accommodation coefficients were determined. Figure 74 represents the comparison of the experimental and calculated temperatures for the evaporator saddle and reservoir for a sink temperature of 10°C. The model results follow the trend of the experimental ones. The last power change from 200 to 175 W shows that the model can predict the transient behavior not only in power-up scenarios but also in power-down scenarios.

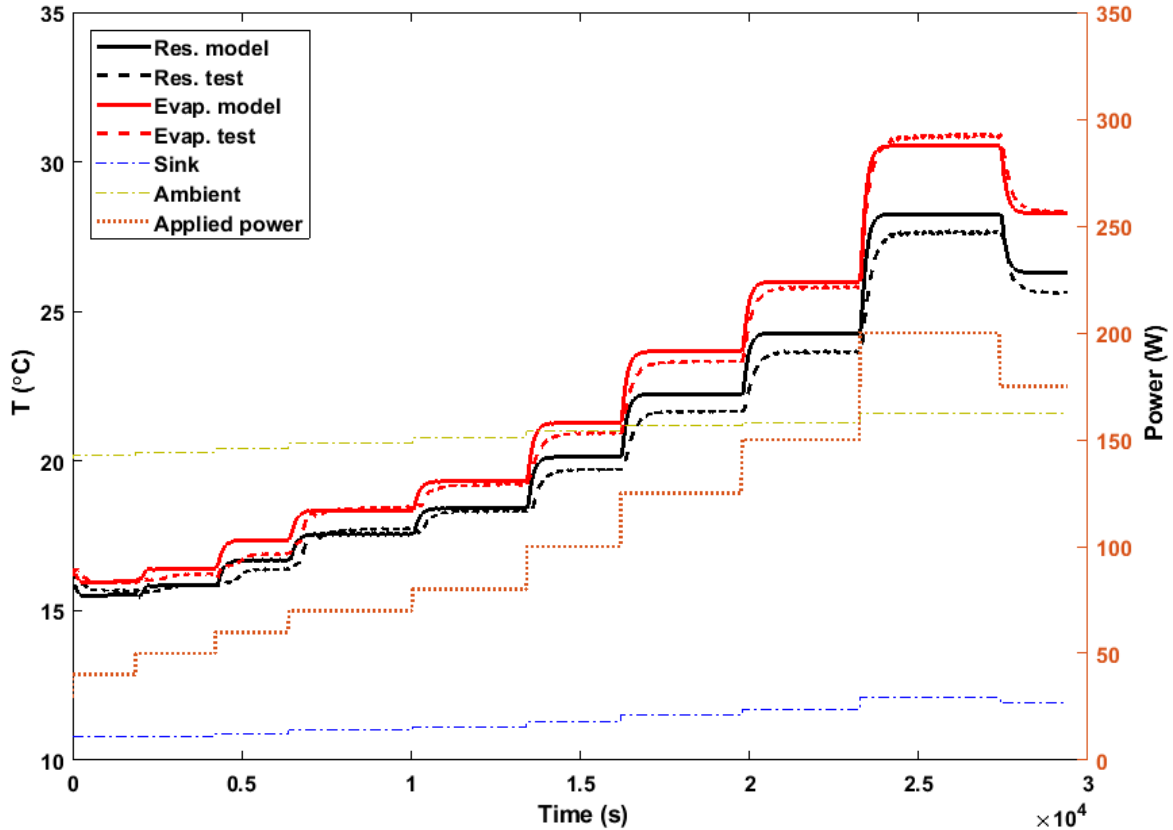


Fig. 74 Comparison of the experimental and calculated temperatures for LHP1 at 10°C sink temperature.

Table 24 summarizes the average and maximum differences in the performance variables, which are introduced previously. The temperature difference of the reservoir is higher for the warmer sink, but their relative averages are still in an acceptable range of less than 2.5%. On the other hand, the evaporator deviations are slightly improved, and their relative averages drop below 1.5%. In the case of the time lag, a warmer sink temperature increases the difference from a relative average of 15% to 26%.

Table 24 Comparison of the experimental and numerical results for the performance variables for LHP1.

Performance Variable	Component	Reservoir				Evaporator Saddle			
		Average		Maximum		Average		Maximum	
	Sink (°C)	5	10	5	10	5	10	5	10
Transient temperature	Abs. (°C)	0.2	0.6	1.0	1.6	0.3	0.3	-0.9	0.9
	Rel. (%)	1.2	2.4	5.2	6.4	1.6	1.3	-5.4	5.2
Steady-state temperature	Abs. (°C)	0.1	0.4	0.5	0.7	0.3	0.2	-0.9	0.5
	Rel. (%)	0.9	1.7	4.0	2.7	2.0	1.0	5.2	2.7
Time lag	Abs. (s)	-109	-210	-200	-300	-121	-229	-230	-310
	Rel. (%)	-14.9	-26.6	-31.9	-38.5	-15.3	-26.2	-25.7	-38.3

The prediction capability of the model is further investigated using a sink cycling experiment instead of a power cycling one. Figure 75 presents the experimental and calculated temperatures during the sink cycling experiment when the applied power is set to 70 W. The sink temperature is increased from 5 to 20°C with 5°C steps. Then, it is decreased with the same step. The ambient temperature remains in the temperature interval of [20.3 21.3]°C. The model predictions follow a similar trend as the experimental results. The small overshoots, occurring experimentally during the sink temperature decrease, are not observed in the model results. These overshoots are increased as the sink temperature is decreased. They are a result of the temporary reduction of subcooling to the reservoir. The decrease in the sink temperature results in the receding of the two-phase/liquid interface inside the condenser as the heat is dissipated to the sink more efficiently. Then, the mass flow rate in the liquid line is temporarily reduced, and the flow is reversed. Thus, the amount of subcooled liquid entering the reservoir is now much less, resulting in the temperature overshoot. The overshoots disappear as the mass flow rate in the liquid line recovers, and more subcooled liquid enters the reservoir.

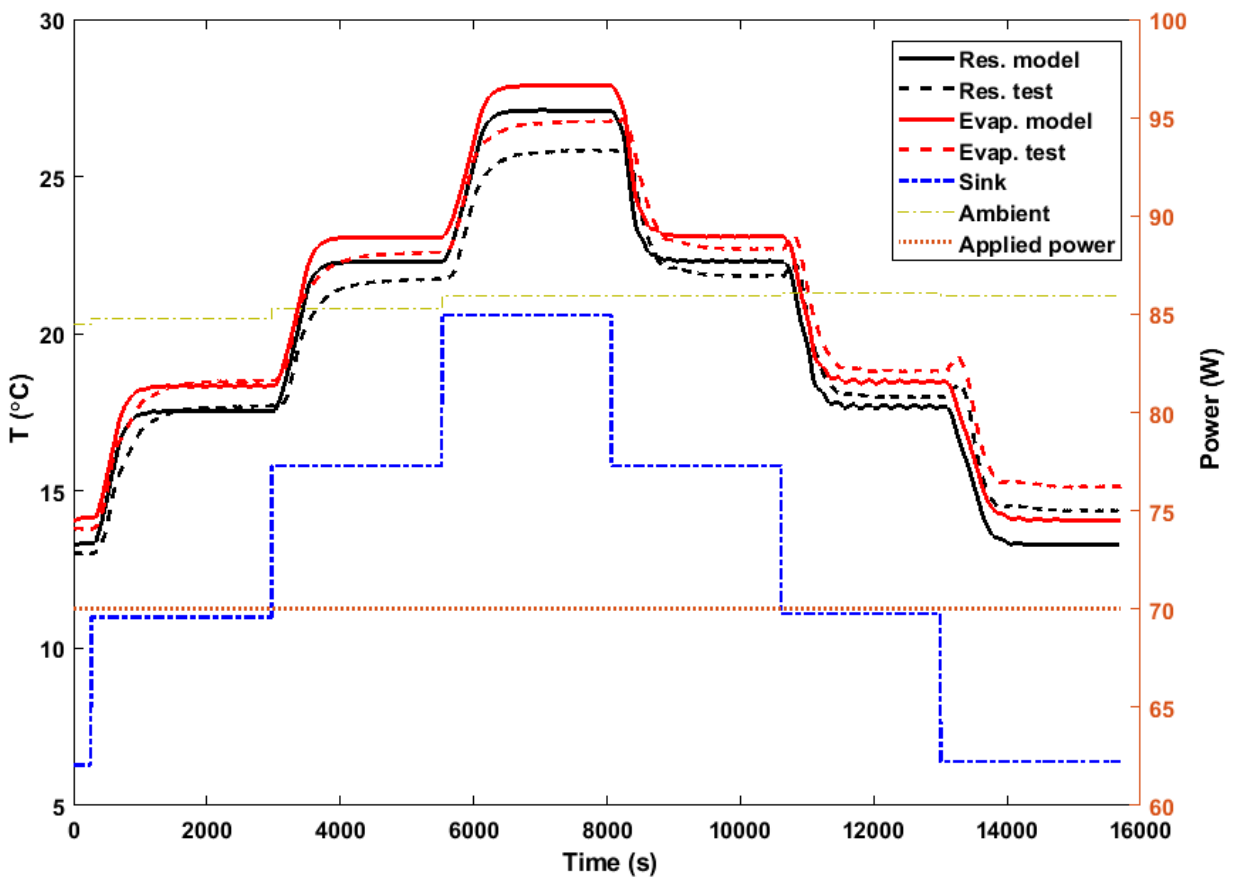


Fig. 75 Comparison of the experimental and calculated temperatures for LHP1 during the sink cycling.

The experimental overshoots are successfully simulated by the model when the sink temperature is reduced using a sudden step instead of a linearly varying transition time obtained from the experimental results. The calculated magnitudes are however higher than experimental values, and it takes less time for the overshoot to be damped.

Table 25 provides the average and maximum values of the difference in the performance variables between the experimental and calculated results for the LHP1 sink cycling. The absolute averages of the temperature difference are nearly the same for the reservoir and evaporator saddle. The relative averages are in the acceptable range of less than 4%. The time lag difference also follows the same trend with the relative average of 16.5% for the reservoir and evaporator saddle. Furthermore, the model prediction capability is compared between the sink cycling and the power cycling scenarios using data provided in Table 15 and Table 25, respectively. The temperature values are predicted more accurately in the power cycling scenario as the sink temperature (10°C) is closer to the reference sink temperature of 5°C.

Table 25 Comparison of the experimental and numerical results for the performance variables for LHP1 sink cycling.

Performance Variable	Component	Reservoir		Evaporator Saddle	
		Average	Maximum	Average	Maximum
Transient temperature	Abs. (°C)	0.7	-2.0	0.7	-1.9
	Rel. (%)	3.9	-11.3	3.3	-10.2
Steady-state temperature	Abs. (°C)	0.6	1.3	0.6	1.1
	Rel. (%)	3.2	4.9	3.0	-7.0
Time lag	Abs. (s)	218	-397	229	-445
	Rel. (%)	16.5	-27.5	16.5	-29.3

### 5.3.5 Model validation for LHP2

The model validation is only performed when the LHP2 PRV is fully open, and it does not control the LHP operation. The operating temperature remains between 29 to 31°C below 150 W due to the active PRV control at the sink temperature of 5°C. The operating temperature exceeds its maximum value of 65°C, set by the manufacturer when the applied power is above 325 W at the same sink temperature. Therefore, the results are presented for an applied power range of 150 W to 325 W. Figure 76 presents the comparison of the reservoir and evaporator saddle temperatures obtained from the experiment and simulation during a power cycling test at the sink temperature of 5°C. The sink and ambient temperatures are varied within 0.5 and 1.1°C, respectively.

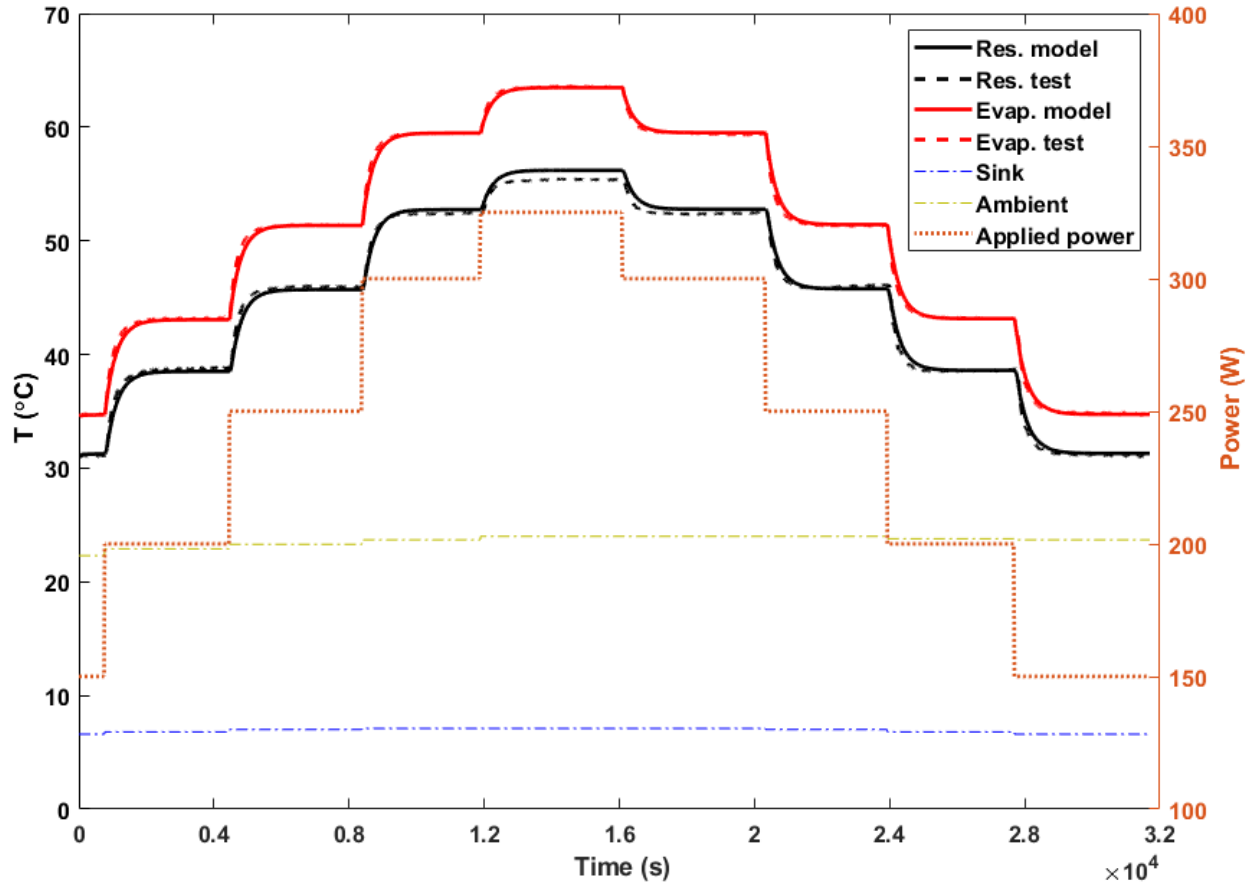


Fig. 76 Comparison of the experimental and calculated temperatures for LHP2 at 5°C sink temperature.

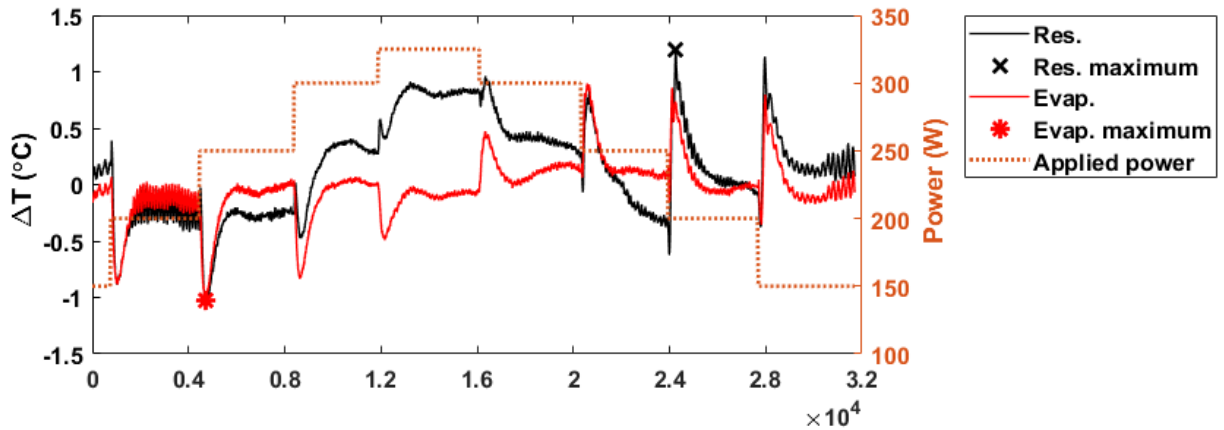
To ensure numerical convergence and optimize the computational time, the following simulation parameters are used as shown in Table 26.

Table 26 The simulation parameters for the LHP2 validation.

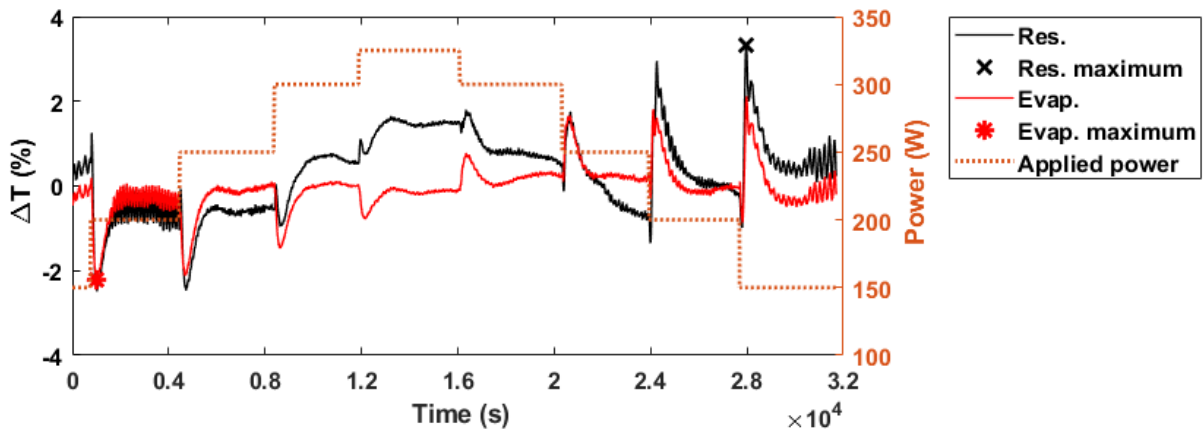
Symbol	Assigned value
$\omega_{int}$	0.25
$\dot{T}_{limit}$	0.1
$n_{max}$	300
$\Delta i_{back,loop}$	2
$\Delta i_{forward,loop}$	35

Figure 77 represents the temperature differences between the experimental and model results calculated from Eqs. (107) and (108) in the form of absolute and relative values. The absolute difference in temperature for the reservoir is in the range of [-1.0 1.2]°C, with an average of 0.4°C.

The maximum deviation of  $1.2^{\circ}\text{C}$  occurs at the transition from 300 to 250 W. The relative temperature difference for the reservoir varies from -2.4 to 3.3% during the simulation time and has an average of 0.8%. The relative difference reaches its maximum of 3.3% when the applied power changes from 200 to 150 W, which is different from the location of the maximum absolute difference.



(a)



(b)

Fig. 77 Temperature difference between the experimental and calculated results for LHP2: (a) absolute and (b) relative.

Regarding the evaporator saddle temperatures in Fig. 77, the absolute temperature difference is in the range of  $-1.0$  to  $0.9^{\circ}\text{C}$  with an average of  $0.2^{\circ}\text{C}$ . The absolute difference has a pick of  $-1.0^{\circ}\text{C}$  when the applied power changes from 200 to 250 W. Also, the relative difference in the temperatures varies from -2.2 to 2.0% with an average of 0.4%. The maximum relative difference of -2.2% occurs at the power change from 150 to 200 W. The temperature differences for the reservoir and evaporator saddle in Fig. 77 follow the same trend except at the power transition to

325 W. In that instance, the evaporator line experiences a sudden drop, whereas the reservoir line has a sharp pick.

Figure 78 presents the steady-state temperatures and their absolute and relative differences, extracted from the transient data. At each applied power, except for 150 and 325 W, there are two different sets of curves for the power-up and power-down. These values are slightly different as the sink, and ambient temperatures vary over the test duration as mentioned earlier. The difference between the power-up and power-down values are noticeable in Fig. 78. For the reservoir, the steady-state temperature obtained from the model closely follows the experimental trends except for 325 W where the LHP is working close to its operational limit. The absolute and relative deviations have an average of  $0.3^{\circ}\text{C}$  and  $0.6\%$ , respectively. The maximum deviation is detected at 325 W with an absolute value of  $0.8^{\circ}\text{C}$  and a relative value of  $1.5\%$ .

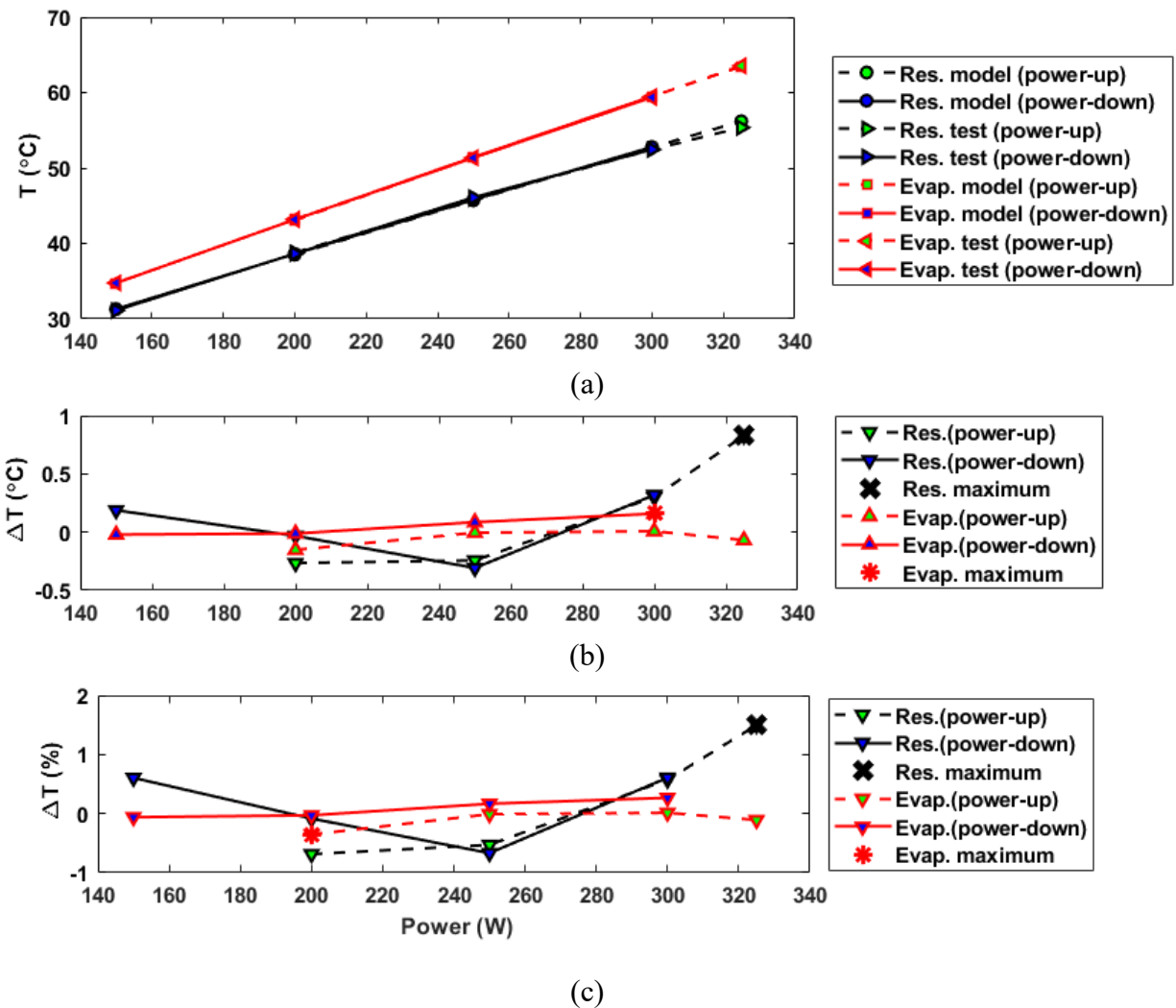


Fig. 78 Steady-state temperatures from the experimental and calculated results for LHP2: (a) value (b) absolute difference and (c) relative difference.

For the evaporator lines in Fig. 78, the calculated steady-state temperatures closely follow the experimental results. The absolute and relative differences are small, with an average of  $0.1^{\circ}\text{C}$  and  $0.1\%$ , respectively. The maximum absolute difference is detected at  $300\text{ W}$  during the power-down with a value of  $0.2^{\circ}\text{C}$ , and the maximum relative difference is  $-0.4\%$  at  $200\text{ W}$  during the power-up even though its absolute difference is smaller than that obtained at  $300\text{ W}$  during the power-down.

Finally, the time lag values are provided in Fig. 79 for each power change and its difference between the experimental and numerical values. The absolute and relative time lag differences are calculated according to Eqs. (109) and (110), respectively.

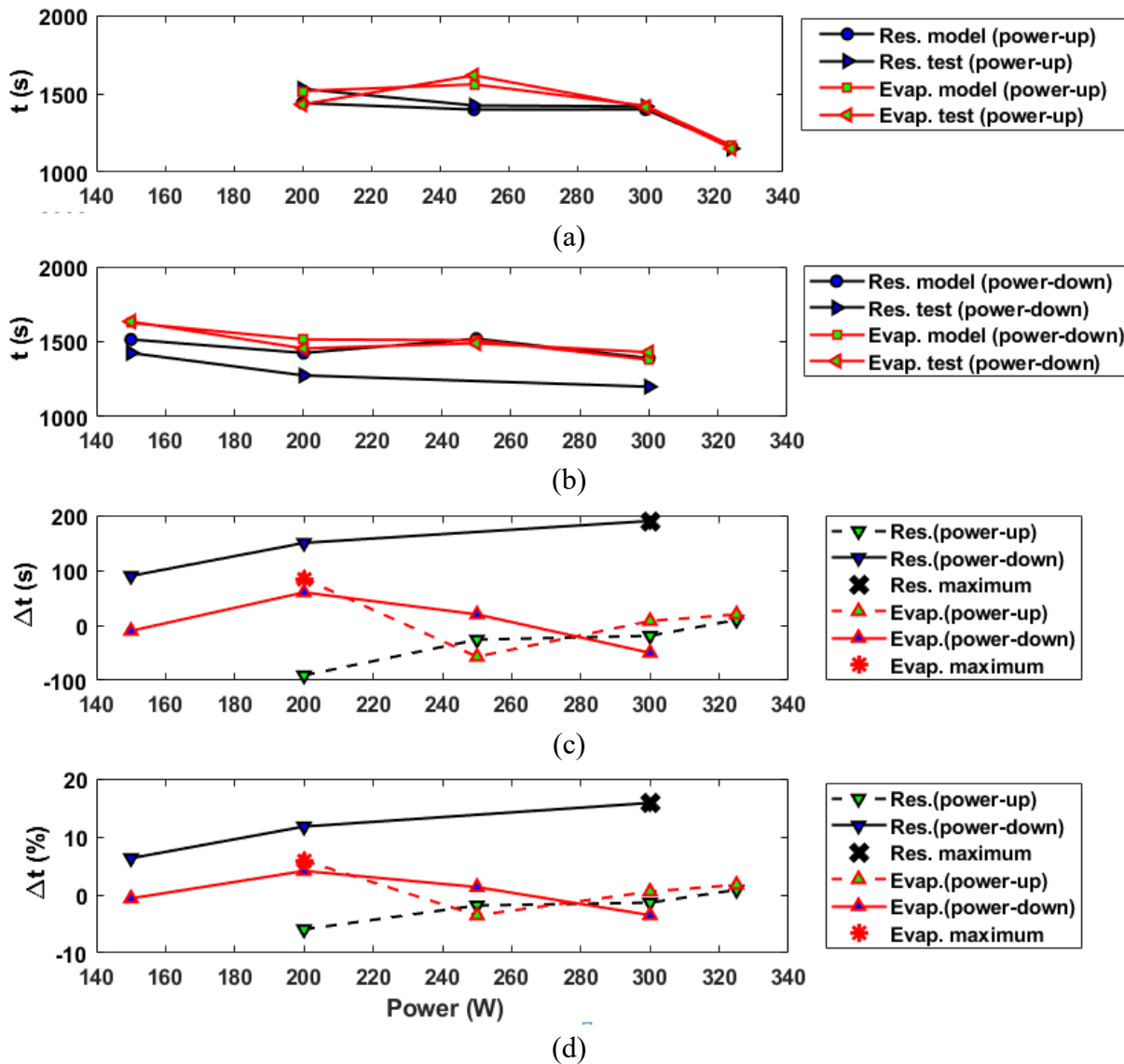


Fig. 79 Time lag from the experimental and calculated results for LHP2: (a) power-up value (b) power-down value (c) absolute difference and (d) relative difference.

The lag-time differences presented in Fig. 79 show a reasonably good agreement between the model and experiment values. For the reservoir, the model slightly underpredicts the time lag in the power-up region. On the contrary, the model prediction exceeds the experiment values in the power-down region. The absolute and relative differences have an average of 82 s and 6.3%, respectively. The maximum difference is detected at the power decrease to 300 W with the 190 s absolute value and 15.8% relative value. In the case of the evaporator, the model slightly overpredicts the time lag value with an average of 39 s and 2.7%. The maximum difference, with the absolute value of 85 s and 6.0%, is detected at the power increase to 200W.

The qualitative investigation is performed on the LHP2 temperature response shown in Fig. 76. At the applied power changes in Fig. 76, the experimental lines have a slightly steeper slope than the model lines. In the power-down section of Fig. 76, an oscillation is observed in the experimental lines at the steady-state region of 200 W. The model results closely follow their corresponding experimental results.

In the power-down section of Fig. 76, the experimental lines oscillate with low amplitude and high frequency when approaching the steady state at 200 and 150 W. These oscillations are damped in the steady-state region at 200 W. For 150 W, the oscillations are not only sustained but also excited at the steady region. It is worth to highlight the different oscillation behavior at 200 W between the power-up and power-down profiles. The power-up oscillations are sustained in contrast to the damped power-down ones. This different behavior proves that the LHP dynamic responses, mainly the oscillations, depend on the initial condition and are sensitive to the slight changes in the sink and ambient temperatures. No oscillation is observed in the model results since the two-phase/liquid interface is located at the end of the condenser or inside the liquid line for the above operating conditions. Similar to the LHP1 results, this is attributed to the underprediction of the friction factor inside the condenser.

The model predictability is evaluated by comparing the model results to the experimental obtained at the sink temperature of 10°C. The model and simulation parameters remain the same as given in Table 20 and Table 26, respectively. The comparison of the time history of the reservoir and evaporator saddle temperatures at a sink temperature of 10°C is presented in Fig. 80. The results are in a very good agreement.

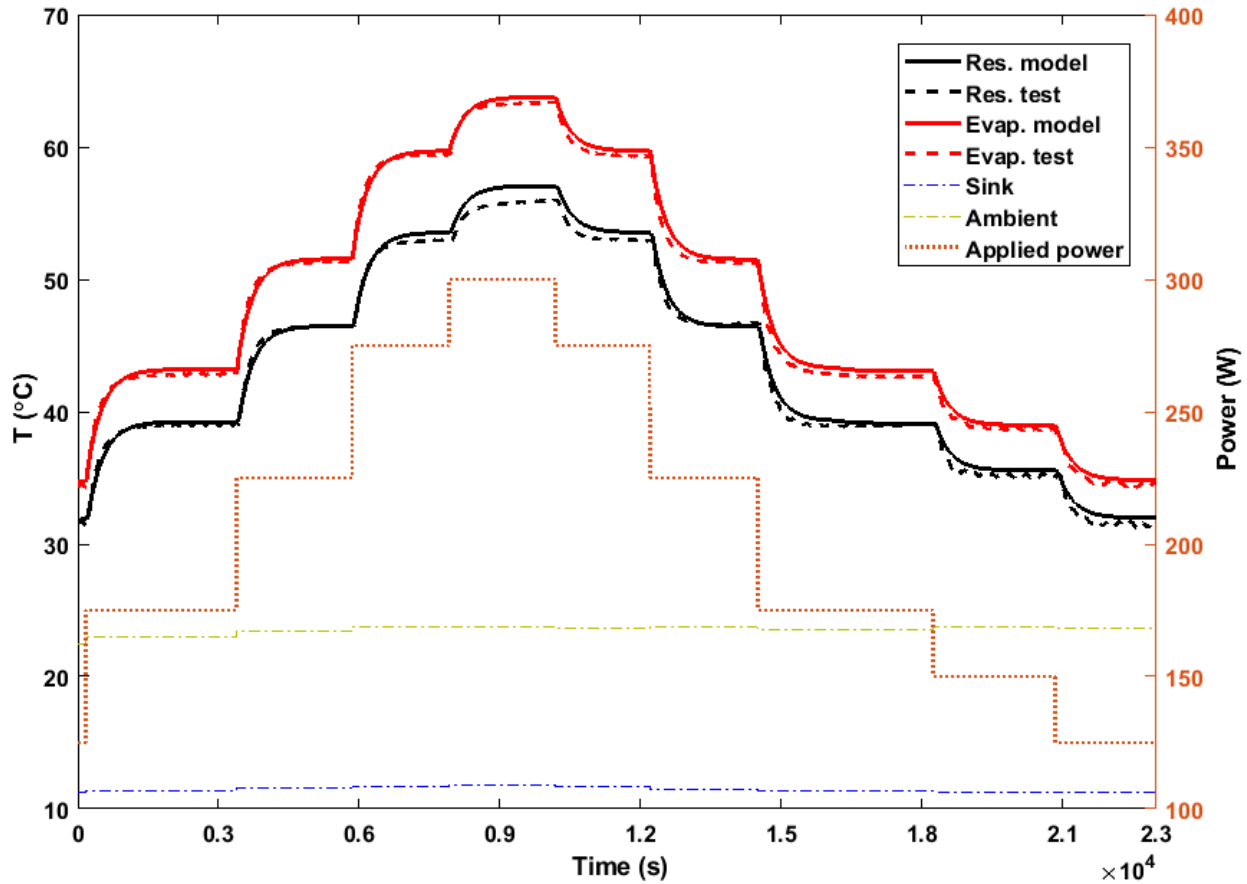


Fig. 80 Comparison of the experimental and calculated temperatures for LHP2 at 10°C sink temperature.

Table 27 summarizes the average and maximum differences for the performance variables. Their relative averages in the transient and steady-state temperatures remain below an acceptable value of 1%. For the time lag, the average relative difference is increased from 6.3% to 13.4% for the reservoir and from 2.7% to 6.4% for the evaporator saddle. The maximum time lag difference is observed in the reservoir for both of the sink temperatures considered.

Table 27 The model deviation of the performance variables from the experiment data for LHP2.

Performance Variable	Component	Reservoir				Evaporator Saddle			
		Average		Maximum		Average		Maximum	
	Sink (°C)	5	10	5	10	5	10	5	10
Transient temperature	Abs. (°C)	0.4	0.5	1.2	1.3	0.2	0.4	-1.0	1.3
	Rel. (%)	0.8	1.0	3.3	3.3	0.4	0.8	-2.4	2.8
Steady-state temperature	Abs. (°C)	0.3	0.4	0.8	1.2	0.1	0.3	0.2	0.4
	Rel. (%)	0.6	0.9	1.5	2.0	0.1	0.7	-0.4	1.1
Time lag	Abs. (s)	82	134	190	330	39	73	85	180
	Rel. (%)	6.3	13.4	15.8	36.5	2.7	6.4	6.0	17.0

Similar to LHP1, a sink-cycling experiment is also used to further investigate the model capability to predict the operation of the LHP2. Figure 81 provides the experimental and calculated temperatures for the sink cycling experiment at 200 W. The sink temperature profile follows 5-20-5°C with 5°C steps. The ambient temperature is varied in a temperature interval of [22.6 23.5]°C. The model predictions are in a very good agreement with the experimental results. Unlike the LHP1 sink cycling, no overshoot is observed in the experiments since the two-phase/liquid interface resides in the liquid line at all times.

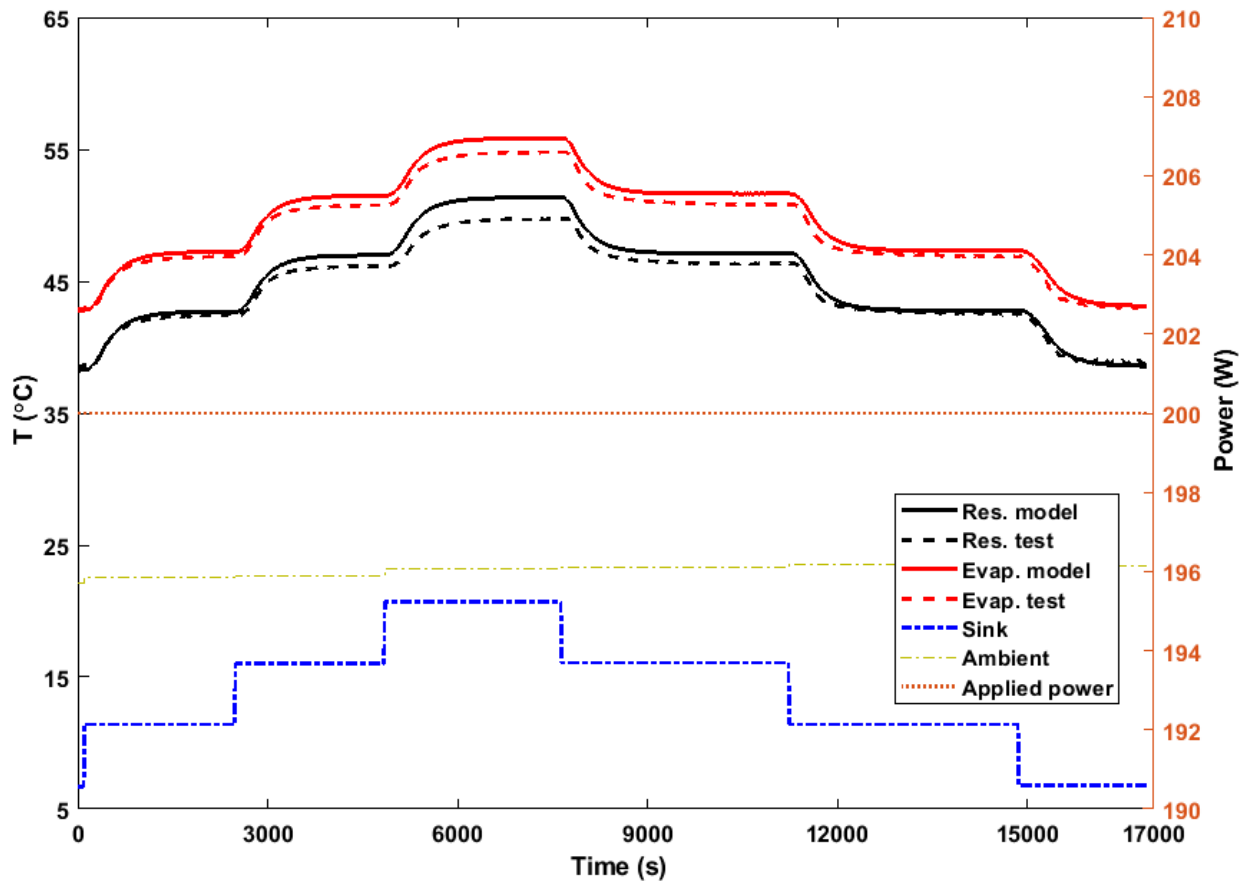


Fig. 81 Comparison of the experimental and calculated temperatures for LHP2 during the sink cycling.

Table 28 presents the average and maximum values of the difference in the performance variables between the experimental and calculated results for the LHP2 sink cycling. The relative averages are within 1.2%, and the maximum temperature differences are less than 1.7°C occurred at the sink temperature of 20°C. The time lag difference has a relative average of 4.4% for the reservoir and 4.9% for the evaporator saddle. The maximum time lag, less than 10%, occurs when the sink temperature is decreasing.

Table 28 Comparison of the experimental and numerical results for the performance variables for the LHP2 sink cycling.

Performance Variable	Component	Reservoir		Evaporator Saddle	
		Average	Maximum	Average	Maximum
Transient temperature	Abs. (°C)	0.6	1.7	0.6	1.1
	Rel. (%)	1.3	3.5	1.2	2.2
Steady-state temperature	Abs. (°C)	0.7	1.6	0.6	1.1
	Rel. (%)	1.4	3.3	1.2	2.0
Time lag	Abs. (s)	68	-140	80	-166
	Rel. (%)	4.4	-7.8	4.9	-9.7

## 5.4 Sensitivity analysis

This section deals with investigating the effects of the modelling parameters on the transient behavior of an LHP. These parameters include the thermal inertia of the heater block and condenser saddle, the contact conductance between the heater block and evaporator saddle, and the cell length used to discretize the transportation lines and condenser. A given parameter value is varied by  $\pm 10\%$ ,  $\pm 20\%$  and  $\pm 50\%$  from a reference value used in the model validation. Two main scenarios (one for each LHP) have been selected to analyze the effect of each parameter. In the LHP1 scenario, the power is changed from 70 W to 80 W with a time interval 500 s while the ambient and chiller temperatures are kept at 22 and 5°C, respectively. The LHP2 scenario is similar to that of LHP1 except that the power is changed from 200 to 150 W.

### 5.4.1 Thermal inertia of heater block

The thermal inertia ( $mc$ ) has a primary effect on the transient behavior as it dictates how fast the heat diffuses in the system. Figure 82 illustrates the effect of the thermal inertia on the operating temperature for the LHP2 scenario. The steady-state temperature is not affected as expected. However, the transient temperature is decreased by decreasing thermal inertia. Increasing the thermal inertia in the heater block decreases the time derivative of the operating temperature and increases the LHP response time to power changes. The thermal inertia acts as a damper by storing the heat in the heater block. The maximum temperature difference is 0.4°C (1%) with respect to the baseline when thermal inertia is varied within  $\pm 50\%$ . Increasing the thermal inertia by 50% results in a 5% increase in the time lag of the operating temperature. The time lag effect is nearly symmetrical as decreasing the thermal inertia by 50% results in a 5.1% reduction in the time lag. Since in an application, we would know the thermal inertia better than within 50%, the uncertainty in the thermal inertia value is not a big concern.

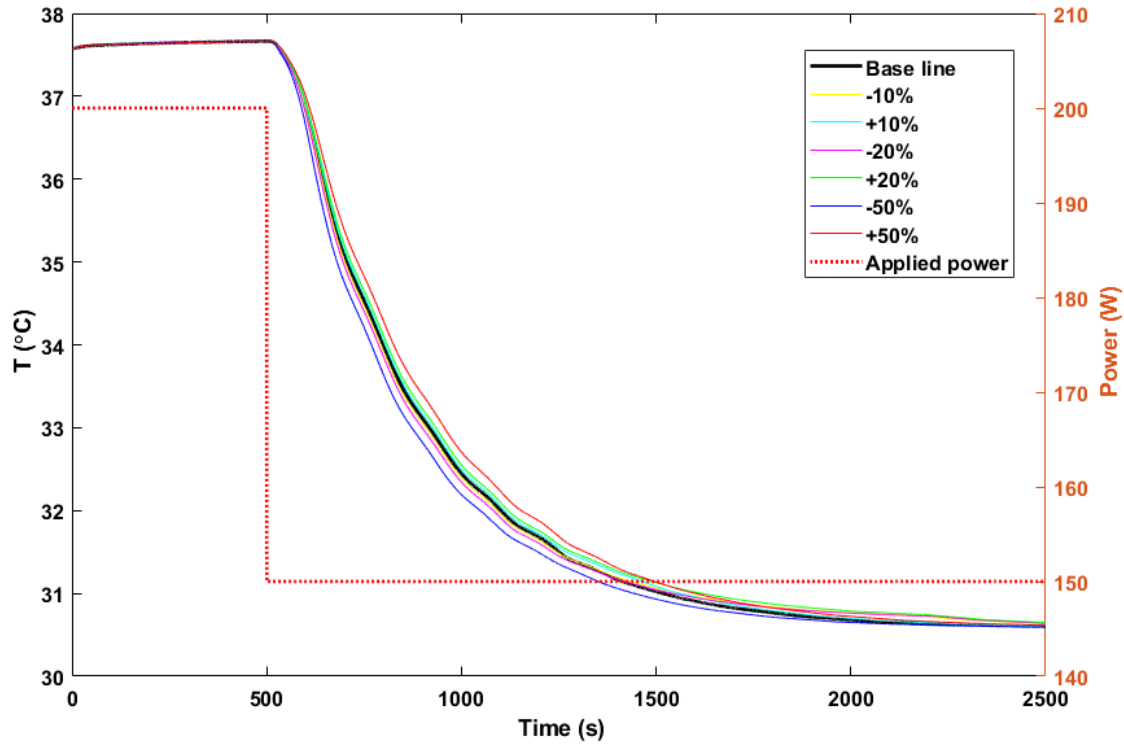


Fig. 82 Effect of the heater-block thermal inertia on the operating temperature of LHP2.

The lower time-derivative of the temperatures, mentioned earlier, contributes to a lower pick in the number of the  $T_{int}$  iterations and a smoother transition in the mass flow rate as shown in Fig. 83 and Fig. 84, respectively. Although increasing the thermal inertia reduces the pick iteration number in Fig. 83, the computational time remains similar. This similarity occurs as the simulation reaches steady state further in time and requires more iterations before reaching a steady state as shown in Fig. 83. The spike in the iteration number is caused by a sudden shift of the vapor/two-phase boundary from the middle of the vapor line to its inlet. The mass flow rate in Fig. 84 experiences less fluctuation and decreases with a slower slope as the thermal inertia increases. The higher thermal inertia reduces the fluctuations and the release rate of the heat load from the heater block to the wick.

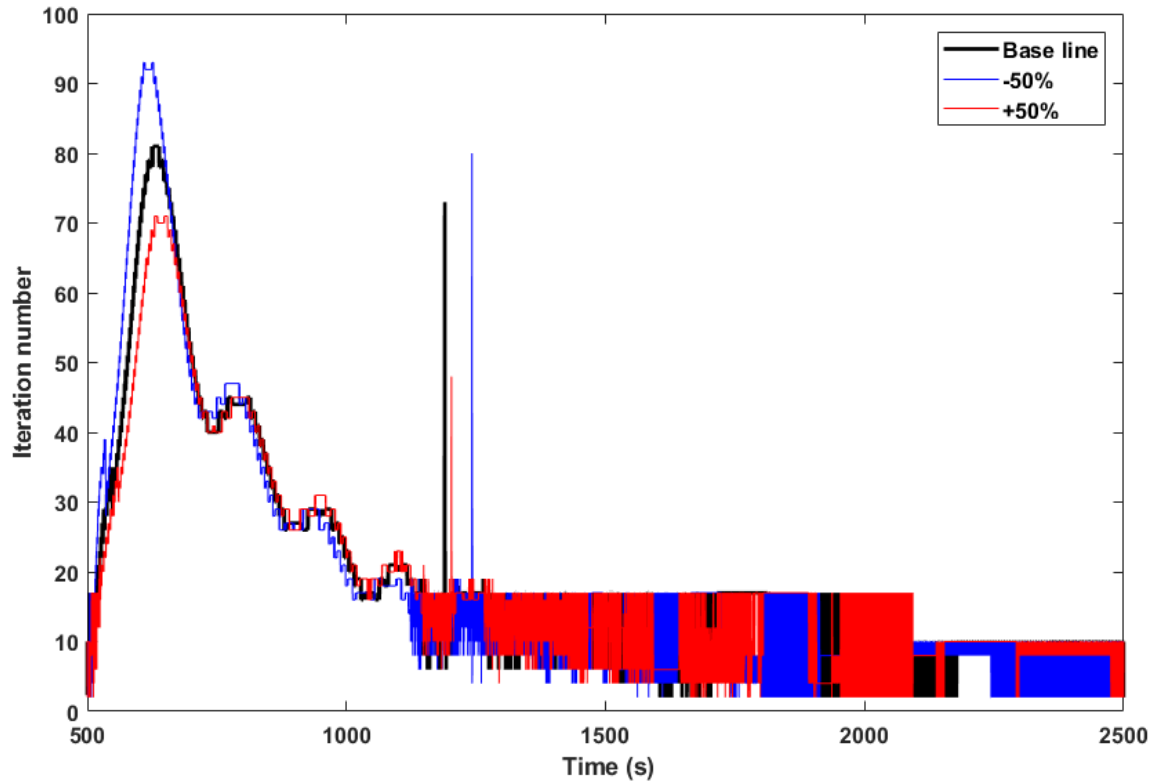


Fig. 83 Effect of the heater-block thermal inertia on the  $T_{int}$  iteration of LHP2 after the power change.

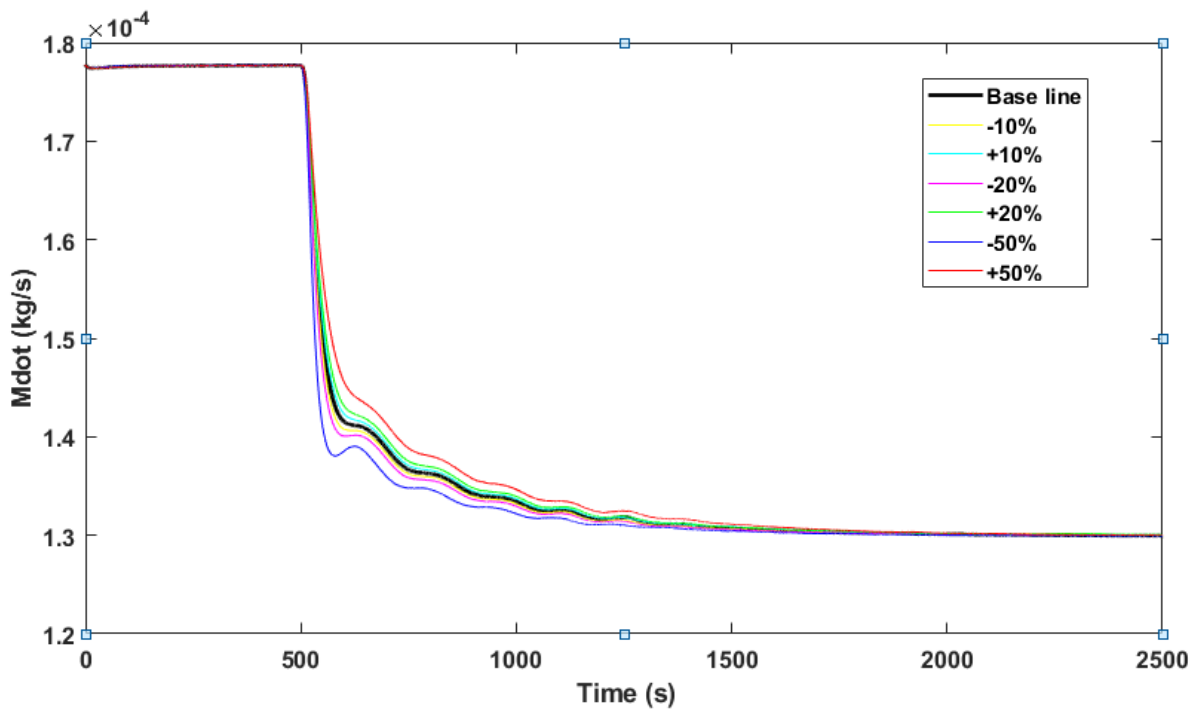


Fig. 84 Effect of the heater-block thermal inertia on the mass flow rate of LHP2.

For the case of LHP1, Fig. 85 shows that the thermal inertia increase results in temperature oscillations, and the higher thermal inertia values are associated with larger amplitudes. These oscillations are later damped, and the same steady state is reached for all cases. The thermal inertia change mainly affects the oscillation amplitude while the frequency remains almost constant. The time lag increases with increasing thermal inertia. A maximum difference of 0.1°C (0.7%) in the transient temperature is identified with respect to the baseline when thermal inertia is varied within  $\pm 50\%$ .

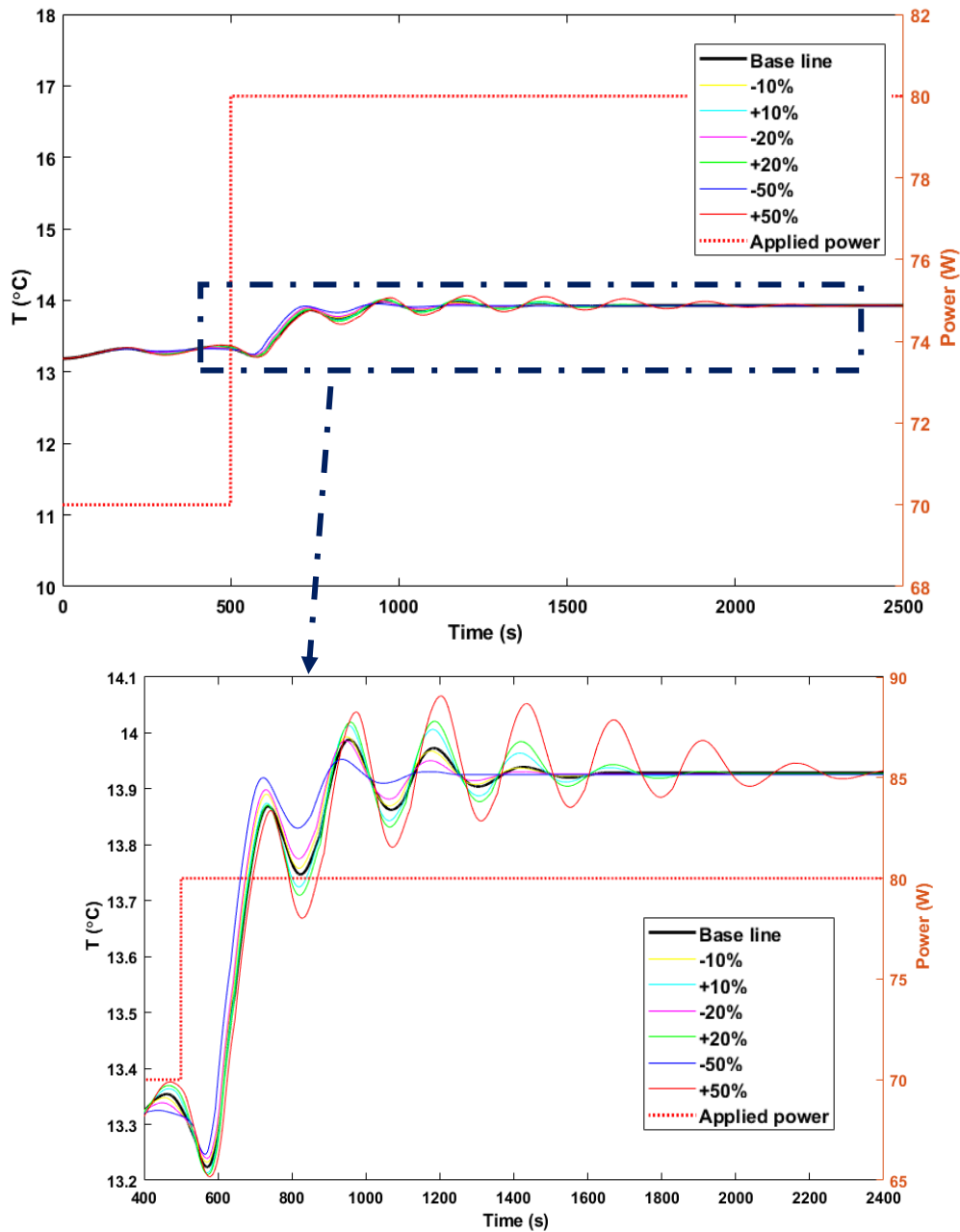


Fig. 85 Effect of the heater-block thermal inertia on the operating temperature of LHP1 with a zoomed-in transient section.

Figure 86 illustrates the effect of the thermal inertia on the two-phase/liquid interface movement. An increase in the thermal inertia delays the interface entering the liquid line and decreases the penetration length into the liquid line before returning inside the condenser. For the different thermal inertia values, the interface slightly oscillates at the end of the condenser. These interface oscillations result in the operating temperature fluctuations as shown in Fig. 85.

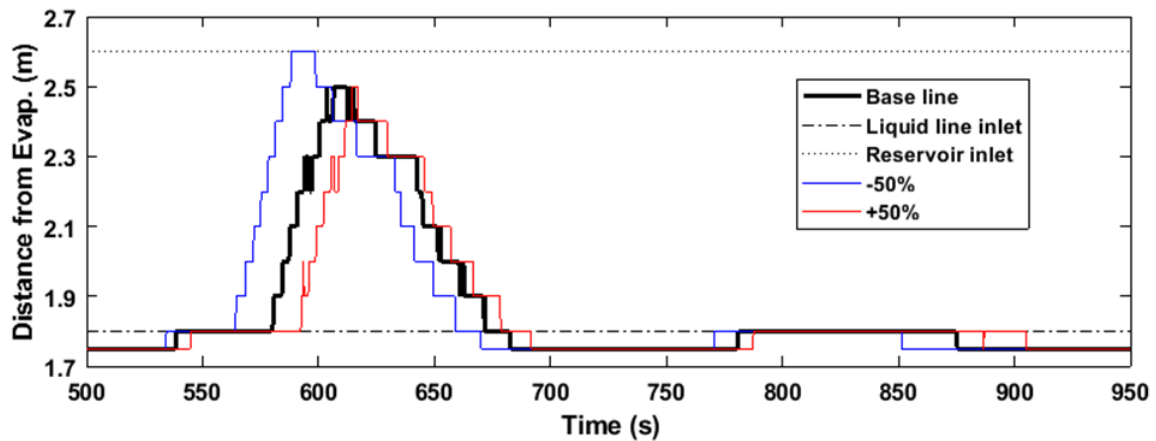


Fig. 86 Effect of the heater-block thermal inertia on the two-phase/liquid interface of LHP1.

#### 5.4.2 Thermal inertia of condenser saddle

The condenser saddle is the main component in the path of dissipating heat to the sink. For the studied power range of LHP1, the condenser is always partially utilized. Therefore, the change in the condenser saddle thermal inertia shows no significant effect on the operating temperature. In other words, the condenser provides enough subcooling so that the change of its thermal inertia does not affect the operating temperature.

Figure 87 presents the results of the LHP2 scenario. Increasing the thermal inertia leads to an increased time required to reach a steady state because the additional thermal inertia slows down the LHP response to any change in the operating condition as it was explained in the heater block section. The time lag of the operating temperature is increased by 12.4% in the case of 50% additional thermal inertia. However, reducing the thermal inertia by 50% only decreases the time lag by 6.7%.

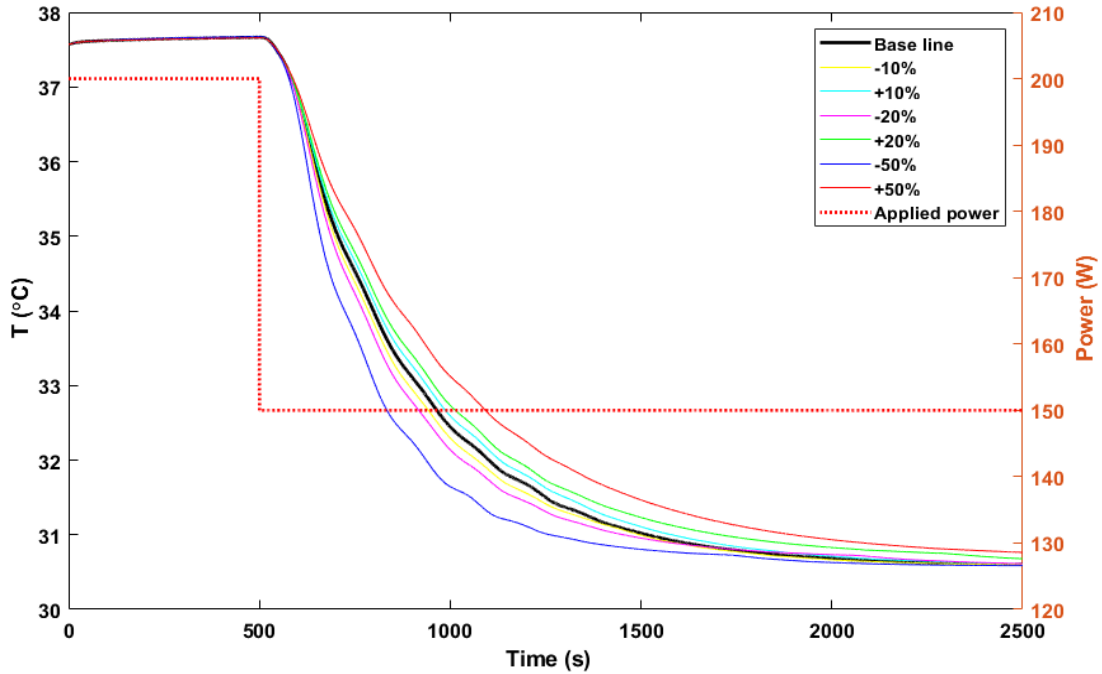


Fig. 87 Effect of the thermal inertia of the condenser saddle on the operating temperature of LHP2.

The difference in the operating temperature with respect to the baseline is plotted in Fig. 88 for each thermal inertia value. The thermal inertia decrease has more effect on the operating temperature. A maximum temperature difference of 1.0°C (-2.9%) is detected for the operating temperature when the thermal inertia is changed by -50%. A 50% increase in the thermal inertia causes a maximum of 0.7°C (2.1%) increase in the operating temperature.

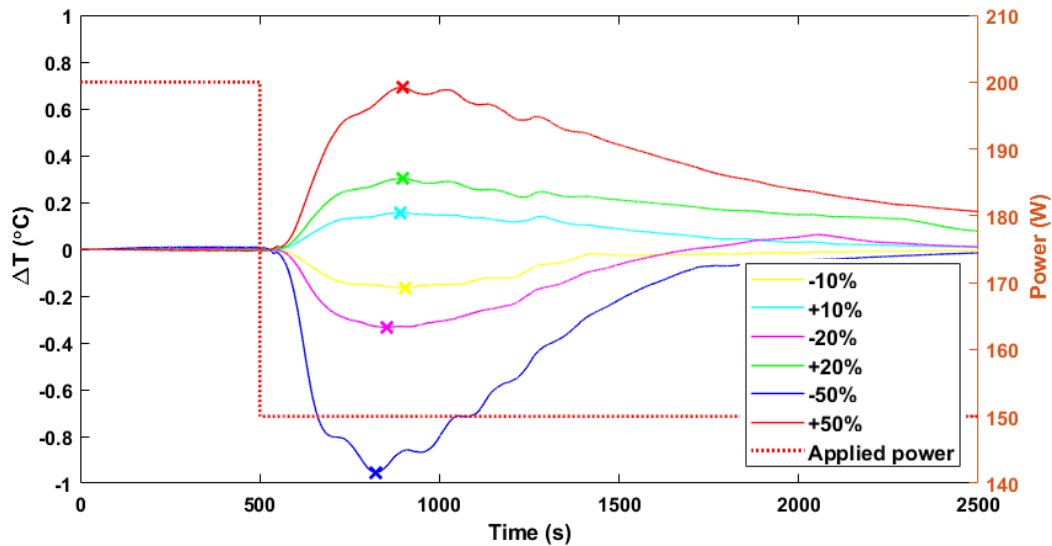


Fig. 88 The operating temperature difference as the condenser saddle thermal inertia changes for LHP2.

The condenser saddle thermal inertia affects the velocity at the inlet of the vapor line as shown in Fig. 89. However, the thermal inertia change has no significant effect on the mass flow rate as the density changes as a function of the operating temperature. The inlet velocity is inversely proportional to the transient operating temperature. An increase of the thermal inertia contributes to a lower inlet velocity during the transient time as illustrated in Fig. 89. The sudden drops in the inlet velocities occur when the vapor/two-phase boundary moves from the middle of the vapor line to its inlet. The oscillations observed in the inlet velocity are caused by the fluctuations of the two-phase/liquid interface between the liquid-line and condenser. The oscillation in the -50% line in Fig. 89 has the highest amplitude as the interface moves further into the condenser and stays there longer.

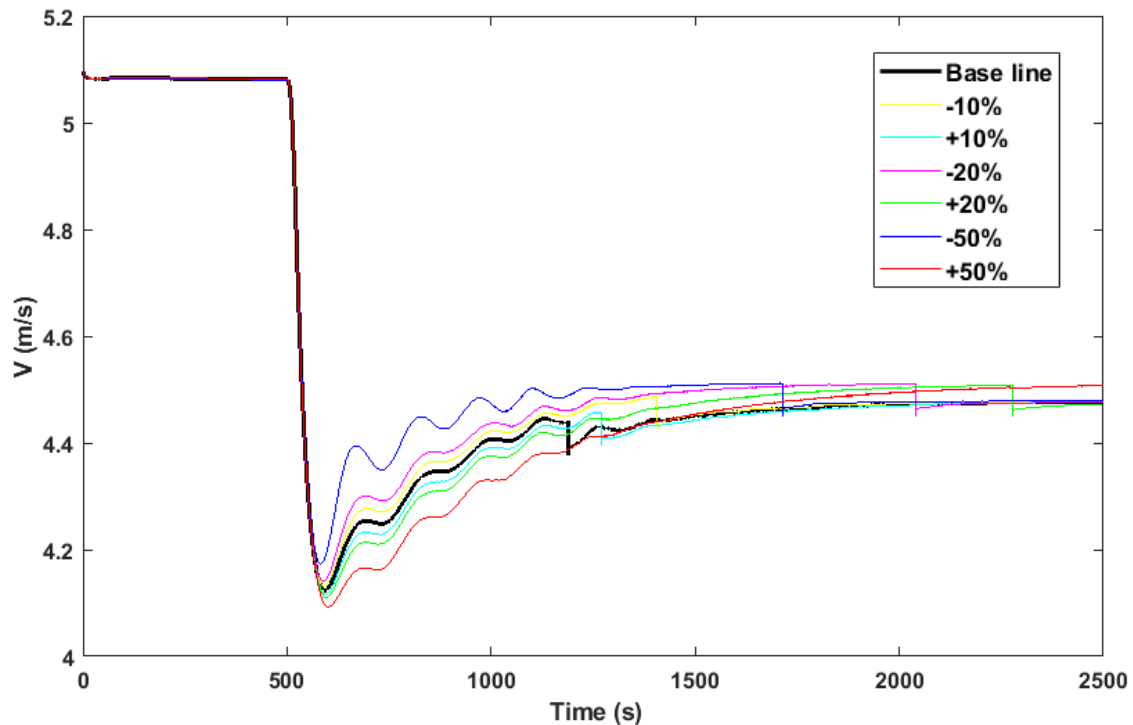


Fig. 89 Effect of the thermal inertia of the condenser saddle on the inlet velocity of the vapor line of LHP2.

### 5.4.3 Contact conductance between the heater block and evaporator saddle

For LHP1, Fig. 90 presents the effect of changing the contact conductance between the heater block and evaporator saddle on the operating temperature. The increase in the contact conductance increases the amplitude of the oscillations. It also shifts the temperature lines to the left because of the better heat transfer from the heater block to the evaporator saddle. Therefore, the temperature difference between the evaporator saddle and heater block are reduced, causing the evaporator saddle and heater block work as a nearly lumped unit. This higher thermal inertia results in increasing the oscillation amplitude and lowering the damping ratio as previously explained for the thermal inertia of the heater block. The maximum difference in the operating temperature is

0.4°C (1%) when the contact conductance is increased by 50%. Lowering the contact conductance has less effect on the operating temperature. For instance, a 50% lower contact conductance results in a maximum temperature difference of -0.1°C (0.4%). In terms of the time lag, a 50% increase in the contact conductance has a more substantial effect (29%) on the time lag than a 50% decrease (-10%).

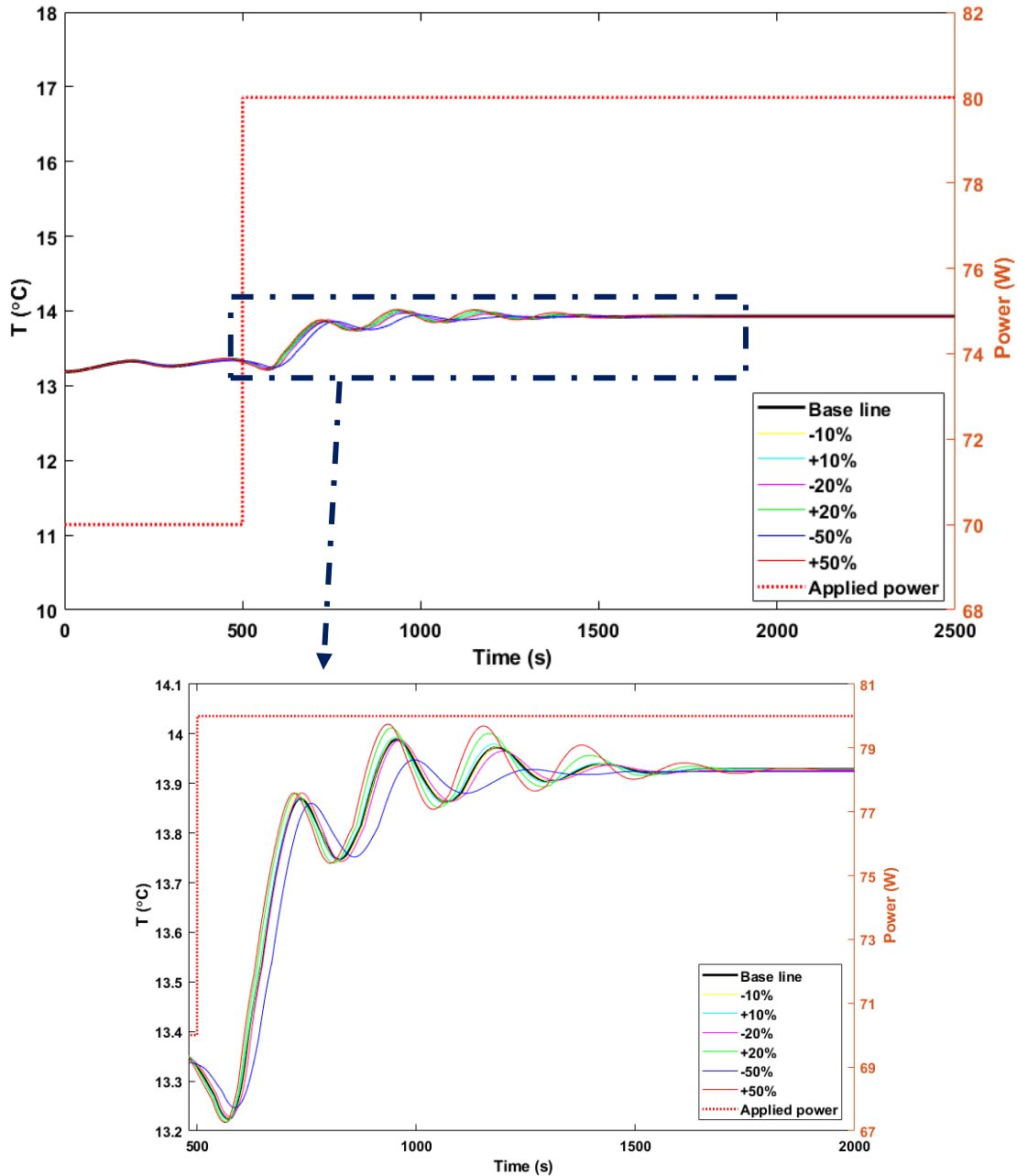


Fig. 90 Effect of the contact conductance of the heater block on the operating temperature of LHP1 with a zoomed-in transient section.

Figure 91 illustrates the effect of the thermal contact conductance on the two-phase/liquid interface as a function of time. The interface enters the liquid line later and returns to the condenser much faster when the contact conductance is decreased. This behavior is due to the fact that the heat load is released slower from the heater block to the LHP1 evaporator.

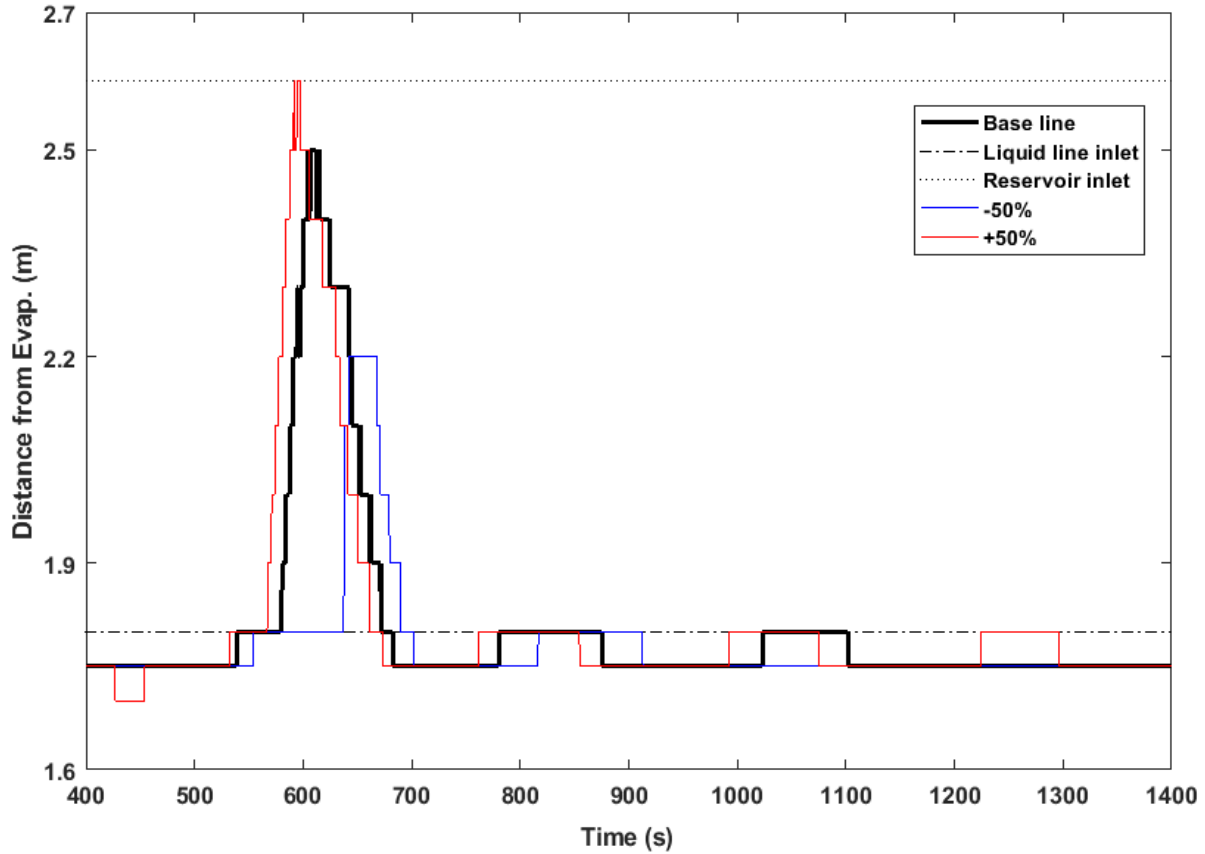


Fig. 91 Effect of the heater-block contact conductance on the two-phase/liquid interface of LHP1.

The LHP1 results indicate that the increasing contact conductance between the heater block and evaporator saddle affects the operating temperature in the presence of oscillations. The negative feedback system, as explained in Section 2.7.2, causing the oscillations is strongly amplified when the contact conductance is increased. In this case, the thermal inertia of the heater block and evaporator saddle is closely coupled. This combined thermal inertia causes an additional lag between the reservoir and evaporator saddle response time that amplifies the oscillation amplitude. Thus, the operating temperature is affected by the change of contact conductance. To prove this point, the contact conductance change does not have any noticeable effect on the operating temperature of the LHP2 scenario when there are no oscillations.

#### 5.4.4 Cell length sensitivity

In this section, the cell length sensitivity analysis for the liquid line, condenser and vapor line is separately presented and analyzed.

#### 5.4.4.1 Liquid line

The cell length in the liquid line has no significant effect on the time step ( $\Delta t$ ) calculated from Eq. (106). This result is due to the lower fluid velocity in the liquid line (approximately 0.1 m/s) than that in the vapor line and condenser (approximately 5.0 m/s). For instance, varying the cell length of the liquid line from 1 to 40 cm has no substantial effect on the simulation time steps for LHP2 as shown in Fig. 92.

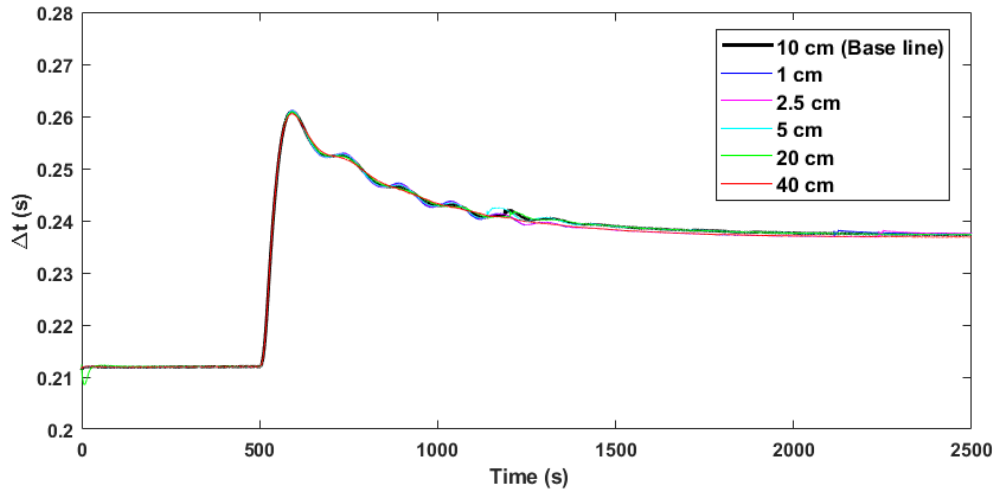


Fig. 92 Effect of the cell length of the liquid line on the time steps for LHP2.

Similarly, Fig. 93 illustrates that the LHP2 operating temperature is not sensitive to change in the liquid line cell length. The maximum temperature difference of  $0.1^\circ\text{C}$  (0.4%) occurs at the simulation time of 2000 s when the cell length is increased from 1 cm to 40 cm.

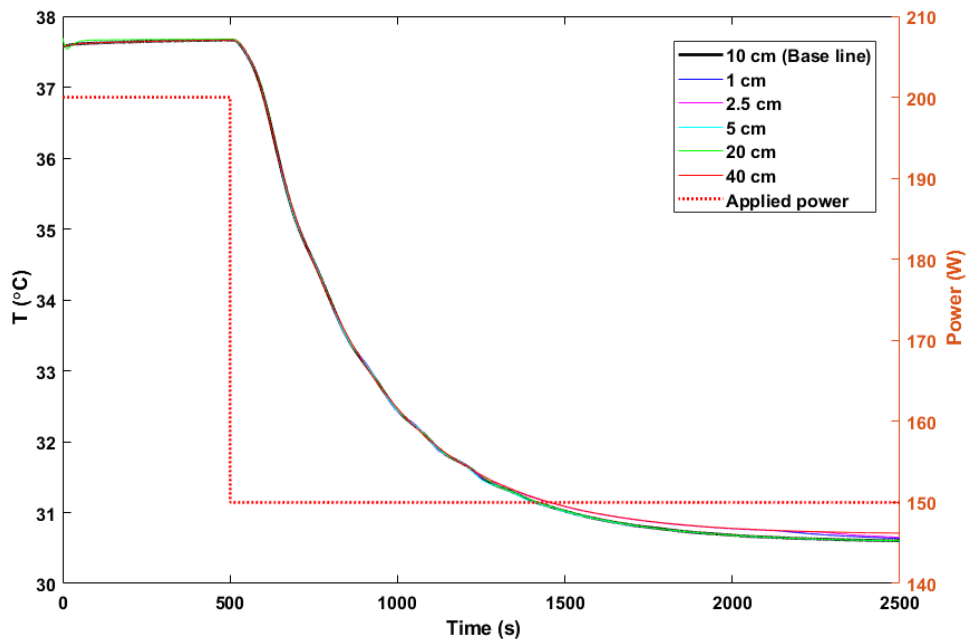


Fig. 93 Effect of the cell length of the liquid line on the operating temperature in LHP2.

As presented in Fig. 94, the two-phase/liquid interface moves closer to the liquid line inlet when the cell lengths are smaller than 20 cm at the time interval [1500 2500] s. Figure 94 also shows that the interface movement becomes smoother as the cell length decreases. The 10-cm base line in the figure follows the pattern of the smaller cell lengths and its computational time is only one-third of the smallest cell length computational time.

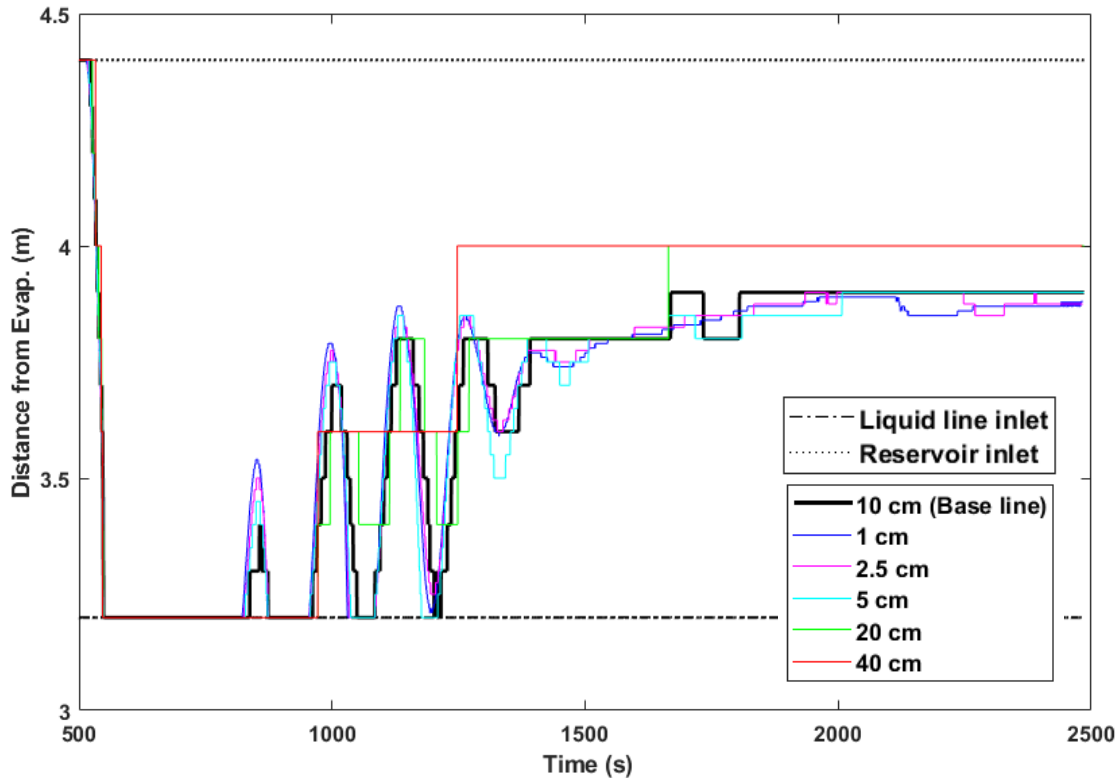


Fig. 94 Effect of the cell length of the liquid line on the two-phase/liquid interface location in LHP2 after the power change.

For LHP1, changing the cell length in the liquid line, particularly reducing it from the base-line value, affects the operating temperature in the VCM as illustrated in Fig. 95. Reducing the cell length increases the oscillation amplitude in the operating temperature and even makes it unstable for the cell lengths of 1 and 2.5 cm. It is found out that the solution does not reach to a steady-state value for smaller cell lengths and results in unrealistic oscillations since an additional liquid/two-phase interface appears in the liquid line. As a result, smaller cell lengths than the base-line length cannot be used in the LHP1 model mainly when the LHP is operating in the VCM.

Heat is transferred from ambient to the liquid line since the operating temperature is less than the ambient temperature (22°C). This heat absorption is a function of the heat transfer coefficient inside the pipe as well as the liquid line discretization especially when the mass flow rate is small. For instance, the heat absorption is equal to 0.84 W with a cell length of 10 cm at the 2000-s

simulation time. The finer discretization results in a 5% more heat absorption from ambient as a result of more precisely calculated temperature values inside the liquid line. This small increase in the heat absorption causes the fluid inside the liquid line to change phase from the subcooled liquid to two-phase. This in turn increases the heat transfer coefficient between the fluid and wall. As a result, more heat transfers from ambient to the fluid (up to 3.2 W for 1-cm cell length). Having a liquid/two-phase boundary and extra heat absorption from ambient show that smaller cell lengths than the base line cannot be used in the LHP1 model particularly when the LHP is operating in the VCM. This is because, in the VCM, the fluid velocity is small inside the liquid line, and the operating temperature is below the ambient temperature. Also, the presence of the liquid/two-phase interface creates a chattering effect in the operating temperature in Fig. 95.

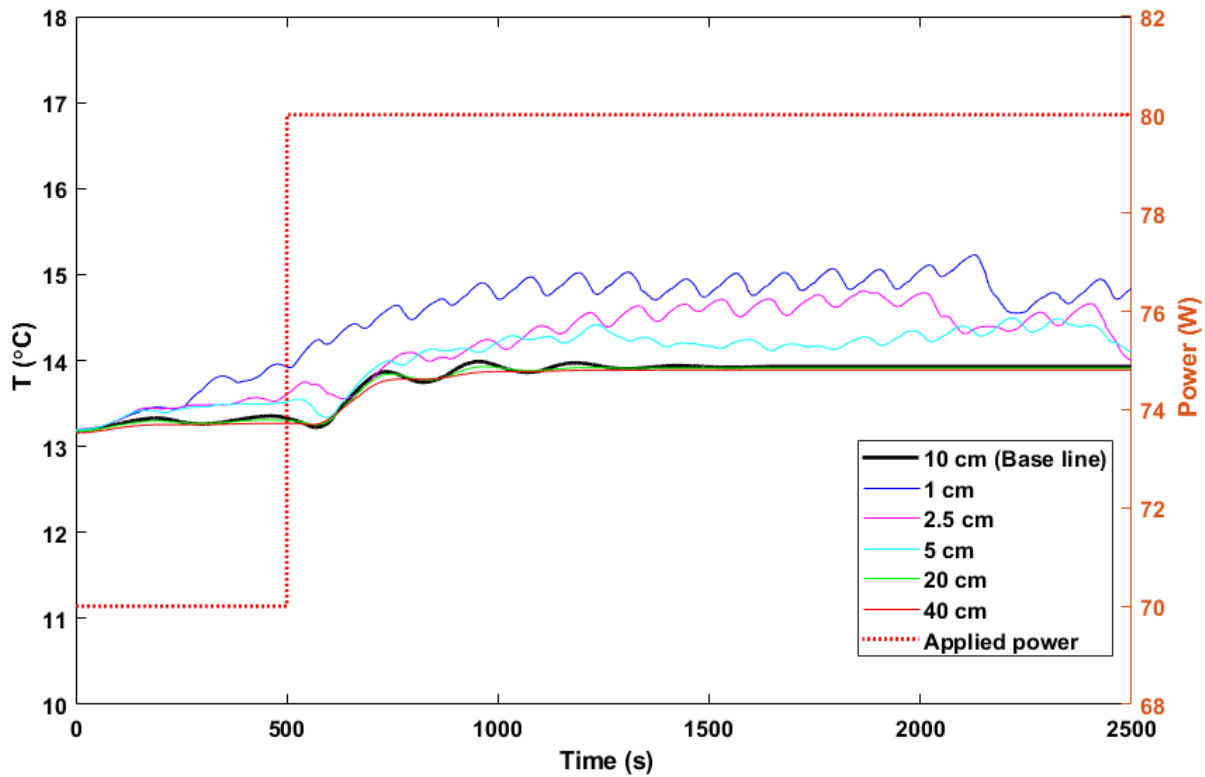


Fig. 95 Effect of the cell length of the liquid line on the operating temperature of LHP1 towards to the end of the VCM.

To analyze the FCM, the sink and ambient temperatures are kept the same as the above scenario (5 and 22°C, respectively), but the applied power is varied from 150 to 200 W. Figure 96 represents the operating temperature for this case, which has a similar pattern as the LHP2 results. The main effect on the steady-state temperature is less than 0.5% when the cell length is reduced from 10 to 1 cm. When the simulation reaches the steady state, the heat transfer from ambient to the liquid line is about 0.05 W which is 16 times smaller than the 70-to-80-W case as the operating temperature is closer to the ambient, and the mass flow rate is 2.6 times higher. The liquid line cell

length does not affect the transient behavior since the heat transfer from ambient to the liquid line is negligible.

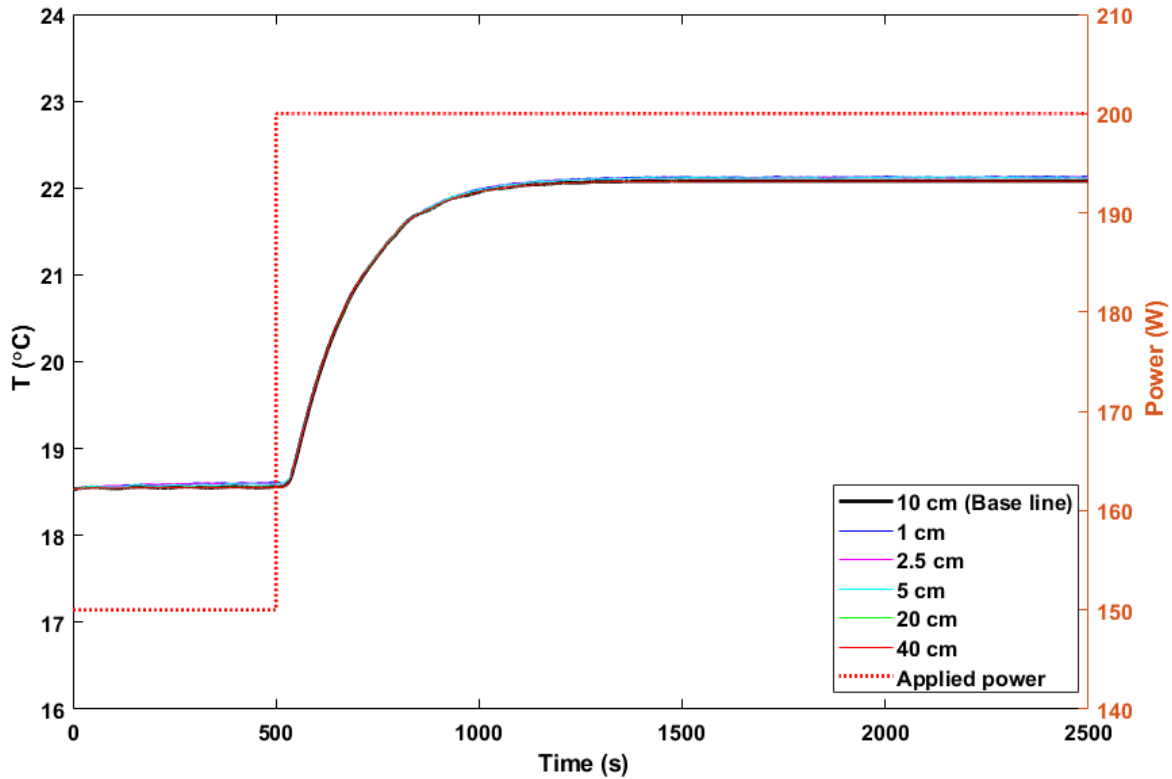


Fig. 96 Effect of the cell length of the liquid line on the operating temperature of LHP1 in the FCM.

#### 5.4.4.2 Condenser

The cell length of the condenser can affect the time step ( $\Delta t$ ) if the cross-sectional area of the condenser is comparable to that of the vapor line. In this case, the fluid velocity in the first condenser cell is very close to the velocity in the vapor line. If the condenser cross section has a bigger area, the fluid velocity inside the condenser is smaller than the velocity in the vapor line. As the condenser cells are discretized finer than the vapor line cells, the condenser cell length determines  $\Delta t_{explicit}$ . As a result, varying the cell length of the condenser from 1 to 20 cm has a significant effect on the time steps of the LHP2 simulation as illustrated in Fig. 97. The LHP2 condenser has the smallest cell length and a fluid velocity close to that in the vapor line. Therefore, condenser has the cell with the minimum length-to-velocity ratio.

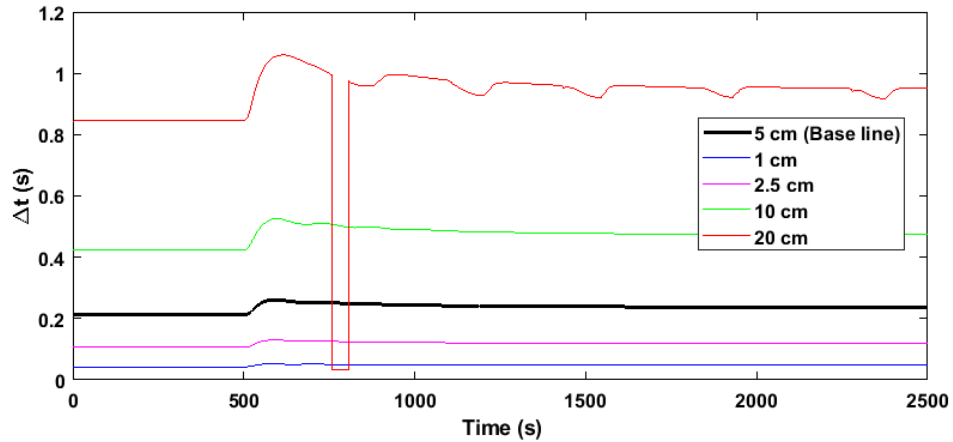


Fig. 97 Effect of the cell length of the condenser on the time steps of LHP2.

The time steps are linearly proportional to the cell length in the condenser. For example, increasing the cell length from 1 to 10 cm increases the time steps ten times from an average of 0.047 to 0.47 s. In the time interval of [757 816] seconds for the 20-cm cell length, a sudden decrease of the time step is observed. This is due to the fact that the number of iterations exceeded the set value of 300, indicating that a finer time step is required to find the operating temperature. The repeated drops are apparent in the 20-cm line because of the oscillations of the operating temperature illustrated in Fig. 98.

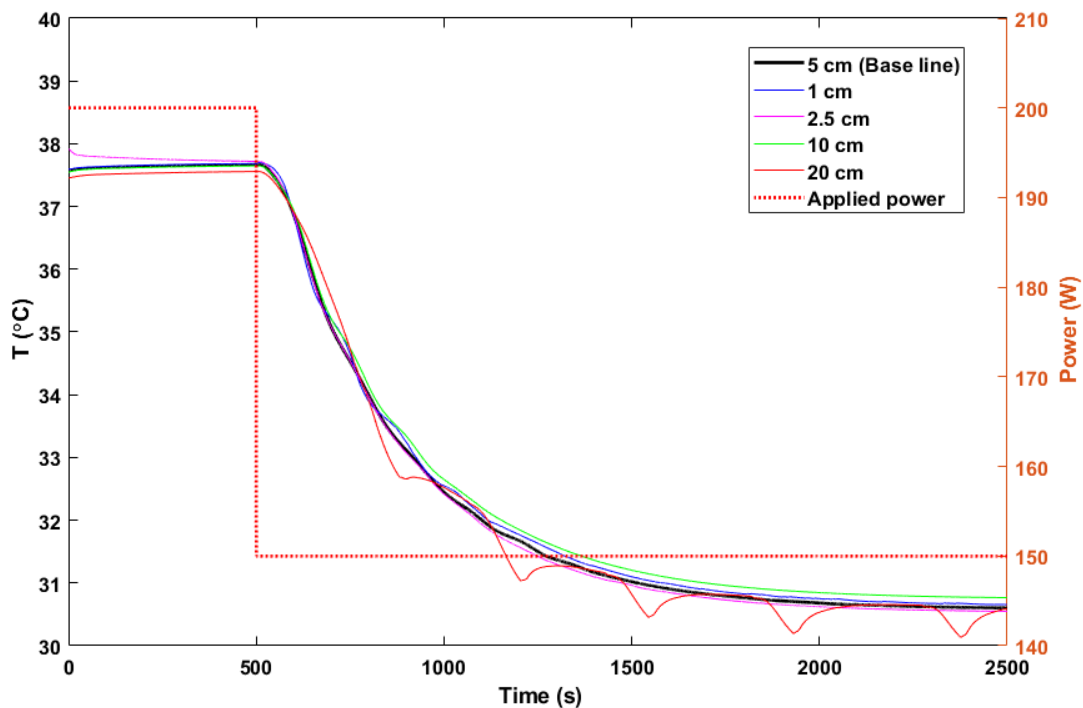


Fig. 98 Effect of the cell length of the condenser on the operating temperature of LHP2.

Figure 98 illustrates that the operating temperature is sensitive to the cell length in the condenser if the cell length is bigger than 5 cm. Oscillations with an amplitude of  $0.5^{\circ}\text{C}$  is observed in the 20-cm line of Fig. 98. A maximum temperature difference of  $-0.6^{\circ}\text{C}$  with respect to the base line occurs at the simulation time of 1205 s for the cell length of 20 cm. When the steady state is reached, the heat dissipation to the sink for the 20-cm cell length is 146 W, which is 1.8 W lower than the heat dissipated for the baseline at the same operating temperature. This lower heat dissipation pushes the two-phase/liquid interface to the exit of the liquid line as shown in Fig. 99. Therefore, the subcooling amount to the reservoir decreases and the operating temperature increases, which in turn initiates the oscillation pattern. This oscillation is sustained in the steady-state region. The results demonstrate that a finer discretization is necessary for the condenser to more accurately calculate the quality and temperature and specially to locate the phase interface as correctly as possible.

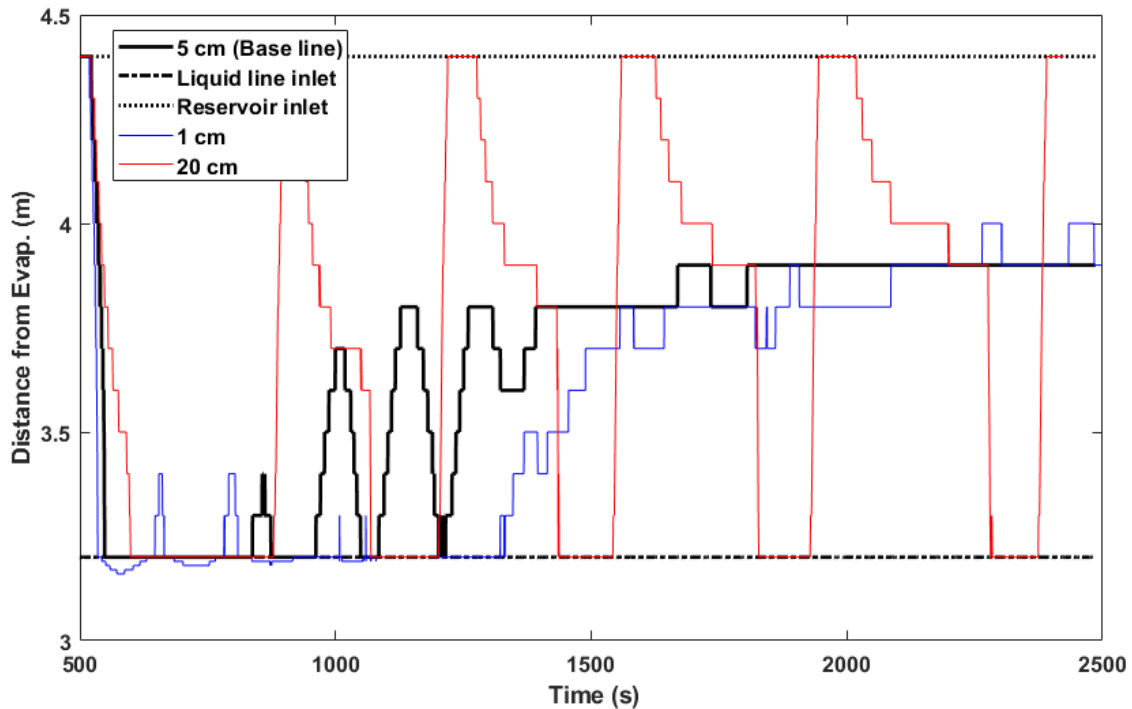


Fig. 99 Effect of the cell length of the condenser on the two-phase/liquid interface location in LHP2 after the power change.

Figure 99 shows that a fine discretization of the condenser not only reduces the length that the interface travels inside the liquid line but also stabilizes the interface location. For instance, the interface location of the 1-cm cell length oscillates only for two cycles with an amplitude of 20 cm compared to three and a half cycles with the amplitude of 50 cm in the 5-cm cell length. The interface stays nearly 70 cm into the liquid line in both 1 and 5 cm cell lengths. Also, the interface of the 1-cm cell length enters the condenser since it is more accurately located with the finer

condenser cells. However, the interface is not stable there and moves in-and-out of the condenser for the interval [535 1055] seconds. When the operating temperature decreases during the transient, the condenser efficiency also decreases (lower temperature difference between the sink and condenser), and the interface moves inside the liquid line. Overall, reducing the condenser cell length results in a more stable location of the two-phase/liquid interface.

For LHP1, changing the cell length in the condenser affects the operating temperature in the VCM as illustrated in Fig. 100. Reducing the cell length from the reference value increases the amplitude of the temperature oscillations without damping during the steady-state section. The interface movement in-and-out of the condenser results in a larger difference between the minimum and maximum subcooling entering the reservoir and consequently a higher oscillation amplitude.

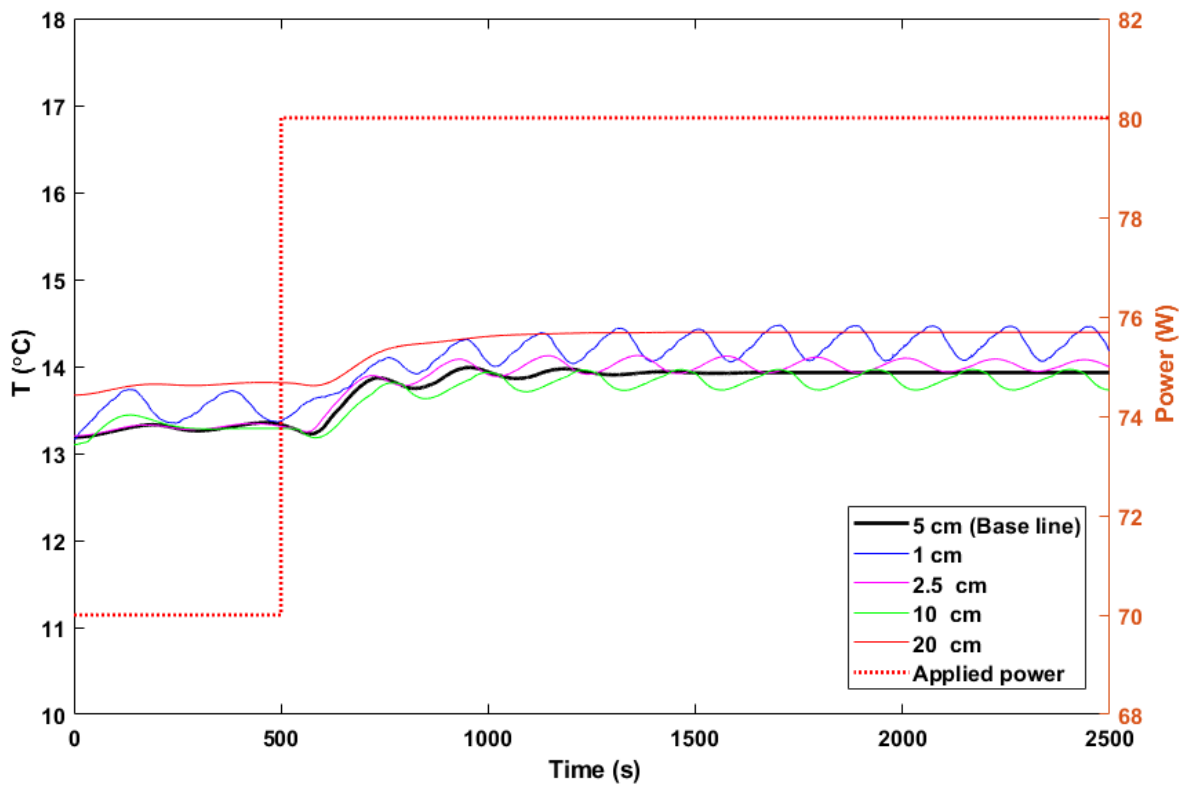


Fig. 100 Effect of the cell length of the condenser on the operating temperature of LHP1 towards to the end of the VCM.

The second LHP1 scenario (the power increase from 150 to 200 W) is presented in Fig. 101 to assess the cell-length effect of the condenser in the FCM. In contrast to the liquid line cell length size, the condenser cell length affects the FCM operating temperature. The main mechanism for this effect is the change of the liquid/two-phase interface location and subcooling. Selecting too large or too small cells is not desirable as the simulation results are subjected to large discretization or rounding errors.

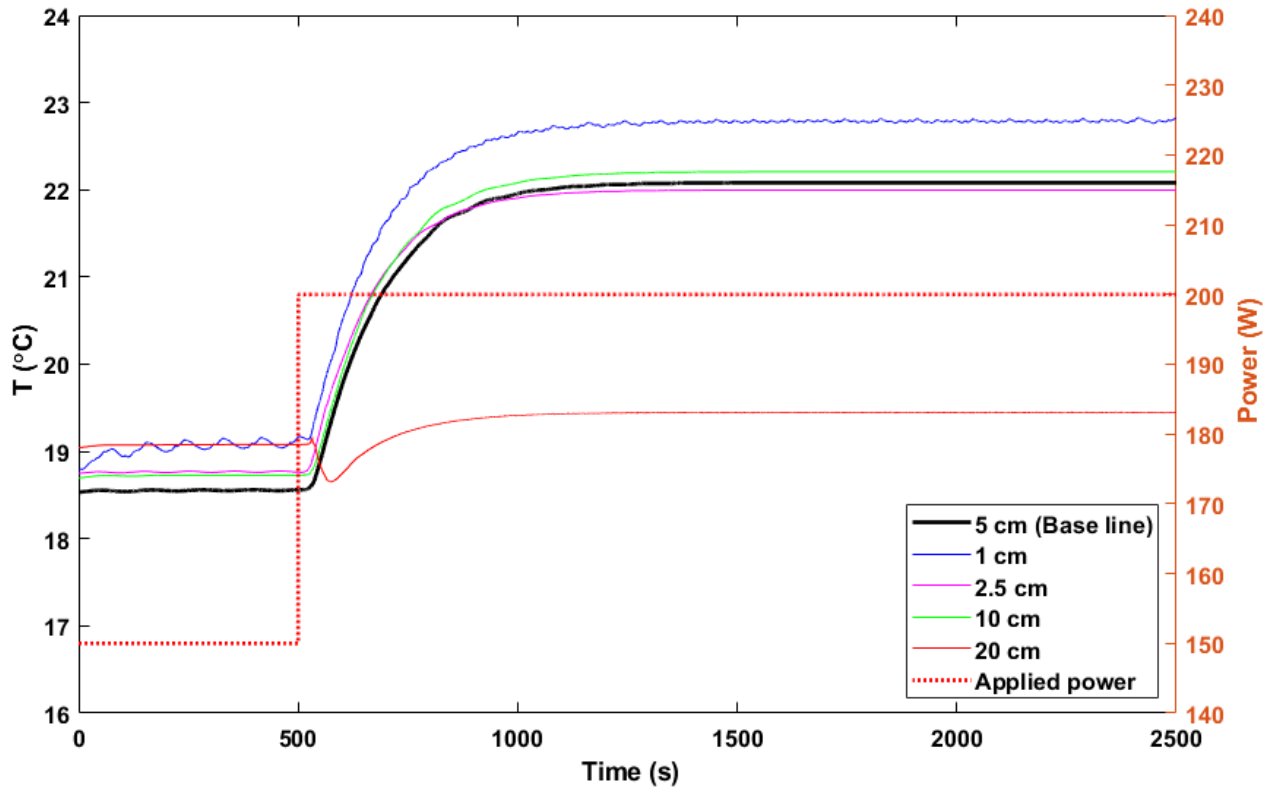


Fig. 101 Effect of the cell length of the condenser on the operating temperature of LHP1 in the FCM.

#### 5.4.4.3 Vapor line

The cell length of the vapor line can affect the simulation time step ( $\Delta t$ ) if the minimum length-to-velocity ratio belongs to one of the vapor-line cells. For instance, the vapor line cell length does not affect the time step ( $\Delta t$ ) for LHP2. As mentioned in Section 5.4.4.2, the time step of LHP2 is determined by the cell length of the condenser since it has the smallest cell length.

The cell length of the vapor line does not have any significant effect on the operating temperature as illustrated in Fig. 102. Small differences are observed in the lines with the cell lengths of 50 and 100 cm at the beginning of the simulation before changing the applied power. The differences are due to the location of the two-phase/liquid interface at the initial steady-state condition. However, this small difference in the initial conditions does not have any effect on the time history of the operating temperature and the final steady-state value as the interface finds its correct location right after the power change.

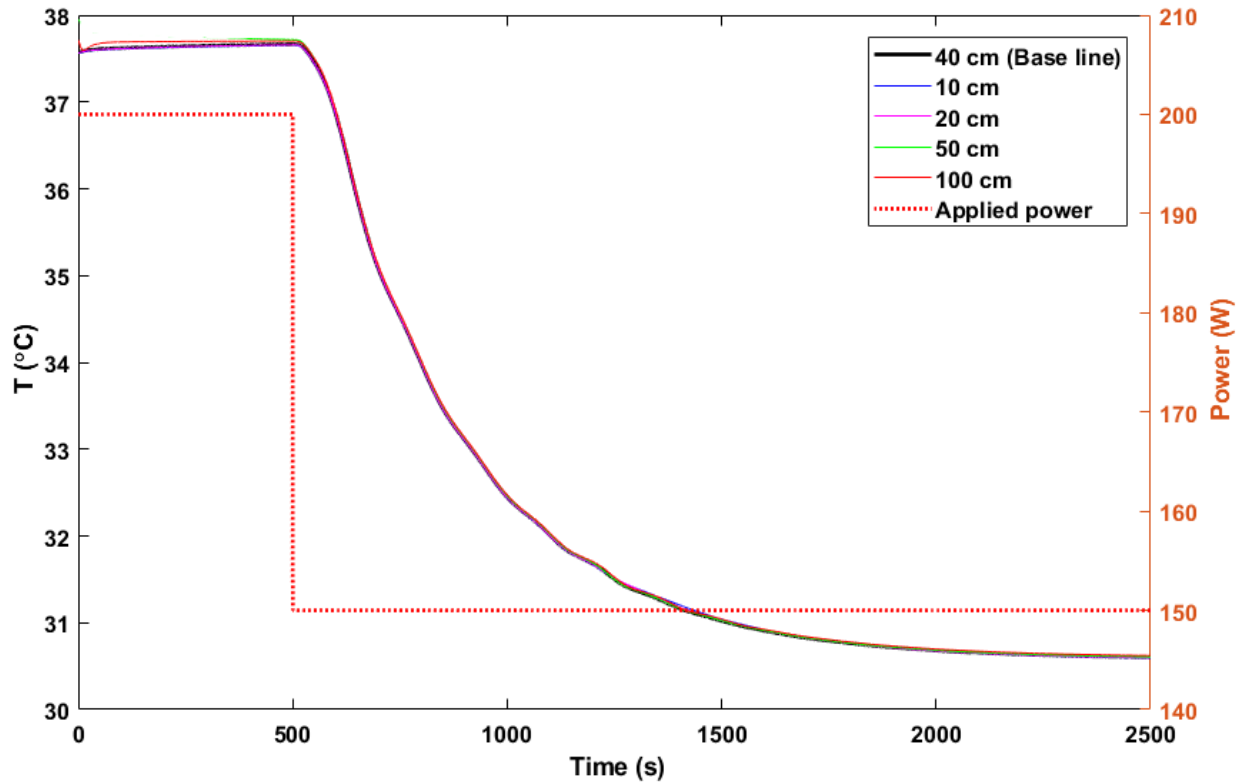


Fig. 102 Effect of the cell length of the vapor line on the operating temperature of LHP2.

The main parameter affected by the cell length variation in the vapor line is the location of the vapor/two-phase interface. Figure 103 demonstrates that reducing the cell length brings the interface closer to the vapor line inlet above 1500 s. A finer discretization of the vapor line leads to a more accurate calculation of the vapor quality of the first two-phase cell. For example, the vapor quality of the first two-phase cell is increased from 99.24% to 99.95% at steady state by decreasing the cell length from 100 to 10 cm. The oscillations observed in the 100-cm line only affect the number of  $T_{int}$  iterations, and it must be a result of the increased discretization error.

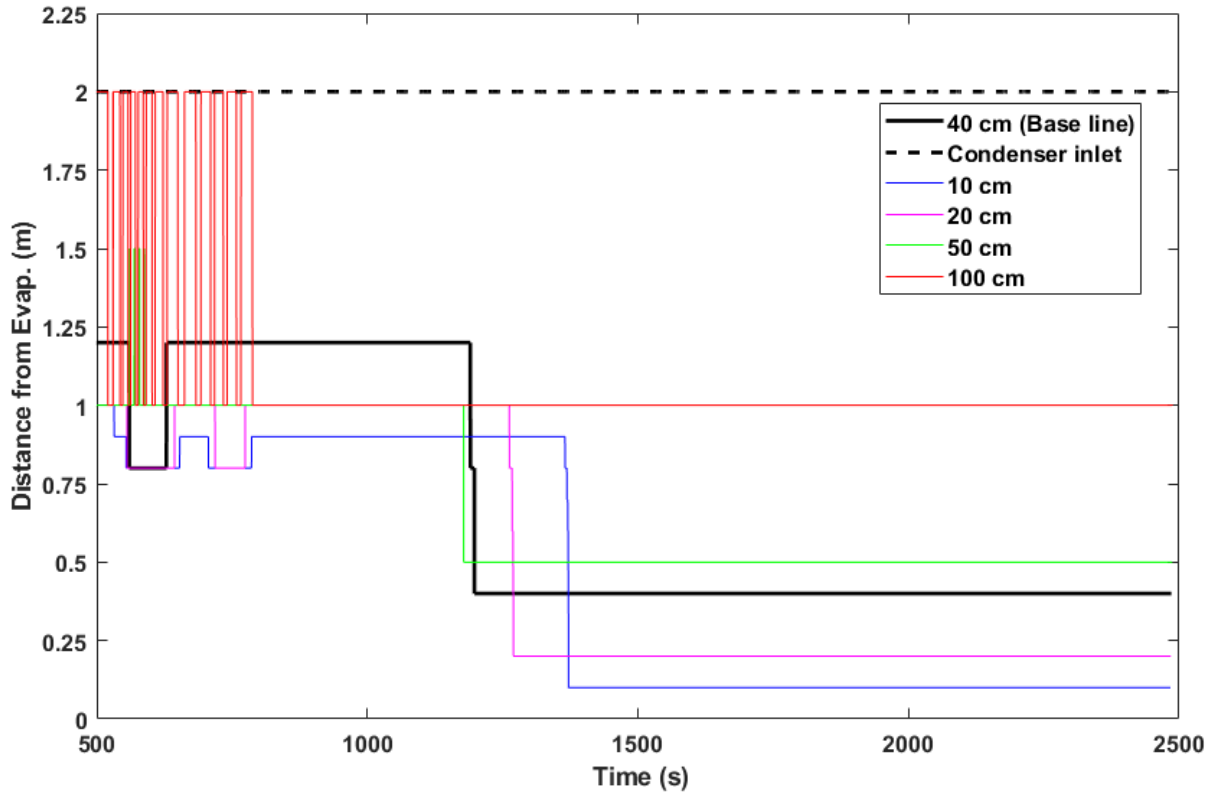


Fig. 103 Effect of the cell length of the vapor line on the vapor/two-phase interface in LHP2 after the power change.

Altering the cell length in the vapor line of LHP1 does not affect the location of the vapor/two-phase interface. The interface resides inside the condenser as the operating temperature is lower than the ambient one. The operating temperature and particularly its fluctuations are affected by the cell length as illustrated in Fig. 104. The oscillation amplitude in the operating temperature is increased as the cell length decreases. Overall, the operating temperatures of the different cell lengths follow the same trend except for 2.5 cm in the zoomed section of Fig. 104.

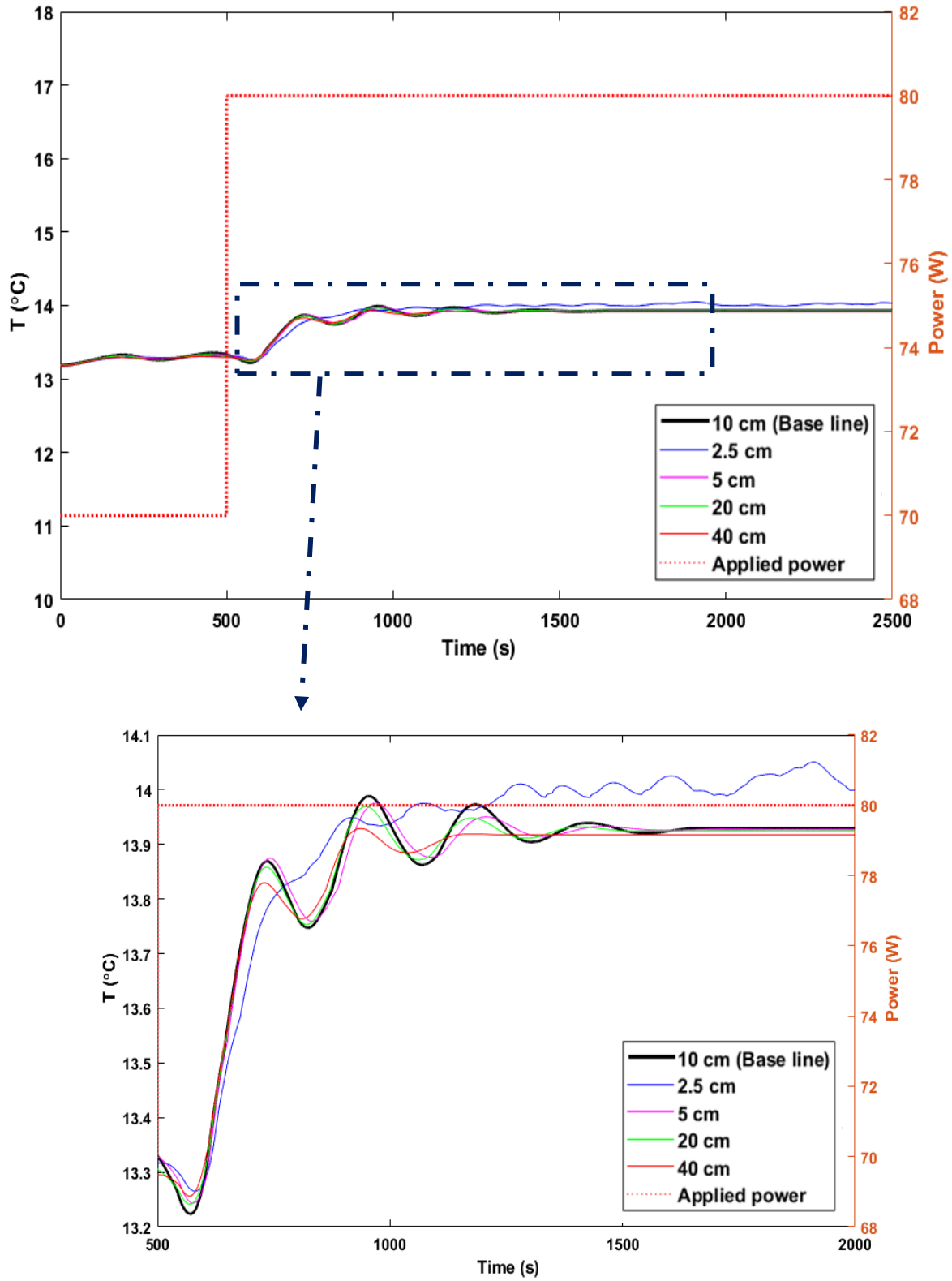


Fig. 104 Effect of the cell length of the vapor line on the operating temperature of LHP1 in the VCM with a zoomed-in transient section.

The simulation with the cell length of 2.5 cm has the smallest time step, as shown in Fig. 105, since the minimum length-to-velocity ratio of the cells occurs inside the LHP1 vapor line. The minimum time step results in more iterations and consequently more rounding errors. Figure 105 also shows that the time steps for the cell lengths bigger than 5 cm quickly vary between the minimum and maximum values in the time interval of [580 690] seconds. These fluctuations occur as the iteration number of  $T_{int}$  exceeds the set maximum value of 300. Then, the code reduces the time step to find the  $T_{int}$  value. After 690 s in the simulation, reducing the time step is no longer required since the  $T_{int}$  value is found without exceeding the maximum iteration number.

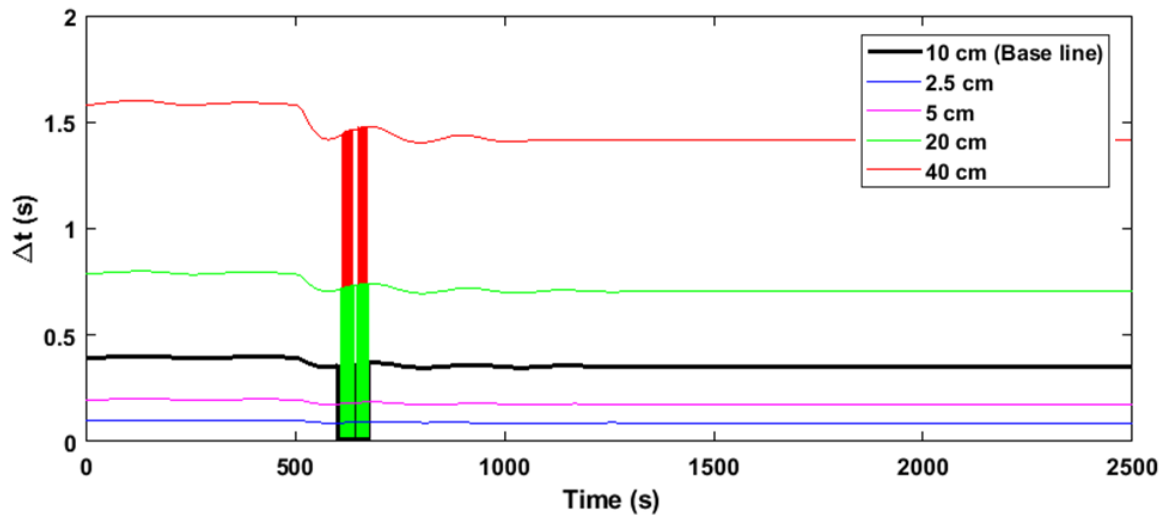


Fig. 105 Effect of the cell length of the vapor line on the time steps for LHP1 in the VCM.

For the power increase from 150 to 200 W, altering the cell length in the vapor line has no significant effect on the operating temperature in the FCM as shown in Fig. 106 except for the largest cell in the transient region. These results suggest that the cell length is becoming too large to accurately discretize the equations.

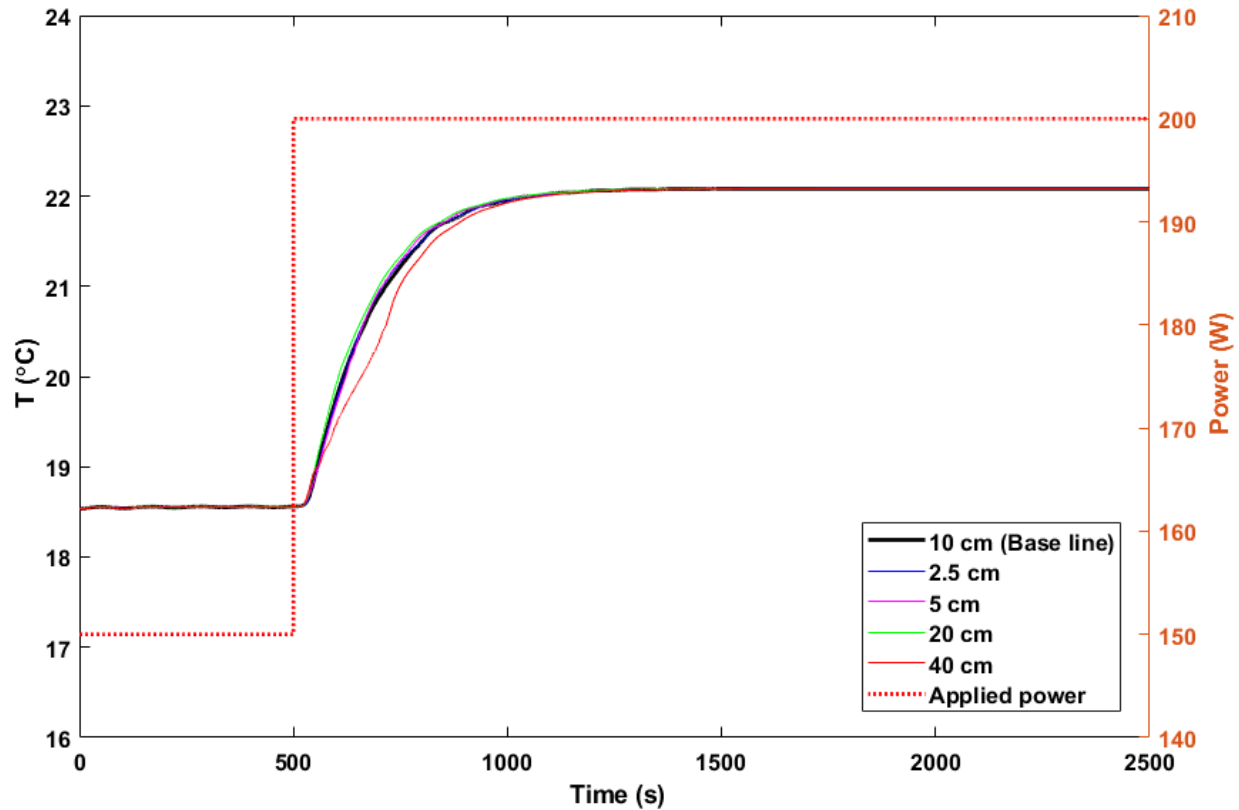


Fig. 106 Effect of the cell length of the liquid line on the operating temperature of LHP1 in the FCM.

## 5.5 Summary

A new transient model is developed to study LHP dynamic response to a change in the operating conditions. Each LHP section is discretized into solid and fluid cells and their physical and geometrical properties are assigned. Then, the time-dependent mass, energy and momentum conservations are solved for the fluid cells in the one-dimensional compressible forms using a staggered-grid, implicit approach. The evaporator wick and reservoir are modelled in three and two different methods, respectively. REFPROP 10.0 is used to obtain the thermodynamic properties of the fluid flow.

The model algorithms implemented in MATLAB include two highly iterative processes to calculate the state of each fluid cell and the LHP operating temperature in every time step. The first process can perform phase-change detection and phase transition to obtain a correct fluid state for each cell. Additionally, the LHP limits, such as the capillary pressure upholding, are verified after obtaining the LHP operating temperature at each time step.

The model uses setting parameters to choose alternative modelling approaches, to adjust the accommodation factors and spatial resolution, and to set the numerical convergence criteria.

Among the alternative approaches, the one-cell-with-inertia one is selected for the wick modelling. In addition, the fluid-charge and the saturated methods are selected for the reservoir modelling and phase transitioning, respectively. The three accommodation factors and cell lengths in the transportation lines are chosen from the steady-state model developed and validated earlier. The four convergence criteria are defined and tuned based on the numerical analysis and validation data.

The developed model is validated against the test results collected from the two LHP set-ups. The first LHP has a conventional design, and the second one utilizes a two-way pressure regulated valve on its vapor line. The values of the converge criteria, including the limit and multiplier of the operating temperature time-derivative, are finalized at a chiller temperature of 5°C. Afterward, the model capability to predict the transient behavior is assessed through comparing the model results to the test data obtained for the power cycling at 10°C sink and the sink cycling at both the VCM and FCM. The comparisons are performed for three performance variables comprising of the transient temperature, the steady-state temperature and the time lag. For LHP1, the temperatures and time lag predictions have average errors lower than 0.7°C (3.9%) and 230 s (26.6%), respectively. The LHP2 temperatures and time lags are predicted within average errors of 0.7°C (1.4%) and 140 s (13.4%), respectively. The model provides better predictions for LHP2 as it works only in the FCM. The quantitative analysis of the time lag is a novel approach that never conducted in previously published numerical models. The qualitative comparison of the time lag in the current model and the previous ones shows that the presented model in this paper has better accuracy in predicting the time lag. Additionally, qualitative investigations are performed on the model predictions to discuss the characteristics of the temperature dynamic response to the change in the power or sink temperature. The model is able to predict the temperature dips, overshoots and oscillations both in the transient regions and steady-state ones. The uncertainty in the oscillation frequency and amplitude is attributed to the underprediction of the friction factor inside the condenser.

The sensitivity analysis demonstrates that the thermal inertia of the heater block or condenser saddle affects the time lag and transient operating temperatures. The contact conductance between the heater block and the evaporator saddle affects the operating temperatures in the presence of the oscillations. LHP oscillations amplitude and frequency is influenced by the thermal inertia and contact conductance. The liquid line cell length affects the operating temperature in the VCM and the two-phase/liquid interface location in the liquid line. The condenser cell length affects oscillation characteristics in the VCM and the operating temperature in the FCM through the location of the two-phase/liquid interface and the subcooling calculation. The vapor line cell length only affects the transient operating temperature at extremely low or high values as they are subjected to discretization or rounding errors.

## Chapter 6: Concluding remarks

The main objective of this research work was to develop a mathematical model to simulate the transient operation of an LHP. The main emphasis was to use a minimum number of accommodation parameters. First, an experimental investigation was conducted to characterize and understand better the fundamental operation of LHPs. Then, based on the experimental observations and acquired knowledge, a stand-alone, modular mathematical model was developed to describe the steady-state and transient operation of LHPs. The model provides a means to predict how changing the operating conditions could contribute to the LHP operating temperature and its response time. The modularity feature of the model allows further improvements or modifications to be easily implemented with minor changes to the model configuration. As a part of modularity, each modelling task is implemented in a separated function that can be used by different algorithms. Also, the LHP information and operating conditions are acquired from the user through input files. Therefore, the model main body code doesn't change. The model functionality is independent from the platform it is coded in by using a minimum number of MATLAB specific functions. Therefore, the model transition to other platform/programming languages required a minimum effort and time. The developed model can be utilized as a design tool to reduce the time and cost in LHP research and development by minimizing the number of validation and qualification tests. Furthermore, the minimum number of accommodation parameters employed in the model makes it highly practical to use as the model relies on only one data set of a power cycling test. Besides being a design tool, the validated model can be utilized for investigation and troubleshooting of an operational LHP in remote applications such as a thermal control system of a spacecraft. Specifically, the mathematical model can be easily integrated into a system level thermal analysis tool because of the modular approach used in developing the model.

The experimental work was conducted to investigate the operational characteristics of the two LHPs of different designs, named as LHP1 and LHP2, and to collect data under various operating conditions to validate the developed numerical model. Whereas LHP1 is of conventional design, LHP2 uses a novel design for the temperature control through a two-way pressure regulated valve (PRV) on its vapor line. More than 25 test scenarios were performed under three categories of different operating conditions to understand the operational limits and to investigate the steady-state and transient characteristics of LHP operation. The most important investigated characteristics include the steady-state operating temperature at a given applied power/sink temperature, the temperature response to a change in the applied power/sink temperature, the location of two-phase/liquid interface, and oscillations in both steady-state and transient regimes. An uncertainty analysis performed for the entire measurement chain showed that the experimental results had an uncertainty of less than  $\pm 1.0^{\circ}\text{C}$  with a 95% confidence level.

The experimentally obtained performance curves for LHP1 showed the typical LHP operation: the operating temperature was inversely proportional to the applied power in the variable conductance mode (VCM), and it was proportional in the fixed conductance mode (FCM). For LHP2, the

applied power was noted to have no significant effect on the operating temperature when the PRV regulated the operating temperature. The regulating power of the PRV ranged from the start-up power to the power at which the operating temperature exceeded the set point of 31°C. After reaching this power limit, LHP2 operated as a conventional LHP in the FCM. The set-point power was decreased from 145 to 70 W by increasing the sink temperature from 5 to 20°C. The temperature hysteresis was only observed in the VCM section of the LHP1 performance curve, and the hysteresis effect was reduced as the applied power or sink temperature increased. No hysteresis effect was detected in the LHP2 results since the PRV prevented LHP2 from operating in the VCM.

A change in the sink temperature propagated from the condenser plate through the liquid line to the reservoir. The liquid line temperatures closely followed the sink temperature change. However, the temperature dynamic response of the other LHP sections followed the temperature trend in the reservoir as its inertia attenuated the dynamic response.

The high frequency and low amplitude temperature oscillations observed in the experiments were associated with the change in the amount of subcooling entering the reservoir when the two-phase/liquid interface moved toward the condenser exit and entered the liquid line. The maximum oscillation amplitude was found in the liquid line. The remaining LHP sections experienced a lower amplitude oscillation since the reservoir inertia attenuated these oscillations.

Several correlations, to calculate the pressure drop and heat transfer coefficients, were investigated to study the correlation range or continuity, prediction capability and computational time. Based on this investigation, the Churchill correlation was selected to obtain the viscous pressure drop for both the single and two-phase flows. The parallel method was chosen to calculate the two-phase viscosity in the Churchill correlation since it had the lowest prediction error and computational time. For the internal heat transfer coefficient, the Gnielinski and Traviss correlations were chosen for the single and two-phase flow, respectively. The Traviss correlation provided the minimum prediction error and computational time. It was shown that the small discontinuity observed in the Traviss results was not significant in the whole vapor quality range.

Other correlations were introduced to calculate the pressure drop contributed by bends in the transportation lines, the heat transfer rate between a solid part and ambient, and between two solid parts. The bent pressure drop was obtained from the geometrical properties of the bends. A natural convection correlation between the pipe outer surface and surrounding air was used to calculate the heat exchange with ambient. The conductive heat transfer formula used the thermal resistance circuit including the contact conductance between the adjacent solid surfaces.

After the validation of the selected correlations, a steady-state mathematical model was developed using one-dimensional compressible mass, momentum and energy conservation equations. The LHP sections were discretized into the fluid and solid cells. The fluid phase was identified for each cell, and its thermodynamic properties were obtained by using REFPROP 10.0. The LHP operating

temperature was calculated through a highly iterative algorithm which also used a series of checkpoints to ensure that the obtained result remained within the LHP operating limits.

Four accommodation factors were introduced in the steady-state model to obtain the operating temperature. These factors included evaporator saddle-to-wick thermal contact conductance, condenser-to-sink thermal contact conductance, transportation lines-to-ambient thermal conductance and vapor velocity in the grooves. Through sensitivity analysis, it was found that the operating temperature could be obtained by knowing only two accommodation factors (condenser-to-sink thermal contact conductance, transportation lines-to-ambient thermal conductance). The accommodation factors were obtained for each LHP using the power-cycling test data obtained at a chiller temperature of 5°C. The model capability in predicting the steady-state performance curves was confirmed through comparing the simulation and test data at the chiller temperatures of 10, 15 and 20°C. The operating temperature predictions had an average relative error of less than 4% across the applied powers and chiller temperatures.

The sensitivity studies of the modelling parameters were conducted to investigate their effects on the steady-state performance curve. The FCM operating temperatures were found to be primarily affected by the heat transfer characteristics in the condenser section; namely the thermal contact conductance, two-phase heat transfer coefficient and two-phase/vapor transition. The VCM temperatures were mostly influenced by the heat transfer between the liquid line and ambient. These sensitivity analyses together with the experimental validation demonstrated that the developed model is an effective tool in studying the steady-state performance characteristics of LHPs. The steady-state model was then utilized to provide initial conditions required to develop the transient model.

The transient model was developed using the similar assumptions as those of the steady-state model. The time-dependent governing equations were solved using an implicit approach. The evaporator wick and reservoir were modelled in several ways and their results were compared. These alternative modelling methods presented in this work are unique approaches to simulate the LHP transient behavior. Some of these methods and their comparisons were not published in the previous works. Each method demonstrated different ways of representing actual physical phenomena taking place in these components with varying degrees of complexity and accuracy.

The transient model algorithms comprised of two highly iterative schemes to obtain the state of each fluid cell and the operating temperature. The fluid cell scheme had the capability to detect the phase-change and executed one of the three phase-transition methods. The operating temperature scheme, similar to the steady-state model, used the heat leak criterion to obtain the operating temperature at each time step. The LHP operating limits were also checked to verify the calculated results.

For the final model validation, the one-cell-with-inertia (WM-3) method was used to represent the evaporator wick. The reservoir and phase-transition were modelled using the fluid charge (RM-2) and saturated (PTM-1) methods, respectively. The spatial resolution (cell lengths) and

accommodation factors were selected in accordance with the results obtained in the steady-state model. Several transient model parameters, such as the iteration convergence criteria and the temporal resolution factor, were identified to accelerate the convergence and handle numerical stability issues.

Similar to the steady-state model, the validation of the transient model was performed against the test data obtained from the power cycling and sink cycling scenarios. The prediction capability of the model was assessed according to the three performance criteria, which consisted of the transient temperature response, steady-state temperature and time lag. The quantitative study of the time lag was a novel method that was not found in the previously published works. The developed model had higher accuracy in the time-lag prediction than those of the previously published models. The transient model was noted to have a varying degree of success in capturing more complex LHP behavior such as the dips, overshoot and oscillations in the operating temperature, and these observations were discussed in detail.

The transient sensitivity analysis demonstrated that the thermal inertia of the heater block and condenser saddle influenced the time lag and transient temperature values strongly. The LHP oscillation characteristics were influenced by the thermal inertia and contact conductance between the heater block and evaporator saddle. The spatial sensitivity analysis indicated that the liquid line cell length affected the VCM temperature and the location of the two-phase/liquid interface when it was residing in the liquid line. It was also found that the condenser cell length affected the FCM operating temperature and the VCM oscillation characteristics through changing the location of the two-phase/liquid interface and the subcooling provided by the condenser. The vapor line cell length affected the transient results, most likely through discretization and rounding errors, when the cell length was set to either very small or large values.

## **6.1 Recommendations for future work**

The following areas are identified for further research to improve the presented work:

1. Although the model in its existing formulation is capable of capturing the temperature oscillations in some scenarios, the oscillation characteristics, including the amplitude and frequency, need to be predicted more accurately. This can be achieved by calculating the pressure drop inside the condenser through implementing more recent two-phase correlations in smaller pipes.
2. The convective boiling inside the liquid line needs to be addressed in the future version of the model. Some literature reported the possibility of the phase change from the subcooled liquid to the two-phase fluid inside the liquid line even though this condition did not occur during the experimental investigation. As a first step, a correlation for the boiling heat transfer coefficient should be added to the model.

3. While the main focus of this study was on the reservoir and evaporator saddle temperature, the existence of temperature oscillations with different amplitudes and time delays in the other LHP sections is of particular interest. The temperature and pressure predictions at the inlet and outlet of the other LHP sections should be validated to investigate further the principal contributor to the change of the oscillation characteristics across the LHP sections. For this purpose, additional sensors, such as a flowmeter and a differential pressure transducer, should be added to the experimental set-up to validate the prediction of the fluid properties across LHP. This investigation could potentially provide the required information to reduce or even eliminate undesirable oscillations in the operating temperature.
4. A specific module can be added to model the two-way PRV operation in detail. This module should contain a mathematical algorithm to impose the required operational constraints on solving the governing equations from the LHP start-up until reaching the set-point. The results could be validated via the experimental investigation. After the successful validation, the model could be utilized in designing more advanced two-way PRV or other similar devices. This topic is an important and timely area of research since many modern electronics such as bolometer and laser resonators require very tight temperature control, within  $\pm 0.1$  K.
5. The two-way PRV operation can be further investigated by changing its set-point. The change can be implemented by varying the PRV temperature or changing the pressure of the PRV control gas. The result of these assessments can provide more data points to refine the PRV modelling approach and enhance the model prediction of the LHP operation under the active PRV control.

## Appendixes

### Appendix A. LHP1 physical properties

Physical properties of LHP1 manufactured by Lavochkin Association, Russia:

Component	Property	Value
Working fluid	Type	Ammonia
	Amount	29.25 g
Evap. casing	Material	SS 304
	Cross section shape	circular
	Inner diameter	14 mm
	Outer diameter	15.3 mm
	Length	20.0 mm
Primary wick	Material	Nickle alloy
	Density	$8000 \frac{kg}{m^3}$
	Specific heat	$500 \frac{J}{kg K}$
	Conductivity	$14 \frac{wW}{m K}$
	Inner diameter	6 mm
	Outer diameter	14 mm
	Length	160 mm
	Porosity	60% (TBC)
	Effective pore diameter	1.8 $\mu$ m
	Permeability	$2 \times 10^{-14} m^2$
Vapor grooves	Number	4
	Length	160 mm
	Cross-section shape	Square

<b>Component</b>	<b>Property</b>	<b>Value</b>
	Cross-section size	Width: 1.5 mm Depth: 1.2 mm
	Location	Inside wick
Vapor line	Material	SS 304
	Length	800 mm
	Inner diameter	2 mm
	Outer diameter	3 mm
Condenser line	Material	SS 304
	Equivalent length	1000 mm
	Equivalent inner depth	1.5 mm
	Equivalent inner width	17.6 mm
Liquid line	Material	SS 304
	Length	800 mm
	Inner diameter	2 mm
	Outer diameter	3 mm
Reservoir	Material	SS 304
	Length	115 mm
	Cross-section shape	circular
	Inner diameter	22.7 mm
	Outer diameter	24.0 mm
Evaporator saddle	Material	Al 6082 T6
	Length	200 mm
	Inner diameter	15.3 mm
	Cross-section area	635.5 mm <sup>2</sup>
Heater	Material	Copper

Component	Property	Value
block	Length	200 mm
	Contact width with evaporator	50 mm
	Cross-section area	1044 mm <sup>2</sup>
	Location	Underneath of evaporator saddle
	Maximum heat transfer capability	750 W

## Appendix B. LHP2 physical properties

Physical properties of LHP2 manufactured by IberEspacio:

Component	Property	Value
Working fluid	Type	Ammonia
	Amount	27.2 g
Evap. casing	Material	AISI 316L
	Cross section shape	circular
	Inner diameter	14 mm
	Outer diameter	15.4 mm
	Length	174.5 mm
Primary wick	Material	Nickle alloy
	Density	$8000 \frac{kg}{m^3}$
	Specific heat	$500 \frac{J}{kg K}$
	Conductivity	$14 \frac{W}{m K}$
	Outer diameter	14 mm
	Length	160 mm
	Porosity	60%

Component	Property	Value
	Pore effective diameter	Approximately 1.8 $\mu\text{m}$
	Permeability	$3 \times 10^{-14} \text{ m}^2$
	Length	160 mm
Vapor line	Material	AISI 316L
	Length	1504 + 400 <sup>1</sup> mm
	Inner diameter	2 mm
	Outer diameter	3 mm
Condenser line	Material	Al 6063 T66
	Length	1187 mm
	Inner diameter	2.5 mm
	Outer diameter	3 mm
Liquid line	Material	AISI 316L
	Length	901 + 200 <sup>2</sup> mm
	Inner diameter	2 mm
	Outer diameter	3 mm
Reservoir	Material	AISI 316L
	Length	127 mm
	Cross-section shape	circular
	Inner diameter	19.5 mm
	Outer diameter	21.5 mm
PRV	Material	AISI 321
	Outer dimension	17 mm

---

<sup>1</sup> From condenser

<sup>2</sup> From condenser

<b>Component</b>	<b>Property</b>	<b>Value</b>
	Control fluid	Argon
	Set point Regulation point	29 °C 31 °C
	Type	two-way valve
Evaporator saddle	Material	Al 6082 T6
	Length	152.4 mm
	Inner diameter	14 mm
	Cross-section area	510 mm <sup>2</sup>
Heater block	Material	Al 6082 T6
	Length	152.4 mm
	Contact width with evaporator	51 mm
	Cross-section area	760 mm <sup>2</sup>
	Location	Underneath of evaporator saddle
	Maximum heat transfer capability	500 W

## References

- [1] S. Launay, V. Sartre, and J. Bonjour, "Parametric analysis of loop heat pipe operation: a literature review," *Int. J. Therm. Sci.*, vol. 46, no. 7, pp. 621–636, Jul. 2007, doi: 10.1016/j.ijthermalsci.2006.11.007.
- [2] D. A. Reay, P. A. Kew, and R. J. McGlen, *Heat pipes: theory, design and applications*, Sixth edition. Amsterdam: Butterworth-Heinemann, an imprint of Elsevier, 2014.
- [3] Yu. F. Mайдanik, "Loop heat pipes," *Appl. Therm. Eng.*, vol. 25, no. 5–6, pp. 635–657, Apr. 2005, doi: 10.1016/j.applthermaleng.2004.07.010.
- [4] M. Nishikawara, H. Nagano, and T. Kaya, "Transient Thermo-Fluid Modeling of Loop Heat Pipes and Experimental Validation," *J. Thermophys. Heat Transf.*, vol. 27, no. 4, pp. 641–647, Oct. 2013, doi: 10.2514/1.T3888.
- [5] K. Cheung, T. T. Hoang, J. Ku, and T. Kaya, "Thermal Performance and Operational Characteristics of Loop Heat Pipe (NRL LHP)," Jul. 1998, p. 981813, doi: 10.4271/981813.
- [6] S. Van Oost, B. Mullender, G. Bekaert, and J. C. Legros, "Secondary wick operation principle and performance mapping in LHP and FLHP evaporators," in *AIP Conference Proceedings*, Albuquerque, New Mexico (USA), 2002, vol. 608, pp. 94–103, doi: 10.1063/1.1449713.
- [7] Yu. Mайдanik, Yu. Fershtater, V. G. Pastukhov, K. Goncharov, O. Zagar, and Yu. Golovanov, "Thermoregulation of Loops with Capillary Pumping for Space Use," *SAE Trans.*, vol. 101, pp. 523–528, 1992.
- [8] Y. F. Mайдanik, Y. G. Fershtater, and K. A. Goncharov, "Capillary-pump loop for the systems of thermal regulation of spacecraft," Florence, Italy, Dec. 1991, pp. 87–92, Accessed: Jan. 16, 2020. [Online]. Available: <http://adsabs.harvard.edu/abs/1991secs.conf...87M>.
- [9] A. A. Orlov, K. A. Goncharov, E. Kotliarov, T. A. Tyklina, S. N. Ustinov, and Y. F. Mайдanik, "The loop heat pipe experiment on board the 'GRANAT' spacecraft," Noordwijk, The Netherlands, Aug. 1997, vol. 400, pp. 341–353, Accessed: Jan. 16, 2020. [Online]. Available: <http://adsabs.harvard.edu/abs/1997ESASP.400..341O>.
- [10] J. Ku, "Operating Characteristics of Loop Heat Pipes," Denver, USA, Jul. 1999, pp. 1999-01–2007, doi: 10.4271/1999-01-2007.
- [11] K. A. Goncharov, M. N. Nikitkin, O. A. Golovin, Yu. G. Fershtater, Yu. F. Mайдanik, and S. A. Piukov, "Loop Heat Pipes in Thermal Control Systems for 'OBZOR' Spacecraft," San Diego, California, Jul. 1995, p. 951555, doi: 10.4271/951555.
- [12] C. Baker, C. Butler, P. Jester, and E. Grob, "Geoscience Laser Altimetry System (GLAS) Loop Heat Pipe Anomaly and On Orbit Testing," presented at the 41st International Conference on Environmental Systems, Portland, Oregon, Jul. 2011, doi: 10.2514/6.2011-5209.
- [13] A. Torres, D. Mishkinis, and T. Kaya, "Mathematical model validation of a thermal architecture system connecting east/west radiators by flight data," *Appl. Therm. Eng.*, vol. 66, no. 1–2, pp. 1–14, May 2014, doi: 10.1016/j.applthermaleng.2014.01.050.
- [14] H. Ishikawa, T. Nomura, Y. Saito, H. Kawasaki, A. Okamoto, and R. Hatakenaka, "Heat transfer characteristics of a reservoir embedded loop heat pipe (Heat transfer characteristics of a deployable radiator for use on the ETS-VIII satellite while in orbit)," *Heat Transf.-Asian Res.*, vol. 40, no. 3, pp. 269–285, May 2011, doi: 10.1002/htj.20346.
- [15] S. Ueno, D. Khrustalev, P. Cologer, and R. Snyder, "Thermal-Vacuum Test Data For Jem/Maxi Loop Heat Pipe System With Two Radiators," Jun. 2008, pp. 2008-01–1999, doi: 10.4271/2008-01-1999.

- [16] T. Hoang, W. Armiger, R. Baldauff, B. Nguyen, D. Mahony, and W. Robinson, "Performance of COMMX Loop Heat Pipe on TacSat 4 Spacecraft," presented at the 42nd International Conference on Environmental Systems, San Diego, California, Jul. 2012, doi: 10.2514/6.2012-3498.
- [17] N. Iwata *et al.*, "Evaluation of In-Orbit Thermal Performance of X-Ray Astronomy Satellite 'Hitomi,'" *J. Spacecr. Rockets*, vol. 55, no. 1, pp. 77–84, 2018, doi: 10.2514/1.A33903.
- [18] A. Okamoto, J. Meléndez, and F. Romera, "Loop Heat Pipes for ASTRO-H/SXS," South Carolina, USA, Jul. 2017, p. 13, Accessed: Feb. 05, 2020. [Online]. Available: <https://ttu-ir.tdl.org/handle/2346/73107>.
- [19] M. Pennybacker, A. Ignatov, O. Jonasson, I. Gladkova, B. Petrenko, and Y. Kihai, "Mitigation of the GOES-17 ABI performance issues in the NOAA ACSPO SST products," in *Ocean Sensing and Monitoring XI*, May 2019, vol. 11014, p. 110140Q, doi: 10.1117/12.2521051.
- [20] B. P. d'Entremont and J. M. Ochterbeck, "[LHP Limits] Vapor pressure limits in capillary pumped loops.pdf," presented at the 14th International Heat Pipe Conference, Brazil, Apr. 2007.
- [21] T. Kaya and J. Goldak, "Numerical analysis of heat and mass transfer in the capillary structure of a loop heat pipe," *Int. J. Heat Mass Transf.*, vol. 49, no. 17, pp. 3211–3220, Aug. 2006, doi: 10.1016/j.ijheatmasstransfer.2006.01.028.
- [22] T. Kaya and D. Mishkinis, "Accurate temperature control using heat pipes," *Int Rev Mech Eng*, vol. 2, no. 1, pp. 104–112, 2008.
- [23] A. Torres, D. Mishkinis, A. Kulakov, F. Romera, C. Gregori, and T. Kaya, "Thermal control of loop heat pipe with pressure regulating valve," *Heat Pipe Sci. Technol. Int. J.*, vol. 1, no. 4, 2010, doi: 10.1615/HeatPipeScieTech.v1.i4.30.
- [24] W. B. Bienert, W. J. Krotiuk, and M. N. Nikitkin, "Thermal Control with Low Power, Miniature Loop Heat Pipes," Jul. 1999, pp. 1999-01–2008, doi: 10.4271/1999-01-2008.
- [25] M. K. Choi, "Thermal Vacuum/Balance Test Results of Swift BAT with Loop Heat Pipe Thermal System," presented at the 2nd International Energy Conversion Engineering Conference, Rhode Island, USA, Aug. 2004, Accessed: Jan. 16, 2020. [Online]. Available: <https://ntrs.nasa.gov/search.jsp?R=20040171444>.
- [26] M. Nikitkin and D. Wolf, "Development of LHP with Low Control Power," Jul. 2007, pp. 2007-01–3237, doi: 10.4271/2007-01-3237.
- [27] T. T. Hoang, T. A. O'Connell, J. Ku, C. D. Butler, and T. D. Swanson, "Miniature Loop Heat Pipes for Electronic Cooling," in *2003 International Electronic Packaging Technical Conference and Exhibition, Volume 2*, Maui, Hawaii, USA, Jan. 2003, pp. 517–525, doi: 10.1115/IPACK2003-35245.
- [28] A. Torres, D. Mishkinis, and T. Kaya, "Mathematical modeling of a new satellite thermal architecture system connecting the east and west radiator panels and flight performance prediction," *Appl. Therm. Eng.*, vol. 65, no. 1–2, pp. 623–632, Apr. 2014, doi: 10.1016/j.applthermaleng.2013.11.040.
- [29] K. A. Gongharov, A. Yu. Kochetkov, and V. N. Buz, "Development of Loop Heat Pipe with Pressure Regulator," Jul. 2006, pp. 2006-01–2171, doi: 10.4271/2006-01-2171.
- [30] M. Nikitkin, E. Kotlyarov, and G. Serov, "Basics of Loop Heat Pipe Temperature Control," Jul. 1999, pp. 1999-01–2012, doi: 10.4271/1999-01-2012.

- [31] F. Bodendieck, R. Schlitt, O. Romberg, K. Goncharov, V. Buz, and U. Hildebrand, "Precision Temperature Control with a Loop Heat Pipe," Jul. 2005, pp. 2005-01–2938, doi: 10.4271/2005-01-2938.
- [32] S. Launay and M. Vallée, "State-of-the-art experimental studies on loop heat pipes," *Front. Heat Pipes*, vol. 2, no. 1, Mar. 2011, doi: 10.5098/fhp.v2.1.3003.
- [33] J. Jose and R. Baby, "Recent advances in loop heat pipes : A review," *IOP Conf. Ser. Mater. Sci. Eng.*, vol. 396, p. 012060, Aug. 2018, doi: 10.1088/1757-899X/396/1/012060.
- [34] "- Recirculating Chillers - Kodiak® - Cooling Capacities of 825W-11kW - Lytron Inc." <https://www.lytron.com/products/Cooling-Systems-Standard/Recirculating-Chillers/Kodiak> (accessed Dec. 13, 2019).
- [35] "Model 9206, Multi-Range Programmable DC Power Supplies - B&K Precision." <https://www.bkprecision.com/products/power-supplies/9206-600w-multi-range-150v-10a-dc-power-supply.html> (accessed Dec. 13, 2019).
- [36] "Keithley Series 2700 Multimeter/Data Acquisition/Switch Systems | Tektronix." <https://www.tek.com/keithley-switching-and-data-acquisition-systems/keithley-2700-multimeter-data-acquisition-switch-sys> (accessed Dec. 13, 2019).
- [37] A. Torres, D. Mishkinis, and T. Kaya, "Mathematical modeling of a new satellite thermal architecture system connecting the east and west radiator panels and flight performance prediction," *Appl. Therm. Eng.*, vol. 65, no. 1–2, pp. 623–632, Apr. 2014, doi: 10.1016/j.applthermaleng.2013.11.040.
- [38] "Thermocouple types," <https://www.omega.ca/en/>. <https://www.omega.ca/en/resources/thermocouple-types> (accessed Dec. 13, 2019).
- [39] R. B. Abernethy, R. P. Benedict, and R. B. Dowdell, "ASME Measurement Uncertainty," *J. Fluids Eng.*, vol. 107, no. 2, pp. 161–164, Jun. 1985, doi: 10.1115/1.3242450.
- [40] American Society of Mechanical Engineers., *Test uncertainty*. New York, N.Y.: American Society of Mechanical Engineers, 2006.
- [41] I. L. Pioro and R. B. Duffey, Eds., "Back Matter," in *Heat Transfer & Hydraulic Resistance at Supercritical Pressures in Power Engineering Applications*, ASME Press, 2007, p. 0.
- [42] J. T. Nakos, "Uncertainty analysis of thermocouple measurements used in normal and abnormal thermal environment experiments at Sandia's Radiant Heat Facility and Lurance Canyon Burn Site.," SAND2004-1023, 918777, Apr. 2004. doi: 10.2172/918777.
- [43] H. Jouhara and R. Meskimmon, "An investigation into the use of water as a working fluid in wraparound loop heat pipe heat exchanger for applications in energy efficient HVAC systems," *Energy*, vol. 156, pp. 597–605, Aug. 2018, doi: 10.1016/j.energy.2018.05.134.
- [44] E. W. Lemmon, I. H. Bell, M. L. Huber, and M. O. McLinden, *NIST Standard Reference Database 23: Reference Fluid Thermodynamic and Transport Properties-REFPROP, Version 10.0*, National Institute of Standards and Technology. 2018.
- [45] I. E. Idel'chik and A. S. Ginevskii, *Handbook of hydraulic resistance*, 4th ed. rev. and augmented. Redding, CT: Begell House, 2007.
- [46] S. W. Churchill, "Friction factor equation spans all fluid-flow regimes," *Chem Eng*, vol. 84, no. 24, pp. 94–95, 1977.
- [47] M. M. Awad and Y. S. Muzychka, "Effective property models for homogeneous two-phase flows," *Exp. Therm. Fluid Sci.*, vol. 33, no. 1, pp. 106–113, Oct. 2008, doi: 10.1016/j.expthermflusci.2008.07.006.
- [48] R. W. Lockhart and R. C. Martinelli, "Proposed correlation of data for isothermal two-phase, two-component flow in pipes," *Chem. Eng. Prog.*, vol. 45, no. 1, pp. 39–48, 1949.

- [49] D. Chisholm, "A theoretical basis for the Lockhart-Martinelli correlation for two-phase flow," *Int. J. Heat Mass Transf.*, vol. 10, no. 12, pp. 1767–1778, Dec. 1967, doi: 10.1016/0017-9310(67)90047-6.
- [50] J. E. Vollrath, P. S. Hrnjak, and T. A. Newell, "An Experimental Investigation of Pressure Drop and Heat Transfer in an In-Tube Condensation System of Pure Ammonia," Air Conditioning and Refrigeration Center, University of Illinois, Urbana, IL, ACRC CR-51, 2003.
- [51] "Absolute Pipe Roughness," *EnggCyclopedia*, Sep. 17, 2011. <https://www.enggcyclopedia.com/2011/09/absolute-roughness/> (accessed Jan. 03, 2020).
- [52] E. Ungar and J. Cornwell, "Two-phase pressure drop of ammonia in small diameter horizontal tubes," presented at the 28th Joint Propulsion Conference and Exhibit, Nashville, TN, U.S.A., Jul. 1992, doi: 10.2514/6.1992-3891.
- [53] D. K. Edwards, V. Denny, and A. Mills, *Transfer processes : an introduction to diffusion, convection, and radiation*. New York : Holt, Rinehart and Winston, 1973.
- [54] V. Gnielinski, "New equations for heat and mass transfer in the turbulent flow in pipes and channels," *NASA STIRecon Tech. Rep. A*, vol. 75, pp. 8–16, 1975.
- [55] T. L. Bergman and F. P. Incropera, Eds., *Fundamentals of heat and mass transfer*, 7th ed. Hoboken, NJ: Wiley, 2011.
- [56] D. P. Traviss, A. G. Baron, and W. M. Rohsenow, "Forced-convection condensation inside tubes," Cambridge, Mass. : M.I.T. Heat Transfer Laboratory, [1971], Technical Report, 1971. Accessed: Oct. 21, 2019. [Online]. Available: <https://dspace.mit.edu/handle/1721.1/61476>.
- [57] R. C. Martinelli, "Prediction of pressure drop during forced-circulation boiling of water," *Trans ASME*, vol. 70, pp. 695–702, 1948.
- [58] C. Y. Park and P. Hrnjak, "NH<sub>3</sub> in-tube condensation heat transfer and pressure drop in a smooth tube," *Int. J. Refrig.*, vol. 31, no. 4, pp. 643–651, Jun. 2008, doi: 10.1016/j.ijrefrig.2008.01.005.
- [59] J. R. Thome, J. El Hajal, and A. Cavallini, "Condensation in horizontal tubes, part 2: new heat transfer model based on flow regimes," *Int. J. Heat Mass Transf.*, vol. 46, no. 18, pp. 3365–3387, Aug. 2003, doi: 10.1016/S0017-9310(03)00140-6.
- [60] J. El Hajal, J. R. Thome, and A. Cavallini, "Condensation in horizontal tubes, part 1: two-phase flow pattern map," *Int. J. Heat Mass Transf.*, vol. 46, no. 18, pp. 3349–3363, Aug. 2003, doi: 10.1016/S0017-9310(03)00139-X.
- [61] B. M. Fronk and S. Garimella, "Heat Transfer and Pressure Drop During Condensation of Ammonia in Microchannels," Jul. 2013, pp. 399–409, doi: 10.1115/MNHMT2012-75265.
- [62] B. M. Fronk and S. Garimella, "Condensation of ammonia and high-temperature-glide ammonia/water zeotropic mixtures in minichannels – Part I: Measurements," *Int. J. Heat Mass Transf.*, vol. 101, pp. 1343–1356, Oct. 2016, doi: 10.1016/j.ijheatmasstransfer.2016.05.049.
- [63] J. P. Holman, *Heat transfer*. New York: McGraw-Hill, 1997.
- [64] B. Siedel, V. Sartre, and F. Lefèvre, "Literature review: Steady-state modelling of loop heat pipes," *Appl. Therm. Eng.*, vol. 75, pp. 709–723, Jan. 2015, doi: 10.1016/j.applthermaleng.2014.10.030.
- [65] T. Kaya and T. T. Hoang, "Mathematical modeling of loop heat pipes and experimental validation," *J. Thermophys. Heat Transf.*, vol. 13, no. 3, pp. 314–320, Jul. 1999, doi: 10.2514/2.6461.
- [66] T. Kaya and J. Ku, "Thermal operational characteristics of a small-loop heat pipe," *J. Thermophys. Heat Transf.*, vol. 17, no. 4, pp. 464–470, Oct. 2003, doi: 10.2514/2.6805.

- [67] P.-Y. A. Chuang, “An improved steady-state model of loop heat pipes based on experimental and theoretical analyses,” Doctor of Philosophy, The Pennsylvania State University, 2003.
- [68] Z. G. Qu, G. Chen, L. Zhou, and J. Y. Miao, “Numerical study on the operating characteristics of cryogenic loop heat pipes based on a one-dimensional heat leak model,” *Energy Convers. Manag.*, vol. 172, pp. 485–496, Sep. 2018, doi: 10.1016/j.enconman.2018.07.036.
- [69] L. Zhou, Z. G. Qu, G. Chen, J. Y. Huang, and J. Y. Miao, “One-dimensional numerical study for loop heat pipe with two-phase heat leak model,” *Int. J. Therm. Sci.*, vol. 137, pp. 467–481, Mar. 2019, doi: 10.1016/j.ijthermalsci.2018.12.019.
- [70] A. A. Adoni, A. Ambirajan, V. S. Jasvanth, D. Kumar, P. Dutta, and K. Srinivasan, “Thermohydraulic modeling of capillary pumped loop and loop heat pipe,” *J. Thermophys. Heat Transf.*, vol. 21, no. 2, pp. 410–421, Apr. 2007, doi: 10.2514/1.26222.
- [71] A. A. Adoni, A. Ambirajan, V. S. Jasvanth, D. Kumar, and P. Dutta, “Effects of mass of charge on loop heat pipe operational characteristics,” *J. Thermophys. Heat Transf.*, vol. 23, no. 2, pp. 346–355, Apr. 2009, doi: 10.2514/1.41618.
- [72] A. A. Adoni, A. Ambirajan, V. S. Jasvanth, D. Kumar, and P. Dutta, “Theoretical studies of hard filling in loop heat pipes,” *J. Thermophys. Heat Transf.*, vol. 24, no. 1, pp. 173–183, Jan. 2010, doi: 10.2514/1.44382.
- [73] L. Bai, G. Lin, H. Zhang, and D. Wen, “Mathematical modeling of steady-state operation of a loop heat pipe,” *Appl. Therm. Eng.*, vol. 29, no. 13, pp. 2643–2654, Sep. 2009, doi: 10.1016/j.applthermaleng.2008.12.040.
- [74] L. Bai, G. Lin, and D. Wen, “Parametric analysis of steady-state operation of a CLHP,” *Appl. Therm. Eng.*, vol. 30, no. 8–9, pp. 850–858, Jun. 2010, doi: 10.1016/j.applthermaleng.2009.12.014.
- [75] L. Bai, G. Lin, Z. Mu, and D. Wen, “Theoretical analysis of steady-state performance of a loop heat pipe with a novel evaporator,” *Appl. Therm. Eng.*, vol. 64, no. 1–2, pp. 233–241, Mar. 2014, doi: 10.1016/j.applthermaleng.2013.12.052.
- [76] L. Bai, J. Guo, G. Lin, J. He, and D. Wen, “Steady-state modeling and analysis of a loop heat pipe under gravity-assisted operation,” *Appl. Therm. Eng.*, vol. 83, pp. 88–97, May 2015, doi: 10.1016/j.applthermaleng.2015.03.014.
- [77] R. Hodot, V. Sartre, F. Lefevre, and C. Sarno, “3D modeling and optimization of a loop heat pipe evaporator,” *Int. J. Heat Pipe Sci. Technol.*, vol. 5, no. 1–4, pp. 335–342, 2014, doi: 10.1615/HeatPipeScieTech.v5.i1-4.370.
- [78] N. Rivière, V. Sartre, and J. Bonjour, “Fluid mass distribution in a loop heat pipe with flat evaporator,” presented at the 15th International Heat Pipe Conference, Clemson, South Carolina (USA), 2010.
- [79] B. Siedel, V. Sartre, and F. Lefèvre, “Numerical investigation of the thermohydraulic behaviour of a complete loop heat pipe,” *Appl. Therm. Eng.*, vol. 61, no. 2, pp. 541–553, Nov. 2013, doi: 10.1016/j.applthermaleng.2013.08.017.
- [80] B. Siedel, V. Sartre, and F. Lefèvre, “Complete analytical model of a loop heat pipe with a flat evaporator,” *Int. J. Therm. Sci.*, vol. 89, pp. 372–386, Mar. 2015, doi: 10.1016/j.ijthermalsci.2014.11.014.
- [81] J. Esarte, A. Bernardini, J. M. Blanco, and R. Sancibrian, “Optimizing the design for a two-phase cooling loop heat pipe: Part A: Numerical model, validation and application to a case

- study,” *Appl. Therm. Eng.*, vol. 99, pp. 892–904, Apr. 2016, doi: 10.1016/j.applthermaleng.2016.01.150.
- [82] C.-Y. Weng and T.-S. Leu, “Two-phase flow pattern based theoretical study of loop heat pipes,” *Appl. Therm. Eng.*, vol. 98, pp. 228–237, Apr. 2016, doi: 10.1016/j.applthermaleng.2015.11.124.
- [83] K. Fukushima and H. Nagano, “New evaporator structure for micro loop heat pipes,” *Int. J. Heat Mass Transf.*, vol. 106, pp. 1327–1334, Mar. 2017, doi: 10.1016/j.ijheatmasstransfer.2016.10.116.
- [84] N. S. Ramasamy, P. Kumar, B. Wangaskar, S. Khandekar, and Y. F. Maydanik, “Miniature ammonia loop heat pipe for terrestrial applications: Experiments and modeling,” *Int. J. Therm. Sci.*, vol. 124, pp. 263–278, 2018, doi: <https://doi.org/10.1016/j.ijthermalsci.2017.10.018>.
- [85] R. Singh, A. Akbarzadeh, C. Dixon, and M. Mochizuki, “Theoretical modelling of miniature loop heat pipe,” *Heat Mass Transf.*, vol. 46, no. 2, pp. 209–224, Dec. 2009, doi: 10.1007/s00231-009-0504-y.
- [86] K. R. Wrenn, S. J. Krein, T. T. Hoang, and R. D. Allen, “Verification of a Transient Loop Heat Pipe Model,” Jul. 1999, pp. 1999-01–2010, doi: 10.4271/1999-01-2010.
- [87] T. Hoang and J. Ku, “Transient Modeling of Loop Heat Pipes,” presented at the 1st International Energy Conversion Engineering Conference (IECEC), Portsmouth, Virginia, Aug. 2003, doi: 10.2514/6.2003-6082.
- [88] T. T. Hoang, R. W. Baldauff, and D. R. Mahony, “Analytical Model for Transient Loop Heat Pipe Operation,” presented at the 53rd AIAA Aerospace Sciences Meeting, Kissimmee, Florida, Jan. 2015, doi: 10.2514/6.2015-0707.
- [89] S. Launay, V. Platel, S. Dutour, and J.-L. Joly, “Transient Modeling of Loop Heat Pipes for the Oscillating Behavior Study,” *J. Thermophys. Heat Transf.*, vol. 21, no. 3, pp. 487–495, Jul. 2007, doi: 10.2514/1.26854.
- [90] G. L. Wedekind, B. L. Bhatt, and B. T. Beck, “A system mean void fraction model for predicting various transient phenomena associated with two-phase evaporating and condensing flows,” *Int. J. Multiph. Flow*, vol. 4, no. 1, pp. 97–114, Mar. 1978, doi: 10.1016/0301-9322(78)90029-0.
- [91] V. V. Vlassov and R. R. Riehl, “Mathematical model of a loop heat pipe with cylindrical evaporator and integrated reservoir,” *Appl. Therm. Eng.*, vol. 28, no. 8–9, pp. 942–954, Jun. 2008, doi: 10.1016/j.applthermaleng.2007.07.016.
- [92] T. Kaya, R. Pérez, C. Gregori, and A. Torres, “Numerical simulation of transient operation of loop heat pipes,” *Appl. Therm. Eng.*, vol. 28, no. 8–9, pp. 967–974, Jun. 2008, doi: 10.1016/j.applthermaleng.2007.06.037.
- [93] N. Blet, V. Platel, V. Ayel, Y. Bertin, and C. Romestant, “Transient Modeling of a Capillary Pumped Loop for Terrestrial Applications,” *J. Heat Transf.*, vol. 138, no. 7, pp. 072802–072802–15, Apr. 2016, doi: 10.1115/1.4032960.
- [94] M. Bernagozzi, S. Charmer, A. Georgoulas, I. Malavasi, N. Michè, and M. Marengo, “Lumped parameter network simulation of a Loop Heat Pipe for energy management systems in full electric vehicles,” *Appl. Therm. Eng.*, vol. 141, pp. 617–629, Aug. 2018, doi: 10.1016/j.applthermaleng.2018.06.013.
- [95] S. Meinicke, P. Knipper, C. Helfenritter, and T. Wetzel, “A lean approach of modeling the transient thermal characteristics of Loop Heat Pipes based on experimental investigations,” *Appl. Therm. Eng.*, vol. 147, pp. 895–907, Jan. 2019, doi: 10.1016/j.applthermaleng.2018.10.123.

